

Computational chemistry for complex systems: open-shell molecules to conjugated organic materials

Peter Repiščák

Submitted for the degree of Doctor of Philosophy
(Chemistry)

Heriot-Watt University

School of Engineering and Physical Sciences

July 2017

The copyright in this thesis is owned by the author. Any quotation from the thesis or use of any of the information contained in it must acknowledge this thesis as the source of the quotation or information.

Abstract

This thesis focuses on two different, but equally challenging, areas of computational chemistry: transition metal organic molecule interactions and parameterisation of organic conjugated polymers for molecular dynamics simulations. The metal-binding properties are important for understanding of biomolecular action of type 2 diabetes drug and development of novel protocols for redox calculations of copper systems. In this area the challenge is mainly related to the complex electronic structure of the open-shell transition metals. The main challenges for the parameterisation of conjugated polymers are due to the size of the studied systems, their conjugated nature and inclusion of environment.

Metal-binding properties as well as electronic structures of copper complexes of type 2 diabetes drug metformin (Metf) and other similar, but often inactive, compounds were examined using DFT method. It was found that for neutral compounds it is not possible to explain the differences in their biological effects solely by examining the copper-binding properties. Further, the proposed mechanism potentially explaining the difference in the biomolecular mode of action involves a possible deprotonation of biguanide and Metf compounds under higher mitochondrial pH which would lead to formation of more stable copper complexes and potentially affecting the mitochondrial copper homeostasis. In addition, redox properties of copper-biguanide complexes could interfere with the sensitive redox chemistry or interact with important metalloproteins in the mitochondria.

Understanding the copper-binding properties is also important for a systematic development and testing of computational protocols for calculations of reduction potentials of copper complexes. Copper macrocyclic complexes previously used as model systems for redox-active metalloenzymes and for which experimentally determined redox potentials are available were used as model systems. First adequacy of using single-reference methods such as DFT was examined for these systems and then various DFT functionals and basis sets were tested in order to develop accurate redox potential protocol. It was shown that good relative cor-

relations were obtained for several functionals while the best absolute agreement was obtained with either the M06/cc-pVTZ functional with the SMD or either M06L or TPSSSTPSS functional with cc-pVTZ basis set and the PCM solvation model.

Organic conjugated polymers have a great potential due to their application in organic optoelectronics. Various wavefunction and DFT methods are utilized in order to systematically develop parameterisation scheme that can be used to derive selected force-field parameters such as torsional potentials between monomer units that are critical for these systems and partial charges. Moreover, critical points of such a parameterisation are addressed in order to obtain accurate MD simulations that could provide valuable insight into material morphology and conformation that affect their optical properties and conductivity. It was shown that a two step approach of geometry optimisation with CAM-B3LYP/6-31G* and single point (SP) energy scan with CAM-B3LYP/cc-pVTZ is able to yield accurate dihedral potentials in agreement with the potentials calculated using higher level methods such as MP2 and CBS limit CCSD(T). Further, investigating partial charge distribution for increasing backbone length of fluorene and thiophene it has been found that it is possible to obtain a three residue model of converged charge distributions using the RESP scheme. The three partial charge residues can be then used to build and simulate much longer polymers without the need to re-parametrize charge distributions. In the case of side-chains, it was found that it is not possible to obtain converged charge sets for side-chain lengths of up to 10 carbons due to the strong asymmetry between the side-chain ends. Initial validation of derived force-field parameters performed by simulations of 32mers of fluorene with octyl side-chains (PF8) and thiophene with hexyl side-chains (P3HT) in chloroform and calculation of persistence lengths and end-to-end lengths showed close correspondence to experimentally obtained values.

Acknowledgements

I would like to express my deepest gratitude to all those who made this thesis and underlying work possible. Especially, I would like to thank my supervisor Prof. Martin Paterson for his guidance, expertise and infinite support and patience that helped me through the PhD. Further, I would like to thank all of my colleagues and friends for many valuable discussions and whose stimulating suggestions and guidance helped me during my research and writing of this thesis.

Most importantly, I would like to thank my family, and especially my wife Barbora for her patience, support and supply of hot food and beverages. Having you by my side makes my life wonderful.

Contents

Contents	v
1 Introduction to Computational Chemistry	1
2 Methods	6
2.1 <i>Ab initio</i> Methods	6
2.1.1 Schrödinger Equation	6
2.1.2 The Adiabatic and Born-Oppenheimer Approximation	8
2.1.3 Hartree-Fock Method	11
2.1.4 Configuration Interaction	18
2.1.5 Many Body Perturbation Theories	20
2.1.6 Coupled Cluster	24
2.1.7 Multi-Configuration Self-Consistent Field	27
2.1.8 Basis Sets	28
2.1.9 Local Methods	31
2.1.10 Frequency Calculations	32
2.1.11 Thermochemistry	33
2.2 Density Functional Theory	36
2.2.1 The Hohenberg-Kohn Theorems	37
2.2.2 Orbital Free Approaches	38
2.2.3 Kohn-Sham Self-consistent Field Methodology	38
2.2.4 Approximations to the Exchange-correlation Functional	39
2.2.5 Dispersion correction DFT (D-DFT)	41
2.3 Molecular Dynamics	42
2.3.1 Force fields	43
2.3.2 Potential Energy and Equations of Motion	44
2.3.3 Molecular Dynamics Simulations	45
2.4 Hybrid QM/MM Methods	47
References	48
3 Biomolecular mode of action of Metformin	51
3.1 Introduction	51

3.2	Copper Binding Properties	53
3.3	Computational Details	55
3.4	Results	56
3.4.1	Comparison of X-ray Structures and Computed Complexes	56
3.4.2	Binding Energies of Cu ^{I/II} Complexes	60
3.4.3	Electronic Properties	63
3.4.4	ESP Maps	65
3.4.5	Discussion and Conclusion	66
	References	68
4	Protocols for Understanding the Redox Behaviour of Copper Con-	
	taining systems	71
4.1	Introduction	71
4.2	Computational Electrochemistry	73
4.3	Results and Discussion	76
4.3.1	Assessing Appropriateness of DFT for Redox Potential Cal-	
	culations.	77
4.3.2	Basis Set Dependence of Calculated Redox Potentials	78
4.3.3	Solvation Models	87
4.3.4	Effect of S for N substitution	90
4.4	Conclusion	93
4.5	Appendix: Comparison of X-ray Structures and Computed Complexes	95
	References	102
5	Development of general low-cost parameterisation scheme for MD	
	simulations of conjugated materials	107
5.1	Introduction	107
5.2	Generating Molecular Dynamics Parameters	110
5.3	Determination of the Appropriate Methodology.	113
5.3.1	Technical Details	113
5.3.2	Results of Methodology Testing	115
5.3.3	Results of Basis Set Testing	123
5.3.4	Results of Dispersion Corrected DFT	126
5.3.5	Discussion and Conclusion	127
5.4	Determining Dihedral Profiles	128
5.5	Partial Charge Calculations	133
5.6	Force-Field Implementation	136
5.7	Molecular Dynamics Results	141
5.8	Discussion and Conclusion	145
	References	146
6	Summary and Future Work	152

Chapter 1

Introduction to Computational Chemistry

Computational chemistry is a research field which uses a broad range of computational techniques, ranging from quantum mechanics to more empirical methods, in order to solve chemically related problems. Nowadays, computational chemistry is an invaluable tool not only able to complement experiments and provide detailed insight into experimental results, but also make novel predictions and help to design new materials and reactions. For example, it can be applied to predict NMR, EPR, rotational, vibrational and electronic spectra. Further, calculating thermodynamic quantities can provide information about activation energies of reactions, binding affinities of complexes, reduction potentials and pK_a values.

The choice of technique strongly depends on the many aspects of the system of interest as well as question asked. Different levels of details about the studied system are required when studying, for example, reaction mechanisms, spectroscopic transition energies and intensities, solvent diffusion and protein folding. The first two would require a detailed understanding of electronic structure, whereas atomistic or even more approximate coarse-grain picture may be sufficient for the question of solvent diffusion and protein folding. Moreover, some systems and calculations can pose challenges due to complex electronic structure such as open-shell states, low-spin metal complexes and excited states; and therefore more approximate methods may not be able to address these challenges. On the other hand, system size and the need to account for environmental effects can be the limiting factor for other systems.

Ideally, solving the non-relativistic time-dependent Schrödinger equation it would be possible to obtain the information about a molecular system with a very high accuracy, however, anything more complex than the smallest few electron system

cannot be handled at this *ab initio* level. Therefore, in order to solve more complex and chemically interesting systems some approximations need to be introduced. For example, a full configuration interaction (CI) which is able to yield exact non-relativistic description of the many electron system would be a suitable candidate. Unfortunately, a full CI is computationally extremely expensive method for any but the smallest gas phase molecules. For instance, if the full CI is applied to a water molecule more than 3.8×10^8 configurations would need to be calculated. Thus, in order to reduce the CI space and at the same time being able to accurately calculate, for example, open-shell systems or excited state phenomena with multi-reference character (different configurations have similar importance) methods such as Multi-reference CI (MRCI), Restricted Active Space SCF (RASSCF), Complete Active Space Self-Consistent (CASSCF) and Monte Carlo CI must be applied. Although, these methods can potentially yield approximate CI wavefunctions and energies that are as close as possible to the exact values, they can still be used only for small systems. Moreover, the first three are not black-box methods and can be especially challenging to use and when defining the important configurations (active spaces). In the case when one dominant configuration is able to accurately describe the system a single reference methods such as truncated CI (CISD), Møller–Plesset (MP2) or coupled-cluster (CCSD, CCSD(T)) may be applied to small to medium sized systems (tens of atoms). Using local variants of some of these methods such as local MP2, CCSD, CCSD(T) it may be possible to extend them to study larger systems, however, at the same time these methods become less black-box and more challenging to use. Density Functional Theory (DFT), which uses the electronic density as a central variable, is very popular single-reference method applicable to large systems (potentially hundreds of atoms). However, due to the fact that the exact functionals are unknown and there is usually no systematic way of improving obtained results by, for example, improving the size of basis set one needs to perform a benchmark of various functionals in order to assess their accuracy and adequacy for the studied system.

As mentioned previously size of the studied system is another important aspect to consider when deciding which method to use. For example, highly accurate *ab initio* methods can be applied to system of few atoms, but as the system size increases more approximations need to be introduced or even replaced by empirical parameters. Force-field methods is a family of methods using either experimentally or *ab initio* derived parameters to describe atomic interaction and the classical mechanics to describe the motion of atoms. These methods are applicable to simulations of molecular systems potentially consisting of thousands of atoms. However, due to the quantum phenomena being usually neglected in force-field methods these cannot be used to study, for example, photochemistry and events such as bond formation/breaking.

Environmental effects is yet another aspect one needs to consider when designing computational experiment. For instance, environment surrounding a photoactive chromophore, whether the photoactive molecule is in a solvent or embedded in a protein, can significantly affect spectroscopic and photodynamical properties. The electronic and molecular structure of a solute, can be influenced either directly through electrostatic interaction (e.g. polarisation by environment) or indirectly by imposed steric constraints on the solute geometry. It is possible to include some environmental effects in the quantum mechanics calculations usually in a form of implicit solvation where solvent is defined as a structureless dielectric continuum. In the case of force-field calculations, such as molecular dynamics simulations, a solvent is commonly included as explicit solvent or a combination of explicit/implicit solvent.

In order to realistically model, for example, complex biological systems with all the necessary environmental effects and to avoid unreasonable computational costs a so-called hybrid schemes are often employed. The hybrid techniques allow a more robust way of considering the active site (e.g. chromophore) and the surrounding environment (e.g. protein) by treating a system of interest at different levels of theory. For example, a part where (photo)chemical reaction occurs is investigated with more accurate QM method and the rest with computationally cheaper and usually less accurate QM, molecular mechanical, semi-empirical methods or even hybrid explicit/implicit solvent setup. Hybrid methods allow to apply advantages from both worlds and treat much larger systems than it would be possible with QM alone and study, for example, reactions and photochemical processes, which would not be possible with force-field methods on their own. However, the main disadvantage of these methods is they are not black-box and therefore require more expertise and deeper insight into the studied system.

Another important aspect is whether one is interested in static equilibrium properties or dynamic properties of a system. Most of the methods mentioned above allow description of important stationary points of a studied system on a potential energy surface(s) and adiabatic (potentially also non-adiabatic) events connecting them. However, in order to follow, for example, the excited state reaction path in details, explore the configurational space and determine the time scales of various phenomena it is necessary to reach for methods able to simulate the dynamic processes. In photochemistry, two main classes of methods based on whether the nuclei are treated as classical (often with the inclusion of quantum effects in semi-classical approaches) or quantum particles are trajectory-based approaches and wavepacket dynamics. The wavepacket propagation methods are computationally very demanding due to the complete QM solution given in full dimensionality and thus applicable only to small number of nuclear coordinates. From the force-field methods, for example, molecular dynamics allows to explore the configurational space and

generate ensembles from which various properties can be calculated. However, classical molecular dynamics with predefined potentials is facing some drawbacks such as need to account for all the different interatomic interactions of the studied system as well as inability to account for quantum effects. Therefore, a family of *ab initio* molecular dynamics methods is unifying molecular dynamics and *ab initio* methods by computing the forces acting on the nuclei using, for example, DFT method. These forces are calculated "on-the-fly" as the molecular dynamics trajectory is generated. Although, these methods present some advantages over the classical molecular dynamics, usually much smaller systems and shorter timescales can be studied.

In this thesis two different areas on the scale of computational chemistry are explored. The first is related to understanding of transition metal organic molecule interactions which are important in drug research and development of new protocols for redox potential calculations of copper systems. In this part the focus is on using accurate *ab initio* methods and the complexity mainly comes from open-shell transition metal systems with potential multi-reference character. The second area focuses on the development of schemes for molecular dynamics parameter derivation of conjugated materials in order to advance the field by allowing dynamics simulation to start to understand how conformation affects morphology. This is especially important as, for example, optical properties and conductivity are sensitive to intra-molecular conjugation and excitation transfer dynamics is affected by the inter-molecular alignment and separation. In this part the challenges and complexity mainly comes from the size of the studied systems and inclusion of the environment.

In the chapter 3 computational techniques of quantum chemistry are applied in order to examine metal-binding properties of important type 2 diabetes drug metformin and structurally similar compounds. The work in this chapter follows a previously published experimental study which points toward the important link between the copper-binding properties of these compounds and their biological effect. This chapter answers some of the observed effects by examining the electronic structures of the studied compounds and their copper-binding energies. Further, potential mechanisms involving metformin deprotonation and metformin-copper redox properties are proposed that could explain the specific biological effects of metformin drug and direct the future research.

Chapter 4 focuses on a systematic development and testing of computational protocol for calculation of reduction potentials of copper complexes. This chapter follows the need for accurate redox potential calculations of copper-binding complexes and indirectly stems from the discovery of previous chapter where redox properties are

implied as one of a potential mechanism explaining biological effects of the metformin. Copper macrocyclic complexes previously used as model systems for redox-active metalloenzymes, such as blue copper proteins involved in the photosynthesis in green plants, and for which experimentally determined redox potentials are available were used as model systems in this chapter. Further, some aspects of accurate calculations of redox potentials of copper complexes are addressed and discussed. This involves, for example, potential multi-reference character of metal-binding systems, spin contamination of open-shell molecules and appropriate choice of method, basis set and solvation.

Chapter 5 is distinct from the previous chapters as its main focus is development of scheme that can be used to obtain force-field parameters for simulations of large organic conjugated polymers with potential application in opto-electronic materials. These polymers are of great interest in rapidly expanding field of organic-based opto-electronics. However, due to the size of studied system (hundreds of atoms) techniques of classical molecular dynamics are more appropriate in order to understand and predict macroscopic properties based on the detailed knowledge of structure-property relationship at atomic level. This chapter first systematically tests and establish various *ab initio* computational methods required in order to obtain accurate critical force-field parameters. In the next step, after force-field parameters are obtained these are validated against available experimental data.

Chapter 2

Methods

In the following chapter basic computational theory used in the experimental part is introduced. The first part describes *ab initio* wave function based methods. In the second part Density Functional Theory is introduced. The chapter finishes with the basic concepts of molecular dynamics theory and hybrid approaches combining quantum mechanical and classical mechanical methods.

2.1 *Ab initio* Methods

Ab initio ("from the beginning" or "from first principles") methods apply the theory of quantum mechanics in order to predict the properties of atomic and molecular systems and to solve problems in chemistry. In quantum chemistry the wave function, Ψ , is a central variable that contains all the measurable information about a chemical system. It is used in the Schrödinger equation which plays the role of the equation of motion (Newton's laws in classical mechanics) and describes the evolution of QM system in time.¹

2.1.1 Schrödinger Equation

The time-dependent Schrödinger equation (TDSE) involves differentiation with respect to both time and position:

$$\overbrace{\left[-\frac{\hbar^2}{2m}\Delta + V(\mathbf{r}, t) \right]}^{\hat{H}(\mathbf{r}, t)} \Psi(\mathbf{r}, t) = i\frac{\partial\Psi(\mathbf{r}, t)}{\partial t} \quad (2.1)$$

where $\hat{H}(\mathbf{r}, t)$ is the Hamiltonian operator[†], the Laplacian is: $\Delta = \nabla^2 \equiv \frac{\partial^2}{\partial x^2} + \frac{\partial^2}{\partial y^2} + \frac{\partial^2}{\partial z^2}$. In most cases, such as systems mainly composed of the first and the second row elements, it is sufficient to take the non-relativistic Hamiltonian as the velocities are small enough for the relativistic effects to be neglected.² The wave function $\Psi(\mathbf{r}, t)$ is a function of particle position, it is not an observable quantity, but the square modulus of the wave function (the product of the wave function with its complex conjugate), $|\Psi|^2 = |\Psi^*\Psi|$, yields the probability of finding the particle at that position \mathbf{r} at a given time t . In addition, the normalized integral of this probability density over all space must be unity (which simply means that the particle must be somewhere in space). And in order to obtain a physically relevant solution of the SE, the wave function must also be continuous, single-valued and antisymmetric with respect to the interchange of electrons.³

In the case of a time-independent potential energy operator we can separate the wave function into a spatial and a phase factor part, $\Psi(\mathbf{r}, t) = \Psi(\mathbf{r})e^{-iEt}$, and after neglecting the phase factor we obtain the time-independent Schrödinger equation (TISE, or in the rest of the text just SE):

$$\hat{H}(\mathbf{r})\Psi(\mathbf{r}) = E(\mathbf{r})\Psi(\mathbf{r}) \quad (2.2)$$

The \hat{H} contains the sum of terms for nuclei and electron kinetic energies and potential energy terms: Coulomb repulsion and attraction of charged particles:

$$\hat{H} = \left(- \sum_A \frac{\hbar^2}{2m_A} \nabla_A^2 - \sum_i \frac{\hbar^2}{2m_e} \nabla_i^2 \right) + \frac{e^2}{4\pi\epsilon_0} \left(\sum_{A<B} \frac{Z_A Z_B}{|\mathbf{R}_A - \mathbf{R}_B|} + \sum_{i<j} \frac{1}{|\mathbf{r}_i - \mathbf{r}_j|} - \sum_i \sum_A \frac{Z_A}{|\mathbf{R}_A - \mathbf{r}_i|} \right) \quad (2.3)$$

where A and B run over all nuclei, i and j run over all electrons, \hbar is Planck's constant divided by 2π , m_A is the mass of the nucleus A , m_e is the mass of electron, e is the charge on an electron, Z is an atomic number and $|\mathbf{R}_A - \mathbf{r}_i| = r_{iA}$ is the relative distance between the position of nucleus and electron.⁴ The above equation can be expressed symbolically as:

$$\hat{H} = (\hat{T}_N + \hat{T}_e) + (\hat{V}_{NN} + \hat{V}_{ee} + \hat{V}_{Ne}) \quad (2.4)$$

[†]Operators (e.g. Hamiltonian operator, corresponding to the total energy of the system) are associated with each measurable parameter and when they carry out a mathematical operation on their *eigenfunction* (e.g. the wave function Ψ) they produce the same eigenfunction multiplied by a scalar value, *eigenvalue* (e.g. energy E) of the selected operator.

Although the time-independent SE (eq. (2.2)) simplifies the problem, we are still able to solve it only for the smallest one electron systems (e.g. hydrogen atom). Hence, approximations have to be introduced for the Hamiltonian \hat{H} as well as for the wave function Ψ in order to solve the SE for many-electron systems. Note that the units used throughout this report are a so called atomic units. In this system of units: the electric charge e , electron mass m_e and reduced Planck constant \hbar are equal to 1. Then the units for distance and energy become bohrs (a_0) and hartrees (E_h), respectively.

2.1.2 The Adiabatic and Born-Oppenheimer Approximation

The total wave function depends on the positions of all particles and their spins, however in the adiabatic approximation, it can be expressed as a product of a nuclear and an electronic wave function

The Born-Oppenheimer approximation (BO) is one of the most important approximations that simplifies the molecular Hamiltonian by separating the electronic and nuclear motions allowing definitions of concepts such as bond-lengths, bond-angles, equilibrium structures and reaction barriers. This separation can be easily justified when we realize there is a large mass difference between electrons and nuclei (a proton is ~ 1836 times heavier than an electron). As a consequence, electrons in a molecule react instantaneously to displacements of nuclei and to a good approximation can be considered to be moving in the field of fixed nuclei. In this approximation, the nuclear kinetic operator $T_N = 0$ is omitted from eq. (2.4) and the potential energy operator for nuclei-nuclei repulsion \hat{V}_{NN} can be considered for the selected molecular geometry to be constant⁵:

$$\hat{H}_e = (\hat{T}_e) + (\hat{V}_{NN} + \hat{V}_{ee} + \hat{V}_{Ne}) \quad (2.5)$$

where \hat{H}_e is the *electronic* Hamiltonian. And after solving SE for the electronic Hamiltonian:

$$\hat{H}_e \Psi_i(\mathbf{r}; \mathbf{R}) = E_i(\mathbf{R}) \Psi_i(\mathbf{r}; \mathbf{R}) \quad (2.6)$$

we obtain the electronic wave function $\Psi_i(\mathbf{r}; \mathbf{R})$ which *explicitly* depends on the electronic coordinates and *parametrically* on the nuclear coordinates as does the electronic energies $E_i(\mathbf{R})$.

In the modern derivation of the BO approximation, the wave functions are adiabatic electronic states[†] (ground state ($i = 0$), first excited state ($i = 1$), second excited

[†]The adiabatic wave functions are *orthonormal*, $\int_{-\infty}^{\infty} \Psi_i^*(\mathbf{r}, \mathbf{R}) \Psi_j(\mathbf{r}, \mathbf{R}) d\mathbf{r} = \delta_{ij}$, where δ_{ij} is Kronecker delta function (for $i = j$ is 1 and 0 otherwise)

state ($i = 1$),). Then the total (exact) wave function can be written as a sum of products of the nuclear and the electronic wave functions:

$$\Psi(\mathbf{r}; \mathbf{R}) = \sum_n \chi_n(\mathbf{R}) \Psi_n(\mathbf{r}; \mathbf{R}) \quad (2.7)$$

where the expansion coefficients $\chi_n(\mathbf{R})$ are the nuclear wave functions. This inserted into the SE and expanded, followed by multiplication by the adiabatic electronic wave function $\Psi_i^*(\mathbf{r}; \mathbf{R})$ from the left (using the orthonormality of the Ψ_i) and integration over the electron coordinates, we obtain the following set of coupled equations^{2,6}:

$$\sum_j H_{ij}(\mathbf{R}) \chi_j(\mathbf{R}) = E(\mathbf{R}) \chi_i(\mathbf{R}) \quad (2.8)$$

Here $H_{ij}(\mathbf{R}) = [\hat{T}_N + V_i(\mathbf{R})] \delta_{ij} - \Lambda_{ij}(\mathbf{R})$ with the kinetic energy operator $\hat{T}_N = -\sum_k \frac{1}{2M_k} \nabla_{\mathbf{R}_k}^2$ (expressed in atomic units), where $2M_k$ is the mass of nucleus k , and the *non-adiabatic* operator elements $\Lambda_{ij}(\mathbf{R})$ are defined as:

$$\Lambda_{ij}(\mathbf{R}) = \sum_k \overbrace{\left(\frac{1}{M_k} \langle \Psi_i(\mathbf{r}; \mathbf{R}) | \nabla_{\mathbf{R}_k} | \Psi_j(\mathbf{r}; \mathbf{R}) \rangle \right)}^{F_{ij}^k(\mathbf{R})} \nabla_{\mathbf{R}_k} + \overbrace{\left(\sum_k \frac{1}{2M_k} \langle \Psi_i(\mathbf{r}; \mathbf{R}) | \nabla_{\mathbf{R}_k}^2 | \Psi_j(\mathbf{r}; \mathbf{R}) \rangle \right)}^{G_{ij}(\mathbf{R})} \quad (2.9)$$

where $F_{ij}^k(\mathbf{R})$ and $G_{ij}(\mathbf{R})$ are the first- and the second-order non-adiabatic coupling elements, respectively, expressed in the Dirac bracket notation ($\langle | \rangle$). These coupling elements connect individual electronic states *via* nuclear motion. In the *adiabatic* approximation, where the nuclei move only on a *single* electronic potential surface, $F_{ij}^k(\mathbf{R})$ and $G_{ij}(\mathbf{R})$ are very small and can be neglected. However, another crucial requirement for these terms to vanish is that there must be a mass difference and also electronic states must not be too close in energy to one another. Although, coupling elements are ignored here, they play a very important role in the photochemical reactions where the system involves more than one electronic surface and this will be discussed later on in the section about conical intersections. In the BO approximation, H_{ij} is assumed to be diagonal and the resulting equation has the form of SE:

$$[\hat{T}_N + V_i(\mathbf{R})] \chi_j(\mathbf{R}) = E_{\text{tot}} \chi_j(\mathbf{R}) \quad (2.10)$$

Here the nuclei move on a potential energy surface (PES) $V_i(\mathbf{R})$ of a given electronic state i which is a solution to the electronic SE. Further, solving equation (2.10) for the nuclear wave function yields the vibrational, rotational and translational states of the nuclei.⁷ The first-order correction to the Born-Oppenheimer electronic energy due to the nuclear motion is the *Born-Oppenheimer diagonal correction* (BODC):

$$E_{\text{DBOC}} = \langle \Psi_i(\mathbf{r}; \mathbf{R}) | \hat{T}_N | \Psi_i(\mathbf{r}; \mathbf{R}) \rangle \quad (2.11)$$

This correction is especially important for molecules with light atoms (e.g. hydrogen-containing molecules) and its effect becomes smaller for heavier nuclei.⁶

Figure 2.1 shows an example a PES, a very important concept in chemistry, from where we can obtain information about the minimum and transition state geometries of the studied system.

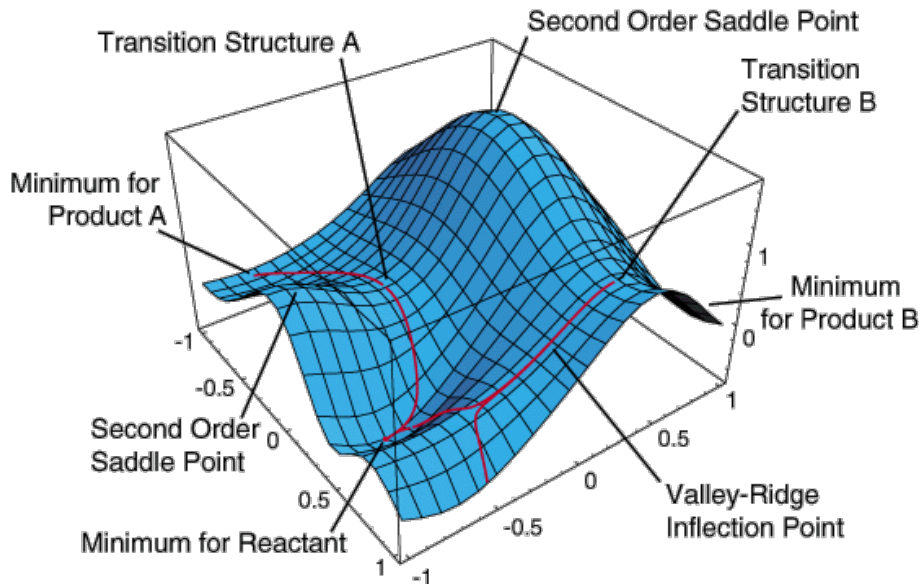


Figure 2.1: Example of a PES (figure taken from⁸).

Conical intersections (CoIn) are a products of a so called nonadiabatic phenomena, which are frequently found in photochemical and photobiological mechanisms. During ground state reactions, thermal chemistry typically plays significant role, where the excited state is usually several eV higher and the BO nonadiabatic coupling terms, which depend not only on the mass but also on the energy difference between electronic states, are neglected. However, in photochemistry one must deal with situations where energy gaps between electronic states get smaller and smaller, reaching the same magnitude of energy difference as vibrational states. This results in stronger coupling between nuclear motion and electronic configuration changes (vibronic coupling).² Ultimately, there are CoIn points with infinitely large coupling at $\Delta E_{\text{PES}}=0$. At this points, the Born-Oppenheimer approximation that represents powerful simplification applicable for the nuclei movement on a single PES, breaks down. In other words, when we recall the nonadiabatic coupling operators Λ_{ij} , where $G_{ii}(\mathbf{R})$ corresponds to the nonadiabatic correction to a single PES and $F_{ij}^k((R))$ is the derivative coupling vector (of dimension equal to the number of nuclear coordinates) that can expressed in the terms of energy difference as:

$$F_{ij}^k(\mathbf{R}) = \frac{1}{M_k} \frac{\langle \Psi_i(\mathbf{r}; \mathbf{R}) | \nabla_{\mathbf{R}_k} H^e | \Psi_j(\mathbf{r}; \mathbf{R}) \rangle}{V_j - V_i} \quad (2.12)$$

which for zero energy difference becomes infinity and provide the most efficient way for radiationless transition between states.⁹

The topology of CoIn is that of a double cone, with a so called branching space at the apex. The branching space is spanned by the energy difference gradient \mathbf{g}_{ij} , and \mathbf{h}_{ij} which represents the interstate coupling gradient and is parallel to the nonadiabatic coupling¹⁰:

$$\mathbf{g}_{ij} = \frac{\partial(E_j - E_i)}{\partial\xi} \quad (2.13)$$

$$\mathbf{h}_{ij} = \langle C_i | \frac{\partial\hat{H}}{\partial\xi} | C_j \rangle \quad (2.14)$$

where C_i, C_j are configuration interaction eigenvectors, \hat{H} is the Hamiltonian and ξ is a vector of Cartesian displacements.

Orthogonal to the branching space is a so called intersection seam, which lies for a molecule with N^{int} internal degrees of freedom on the $N^{int} - 2$ dimensional subspace formed by an infinite number of connected CoIns.

2.1.3 Hartree-Fock Method

The Hartree-Fock method (HF), also known as self-consistent field (or SCF method), is a central *ab initio* method able to solve the electronic SE (eq. (2.6)) of a many-electron system. The HF is often a starting point leading after some improvements towards more accurate methods or after additional approximations to semi-empirical methods.⁶

The key aspect of the HF approximation is the assumption that the exact N -electron wave function and associated energy of a system can be approximated by a single expression of N spin-orbitals that is derived by applying the variational principle. But before we establish HF theory in more details a few theoretical concepts need to be presented.

First a *spatial orbital* $\phi_i(\mathbf{r})$ is defined as a wave function that describes the spatial distribution of an electron and depends on the position vector \mathbf{r} , such that $|\phi_i(\mathbf{r})|^2 d\mathbf{r}$ is the probability of finding the selected electron within small volume $d\mathbf{r}$ surrounding \mathbf{r} . Further, in context of neglecting the non-relativistic effects and in order to complete the description of an electron, we introduce electron *spin*. The spin of an electron can be in one of the two states α (spin up) and β (spin down) and these two functions obey the orthonormal conditions ($\langle\alpha|\alpha\rangle = \langle\beta|\beta\rangle = 1$ and $\langle\alpha|\beta\rangle = \langle\beta|\alpha\rangle = 0$).⁶ Two *spinorbitals* $\chi(\mathbf{x}) = \phi_i(\mathbf{r})\alpha$ or $\chi(\mathbf{x}) = \phi_i(\mathbf{r})\beta$ can be

formed combining *spatial orbital* and either the spin function α or β . In the case of solving the electronic SE for a molecule, the term *molecular orbitals* is used for the wave functions of electrons in a molecule.

After neglecting electron-electron repulsion a many-electron wave function, termed as *Hartree product*, can be expressed as a product of spinorbitals for each electron:

$$\Psi^{\text{HP}}(\mathbf{x}_1, \mathbf{x}_1, \dots, \mathbf{x}_N) = \chi_i(\mathbf{x}_1)\chi_j(\mathbf{x}_2) \cdots \chi_k(\mathbf{x}_N) \quad (2.15)$$

However, the *Hartree product* is inadequate since it is required for the electronic wave function to be antisymmetric (change sign) with respect to interchange of any two electron space and spin coordinates (since electrons are fermions with spin quantum number of $1/2$). Hence, an antisymmetric wave function is introduced in the form of a so called *Slater determinant*⁵:

$$\Psi(\mathbf{x}_1, \mathbf{x}_1, \dots, \mathbf{x}_N) = \frac{1}{\sqrt{N!}} \begin{vmatrix} \chi_i(\mathbf{x}_1) & \chi_j(\mathbf{x}_1) & \cdots & \chi_k(\mathbf{x}_1) \\ \chi_i(\mathbf{x}_2) & \chi_j(\mathbf{x}_2) & \cdots & \chi_k(\mathbf{x}_2) \\ \vdots & \vdots & \ddots & \vdots \\ \chi_i(\mathbf{x}_N) & \chi_j(\mathbf{x}_N) & \cdots & \chi_k(\mathbf{x}_N) \end{vmatrix}. \quad (2.16)$$

where $\frac{1}{\sqrt{N!}}$ is a normalization factor and in each row all possible assignments of electron i to all molecular spinorbital combinations are presented.

Now, we will proceed with derivation of Hartree-Fock equations. First, the simplest antisymmetric wave function, Ψ_{guess} , able to describe the ground state of an N-electron system is taken as a trial wave function (as the exact wave function is unknown) in a form of a single Slater determinant. Given the trial wave function, the expectation value $E[\Psi_{\text{guess}}]$ of the full electronic Hamiltonian \hat{H}_e is expressed as:

$$E[\Psi_{\text{guess}}] = \langle \Psi_{\text{guess}} | \hat{H}_e | \Psi_{\text{guess}} \rangle \quad (2.17)$$

where in this case the energy $E[\Psi_{\text{guess}}]$ is a function of the trial wave function, which is in turn a function of molecular spinorbitals. Further, in order to minimize the energy the variational theorem for a normalized wave functions is applied:

$$E_{\text{approx}} = \langle \Psi_{\text{guess}} | \hat{H}_e | \Psi_{\text{guess}} \rangle \geq E_{\text{exact}} \quad (2.18)$$

Thus, we have a tool to judge the quality of an approximate wave function and further improve our guess towards the limit of an exact wave function E_0 by altering the spinorbitals, but they must still remain orthonormal.

In the process of finding such spinorbitals χ_i that would lead to E_0 , an eigenvalue

Hartree-Fock equation (in typical form for closed-shell systems) is derived, which determines the optimal spinorbitals⁵:

$$f(i)\chi(\mathbf{x}_i) = \varepsilon\chi(\mathbf{x}_i) \quad (2.19)$$

where $f(i)$ is the one-electron *Fock* operator defined as:

$$f(i) = \overbrace{-\frac{1}{2}\nabla_i^2}^{\hat{T}_e} - \overbrace{\sum_{A=1}^M \frac{Z_A}{r_{iA}}}_{\hat{V}_{Ne}} + V_i^{\text{HF}}\{j\} \quad (2.20)$$

Here, the electron-electron repulsion is substituted with the interaction of i th electron with the mean-field, $V_i^{\text{HF}}\{j\}$, created by other electrons occupying orbitals $\{j\}$ (i.e. charge density associated with orbital χ_j). Hence, the complicated many-electron problem is replaced by the one-electron problem. However, this implies that mutual correlation of electron motion (electron correlation) is ignored. The average potential $V_i^{\text{HF}}\{j\}$ has the form $V_i^{\text{HF}}\{j\} = \sum_{j \neq i} \hat{J}_j - \hat{K}_j$, with the Coulomb operator \hat{J}_j defined as⁶:

$$\hat{J}_j\chi_i(\mathbf{x}_1) = \left(\int \frac{|\chi_j(\mathbf{x}_2)|^2}{r_{12}} d\mathbf{x}_2 \right) \chi_i(\mathbf{x}_1) = \left(\int \frac{\rho_j}{r_{12}} d\mathbf{x}_2 \right) \chi_i(\mathbf{x}_1) \quad (2.21)$$

and the Exchange operator \hat{K}_j :

$$\hat{K}_j\chi_i(\mathbf{x}_1) = \left(\int \frac{\chi_j^*(\mathbf{x}_2)\chi_i(\mathbf{x}_2)}{r_{12}} d\mathbf{x}_2 \right) \chi_j(\mathbf{x}_1) \quad (2.22)$$

From the above equations we can see that $V_i^{\text{HF}}\{j\}$ depends on the spinorbitals of other electrons (i.e. Fock operator depends on its own eigenfunctions) and thus this nonlinear problem must be solved iteratively using a so called Self-consistent field method (SCF).

Finally, we can evaluate the energy of a Slater determinant composed of an optimised set of molecular orbitals obtained from SCF as:

$$E^{\text{HF}} = \sum_i^{\text{elec.}} h_i^c + \sum_{i < j}^{\text{elec.pairs}} (J_{ij} - K_{ij}) \quad (2.23)$$

with h_i^c being one-electron integrals, i.e. electron kinetic energy and electron-nucleus repulsion.

In modern chemistry an unknown molecular orbital (MO) (guess wave function) Ψ_i is constructed as a linear combination of known atomic orbitals (MO LCAO), i.e.

an expansion of MOs in terms of the known basis functions ϕ_μ ^{5,6}:

$$\Psi_i = \sum_{\mu=1}^{K_{\text{basis}}} C_{\mu i} \phi_\mu \quad (2.24)$$

where $C_{\mu i}$ are the molecular orbital expansion coefficients and ϕ_μ are basis functions chosen to be normalized. More on a mathematical form of basis functions will be discussed in the section about basis sets.

In the atomic orbital approximation in order to solve the Hartree-Fock equations numerically for molecular systems the operator eigenvalue equations eq. (2.19) are converted to a matrix representation by first substituting the linear expansion eq. (2.24) to obtain:

$$f(\mathbf{r}_1) \sum_{\mu=1}^{K_{\text{basis}}} C_{\mu i} \phi_\mu = \varepsilon_i \sum_{\mu=1}^{K_{\text{basis}}} C_{\mu i} \phi_\mu \quad (2.25)$$

Multiplying the above equations by a specific basis function on the left and integrating yields matrix equations, a so-called *Roothaan-Hall* equations^{11,12}:

$$\sum_{\mu=1}^{K_{\text{basis}}} C_{\mu i} \langle \phi_\nu | f(\mathbf{r}_1) | \phi_\mu \rangle = \varepsilon_i \sum_{\mu=1}^{K_{\text{basis}}} C_{\mu i} \langle \phi_\nu | \phi_\mu \rangle \quad (2.26)$$

These can be compactly written as a single matrix equation:

$$\mathbf{FC} = \mathbf{SC}\varepsilon \quad (2.27)$$

where \mathbf{F} is the *Fock matrix*, \mathbf{S} is the *overlap matrix* of overlap elements between basis functions and \mathbf{C} is a $K \times K$ matrix of the expansion coefficients. Further, a density matrix which is needed in the SCF calculation is obtained from the total charge density:

$$\rho(\mathbf{r}) = 2 \sum_i^{N/2} |\psi_i(\mathbf{r})|^2 \quad (2.28)$$

by inserting the MO expansion (eq. (2.25)) into the above equation and then the charge density matrix is defined as:

$$\begin{aligned} \rho(\mathbf{r}) &= 2 \sum_i^{N/2} \sum_\nu C_{\nu i}^* \phi_\nu^*(\mathbf{r}) \sum_\mu C_{\mu i} \phi_\mu(\mathbf{r}) \\ &= \sum_{\mu\nu} \left[2 \sum_i^{N/2} C_{\mu i} C_{\nu i}^* \right] \phi_\mu(\mathbf{r}) \phi_\nu^*(\mathbf{r}) \\ &= \sum_{\mu\nu} P_{\mu\nu} \phi_\mu(\mathbf{r}) \phi_\nu^*(\mathbf{r}) \end{aligned} \quad (2.29)$$

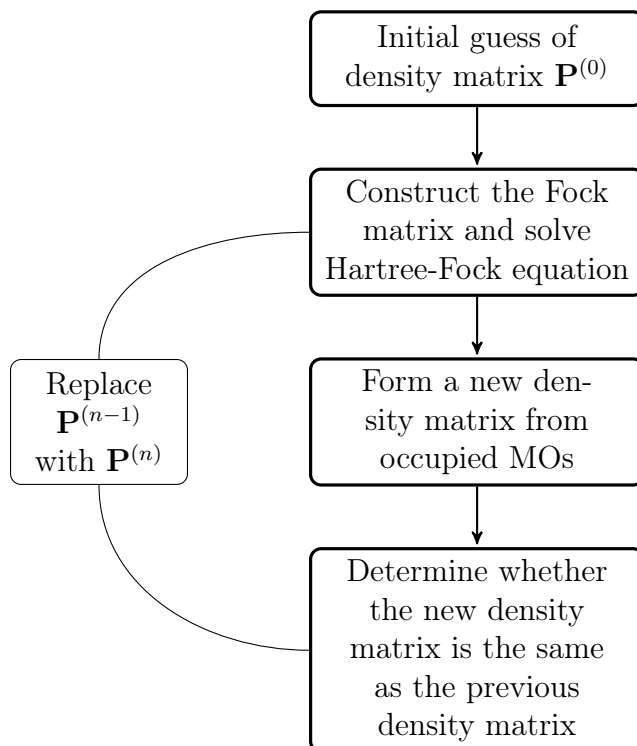


Figure 2.2: Illustration of the SCF procedure.

where $P_{\mu\nu}$ is a *density matrix* related to expansion coefficients \mathbf{C} by $P_{\mu\nu} = 2 \sum_i^{N/2} C_{\mu i} C_{\nu i}^*$. The density matrix is used in the SCF procedure together with the one- and two-electron integrals to construct the Fock matrix:

$$F_{\mu\nu} = \underbrace{T_{\mu\nu} + V_{\mu\nu}^{\text{nucl}}}_{H_{\mu\nu}^{\text{core}}} + \underbrace{\sum_{\lambda\sigma} P_{\lambda\sigma} [(\mu\nu|\sigma\lambda) - \frac{1}{2}(\mu\lambda|\sigma\nu)]}_{G_{\mu\nu}} \quad (2.30)$$

In the equation (2.30) $H_{\mu\nu}^{\text{core}}$ is the core-Hamiltonian matrix, which involves the kinetic energy integrals $T_{\mu\nu}$ and the nuclear attraction integrals $V_{\mu\nu}^{\text{nucl}}$ and $G_{\mu\nu}$ is the two-electron part of the Fock matrix involving the density matrix \mathbf{P} and a set of two-electron integrals.

The SCF procedure, illustrated in the Figure 2.2, is iterated until the new density matrix is sufficiently similar (converges to within a selected treshold) to the previous density matrix.

In the basis set approximation improving the quality of a basis set of atomic orbitals leads to a lower and lower expectation value E_0 , converging ultimately to the basis set limit of the method, the so called HF limit. We have neglected the electron correlation effect, but the HF limit is only a small step away from the exact (non-relativistic) energy (in most cases it accounts for $\sim 99\%$ of total energy) and the remainder of the energy is called the correlation energy $E_{\text{corr}} = E_{\text{exact}} - E_{\text{HF}}$.

The correlation energy can be further divided into a static and dynamic electron correlation. In order to understand the difference between these two correlations we introduce an improvement to HF wave function (single slater determinant) by constructing a wave function as a linear combination of multiple slater determinants⁴:

$$\Psi = c_0\Psi^{\text{HF}} + c_1\Psi_1 + c_2\Psi_2 + \dots \quad (2.31)$$

where the coefficients c represents weights of each determinant in the expansion as well as ensures normalization. For most systems the HF wave function dominates the linear expansion and the main contribution to correlation energy is due to the dynamic correlation, which is related to the instantaneous correlation of the movement of electrons and tends to be made up from a sum of individually small contributions from other determinants. However, static correlation takes place in situations where different determinants have similar weights (i.e. configurations have similar energies) and thus a single configuration becomes inappropriate for an accurate system description, e.g. stretched bonds and excited states.

There are various approaches trying to include the dynamic and static electron correction into the HF calculation, referred to as *electron correlation methods* or *Post-HF methods*. Some of these methods are, for example, Configuration Interaction (CI), Coupled cluster, Møller-Plesset perturbation theory (MP n , where n is the order of correction), multi-configurational self-consistent field (MCSCF) and coupled cluster theory (CC). Density functional theory (DFT), which will be covered in more details in a separate chapter, is yet another approach capable of recovering some of the correlation energy.

Solving the Hartree-Fock eigenvalue equation an unique set of spin orbitals, which are called *canonical spinorbitals*, is obtained. These orbitals are diagonal matrix representation of $\langle\psi_i|\hat{f}|\psi_j\rangle = \varepsilon_i\delta_{ij}$ and also include the unoccupied spinorbitals as additional eigenfunctions of \hat{f} . The *canonical spinorbitals* are generally delocalized, but since the Hartree-Fock state is invariant to unitary transformations among the occupied spinorbitals $\Psi_i, i = 1, 2, \dots, N$ and *canonical spin orbitals* are just one possible choice of spinorbitals for the optimized N -particle state it is possible by unitary transformation to generate an alternative more chemically intuitive picture of orbitals localized to individual bonds or atoms. The *non – canonical* representation of the HF solution leads to a block-diagonal matrix form of the Fock operator with two non-diagonal blocks that belong to the occupied and unoccupied spinorbitals, respectively.¹³

There are several variants of the HF method depending on whether any restrictions are imposed on the spinorbitals used to build the trial wave function. For a closed-shell systems near their equilibrium geometry, a *Restricted Hartree-Fock* (RHF)

approach is usually used which allows to simplify the problem by restricting pairs of α and β spinorbitals to the same spatial orbital. In the case of open shell systems there is a possibility to restrict only the spatial part of the doubly occupied orbitals in a *Restricted Open-shell Hartree-Fock* (ROHF).⁶ Other option for the open shell systems is to use the *Unrestricted Hartree-Fock* (UHF) which uses two complete sets of orbitals, one for the α and one for the β electrons. The advantage of UHF is that it can perform very efficiently for an open-shell system and yields lower or equal energy to a corresponding R(O)HF. On the other hand, the UHF wave function is no longer an eigenfunction of the total spin operator, \mathbf{S}^2 , which results in an incorrect wave function that has some other spin states mixed in (a so called spin contamination error).

Koopmans' theorem provides a physical interpretation of the orbital energies ε_i , it states that energies associated with orbitals χ_i are approximations to the ionization energies of the system.⁵ Given two systems one with N -electron Hartree-Fock single determinant and other with $(N - 1)$ -electron determinant, where electron was removed from χ_a , will have in general different orbitals. But when we assume the orbitals are identical ("frozen" orbitals), all the one electron terms cancel out except for the unoccupied orbital χ_a (removed orbital) in the $N - 1$ electron system. Also, majority of the two-body terms cancel as well except for the ones involving the removed orbital χ_a :

$$E_N - E_{N-1} = h_a + \frac{1}{2} \sum_{i=1}^{Nelec} (J_{ia} - K_{ia}) + \frac{1}{2} \sum_{j=1}^{Nelec} (J_{aj} - K_{aj}) \quad (2.32)$$

The last two terms are identical and the ionization energy is given as:

$$E_N - E_{N-1} = h_a + \sum_{i=1}^{Nelec} (J_{ia} - K_{ia}) = \varepsilon_a \quad (2.33)$$

From the above equation it can be seen that $-\varepsilon_a$ is the HF approximation to the ionization energy. Similarly, it can be shown that $-\varepsilon_r$ of virtual spin orbital χ_r is the HF approximation to electron affinity when, for example, an $(N + 1)$ -electron system is generated from an N -electron system. The error in this approximation is due to the fact that orbital relaxation was neglected and this error becomes more significant when more and more electrons are removed. Moreover, including the correlation effects can correct further the Koopmans' results for calculated ionization potentials and electron affinities.

2.1.4 Configuration Interaction

Configuration Interaction (CI), which is based on the variational principle, is in comparison to other correlation methods conceptually the simplest one.⁵ Even though without proper denoting, CI's form has already been introduced in eq. (2.31). The principle of the CI method is that it augments ground state HF wave function by including additional configurations, i.e. it utilizes virtual (empty) orbitals where electrons from occupied HF orbitals can be substituted (equivalent to exciting electron to a higher energy orbital). This has the effect that electrons can partially spread across virtual orbitals and we can recover part of the correlation energy. And thus the exact wave function can be constructed as a linear combination of all the possible substitutions (configurations):

$$\Psi^{\text{CI}} = c_0 \Psi^{\text{HF}} + \sum_{c_i^S}^{\text{Singles}} c_i^S \Psi_i^S + \sum_{c_i^D}^{\text{Doubles}} c_i^D \Psi_i^D + \sum_{c_i^T}^{\text{Triples}} c_i^T \Psi_i^T + \dots + \sum_{c_i^N}^{N\text{-folds}} c_i^N \Psi_i^N \quad (2.34)$$

where c represents the weight of each determinant in the expansion, the first term is the fully occupied HF ground state and the rest of terms represent, respectively, orbitals that are Singly (sum of all the single substitutions), Doubly (D), Triply (T), etc., excited relative to the HF configuration.⁶ For the excited configurations initial MOs are taken from HF calculation and their coefficients held fixed. eq. (2.34) represents a Full CI, the most complete non-relativistic treatment of the many electron system, within the limitations imposed by chosen basis set (i.e. Full CI yields exact correlation energy for an infinite basis set). The full CI is well-defined, size-consistent, size-extensive[†] and variational, however very computationally expensive and feasible only for the smallest systems.⁷ In practice, only truncated CI is used, e.g. CIS that consists of the HF determinant with inclusion of single excitations, CISD adds singles and doubles, etc. Unfortunately, a major disadvantage of truncated CI methods is that they are not size-consistent nor size-extensive.

Brillouin theorem states that the Hamiltonian matrix elements between the HF determinant and the singly excited determinants are zero ($\langle \Phi_{\text{HF}} | \hat{H} | \Phi_i^a \rangle = 0$), in other words there is no mixing between the HF ground state and the singly excited determinants. Although HF and singles are decoupled there is an indirect mixing through higher excited states, for example, through double excited determinants. One of the results of the Brillouin's theorem is that single excitations in CI expansion provide no improvement over the HF. Therefore, it is possible to eliminate the contribution of singles completely by a suitable transformation involving mixing of

[†]*Size-consistency*: the energy calculated for a system of infinitely separated molecules should be equal to the sum of the energies for individual molecules. *Size-extensivity*: the energy scales linearly with the size of the system.

occupied and unoccupied orbitals that produces a so called *Brueckner orbitals*. This transformation in terms of $\hat{T}_1 = 0$ is applied in the *Bruckner theory*^{14,15}, which is a variation of the coupled cluster theory.

Natural orbitals and *reduced density matrix* are important concepts potentially leading to more rapidly convergent CI expansion and are often used in evaluation of which orbitals should be included in, for example, MCSCF wave function. The *reduced density function* for a single electron in an N -electron system, defined as the probability of finding an electron in dx_1 at x_1 independent of position of other electrons, has the following form:

$$\rho(x_1) = N \int \Phi^*(x_1, \dots, x_N) \Phi(x_1, \dots, x_N) dx_2 \cdots dx_N \quad (2.35)$$

where N is the normalization factor ensuring the integral of the density equals the total number of electrons and Φ is a normalized wave function. From there, the *first-order reduced density matrix* $\gamma(x_1, x'_1)$ is defined as:

$$\gamma(x_1, x'_1) = N \int \Phi^*(x'_1, x_2, \dots, x_N) \Phi(x_1, x_2, \dots, x_N) dx_2 \cdots dx_N \quad (2.36)$$

In the above equation the diagonal element is the density of electrons $\gamma(x_1, x_1) = \rho(x_1)$. The equation (2.36) can be generalized to define the reduced density matrix of order k , γ_k ^{6,16}:

$$\begin{aligned} & \gamma_k(x_1, \dots, x_k, x'_1, \dots, x'_k) \\ &= \left(\frac{N_{\text{elec}}}{k} \right) \int \Phi^*(x'_1, \dots, x'_k, x_{k+1} \dots x_{N_{\text{elec}}}) \int \Phi(x_1, \dots, x_k, x_{k+1} \dots x_{N_{\text{elec}}}) dx_{k+1} \cdots dx_{N_{\text{elec}}} \end{aligned} \quad (2.37)$$

The first-order density matrix defined in the basis of HF spin orbitals may be diagonalized to obtain eigenvectors a so called *Natural orbitals* and eigenvalues a so called *Occupation Numbers*. For the single-determinant HF the occupation numbers (diagonal elements) are ones for occupied spin orbitals and zeros for unoccupied spin orbitals (alternatively 2 or 0 in the case of RHF).⁵ The occupation numbers may have fractional values between 0 and 2 in the case of multi-determinant wave function (CI, MP, CC, MCSCF).⁶

When the configurations in the CI expansion are constructed from natural orbitals with the largest occupation numbers this leads to fewer configurations required (at a given accuracy) and hence much faster convergence of the expansion. Another application of the natural orbitals is, for example, in the MCSCF active space construction when importance of included orbitals is evaluated.

2.1.5 Many Body Perturbation Theories

Many body perturbation methods is yet another family of methods trying to bring in the missing dynamic electron correlation and improve the hartree-fock solution. In contrast to, for example, truncated CI energy calculated by most of the perturbation methods scales correctly with the system size and therefore they are *size-extensive*.¹³ Further, effects of higher order excitations can be included more efficiently than in the case of configuration interaction by combination of contributions of most important high order excitations with low order excitations. The main disadvantages of many body perturbation methods are in many cases slow convergence and that they are in general non-variational.

The main idea behind the perturbational approach is to apply a small perturbation (\hat{V}) to the well described non-perturbed system (\hat{H}_0) in order to estimate solution to a more complete perturbed system. This can be expressed as:

$$\hat{H} = \hat{H}_0 + \lambda\hat{V} \quad (2.38)$$

where λ is a dimensionless parameter that determines the strength of perturbation. The zero-order unperturbed Schrödinger equation has the following form:

$$\hat{H}_0\Phi_n = E_n^{(0)}\Phi_n \quad (2.39)$$

The solution to the unperturbed SE form an orthonormal complete set $\langle\Phi_m|\Phi_n\rangle = \delta_{mn}$. Considering the time-independent perturbation and a non-degenerate reference wave function the perturbed SE can be written as:

$$\hat{H}\Psi_n = E_n\Psi_n \quad (2.40)$$

At the limit of $\lambda \rightarrow 0$ $\Psi_n^{(0)} = \Phi_n$ and $E_n = E_n^{(0)}$. Increasing the perturbation to a finite value energy and wave function must also change continuously and can be expanded in series of λ :

$$\begin{aligned} \Psi_n &= \Phi_n + \chi_n = \Psi_n^{(0)} + \lambda\Psi_n^{(1)} + \lambda^2\Psi_n^{(2)} + \dots \\ E_n &= E_n^{(0)} + \Delta E_n = E_n^{(0)} + \lambda E_n^{(1)} + \lambda^2 E_n^{(2)} + \dots \end{aligned} \quad (2.41)$$

Substituting eqs. (2.41) into SE eq. (2.40) with the perturbed hamiltonian expressed as in equation (2.38) and collecting terms with the same power of λ gives the fol-

lowing equations¹³:

$$\begin{aligned}
(\hat{H}_0 - E_n^{(0)})\Psi_n^{(0)} &= 0 && \text{(zero order)} \\
(\hat{H}_0 - E_n^{(0)})\Psi_n^{(1)} &= (E_n^{(1)} - \hat{V})\Psi_n^{(0)} && \text{(first order)} \\
(\hat{H}_0 - E_n^{(0)})\Psi_n^{(2)} &= (E_n^{(1)} - \hat{V})\Psi_n^{(1)} + E_n^{(2)}\Psi_n^{(0)} && \text{(second order)} \\
(\hat{H}_0 - E_n^{(0)})\Psi_n^{(m)} &= (E_n^{(1)} - \hat{V})\Psi_n^{(m-1)} + \sum_{l=0}^{m-2} E_n^{(m-l)}\Psi_n^{(l)} && \text{(mth-order)}
\end{aligned} \tag{2.42}$$

The m th-order equation can also be rewritten as:

$$(E_n^{(0)} - \hat{H}_0)\Psi_n^{(m)} = \hat{V}\Psi_n^{(m-1)} + \sum_{l=0}^{m-1} E_n^{(m-l)}\Psi_n^{(l)} \tag{2.43}$$

For example, in order to solve the first order equation for λ^1 to obtain expression for $E_n^{(1)}$, $\langle \Phi_n |$ is applied to the equation and after integrating it results in the following equation:

$$\underbrace{\langle (\hat{H}_0 - E_n^{(0)})\Phi_n |}_{=0} \Psi_n^{(1)} \rangle = E_n^{(1)} - \underbrace{\langle \Phi_n | \hat{V} | \Phi_n \rangle}_{V_{nn}} \tag{2.44}$$

and from there the first-order correction to the energy is obtained as:

$$E_n^{(1)} = V_{nn} \tag{2.45}$$

Similarly, it is possible to obtain each $E_n^{(m)}$ without the knowledge of $\Psi_n^{(m)}$ using the previous $\Psi_n^{(m-1)}$ and then solve the inhomogeneous differential equation for $\Psi_n^{(m)}$.¹³ A condition of *intermediate normalization* $\langle \Phi_n | \Psi_n^{(m)} \rangle = 0$ ($m > 0$) is applied for each order in order to achieve that correction terms are orthogonal to the reference wave function.

In order to solve the inhomogeneous differential equation to calculate the m th-order correction to the wave function $\Psi_n^{(m)}$ this unknown function is expanded in terms of known zero-order solutions Φ_k .

$$\Psi_n^{(m)} = \sum_k a_{kn}^{(m)} \Phi_k = \sum_k |\Phi_k\rangle \langle \Phi_k | \Psi_n^{(m)} \rangle \tag{2.46}$$

where $a_{kn}^{(m)} = \langle \Phi_k | \Psi_n^{(m)} \rangle$ are expansion coefficients to be determined. In order to calculate $a_{kn}^{(m)}$ the m th-order equation is multiplied by $\langle \Phi_k |$ and integrated to yield:

$$\underbrace{\langle \Phi_k | E_n^{(0)} - \hat{H}_{(0)} |}_{=(E_n^{(0)} - E_k^{(0)})\langle \Phi_k |} \Psi_n^{(m)} \rangle = \underbrace{\langle \Phi_k | \hat{V} | \Psi_n^{(m-1)} \rangle}_{\sum_j \langle \Phi_k | \hat{V} | \Phi_j \rangle \langle \Phi_j | \Psi_n^{(m-1)} \rangle} - \sum_{l=0}^{m-1} E_n^{m-l} \underbrace{\langle \Phi_k | \Psi_n^{(l)} \rangle}_{=a_{kn}^{(l)}} \tag{2.47}$$

which becomes

$$(E_n^{(0)} - E_k^{(0)})a_{kn}^{(m)} = \sum_j V_{kj}a_{jn}^{(m-1)} - \sum_{l=0}^{m-1} E_n^{(m-l)}a_{kn}^{(l)} \quad (2.48)$$

and since the overlap integrals between different solutions of the same SE are 0, the $l=0$ contributions are $a_{kn}^{(0)} = \langle \Phi_k | \Phi_n \rangle = \delta_{kn}$. The above equation leads to series of equations for the $a_{kn}^{(m)}$ coefficients, which are solved order by order. One thing to notice is that the choice of intermediate normalization for each order results in $a_{nn}^{(m)} = \delta_{m0}$. The first-order equation is defined as (since $a_{kn}^{(0)} = \delta_{kn}$):

$$(E_n^{(0)} - E_k^{(0)})a_{kn}^{(1)} = V_{kn} - E_n^{(1)}a_{kn}^{(0)} = V_{kn} \quad (n \neq k) \quad (2.49)$$

and from there the first-order coefficient becomes:

$$a_{kn}^{(1)} = \frac{V_{kn}}{E_n^{(0)} - E_k^{(0)}} \quad (n \neq k) \quad (2.50)$$

substituting the above solution into the equation (2.46) yields the first-order correction to the wave function:

$$\Psi_n^{(1)} = \sum_k \frac{V_{kn}}{E_n^{(0)} - E_k^{(0)}} \Phi_k \quad (n \neq k) \quad (2.51)$$

which can be used to obtain the second-order energy correction as:

$$\begin{aligned} E_n^{(2)} &= \langle \Phi_n | \hat{V} | \Psi_n^{(1)} \rangle = \sum_k a_{kn}^{(1)} V_{nk} \quad (2.52) \\ &= \frac{|V_{kn}|^2}{E_n^{(0)} - E_k^{(0)}} \quad (n \neq k) \end{aligned}$$

These steps can be repeated in order to calculate higher order corrections to the energy and wave function. The knowledge of the m th-order wave function $\Psi_n^{(l)}$ for $l = 1, 2, \dots, m$ actually allows a calculation of the $(2m + 1)$ th-order energy by applying a so called Wigner's rule.¹³

The general theory introduced above is also known as *Rayleigh-Schrödinger* perturbation theory. In order to use this theory for calculations of correlation energy an unperturbed Hamiltonian has to be selected. Møller-Plesset perturbation theory

uses the partitioning of the Hamiltonian based on the HF reference function and the Fock operator. The unperturbed hamiltonian has the form of $\hat{H}_0 = \sum_{i=1}^{N_{elec}} F_i$ and the perturbation operator is defined as the exact electron-electron repulsion operator minus twice the averaged electron-electron repulsion $\hat{V} = \hat{V}_{ee} - 2\langle V_{ee} \rangle$.⁶ The total energy with correction up to order m can be expressed in MP m notation as:

$$MP0 = E(MP0) = \sum_{i=1}^{N_{elec}} \varepsilon_i \quad (2.53)$$

$$MP1 = E(MP0) + E(MP1) = E(HF) \quad (2.54)$$

In this partitioning the zeroth-order wave function is the HF determinant and the zeroth-order energy is described as a sum of molecular orbital energies. The first-order energy correction brings in a correction for counting the electron-electron repulsion twice at the zeroth-order and is exactly the HF energy. Since MP1 does not provide improvement beyond the HF level in determining the energy at least the second-order correction must be used in order to obtain estimate of correlation energy. In order to evaluate the second-order correction within a finite basis set approximation all possible excited Slater determinants are constructed from the HF reference. After application of Slater-Condon rules, which is a set of rules for matrix elements evaluation between Slater determinants, to matrix elements involving two different Slater determinants and also applying Brillouin theorem ($\langle \Phi_{HF} | \hat{H} | \Phi_i^a \rangle = 0$, where Φ_i^a is a singly excited determinant) the second-order energy correction only involves a sum over doubly excited determinants and can be obtained as follows:

$$E(MP2) = \sum_{i < j}^{occ} \sum_{a < b}^{vir} \frac{(\langle \phi_i \phi_j | \phi_a \phi_b \rangle - \langle \phi_i \phi_j | \phi_b \phi_a \rangle)}{\varepsilon_i + \varepsilon_j - \varepsilon_a - \varepsilon_b} \quad (2.55)$$

As mentioned previously perturbation methods are in general non-variational and therefore obtained energy may fluctuate around the exact value (i.e. may be even lower than the exact energy). Moreover, calculations may suffer with convergence problems when the HF reference is a poor zeroth-order approximation. On the other hand, the main advantage of MP2 is that it is *size-extensive* method. Moreover, MP2, which is able to recover 80-90% of the correlation energy, is one of the computationally cheapest methods for the correlation energy calculation.⁶

2.1.6 Coupled Cluster

Coupled cluster (CC) theory is an elegant technique for estimating the electron correlation energy of small to medium-sized molecules. The main idea behind CC is using the exponential ansatz for the excitation operator T , which leads to the full-CI wave function within the basis set approximation and thus provides the exact solution to the time-independent SE.

The excitation operator T is defined as:

$$T = T_1 + T_2 + T_3 + \dots + T_{N_{\text{elec}}} \quad (2.56)$$

where T_i is an excitation operator generating i th excited Slater determinants from a HF reference wave function⁶:

$$T_1 \Phi_0 = \sum_i^{\text{occ}} \sum_a^{\text{vir}} t_i^a \Phi_i^a \quad (2.57)$$

$$T_2 \Phi_0 = \sum_{i < j}^{\text{occ}} \sum_{a < b}^{\text{vir}} t_{ij}^{ab} \Phi_{ij}^{ab} \quad (2.58)$$

where t are the expansion coefficients also often called amplitudes. For example, in the above equations T_1 and T_2 generates all singly and doubly excited states, respectively. In the case of CI theory CI wave function is generated from a HF wave function by excitation operator as:

$$\Psi_{\text{CI}} = (1 + T)\Phi_0 = (1 + T_1 + T_2 + T_3 + \dots)\Phi_0 \quad (2.59)$$

In contrast the CC wave function $\Psi_{\text{CC}} = e^T \Phi_0$ is generate by applying an exponential operator:

$$e^T = 1 + T + \frac{1}{2}T^2 + \frac{1}{6}T^3 + \dots = \sum_{k=0}^{\infty} \frac{1}{k!} T^k \quad (2.60)$$

Substituting the excitation operator defined in eq. (2.56) into the above equation and rearranging the excitation exponential operator can be written as:

$$e^T = 1 + T_1 + (T_2 + \frac{1}{2}T_1^2) + (T_3 + T_2T_1 + \frac{1}{6}T_1^3) + \dots \quad (2.61)$$

The first term generates the reference HF, the second all singly excited states and following terms higher order excited states. For example, the first paranthesis generates all doubly excited states, the second paranthesis all triply excited states and so on. Further, terms in paranthesis can be divided into "true" or a so called *connected* (T_2, T_3, \dots) terms and "product" or a so called *disconnected* ($T_1^2, T_2T_1, T_1^3, \dots$) terms.⁶ The connected terms represent and instantenous interaction of n number of

electrons (e.g. four electrons for T_4) and disconnected terms, such as T_2^2 , represent two non-interacting pairs of interacting electrons. At each excitation level the CC wave function, in contrast to the CI wave function, contains additional terms for products of excitations. Solving the Schrödinger equation with the coupled cluster wave function variationally the energy and the amplitudes are determined as:

$$E_{CC}^{\text{var}} = \frac{\langle (1 + T + \frac{1}{2}T^2 \cdots \frac{1}{N!}T^N)\Phi_0 | \hat{H} | (1 + T + \frac{1}{2}T^2 \cdots \frac{1}{N!}T^N)\Phi_0 \rangle}{\langle (1 + T + \frac{1}{2}T^2 \cdots \frac{1}{N!}T^N)\Phi_0 | (1 + T + \frac{1}{2}T^2 \cdots \frac{1}{N!}T^N)\Phi_0 \rangle} \quad (2.62)$$

However, using the variational approach leads to a series of non-vanishing terms up to order N_{elec} , which is difficult to solve for all but the smallest systems.¹⁷ Instead, in the standard formulation of CC a more manageable approach is applied where the CC SE, $\hat{H}e^T\Phi_0 = Ee^T\Phi_0$, is projected onto the reference wave function, multiplied from the left by Φ_0^* and integrated to eventually obtain the equation for the CC energy:

$$\langle \Phi_0 | \hat{H}e^T | \Phi_0 \rangle = E_{CC} \langle \Phi_0 | e^T \Phi_0 \rangle \quad (2.63)$$

$$E_{CC} = \langle \Phi_0 | \hat{H}e^T | \Phi_0 \rangle \quad (2.64)$$

Inserting eq. (2.60) into the above equation and after using the fact that the Hamiltonian contains only one- and two-electron operators the following equation are obtained⁶:

$$E_{CC} = \langle \Phi_0 | \hat{H}(1 + T_1 + T_2 + \frac{1}{2}T_1^2) | \Phi_0 \rangle \quad (2.65)$$

$$E_{CC} = \langle \Phi_0 | \hat{H} | \Phi_0 \rangle + \langle \Phi_0 | \hat{H} | T_1 \Phi_0 \rangle + \langle \Phi_0 | \hat{H} | T_2 \Phi_0 \rangle + \frac{1}{2} \langle \Phi_0 | \hat{H} | T_1^2 \Phi_0 \rangle \quad (2.66)$$

$$E_{CC} = E_0 + \underbrace{\sum_i^{\text{occ}} \sum_a^{\text{vir}} t_i^a \langle \Phi_0 | \hat{H} | \Phi_i^a \rangle}_{=0} + \sum_{i < j}^{\text{occ}} \sum_{a < b}^{\text{vir}} (t_{ij}^{ab} + t_i^a t_j^b - t_i^b t_j^a) \langle \Phi_0 | \hat{H} | \Phi_{ij}^{ab} \rangle \quad (2.67)$$

where the second term in the last equation is equal to zero due to the application of Brillouin's theorem when HF orbitals are used for constructing Slater determinants. Further, the third term $\langle \Phi_0 | \hat{H} | \Phi_{ij}^{ab} \rangle$ represents two-electron integrals as $\langle \phi_i \phi_j | \phi_a \phi_b \rangle - \langle \phi_i \phi_j | \phi_b \phi_a \rangle$. From the above it can be seen that in order to determine the coupled cluster correlation energy the singles, doubles amplitudes and the two electron integrals need to be calculated. One way to determine amplitudes is to apply a similarity transformation of the Hamiltonian operator:

$$e^{-T} \hat{H} e^T \Phi_0 = E_{CC} \Phi_0 \quad (2.68)$$

where CC SE was multiplied by deexcitation operator e^{-T} from the left. From there the projected energy equation and amplitude equations are obtained by multiplying

with the reference state and an excited state, respectively, as:

$$\langle \Phi_0 | e^{-T} \hat{H} e^T | \Phi_0 \rangle = E_{CC} \quad (2.69)$$

$$\langle \Phi_m^e | e^{-T} \hat{H} e^T | \Phi_0 \rangle = 0 \quad (2.70)$$

$$\langle \Phi_{mn}^{ef} | e^{-T} \hat{H} e^T | \Phi_0 \rangle = 0 \quad (2.71)$$

$$\vdots \quad (2.72)$$

In the first equation since e^{-T} is deexciting the reference function, which is impossible, $\langle \Phi_0 | e^{-T} = \langle \Phi_0 |$. The second equation describes e^{-T} acting on singly excited determinants Φ_m^e which results in:

$$\langle \Phi_m^e (1 - T_1) | \hat{H} | (1 + T_1 + (T_2 + \frac{1}{2}T_1^2) + (T_3 + T_2T_1 + \frac{1}{6}T_1^3)) \Phi_0 \rangle = 0 \quad (2.73)$$

where from the infinite expansion only certain terms survive using again the fact that the Hamiltonian operator contains only one- and two-electron terms and due to Brillouin's theorem terms involving singly excited states and the reference wave function are zero. The eq. (2.73) represents a coupled set of equations for single, double and triple amplitudes. Similarly, when the deexcitation operator e^{-T} is working on Φ_{mn}^{ef} the reference HF, singly and doubly excited states are generated and the resulting equation contains additional terms for quadruple amplitudes and connected terms. Following this procedure equations for higher order amplitudes and additional connecting amplitudes can be generated by projecting the deexcitation operator against higher excited determinants. However, in practical calculations it is not possible to include all cluster operators up to T_N , which would lead to the coupled cluster wave function equivalent to the full CI wave function, and thus a truncation to the cluster operator expansion has to be introduced. Truncating the T operator leads to the coupled cluster energy being approximate due to some of the derived amplitudes not being exact. The impact of truncation on the calculated energy depends on the excitation level at which truncation is introduced and importance of this level contribution to the overall energy. For example, truncating at double substitutions from the Hartree-Fock determinant ($T = T_2$) leads to the lowest level of approximation often referred to as Coupled Cluster Doubles (CCD).⁶ A popular CCSD include both single and double substitutions ($T = T_1 + T_2$). Higher order truncations such as CCSDT are rarely used but for the smallest systems and rather, such as in the case of a more popular CCSD(T), a full treatment of singles and doubles is included together with an estimate to the connected triples contribution.

When comparison is made between CC and CI, in both methods we are trying to

generate full CI from the reference HF wave function by applying $(1+T)$ in the case of CI and e^T in the case of CC. The advantage of using the exponential of T becomes apparent when truncation of T is introduced in both CI and CC. As an example, when excitation operator is truncated at double substitutions (T_2), the Taylor expansion of the exponential function leads to CCD:

$$\Psi_{\text{CCD}} = e^T \Psi_{\text{HF}} = \left(1 + T_2 + \frac{T_2^2}{2!} + \frac{T_2^3}{3!} + \dots \right) \Psi_{\text{HF}} \quad (2.74)$$

In the above equation the $1 + T_2$ terms define the configuration interaction with all double substitutions (CID) method and the remaining terms involve products of excitation operators (quadruple, hextuple substitutions,...). The inclusion of these products of excitation operators is the reason for size-consistency of CC method.⁴ Moreover, with increasing number of electrons method such as CCSD is thanks to the disconnected terms able to recover higher percentage of the correlation energy than CISD.

2.1.7 Multi-Configuration Self-Consistent Field

Another class of methods able to recover part of the HF missing electron correlation energy, in this case static correlation, are multi-configuration self-consistent field (MCSCF) methods. They are in principle CI methods that in addition to calculation of expansion coefficient also optimize MOs used for construction of the determinants in order to minimize the energy for a given CI wave function. They achieve this, similarly as in HF method, by using the SCF procedure. In the original HF theory, there are only two types of orbitals, occupied and unoccupied (virtual). In MCSCF an orbital space is partitioned into different sub-spaces, in order to obtain the most important configurations, where the electrons obey rules specified for that particular sub-space.¹⁸

One of the most common approaches is the Complete Active Space Self-Consistent Field (CASSCF) method. In the CASSCF, orbitals are divided into inactive (core orbitals), active and virtual orbitals. Here, the inactive orbitals are always doubly occupied, the active space orbitals typically include chosen valence orbitals together with some of the lowest unoccupied MOs, and virtual orbitals represent the rest of the unoccupied orbitals. A full CI expansion is performed within the active space orbitals which yields accurate representation of the potential energy surface for virtually any type of electronic state: closed or open shell, ground or excited state, neutral or ionic, etc.¹⁸ This also allows to recover a major part of the static correlation, if the active orbitals are chosen well.¹⁹ However, the choice of active

orbitals is not a trivial task and knowledge about the studied system and related chemistry is needed. Furthermore, we are limited in the size of the active space as inclusion of all the valence electrons is impossible for all but the smallest systems.

A mean to overcome the problem with the size of the active space is presented in a so called Restricted Active Space Self-Consistent Field (RASSCF) method, which divides orbitals into three sections RAS1, RAS2 and RAS3.⁶ Here, RAS1 and RAS3 represent in the HF reference doubly occupied and unoccupied orbitals, respectively. Further, both RAS1 and RAS2 have limitations on the allowed excitation levels (occupation numbers), i.e. only n number of excitations are allowed from RAS1 and to RAS3 (e.g. CISD). RAS2 is similar to the CASSCF active space where usually all the excitation are permitted (the Full CI). Sometimes an additional step is included by freezing the shapes of the core orbitals to the initial HF orbitals. A comparison of different orbital space partitioning is depicted in the Figure 2.3.

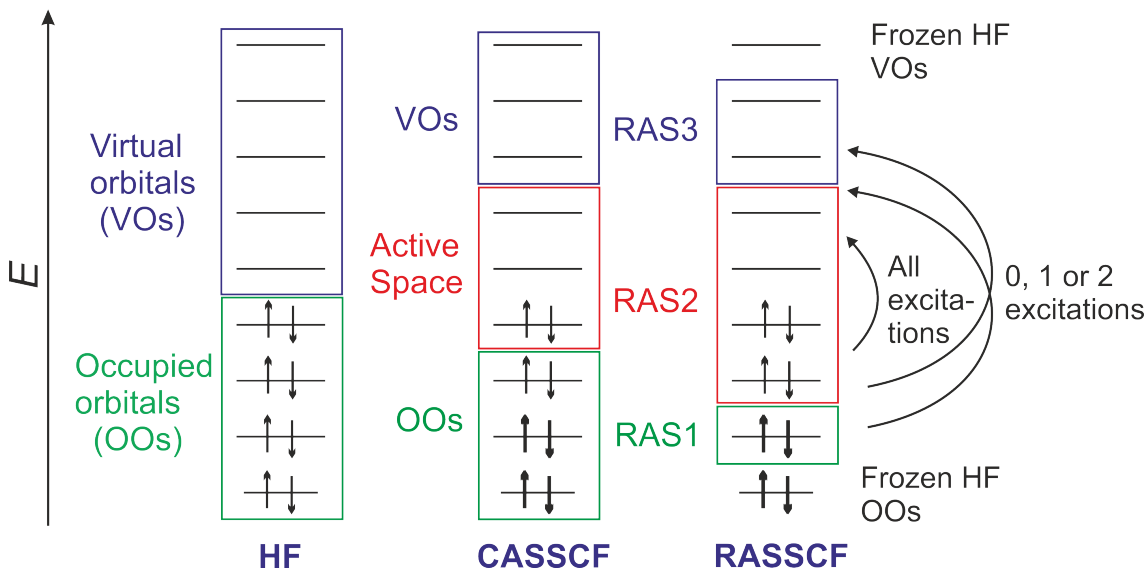


Figure 2.3: Illustrating orbital partitions for HF, CASSCF and RASSCF methods.

MCSCF methods provide a very powerful tool for investigation of multi-configurational states and conical intersections typical in, for example, photochemical reactions. Moreover, where needed it is possible to include some dynamic correlation to the CASSCF calculation by complementing it with, for example, the second order perturbation theory (MP2) in a so called CASPT2 method.

2.1.8 Basis Sets

In order to approximate the unknown molecular orbitals these are expressed as an expansion of known mathematical functions, denoted as basis functions. More mathematical functions are used, lower are restrictions on an electron location in

space thus simulating the true quantum nature of being anywhere in space, and it results in better description of orbitals. In principle any type of basis functions may be used, such as Gaussian, plane waves, etc., but when it comes to the choice of basis functions they should agree with the physics of the problem and be able to adequately describe the studied system. For example, for atomic and molecular systems functions such as Slater functions ($\exp(-\zeta r)$), denoted also as STO (Slater-type orbitals), and Gaussian functions ($\exp(-\zeta r^2)$), which is similarly denoted as GTO, are suitable choice as both of these functions and go towards zero with the increasing distance between the nucleus and the electron. On the other hand, the use of plane waves may be more appropriate for the use with periodic systems. Further, when choosing basis functions it should be easy to solve the required integrals with the chosen functions and they should converge relatively quickly.

Slater-type functions expressed in cartesian coordinates have the following form:

$$\phi(\mathbf{r}) = x^l y^m z^n e^{-\zeta r} \quad (2.75)$$

where $r = \sqrt{x^2 + y^2 + z^2}$ and $L = l + m + n$ is similar to the angular momentum ($L = 0, 1, 2, 3, \dots$ as s, p, d, f, \dots). These type of functions are useful for calculations on atoms as, for example, s -type Slater functions are similar to hydrogenic orbitals and have proper analytical structure with good description at singularities (nuclear cusp) and exponential decay. However, it is very difficult to compute matrix elements for molecular systems with the Slater type orbitals. Therefore, other type of basis functions such as atom-centered Gaussian functions are commonly used. The Gaussian functions, also referred to as primitive GTO, in the cartesian coordinates can be expressed as:

$$\phi(\mathbf{r}) = x^l y^m z^n e^{-\alpha r^2} \quad (2.76)$$

where $L = l + m + n$ is referred to as the angular momentum. These functions tend to decay at infinity faster than Slater functions and s -type Gaussians are missing nuclear cusp, but it is much easier to compute matrix elements using Gaussians. An example of STO and GTO function is depicted in the Figure 2.4.

As mentioned previously, although STO functions have better description for electron density they are computationally more expensive and hence this problem is circumvented by constructing the STO basis function as a linear combination of computationally more convenient gaussian functions. In practice, a so called *contracted* GTOs (CGTOs) are used, which are smaller sets of functions formed from fixed linear combinations of primitive GTOs:

$$\chi(\mathbf{r}) = \sum_{i=1}^n c_i \phi_i(\mathbf{r}) \quad (2.77)$$

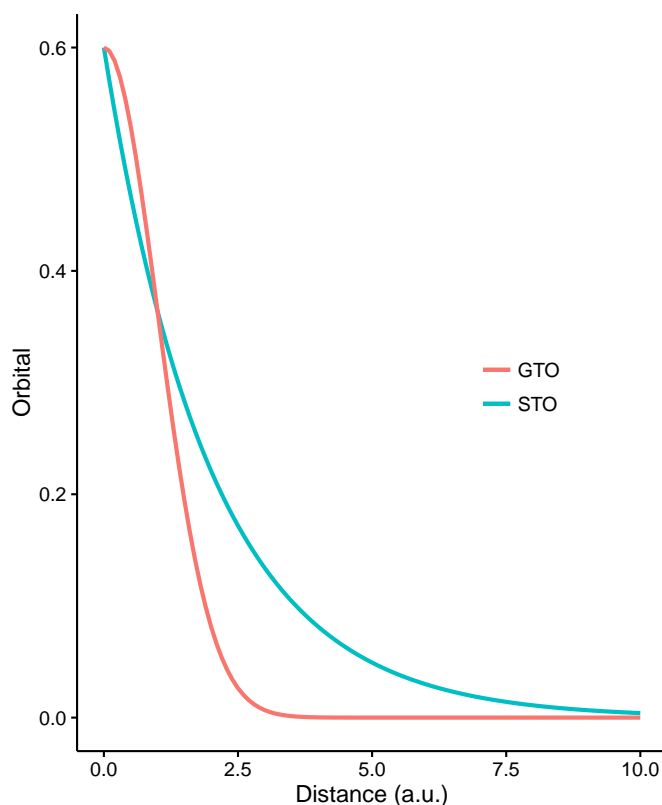


Figure 2.4: An example of STO and GTO function.

where c_i are contraction coefficients. The main reason behind using CGTOs is the fact that the molecular orbital expansion coefficients in front of the core electron basis functions change very little. Therefore, reducing the number of exponents to be optimized by a variational calculation using the constant variational coefficients in front of the inner electrons it is possible to dedicate more computational effort to description of chemically more interesting outer valence electrons.

One example of STO basis set constructed from GTOs is a STO-3G that used three GTOs to simulate one STO. The STO-3G basis set is also known as a *minimal basis set*, which means it contains the smallest number of basis functions that are needed for all the electrons of each neutral atom.⁷ For example, this means two s -functions (1s and 2s) and one set of p -functions ($2p_x$, $2p_y$ and $2p_z$) for the first row in the periodic table. The problem with minimal basis set is the lack of flexibility when, for example, bonds are formed and thus an improvements need to be introduced. *Split valence*, also referred to as n -tuple- ζ (double-zeta, triple-zeta, etc.), basis sets are the first example of improving the minimal basis set that allows orbitals to change size by inclusion of two or more basis functions for each valence orbital. A further way of making basis set larger (better) and especially to account for orbital polarization in molecular environments is to include higher angular momentum in a so called *polarized basis set*, which allows orbitals to change shape. The last way of enhancing basis set is to enlarge it with *diffuse functions*, a large versions (smaller exponent

ζ) of standard valence-size functions that enables orbitals to occupy a larger area of space. The diffuse functions are especially important for systems with loosely bound electrons such as anions, Rydberg states and excited states.

An example of an actual basis set commonly used is 6-31+G(d,p), which contains 6 GTOs for core orbitals, 3 GTOs for the first STO of the valence orbital and 1 GTO for the second STO description. Moreover, it contains d orbital functions on heavy atoms and p orbital functions on hydrogen atoms. This basis set is completed by adding diffuse function to heavy atoms only. The above introduced STO-3G and 6-31+G(d,p) basis sets are from a family of Pople style basis sets developed by John Pople and co-workers.

Correlation consistent (cc) basis sets developed by Dunning and co-workers represent a family of basis sets which should be mostly used with correlated calculations such as coupled cluster and Møller-plesset methods. In contrast to, for example, Pople basis sets which are optimized by variational procedure at the HF level the cc basis sets are optimized using correlated (CISD) wave functions and thus are designed to recover the correlation energy of the valence electrons. These basis sets are designed to converge smoothly towards the complete basis set limit. The cc are commonly denoted as (aug)-cc-pVXZ, which stands for correlation consistent polarized valence X-zeta ($X=D, T, Q, 5$, etc.) basis set. Optionally a prefix "aug" in front of the basis set means that it was augmented by inclusion of diffuse functions.

Another type of basis sets used within this work are all-electron split valence def2- x VP ($x = S, TZ, QZ$) basis sets originally developed by Ahlrich and co-workers²⁰. These are property-optimized (specifically dipole polarizabilities) split valence, polarized, n -zeta basis sets and, for example, Def2-TZVPD²¹ basis set is also augmented with diffuse functions.

2.1.9 Local Methods

Treatment of electron correlation at high level of *ab initio* calculations is essential for an accurate description of molecular structures, energetics and properties. Computational cost of conventional electron correlation methods, such as, CCSD (CCSD(T)) increases very steeply with the number of electrons and become prohibitively expensive for anything but small molecules. One of the reasons of this unfavourable scaling is that usually canonical molecular orbitals, which are generally delocalized over the whole system, are used as a basis for these calculations. On the other hand, localizing the molecular orbitals allows us to reduce the number of electron pairs to be correlated since there are small correlation effects coming from

interaction of distant electrons. Furthermore, this reduces the steep increase in the number of virtual orbitals needed.

In the case of local method, such as LCCSD, it is formulated in a basis of nonorthogonal local correlation functions.²² Excitations are made from localized molecular orbitals into subspaces (domains) of the local basis in order to significantly reduce the number of amplitudes to be optimized in LCCSD calculations. Moreover, this allows to completely neglect (or treat in a simplified way, e.g. MP2) the correlation of distant electrons. Local correlation methods have a potential to approach linear scaling with molecular size and to suffer less from the basis set superposition error.^{23,24} The basis set superposition error is often encountered in the case of weakly bound clusters where it leads to an artificial overestimation of the binding energy and shortening of inter-molecular distances. The reason is, due to finite basis sets being used, when monomers are approaching each other they can utilize extra basis functions from each other and thus improve their description of electron distribution. The error is coming from the fact that this electron distribution improvement is inconsistent, happening especially at shorter inter-molecular distances, which leads to inconsistent treatment of monomers at different inter-molecular distances.

2.1.10 Frequency Calculations

The following section, which mainly follows *the Vibrational Analysis in Gaussian* article by Ochterski²⁵, gives a short introduction to the frequency calculations.

Frequency calculations are not only important in order to predict the IR/Raman spectra, but also in order to characterize stationary points on the potential energy surface, for example, identifying a minimum, transition state or a higher order saddle point. Moreover, frequencies are needed for calculations of various thermochemical values, such as enthalpies, entropies and zero-point vibration and thermal energy corrections to the total energy.

Vibrational frequencies are calculated at the stationary point geometries by determining the second derivatives of the energy with respect to the cartesian nuclear coordinates and then transforming to mass weighted coordinates. This starts with calculation of the Hessian matrix, which contains the second partial derivatives of the energy with respect to displacement of the atoms in cartesian coordinates under the condition that the first derivatives with respect to displacement of the atoms are zero. These force constants are then converted to mass weighted cartesian coordinates. Next step is diagonalization of mass weighted force constant matrix which yields a set of $3N$ eigenvalues (the fundamental frequencies) and eigenvectors (the normal

modes). The eigenvectors are initially discarded and recalculated again after the rotation and translation modes are separated out leaving $3N - 6$ or $3N - 5$ vibrational modes. This is done by finding the transformation matrix, which is used to transform mass weighted cartesian coordinates to internal coordinates where rotation and translation modes are separated out. After the transformation the $N_{vib} \times N_{vib}$ submatrix, which represents the force constants internal coordinates, is diagonalized and yields N_{vib} eigenvalues $\lambda = 4\pi^2\nu^2$ and N_{vib} eigenvectors. These eigenvalues are then converted to frequencies in units of reciprocal centimeters.

2.1.11 Thermochemistry

In the following section basic concepts and equations for computing thermochemical quantities, specifically as defined in *Gaussian* program but applicable in general, are introduced in order to understand how these are obtained. This section mainly follows the paper on computing thermochemistry in *Gaussian* by Ochterski²⁶, which in return refers to equations from the textbook by McQuarrie and Simon²⁷.

All of these equations are derived under the special case of ideal gas approximation, therefore particles have no potential energy of interaction of any kind. Further, it is assumed that excitation energies even to the first electronically excited state are much higher than $k_B T$ at room temperature and thus there is usually no electronic energy contribution to the internal energy from occupation of electronically excited states.

In the following section equations describing how partition functions $q(V, T)$ from translational, electronic, rotational and vibrational motion components are used to determine entropy contribution, internal thermal energy and heat capacity. The following relation can be used to determine the entropy contribution:

$$S = Nk_B + Nk_B \ln \left(\frac{q(V, T)}{N} \right) + Nk_B T \left(\frac{\partial \ln q}{\partial T} \right)_V \quad (2.78)$$

In *Gaussian* package, special form of the above equation is used where molar values are given, so after division by $n = N/N_A$, substitution of $N_A k_B = R$ and moving the first term into the logarithm (as e), it yields (with $N = 1$):

$$\begin{aligned} S &= R + R \ln (q(V, T)) + RT \left(\frac{\partial \ln q}{\partial T} \right)_V \\ &= R \left(\ln(q_t q_e q_r q_v e) + T \left(\frac{\partial \ln q}{\partial T} \right)_V \right) \end{aligned} \quad (2.79)$$

Further, the partition function can be used to obtain the internal thermal energy E :

$$E = Nk_B T^2 \left(\frac{\partial \ln q}{\partial T} \right)_V \quad (2.80)$$

And this equation can be used to obtain the heat capacity:

$$C = \left(\frac{\partial E}{\partial T} \right)_{N,V} \quad (2.81)$$

In the following paragraph individual partition functions, as defined in *Gaussian* package, are introduced. Their definition may be slightly different and simplified in comparison to the usual definitions commonly found in textbooks. For example, contribution from the translation partition function q_t is defined as:

$$q_t = \left(\frac{2\pi m k_B T}{h^2} \right)^{3/2} \frac{k_B T}{P} \quad (2.82)$$

which when substituted to eq. (2.79) (and partially derived with respect to T to get the third term) yields the translational entropy:

$$S_t = R \left(\ln(q_t e) + \left(\frac{3}{2} \right) \right) \quad (2.83)$$

In the above equation factor e comes from Stirling's approximation. Similarly, translational contribution to the internal thermal energy can be derived as:

$$E_t = N_A k_B T^2 \left(\frac{\partial \ln q}{\partial T} \right)_V = \frac{3}{2} RT \quad (2.84)$$

and the constant volume heat capacity as:

$$C_t = \frac{\partial E_t}{\partial T} = \frac{3}{2} R \quad (2.85)$$

In the case of contribution from electronic partition function, it is assumed there is no contribution from the first and higher excited states, as these lie much higher in energy than $k_B T$. This assumption together with treating the ground state energy as a reference value of zero greatly simplifies the electronic partition function into contribution only from ground state degeneracy of the system $q_e = \omega_0$. Since there are no temperature dependent terms, this results in the electronic heat capacity and the internal thermal energy due to the electronic partition function being both zero and the electronic entropy of $S_e = R(\ln q_e)$.

In the general case of a nonlinear polyatomic molecule rotational partition function

has the following form:

$$q_r = \frac{\pi^{1/2}}{\sigma_r} \left(\frac{T^{3/2}}{(\Theta_{r,x}\Theta_{r,y}\Theta_{r,z})^{1/2}} \right) \quad (2.86)$$

where $\Theta_{r,n}$, $n = x, y, z$ are the rotational temperatures defined as $\Theta_r = h^2/8\pi^2 I_n k_B$, $n = x, y, z$ for three values of the moment of inertia I_n for three rotation axes. The contribution arising from rotational partition function for entropy is $S_r = R(\ln q_r + 3/2)$, to the internal thermal energy is $E_r = 3/2RT$ and finally $3/2R$ for the heat capacity. When compared with the average contribution to the entropy, the internal energy and heat capacity in the case of a linear polyatomic molecule, which has only two rotational degrees of freedom, it is $1/2RT$ less for the internal thermal energy, $1/R$ for the entropy and heat capacity.

Contributions from vibrational motion are represented as a product of the contributions from each real vibrational mode K , ignoring imaginary (minus sign) frequencies. There is a characteristic vibrational temperature, $\Theta_{v,K} = hv_K/k_B$, for each of the $3N - 6$ or $3N - 5$ modes for linear molecules. In the case when zero-point energy contributions are computed separately and bottom of the internuclear potential energy well is taken as zero energy reference point, then vibrational partition function is expressed as a product of individual partition functions for each vibrational mode K :

$$q_v = \prod_K \frac{e^{-\Theta_{v,K}/2T}}{1 - e^{-\Theta_{v,K}/T}} \quad (2.87)$$

After using the above partition function to calculate entropy and few algebraic operations the total vibrational entropy has the following form:

$$S_v = R \sum_K \left(\frac{\Theta_{v,K}/T}{e^{\Theta_{v,K}/T} - 1} - \ln(1 - e^{-\Theta_{v,K}/T}) \right) \quad (2.88)$$

Similarly, contribution to the internal energy from vibrational modes can be calculated as follows:

$$E_v = R \sum_K \Theta_{v,K} \left(\frac{1}{2} + \frac{1}{e^{\Theta_{v,K}/T} - 1} \right) \quad (2.89)$$

And finally contribution to the heat capacity is calculated as:

$$C_v = R \sum_K e^{\Theta_{v,K}/T} \left(\frac{\Theta_{v,K}/T}{e^{\Theta_{v,K}/T} - 1} \right)^2 \quad (2.90)$$

The above defined terms for partition functions, entropies and energies are used in

calculation of, for example, the Gibbs free energy defined as:

$$\Delta G = \overbrace{E_{elec} + E_{ZPE} + E_{tot} + k_B T}^{\Delta H} - T S_{tot} \quad (2.91)$$

where E_{elec} is electronic energy calculated at a given level of theory relative to separate nuclei and electrons. E_{ZPE} is zero-point energy correction, correcting for vibrational motion of the system described by a harmonic oscillator at 0 K and computed as a sum of contributions from all non-imaginary K vibrational modes $E_{ZPE} = \sum_K 1/2 h c \nu_K$. In the eq. (2.91) $E_{tot} = E_t + E_r + E_v + E_e$ represents correction to the internal thermal energy at given temperature T and calculated as a sum over contributions from individual partition functions. Similarly, S_{tot} is given as a sum of contributions from translational, rotational, vibrational and electronic degrees of freedom.

The Gibbs free energies calculated using the eq. (2.91) can be used, for example, in calculations of binding energies from free energies of reactants and products (see Chapter 3) and in calculations of reduction potentials using the thermodynamic cycle (see Chapter 4).

2.2 Density Functional Theory

Researchers have intensively tried to find a simplifying substitution for the very complex many-body wave function, which depends on $4N$ coordinates (three spatial and one spin coordinate for each of N electrons in the system). A suitable candidate seems to be the electronic density, a central variable in the Density Functional Theory (DFT), which is a simple function that depends solely on the three spatial variables (or in the case of systems including spin polarisation, such as open-shell systems, a spin-polarized formalism is used and the density is divided into spin up (ρ_α) and spin down (ρ_β) density). Moreover, in contrast to wave function methods, the density is an observable quantity that can be obtained from experiments, e.g. X-ray diffraction.

One of the advantages of DFT methods is their ability to directly include some of the effects of electron correlation (less expensively than post-Hartree-Fock correlated methods), in comparison to Hartree-Fock method that considers these effects only in an average sense. The best DFT methods achieve significantly greater accuracy than HF theory at only a modest increase in computational cost.⁷ On the other hand, the biggest disadvantage of DFT is that it is an exact method with the approximated functionals (as the real functionals are not known) and cannot be

further systematically improved, e.g. with increasing basis set. In the following section the basic theory behind DFT will be introduced.

The ultimate goal of the DFT method is the calculation of the total energy of the system and the ground-state electron density distribution without using the wave function of the system.¹ Starting from the Born-Oppenheimer approximation a relation between a central quantity in the DFT method, the electron density ρ , and the electronic wave function can be established:

$$\rho(r) = \sum_{\sigma_1=-\frac{1}{2}, \frac{1}{2}} \int |\Psi_0(r, \sigma_1, r_2, \sigma_2, \dots, r_N, \sigma_N)|^2 d\tau_2 d\tau_3 \dots d\tau_N \quad (2.92)$$

where Ψ_0 is a ground state wave function and τ is a spatial-spin coordinate. From the above equation a function of the position of electron 1 in space $\rho(r)$ is obtained after integration of the square of $|\Psi_0|^2$ over spin-space coordinates and summation over electron 1 spin coordinate.⁴

2.2.1 The Hohenberg-Kohn Theorems

The Hohenberg-Kohn Existence Theorem:

Hohenberg-Kohn in their existence theorem proved that for a ground state the electron density uniquely determines the Hamiltonian operator and thus all properties of the system.¹ This can be shown by constructing a Hamiltonian operator as in the following equation using only the density:

$$\hat{H} = \sum_{j=1}^N \left(-\frac{\hbar^2}{2m_e} \nabla_j^2 - \sum_{A=1}^M \frac{Z_A e^2}{|\vec{r}_j - \vec{R}_A|} + \frac{1}{2} \sum_{k \neq j}^N \frac{e^2}{|\vec{r}_j - \vec{r}_k|} \right) \quad (2.93)$$

where the number of electrons (N) is defined by the integral of the density over the whole space. Further, searching for the positions of potential spikes, number of spikes and steepness of each spike on the $\rho_0(r)$ landscape we obtain positions (\vec{R}_A), number (M) and charge (Z_A) of the nuclei, respectively.

The Hohenberg-Kohn Variational Theorem:

This theorem states that for a given number of electrons N and an external potential $V_{\text{ext}}(r)$ (substituting for the interaction of electrons with nuclei) there exists an energy functional[†] of electron density E^{HK} which obeys the following variational principle:

$$E^{\text{HK}}[\rho_{\text{guess}}] \geq E^{\text{HK}}[\rho_0] = E_0 \quad (2.94)$$

[†]the functional is a function that takes a function for its input argument

where ρ_0 is the exact electronic density distribution for the ground state energy E_0 . Unfortunately, the major goal of the method to find out the mathematical form of this functional has not yet been successful.

2.2.2 Orbital Free Approaches

Early orbital free approaches to define the energy functional considered the system to be classical and the energy consist of separable kinetic and potential components.⁶ In a so-called Thomas-Fermi (TF) model, the density is derived from an uniform electron gas and equations are based on fermion statistical mechanics. The electron-electron repulsion (E_{ee}) is with reference to the Hartree approximation divided into a Coulomb ($J[\rho]$) and exchange part ($K[\rho]$), and nuclear-nuclear repulsion is constant within the BO approximation. Finally, the total electronic energy functional $E_{0,\text{TF}}[\rho]$ has the following form:

$$E_{0,\text{TF}}[\rho] = \overbrace{C_{\text{F}} \int \rho^{5/3}(r) dr}^{T_{\text{TF}}[\rho]} - \overbrace{\sum_{A=1}^{N_{\text{nuclei}}} \int \frac{Z_A(R_A)\rho(r)}{|R_A - r|} dr}^{E_{\text{en}}[\rho]} + \overbrace{\frac{1}{2} \iint \frac{\rho(r)\rho(r')}{|r - r'|} dr dr'}^{J[\rho]} \quad (2.95)$$

where $C_{\text{F}} = \frac{3}{10}(3\pi^2)^{2/3}$, T_{TF} refers to the Thomas-Fermi approximate kinetic energy, E_{en} is the exact expression for electron-nuclei attraction. Further, inclusion of the exchange energy term $K_{\text{D}}[\rho] = -C_{\text{x}} \int \rho^{4/3}(r) dr$, with $C_{\text{x}} = \frac{3}{4}(\frac{3}{\pi})^{1/3}$, derived by Dirac into the above equation (2.95) forms a Thomas-Fermi-Dirac model. Limitations of these models are, for instance, the approximate kinetic energy term, self-interaction term in E_{ee} as well as missing electron correlation effects. Although there have been some improvements in these orbital free models and some of the ideas and equations derived from uniform electron gas models are used in the so-called Local Density Approximation that will be discussed further below, their accuracy is still too low to be of general use.

2.2.3 Kohn-Sham Self-consistent Field Methodology

Kohn and Sham (KS) realised that the main flaw of orbital free models (i.e. the Thomas-Fermi model) is connected with the way the kinetic energy is determined.²⁸ In their report from 1965 they introduced an approach to the unknown universal functional, mentioned in the second Hohenberg-Kohn theorem, in a form of a fictitious non-interacting system of electrons. In this non-interacting system the total Hamiltonian is expressed as a sum of one-electron operators ($(-\frac{1}{2}\Delta + V_{\text{ext}})$) where electrons are subject to an external potential V_{ext} ingeniously tailored such that

the overall density ρ is same as the ground-state density ρ_0 of a real system. The eigenfunction for the total Hamiltonian is a KS determinant Ψ^{KS} (similar form as Slater determinant) constructed from KS spinorbitals ϕ_i^{KS} and the electronic density can be expressed as $\rho_{\text{exact}}(r) = \sum_i n_i |\Psi_i^{\text{KS}}(r)|^2$ with $n_i = 0, 1, 2$ denoting orbital occupancy in the KS determinant. The total energy functional is written as:

$$E_{\text{DFT}}[\rho(r)] = T_{\text{ni}}[\rho(r)] + V_{\text{ne}}[\rho(r)] + V_{\text{ee}}[\rho(r)] + E_{\text{xc}}[\rho(r)] \quad (2.96)$$

where the terms on the r.h.s. refer, respectively, to the kinetic energy of the non-interacting electrons, standard Coulomb electron-nuclei interaction, the classical Coulomb electron-electron repulsion and E_{xc} includes quantum in nature exchange, electron-electron correlation terms, correction for the classical self-interaction energy and the difference in the kinetic energy between the non-interacting and the real system. The problem with the kinetic energy was partially solved by splitting it into a major fraction that can be computed exactly (equation (2.97)) and a small part that is merged into a so called exchange-correlation energy E_{xc} together with all non-classical corrections to the electron-electron repulsion energy.

$$T_{\text{ni}}[\rho(r)] = \sum_{i=1}^N \left\langle \phi_i \left| -\frac{1}{2} \nabla_i^2 \right| \phi_i \right\rangle \quad (2.97)$$

Kohn-Sham orbitals are expressed within a basis set of functions ϕ_i and individual orbital coefficients are determined by solving a secular equation (analogous to HF theory) which is done iteratively using SCF procedure:

$$K_{\mu\nu} = \left\langle \phi_\mu \left| -\frac{1}{2} \nabla^2 - \sum_k^{\text{nuclei}} \frac{Z_k}{|r - r_k|} + \int \frac{\rho(r')}{|r - r'|} d^3 r' + V_{\text{xc}} \right| \phi_\nu \right\rangle \quad (2.98)$$

Here, $V_{\text{xc}} = \frac{\delta E_{\text{xc}}}{\delta \rho}$ is a potential corresponding to the exchange-correlation energy E_{xc} , and $K_{\mu\nu}$ is similar to $F_{\mu\nu}$ from the HF method.^{4,28} Most of the terms on r.h.s. of the equation (2.98) can be solved exactly except for the V_{xc} and thus E_{xc} parts for which approximations have to be introduced.

2.2.4 Approximations to the Exchange-correlation Functional

The electronic density distribution can be described locally within a small volume approximated as homogenous. Following this assumption the exchange-correlation energy can be estimated as a sum of contributions from infinitesimally small volumes using the uniform electron gas model.¹ The Thomas-Fermi-Dirac model, introduced

in section 2.2.2, is an example of total electronic energy in Local Density Approximations (LDA). In the LDA, the term "local" means that the energy is given as a functional which depends only on $\rho(r)$ at points in space but not on $\rho(r)$ at more than one point in space or on spatial derivatives of $\rho(r)$. Unfortunately, the uniform electron gas approximation is insufficient especially in the region near the nuclei where the electron densities vary rather strongly. This inhomogeneity of the electron density can be taken into account using non-local corrections, Generalized Gradient Approximations (GGA), involving gradient of $\rho(r)$, $\nabla\rho(r)$.

In most cases a gradient corrected functional is constructed by adding a gradient correction to the LDA functional:

$$E_{\text{XC}}^{\text{GGA}} = E_{\text{XC}}^{\text{LDA}} + \int B_{\text{XC}}(\rho, \nabla\rho) d^3r \quad (2.99)$$

where the exchange-correlation function B_{XC} is carefully selected as a function of ρ and its gradient in order to:

- reproduce experimental properties of atoms and molecules (training sets of molecules)
- reproduce properties of exchange and correlation effects resulting from quantum mechanical equations (limiting values for high and low electron densities, properties of the exchange "hole")

Typically, complete exchange-correlation functionals are built as a combination of correlation and exchange GGA functionals, for instance, a BLYP functional is a combination of Becke's (B) GGA exchange with the GGA correlation functional of Lee, Yang, and Parr (LYP).⁴

Additional improvement to the GGA functionals is an inclusion of the second derivative of the density (the Laplacian operator, $\Delta\rho$) or the kinetic energy density, defined as $\tau(r) = \sum_{i=1}^{\text{occupied}} \frac{1}{2} |\nabla\Psi_i(r)|^2$, in a so-called meta-GGA functionals. For example, TPSS²⁹ and M06-L³⁰ (in the rest of the text written as M06L) are examples of meta-GGA functionals.

Another family of exchange-correlation approximations are hybrid functionals, which define the exchange functional by mixing exact HF with DFT (LDA and/or GGA) exchange term and this functional is then combined with a local and/or gradient-corrected correlation functional. This is theoretically justified by the adiabatic connection theorem, which connects the non-interacting (KS) and fully interacting (exact) system.

$$E_{\text{XC}}^{\text{hybrid}} = \alpha(E_{\text{X}}^{\text{HF}} - E_{\text{X}}^{\text{DFT}}) + E_{\text{XC}}^{\text{DFT}} \quad (2.100)$$

An example of one of the most popular three-parameter hybrid functional B3LYP has the following form for E_{XC} :

$$E_{XC}^{B3LYP} = E_X^{LDA} + c_0(E_X^{HF} - E_X^{LDA}) + c_X E_X^{B88} + E_C^{VWN3} + c_C(E_C^{LYP} - E_C^{VWN3}) \quad (2.101)$$

where the c parameters were obtained fitting into experimental data. The parameter $c_0 = 0.20$ controls admixture of HF and LDA local exchange and exchange functional is further supplemented with gradient-corrected Becke's (B88) functional, scaled by the parameter $c_X = 0.72$. Finally, exchange-correlation functional is completed by addition of the Vosko-Wilk-Nusair (VWN3) local correction functional, which can be optionally corrected by the LYP correlation correction via the parameter $c_C = 0.81$.⁷

A major drawback of DFT is that we are not able to systematically improve the current methods to yield the exact results, not even when a complete basis set is used, since the functional form of the exact exchange-correlation energy is not known. Moreover, we cannot use DFT (in the Hohenberg-Kohn ground state theory) on its own to probe processes in photochemistry and to predict excited state properties. Although it was shown that the density contains information about excited state properties, as we are able to construct a Hamiltonian operator (wave function) from the density, there is no practical way to extract this information so far.²⁸

2.2.5 Dispersion correction DFT (D-DFT)

One of the areas where the current DFT functionals usually perform poorly is a so called dispersion energy problem. This problem is related to inability of modern functionals to describe contribution that stem from dispersion forces and poses challenge especially when studying weakly bound systems such as rare gas dimers, hydrogen bonded complexes and complexes dominated by π - π -stacking. Dispersion forces, sometimes also referred to as London forces, are long-range attractive forces arising from the induced dipole-induced dipole interaction generated as a result of instantaneous correlation of electronic motion. The induced dipole-induced dipole interaction, which is usually dominating the interaction, decays with the inverse sixth power ($1/R^6$) of the intermolecular distance.

The main reason for the missing dispersion forces is that the exchange-correlation potential $V_{XC}(\mathbf{r})$ at a point \mathbf{r} is determined by the density exactly at this point.²⁸ This means that if there is no overlap of electron densities between the local and another distant system, which means that these are not directly bonded to each other, only the local exchange-correlation energy is considered. Therefore some kind of improvement has to be introduced in order to account for this nonlocal long-range

correlation effects.

There are several approaches trying to address the dispersion energy problem. For example, time-dependent DFT based approaches³¹, vdW-Density Functional method^{32,33} which uses the electron density to compute the dispersion energy and DFT-D methods³⁴⁻³⁷ utilizing a damped, atom-pair wise potential which is added to a standard Kohn-Sham DFT.

The GD3BJ dispersion correction, which is used in this work, belongs to the family of DFT-D methods and uses the D3 version of Grimme’s dispersion with Becke-Johnson (BJ) finite-damping to ensure more physically correct short-range behavior.³⁸ The DFT-D3 is atom pairwise additive scheme in which the dispersion energy is defined as:

$$E_{\text{disp}}^{D3(BJ)} = -\frac{1}{2} \sum_{A \neq B} s_6 \frac{C_6^{\text{AB}}}{R_{\text{AB}}^6 + [f(R_{\text{AB}}^0)]^6} + s_8 \frac{C_8^{\text{AB}}}{R_{\text{AB}}^8 + [f(R_{\text{AB}}^0)]^8} \quad (2.102)$$

where the sum runs over all atom pairs in the system and $f(R_{\text{AB}}^0) = a_1 R_{\text{AB}}^0 + a_2$ contains free fit parameters a_1 and a_2 introduced by BJ. Further, R_{AB}^0 is defined as $R_{\text{AB}}^0 = \sqrt{C_8^{\text{AB}}/C_6^{\text{AB}}}$.³⁹

2.3 Molecular Dynamics

Molecular dynamics (MD) is an advanced computational method based on a rather simple physical model that can provide insight into the structural dynamics and energetics of molecular systems at atomic level. It belongs to the family of a so-called *force-field* methods (or sometimes referred to as *Molecular Mechanics* methods) where the step of obtaining a potential energy surface by calculating the electronic energy is greatly simplified by using the parametric functions of the electronic energy with parameters fitted to usually *ab initio* calculations or experimental data. The smallest building blocks are typically atoms or groups of atoms in the case of, for example, Coarse-Grained Molecular Dynamics. Force-field based methods do not take into account electrons and hence the bonding information must be part of the parameters provided for the system. Potential energy surface is sampled using the classical mechanics (Newton’s second law), which means that quantum phenomena are neglected and events such as bond formation/breaking and quantum tunnelling cannot be observed.

Molecular dynamics simulations are performed in order to provide conformational sampling, to understand structure-energy relationship and to estimate equilibrium

and non-equilibrium properties of molecular systems. One of the major advantages of MD simulations over, for example, Monte-Carlo method is the possibility to study time-dependent properties, using a so called *time-correlation functions*, due to the time connection between simulation steps.⁴⁰ Macroscopic properties that can be studied by MD are, for example, the radial distribution function of a solvent, viscosity of a liquid, reaction kinetics and diffusion processes.

2.3.1 Force fields

Force fields used in MD are simple analytical atomistic functions relating structure with potential energy. In MD a set of approximations is introduced to the molecular system. For example, parameters for both bond-stretching and angle-bending are present in the form of spring constants describing generally a harmonic potential. These are further supplemented by torsion profiles for dihedral angles. Atoms are approximated as Lennard-Jones spheres with constant point partial charges localized at the atomic centres. The partial charges are normally derived based on fitting to the molecular electrostatic potential calculated using an *ab initio* method. It is the quality of these partial charges that determine the accuracy of MD calculations especially for polar molecules where the electrostatic terms will dominate the potential function.⁶ Moreover, the partial charges are geometry dependent and this has to be taken into account during their derivation. The force fields commonly used are pair-additive, neglect explicit polarization and charge-transfer effects though these contributions are included indirectly by some parameters. The result is that some important effects are not well described, for example, inclusion of divalent ions, hydrogen bonding and solute polarization by solvent.⁴¹

There are various types of force-fields designed for different purposes and can differ in aspects such as⁶:

- Potential energy functional form
- Number of cross terms[†] included
- Type of information used for fitting the parameters

For example, in the case of force fields designed to treat large systems, such as nucleic acids or proteins, the harmonic form of potentials for bonds and angles are used. Furthermore, a Lennard-Jones potential is used for the Van der Waals term and the cross term is not present.⁶ Force fields are usually designed to work for

[†]in general all kind of terms that couple two (or more) of the bonded terms

specific systems of interest. For instance, the OPLS^{42,43} force field was developed for organic liquids simulations, the AMBER force field mainly to work with nucleic acids and proteins in comparison to the CHARMM that is used mainly for proteins. One of the key ideas that is often used during force-field parametrization is that structural units (bond-stretching, angle-bending, etc.) defined for similar chemical environments are transferable between different molecules. An overview of some of the available force fields can be found in, for example, *Introduction to Computational Chemistry* by Jensen⁶ and *Essentials of Computational Chemistry* by Cramer⁴. Below generic aspects of force fields are given.

2.3.2 Potential Energy and Equations of Motion

Propagation of the studied system in time is acquired by calculating the Newton's equations of motion (2.103) for a system of N interacting atoms:

$$f_i = m_i \frac{\partial r_i}{\partial t^2} = -\frac{\partial \mathcal{U}}{\partial r_i} \quad (2.103)$$

where forces f_i acting on the atoms are usually derived from a potential energy \mathcal{U} which is given as a sum of individual energy terms for covalent and noncovalent contributions eq. (2.104):

$$\mathcal{U} = \mathcal{U}_{\text{covalent}} + \mathcal{U}_{\text{noncovalent}} \quad (2.104)$$

Continuing to discuss, for simplicity, a system composed of atoms with coordinates r_1, \dots, r_N and potential energy $\mathcal{U}(r_1, \dots, r_N)$, we introduce an atomic momenta p_1, \dots, p_N , in terms of which the kinetic energy may be written as $\mathcal{K}(p_1, \dots, p_N) = \sum_{i=1}^N |p_i|^2 / 2m_i$. The covalent part of the potential energy consists of bond-stretching, angle-bending and dihedral (torsion) angle contributions. Illustrative figure of covalent contributions is shown in Figure 2.5 and the related equations (2.105):

$$\begin{aligned} \mathcal{U}_{\text{covalent}} &= \frac{1}{2} \sum_{\text{bonds}} k_{ij} (r_{ij} - r_{ij0})^2 \\ &+ \frac{1}{2} \sum_{\substack{\text{bend} \\ \text{angles}}} k_{ijk} (\theta_{ijk} - \theta_{ijk0})^2 \\ &+ \frac{1}{2} \sum_{\substack{\text{torsion} \\ \text{angles}}} \sum_n k_{ijkl} (1 + \cos(n\phi_{ijkl} - \phi_{ijkl0})) \end{aligned} \quad (2.105)$$

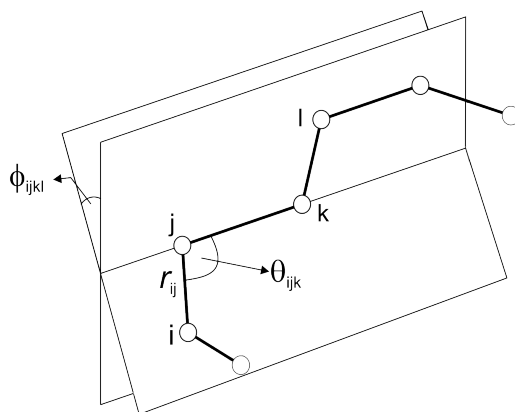


Figure 2.5: Illustrating picture for the definition of bond r_{ij} (interatomic distance), bend angle θ_{ijk} and torsion angle ϕ_{ijkl} .

The noncovalent part of potential energy is in the form of a pair-additive potential where three-body and higher order interactions are neglected. A model of pair potential can be seen in eq. (2.106) and a real noncovalent potential used in simulations eq. (2.107) consist of a VdW part, which has the form of the Lennard-Jones potential, and a Coulomb part for electrostatic charges.

$$\mathcal{U}(r_1, \dots, r_N) = \sum_{i < j} u(r_i, r_j) \quad (2.106)$$

$$\mathcal{U}_{\text{noncovalent}} = \underbrace{4\epsilon \left[\left(\frac{\sigma}{r_{ij}} \right)^{12} - \left(\frac{\sigma}{r_{ij}} \right)^6 \right]}_{\text{Lennard-Jones potential}} + \underbrace{\frac{1}{4\pi\epsilon_0} \frac{q_i q_j}{r_{ij}}}_{\text{Coulomb potential}} \quad (2.107)$$

2.3.3 Molecular Dynamics Simulations

The MD simulations are carried out from a starting set of atomic coordinates, which are usually obtained from X-ray crystallography or NMR experiments. The high quality starting structure is of an essential importance for MD sampling a proximity of X-ray potential minimum on a potential energy surface. The reason is that for most of the simulations due to a limited simulation time only a small conformational space is sampled around the crystal structure minimum. Moreover, MD cannot overcome large energy barriers due to usually limited kinetic energy related to reasonable simulation temperatures.^{41,44}

In a typical MD simulation, an initial geometry of the studied system is placed in the environment of solvent (e.g. water) and ions. Immersing the structure into a solvent box with ions, we are trying to get as close as possible to real conditions.

Initial velocities are assigned to each of the atoms according to randomly selecting from a Maxwell-Boltzmann distribution at the simulated temperature:

$$p(v_{ix}) = \left(\frac{m_i}{2\pi k_B T} \right)^{1/2} \exp \left[-\frac{1}{2} \frac{m_i v_{ix}^2}{k_B T} \right] \quad (2.108)$$

where at a given temperature T atom i of mass m_i is assigned a velocity v_{ix} in the x direction.

When MD is performed without temperature and pressure coupling this generates NVE (constant moles, constant volume and constant energy) ensemble. However, most desired quantities are commonly calculated from MD simulations performed in the constant temperature NVT or constant pressure NPT ensemble. The NVT ensemble is usually achieved by coupling the system to a heat bath and there are various schemes available to simulate the constant temperature or if needed to control the temperature of the system. For example, since the temperature of the system is related to the time averaged kinetic energy as $\langle E_k \rangle_{NVT} = 3/2 N k_B T$ an obvious scheme would adjust the temperature by re-scaling the velocities of particles. Such a scheme is the Berendsen thermostat⁴⁵ that corrects a deviation of the system temperature by weak coupling to an external heat bath with reference temperature T_0 using the following equation:

$$\frac{dT}{dt} = \frac{T_0 - T}{\tau} \quad (2.109)$$

which assures that a temperature deviation decays exponentially with a constant coupling time τ . However, this thermostat does not generate a correct canonical ensemble and therefore this is achieved by more advanced thermostats such as velocity-rescaling⁴⁶ or Nosé-Hoover scheme^{47,48}. For the generation of the NPT ensembles the constant pressure is maintained by changing the volume of the simulation cell by scaling the coordinates and simulation box vectors. The Berendsen⁴⁵ or the Parrinello-Rahman^{49,50} scheme are examples of common pressure coupling algorithms used to ensure the constant-pressure simulations.

MD run generates a series of time-correlated configurations, or "snapshots" of the simulated system at a given time, which form a trajectory of the system. The time step is one of the limiting factors of MD and is determined by the rate of the fastest molecular motions, which are usually vibrations involving hydrogen atoms. Therefore, the maximum time step is typically of the order of femtoseconds (10^{-15} s). Another issue is that the classical harmonic oscillator approach is unsuitable for high frequency motions with $\nu \gg k_B T/h$. Around the room temperature of 300 K this corresponds to the wavenumber of approximately 208 cm^{-1} . Therefore, in order to achieve longer time steps and thus longer simulation times it is common to

remove the highest frequencies by treating the bonds and angles (typically involving hydrogen) as constraints.⁶

Most MD calculations use leap-frog algorithm⁵¹, which step-by-step numerically integrate coupled differential equations of motion (2.110) and (2.111). In the case of leapfrog, positions are defined at times $t_i, t_{i+1}, t_{i+2}, \dots$, spaced at constant intervals dt , while the velocities are defined at times halfway in between, indicated by $t_{i-1/2}, t_{i+1/2}, t_{i+3/2}, \dots$.

$$\mathbf{r}(t + \delta t) = \mathbf{r}(t) + \mathbf{v}(t + \frac{1}{2}\delta t)\delta t \quad (2.110)$$

$$\mathbf{v}(t + \frac{1}{2}\delta t) = \mathbf{v}(t - \frac{1}{2}\delta t) + \frac{1}{m}\mathbf{F}(t)\delta t \quad (2.111)$$

The analysis of the outcome from simulations may provide detailed information about all aspects of the time evolution (with sub-ps time resolution) of the three-dimensional structure and interactions within studied system.⁴¹ Despite the enormous advance of MD in recent years, the method still encounters two basic limitations. The first one deals with problems of short simulation timescales, which result in limited sampling of conformational space. However, this limitation is slowly waning with faster computers, use of graphic cards for some of the calculations and improvements in the codes used in MD. The second, more critical limitation that cannot be easily overcome, is because of the approximate nature of the force fields used in MD. In comparison to more accurate quantum mechanical calculations, however MD is able to work with larger systems with reasonable computational cost and provide dynamical, not just static molecular information.

2.4 Hybrid QM/MM Methods

Hybrid QM/MM methods treat a system of interest at multiple levels of theory, combining high accuracy of quantum mechanical (QM) calculations with the low computational cost of empirical molecular mechanical (MM) approach. A challenge for computational chemistry at present is to study reactions and photochemical processes in large systems or molecules in a realistically modeled environment of chemical and/or biological interest. However, this goal is currently out of reach of traditional electronic structure methods for which the computational costs scale unfavourably with the size of the system, typically limiting them to small model systems *in vacuo*. In contrast, methods of molecular mechanics have the advantage of lower computational requirements than QM methods, but on the other hand

suffer from several limitations, as they are not able to describe the details of bond breaking/forming or electron transfer reactions.^{4,44} The QM/MM approach provides a means for overcoming these limitations by partitioning the studied system into two (or more) parts, which are calculated with different computational methods and are coupled with each other.

In a typical approach a part of the molecule where a (photo)chemical reaction takes place, denoted as QM core, is investigated with a reliable QM method (*ab initio* or DFT), semi-empirical, or Empirical Valence Bond (EVB) level. The remainder of the molecule, which impose sterical and polarization constraints on the QM core, is included using a lower level of theory, typically using molecular mechanics (MM region). The result is that the complete Hamiltonian and thus the total energy of the system must be some kind of hybrid of QM and MM.

References

- [1] Pielak, L. *Ideas of Quantum Chemistry*; Elsevier, 2007.
- [2] Groenhof, G.; Boggio Pasqua, M.; Schäfer, L. V.; Robb, M. A. In *Combining Quantum Mechanics and Molecular Mechanics. Some Recent Progresses in QM/MM Methods*; Sabin, J. R., Brändas, E., Eds., Vol. 59; Academic Press, 2010; pages 181–212.
- [3] Young, D. *Computational Chemistry: A Practical Guide for Applying Techniques to Real World Problems*; John Wiley & Sons, 2001.
- [4] Cramer, C. *Essentials of computational chemistry: theories and models*; J. Wiley, 2002.
- [5] Szabo, A.; Ostlund, N. *Modern Quantum Chemistry: Introduction to Advanced Electronic Structure Theory*; Dover Publications, 1996.
- [6] Jensen, F. *Introduction to Computational Chemistry*; John Wiley & Sons, 2007.
- [7] Foresman, J.; Frisch, A.; Gaussian, I. *Exploring chemistry with electronic structure methods*; Gaussian, Inc., 1996.
- [8] Schlegel, H. B. *WIREs Comput Mol Sci* **2011**, 1(5), 790–809.
- [9] Matsika, S.; Krause, P. *Annu. Rev. Phys. Chem.* **2011**, 62(1), 621–643.
- [10] Paterson, M. J.; Bearpark, M. J.; Robb, M. A.; Blancafort, L.; Worth, G. A. *Phys. Chem. Chem. Phys.* **2005**, 7(10), 2100–2115.

- [11] Roothaan, C. C. J. *Rev. Mod. Phys.* **1951**, *23*, 69–89.
- [12] Hall, G. G. *Proc. R. Soc. A* **1951**, *205*(1083), 541–552.
- [13] Shavitt, I.; Bartlett, R. J. *Many-Body Methods in Chemistry and Physics*; Cambridge University Press, 2009.
- [14] Nesbet, R. K. *Phys. Rev.* **1958**, *109*, 1632–1638.
- [15] Löwdin, P.-O. *J. Math. Phys.* **1962**, *3*(6), 1171–1184.
- [16] Parr, R.; Weitao, Y. *Density-Functional Theory of Atoms and Molecules*, International Series of Monographs on Chemistry; Oxford University Press, 1989.
- [17] Van Voorhis, T.; Head-Gordon, M. *J. Chem. Phys.* **2000**, *113*(20), 8873–8879.
- [18] Roos, B. O. In *Theory and Applications of Computational Chemistry*; Dykstra, C. E., Frenking, G., Kim, K. S., Gustavo E. Scuseria., Eds.; Elsevier: Amsterdam, 2005; pages 725–764.
- [19] Robb, M. A.; Bernardi, F.; Kluwer Academic Publishers, 1991; Vol. 339 of *NATO ASI series: Mathematical and physical sciences*; chapter Ab-Initio Modelling of Chemical Reactivity using MC-SCF and VB Methods.
- [20] Weigend, F.; Ahlrichs, R. *Phys. Chem. Chem. Phys.* **2005**, *7*, 3297–3305.
- [21] Rappoport, D.; Furche, F. *J. Chem. Phys.* **2010**, *133*(13).
- [22] Hampel, C.; Werner, H.-J. *J. Chem. Phys.* **1996**, *104*(16), 6286–6297.
- [23] Murphy, R. B.; Beachy, M. D.; Friesner, R. A.; Ringnalda, M. N. *J. Chem. Phys.* **1995**, *103*(4), 1481–1490.
- [24] DuBay, K. H.; Hall, M. L.; Hughes, T. F.; Wu, C.; Reichman, D. R.; Friesner, R. A. *J. Chem. Theory Comput.* **2012**, *8*(11), 4556–4569.
- [25] Ochterski, J. W. *Gaussian Inc, Pittsburgh, PA* **1999**, pages 1–17.
- [26] Ochterski, J. W. *Gaussian Inc, Pittsburgh, PA* **2000**, pages 1–17.
- [27] McQuarrie, D.; Simon, J. *Molecular Thermodynamics*; University Science Books, 1999.
- [28] Koch, W.; Holthausen, M. *A chemist's guide to density functional theory*; Wiley-VCH, 2000.
- [29] Tao, J.; Perdew, J. P.; Staroverov, V. N.; Scuseria, G. E. *Phys. Rev. Lett.* **2003**, *91*, 146401.

- [30] Zhao, Y.; Truhlar, D. G. *J. Chem. Phys.* **2006**, *125*(19), 194101–18.
- [31] Heßelmann, A.; Jansen, G. *Chem. Phys. Lett.* **2003**, *367*(5–6), 778 – 784.
- [32] Dion, M.; Rydberg, H.; Schröder, E.; Langreth, D. C.; Lundqvist, B. I. *Phys. Rev. Lett.* **2004**, *92*, 246401.
- [33] Lee, K.; Murray, E. D.; Kong, L.; Lundqvist, B. I.; Langreth, D. C. *Phys. Rev. B* **2010**, *82*, 081101.
- [34] Grimme, S.; Antony, J.; Ehrlich, S.; Krieg, H. *J. Chem. Phys.* **2010**, *132*(15).
- [35] Grimme, S. *J. Comput. Chem.* **2004**, *25*(12), 1463–1473.
- [36] Jurecka, P.; Cerny, J.; Hobza, P.; Salahub, D. R. *J. Comput. Chem.* **2007**, *28*(2), 555–569.
- [37] Grimme, S. *WIREs Comput. Mol. Sci.* **2011**, *1*(2), 211–228.
- [38] Grimme, S.; Ehrlich, S.; Goerigk, L. *J. Comput. Chem.* **2011**, *32*(7), 1456–1465.
- [39] Johnson, E. R.; Becke, A. D. *J. Chem. Phys.* **2006**, *124*(17).
- [40] Leach, A. *Molecular Modelling: Principles and Applications*, Pearson Education; Prentice Hall, 2001.
- [41] Ditzler, M. A.; Otyepka, M.; Sponer, J.; Walter, N. G. *Acc Chem Res* **2010**, *43*(1), 40–7.
- [42] Jorgensen, W. L.; Maxwell, D. S.; Tirado-Rives, J. *J. Am. Chem. Soc.* **1996**, *118*(45), 11225–11236.
- [43] Kaminski, G. A.; ; Friesner, R. A.; Tirado-Rives, J.; Jorgensen, W. L. *J. Phys. Chem. B* **2001**, *105*(28), 6474–6487.
- [44] Banas, P.; Jurecka, P.; Walter, N. G.; Sponer, J.; Otyepka, M. *Methods* **2009**, *49*(2), 202–16.
- [45] Berendsen, H. J. C.; Postma, J. P. M.; van Gunsteren, W. F.; DiNola, A.; Haak, J. R. *J. Chem. Phys.* **1984**, *81*(8), 3684–3690.
- [46] Bussi, G.; Donadio, D.; Parrinello, M. *J. Chem. Phys.* **2007**, *126*(1).
- [47] Nosé, S. *Mol. Phys.* **1984**, *52*(2), 255–268.
- [48] Hoover, W. G. *Phys. Rev. A* **1985**, *31*, 1695–1697.
- [49] Parrinello, M.; Rahman, A. *J. Appl. Phys.* **1981**, *52*(12), 7182–7190.
- [50] Nosé, S.; Klein, M. *Mol. Phys.* **1983**, *50*(5), 1055–1076.
- [51] Hockney, R.; Goel, S.; Eastwood, J. *J. Comp. Phys.* **1974**, *14*(2), 148 – 158.

Chapter 3

Biomolecular mode of action of Metformin

3.1 Introduction

The following chapter presents a project studying metal-binding properties of type 2 diabetes drug metformin and structurally closely related compounds. This study was done in collaboration with Stefan Erhardt and a group of Graham Rena and was published in 2014 in the journal of Biochemistry.¹

Type 2 diabetes (T2D), which covers 90% of all diabetes patients, is characterized by hyperglycaemia due to insulin resistance in peripheral tissues. One of the most effective and commonly used antihyperglycemic T2D drugs is metformin, which is the first-line treatment because of better long-term outcomes compared with those of other therapies such as insulin secretagogues.² Metformin [*N,N*-dimethylbiguanide, Metf (for its chemical structure, see Figure 3.2) belongs to the biguanide family that also includes other compounds, such as phenformin and buformin, with antihyperglycemic properties. Metf and other biguanide derivatives have been developed after it was discovered that the blood glucose-lowering ingredient in Goat's Rue is guanidine and other guanidine derivatives such as galegine. In attempt to mimic properties of guanidine a synthetic diguanide drug Synthalin was developed, which was more potent and showed lower toxicity. However, the liver damage caused by both guanidine and diguanides stimulated a search for safer alternatives, which led to the development of biguanides as T2D drugs.²

Although, metformin has been in use as well as studied for decades its exact molecular mechanism of therapeutic action and direct target are poorly understood. One

suggested mechanism of action is suppression of mitochondrial respiration by inhibition of complex I,^{3,4} however, the precise mechanism of this inhibition remains unclear.

It has been shown recently that the cellular effects of metformin significantly depend on its metal-binding properties, particularly towards copper.⁵ In the above study it was found that both Metf and biguanide (BG) show antihyperglycemic properties and no free copper Cu^{II} levels after drug treatment could be detected by a Cu^{II} specific fluorescence probe. In contrast propanediimidamide (PDI) showed no antihyperglycemic effect and free Cu^{II} was detected. Interestingly, Metf does not lower the urinal copper concentration which in T2D patients is increased, whereas triethylenetetramine (trien) decreases the urinal copper concentration, but has no antihyperglycemic effect.

It remained unclear whether Metf binds to Cu^{I} or Cu^{II} . In water Cu^{II} is the more stable oxidation state. However, in living organisms a complex machinery of cupric reductase, a Cu^{I} specific membrane transport protein, and chaperone proteins within the cells exist which effectively does not allow free copper ions at cellular level.⁶⁻¹² The chaperone proteins play a vital role in the copper transport system and are not only abundant in the cell but also in the mitochondria where the biomolecular effects of metformin are observed. Moreover, copper metalloenzymes, where the unique copper redox chemistry is needed, are able to bind both Cu^{I} and Cu^{II} . The idea of potential metformin interaction with the redox active parts inside the cell is further supported by a study of the antimicrobial properties of binary metformin metal complexes.^{13,14} In that study among other physico-chemical properties, the cyclic voltammogram of $[\text{Cu}^{\text{II}}(\text{Metf})_2]^{2+}$ was measured against a Ag/AgCl electrode and showed a reduction peak at 320mV and oxidation peak at 490mV giving a $E_{1/2}$ of +405 mV, which is in the range of the reduction potentials of copper containing enzymes.¹⁵ Therefore, there are various possibilities of drug interaction with $\text{Cu}^{\text{I/II}}$ proteins and Metf could potentially interact with protein bound $\text{Cu}^{\text{I/II}}$ ions.

The study presented in this chapter builds upon the previous work of our collaborators on the cellular response to T2D drugs and in particular on the observed variations of free copper levels after drug treatment. It provides deeper insight into the copper binding properties of BG and Metf with focus on possible differences to PDI, which may be important for their different biological antihyperglycemic properties. In the first part of this chapter, the differences in copper-binding properties of studied compounds are discussed. In the second part, the optimized structures are compared to known crystal structures and binding energies are computed. The last part investigates and discuss the electronic properties such as molecular orbitals and electrostatic potentials of these molecules.

3.2 Copper Binding Properties

In order to understand in details copper-binding properties of Metf and similar compounds, an initial computational study of copper complexes of Metformin (Metf), Biguanidine (BG), Propanediimidamide (PDI), Ethylenediamine (en) and Triethylenetetramine (trien), see Figure 3.1, was conducted. In this section the differences in copper-binding between the studied compounds is first examined from the theoretical point of view.

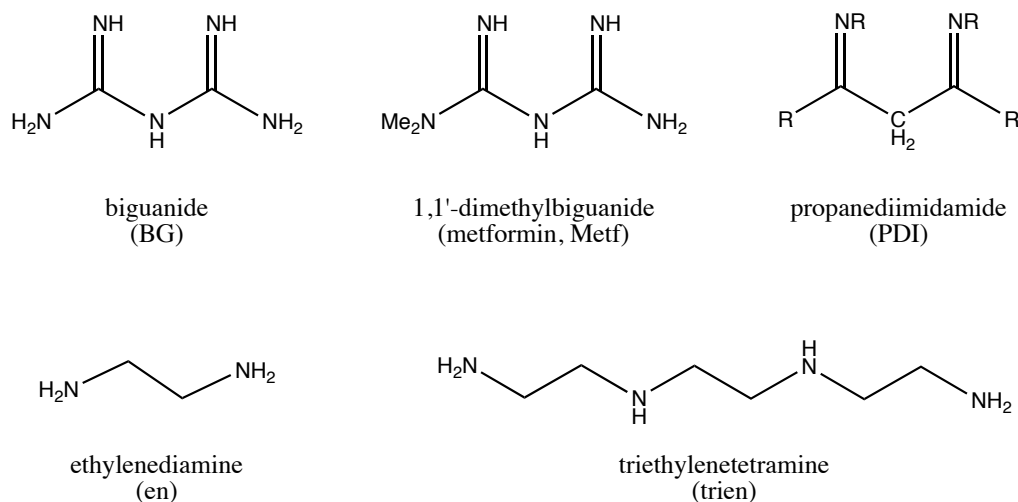


Figure 3.1: Compounds used as ligands.

A sp^2 hybridised N1 (for atom labels see Figure 3.2) is the ligand atom for BG, Metf and PDI. This means that π -backbonding can occur and stabilize the lower Cu^I oxidation state by transferring electron density into the π -orbitals of the ligands, see Figure 3.3. This type of molecular orbital (MO) interaction may also be important for $Cu^{I/II}$ as its 3d orbitals are almost filled up. The methylene CH_2 moiety in PDI compared to the secondary amine N2 in BG and Metf causes a disruption of the π -system, whereas the lone-pair of N2 can contribute electron density into the adjacent carbon p_z -orbital in BG and Metf, which results in a planar molecular structure for the latter ones and a nonplanar geometry for PDI in the complex. This is similar to the stabilisation effect detected in peptide bonds.

Additionally, the N2H group contains a protic hydrogen whereas the methylene hydrogens cannot undergo proton exchange in aqueous media. Deprotonated metal complexes of PDI are known, however, those are synthesised in non-protic solvents under conditions that prevent any water contamination.¹⁶⁻¹⁸ Due to the protic hydrogen, the most stable neutral form of BG and Metf in water is a tautomer in which the N2H proton is formally transferred to N1 or N3.¹⁹ This leads to a fully conjugated π -system in the ligands. However, only the N2 can then act as a donor atom as has been observed with a similar ligand in a known Ag^I complex.²⁰

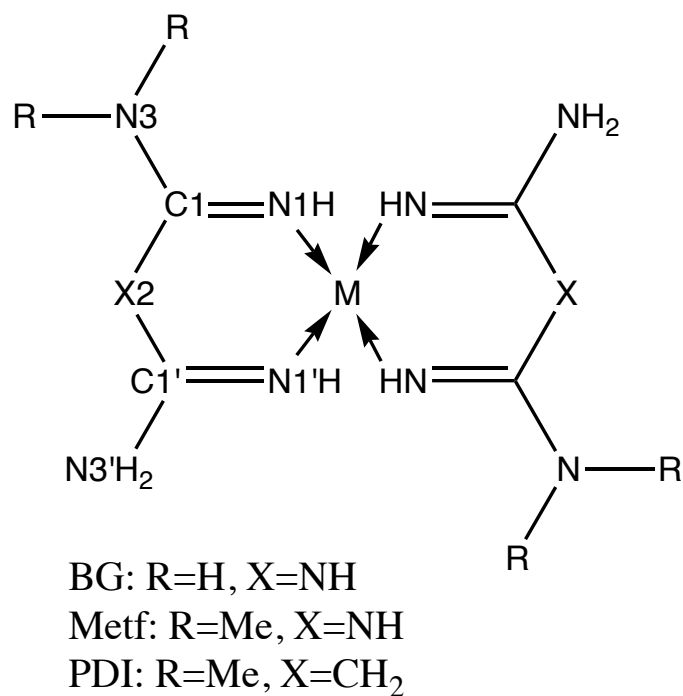


Figure 3.2: Numbering of atoms in X-ray and computed structures.

Biguanides formally belong to the 1,3,5-triazapentadienyl^{21,22} (also known as imidoamidate) ligand family and PDI is a member of the 1,5-diazapentadienyl^{15,18} (also known as β -diketiminate) ligand class, each of which are well established as metal ion ligands in inorganic coordination chemistry. However, their structure and chemistry is mainly established in nonaqueous solvents; hence, their properties cannot be transferred directly to aqueous environments, particularly biosystems with very sensitive pH range.

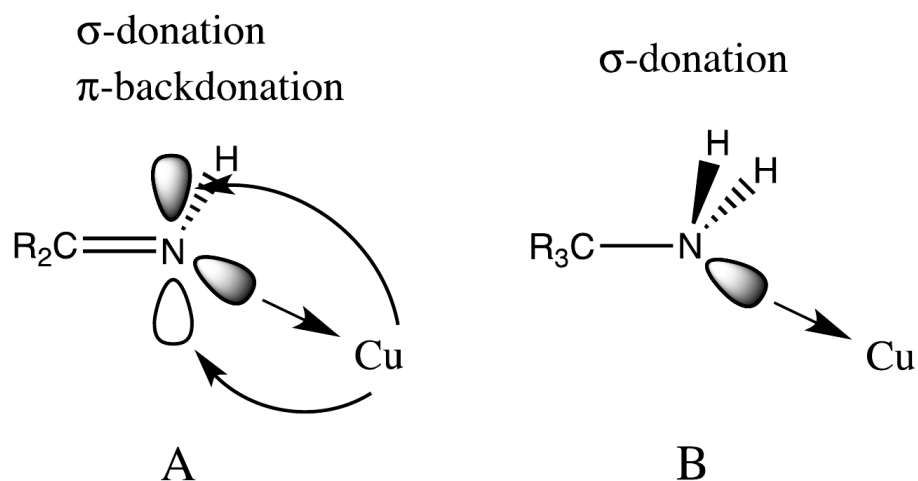


Figure 3.3: Schematic representation of possible orbital interactions Cu complexes with BG, Metf and PDI (A) and with en and trien (B).

The protonation equilibria of BG have been studied along with complex formation with Cu^{II} at a pH range of 2-12.^{23,24} First, BG predominately exists in an equilibrium between its monoprotonated and neutral forms at physiological pH, and no

deprotonated BG-H was reported for the given pH range. Second, the formation of $[\text{Cu}^{\text{II}}(\text{OH})(\text{BG})]^+$ was observed to be the major Cu-BG complex; however, binary Cu^{II} -BG complexes such as $[\text{Cu}(\text{BG})_2]^{2+}$, $[\text{Cu}(\text{BG})(\text{BG-H})]^+$ and $[\text{Cu}(\text{BG-H})_2]^0$ were also observed at slightly higher pH values. The pK_a value of 6.88 was reported for $[\text{Cu}(\text{OH})(\text{BG})]^+$, hence indicating the possibility of deprotonated BG while being coordinated to Cu^{II} . Neither Metf nor PDI has been studied in this detail. However, these results are at least qualitatively transferred to Metf.

3.3 Computational Details

Geometries of all the computed structures were optimized using B3LYP²⁵⁻²⁹ with all-electron Def2-TZVPD³⁰ basis set and the calculations were performed using Gaussian09³¹ (A.02 and C.01). Further, frequency analysis was performed in order to verify that each structure is a true minimum by the absence of imaginary frequencies. Spin multiplicities considered were singlet and doublet for Cu(I) and Cu(II), respectively. In the case of open-shell species spin contamination was found to be negligible. Other DFT functionals tested were BP86^{27,32}, M06³³ and M06L³⁴. As can be seen in Table 3.1 and Table 3.2, although standard deviation in calculated binding energies between functionals can be up to ≈ 10 kcal/mol, the overall trends in binding energies of the BG and PDI Cu complexes are not changing between different functionals used. Therefore, mainly B3LYP results are presented in this chapter. Natural bond orbital (NBO) charges were calculated using NBO 3.1³⁵ tool integrated within Gaussian09.

Table 3.1: Mean and standard deviation (STD) of B3LYP, BP86, M06, M06L calculated binding energies (in kcal/mol) for BG and PDI $[\text{Cu}^{\text{I/II}}(\text{L})_2]$ and $[\text{Cu}^{\text{I/II}}(\text{L-H})_2]$ complexes.

	BG		PDI	
	Mean	STD	Mean	STD
$[\text{Cu}^{\text{I}}(\text{L})_2]^+$	115.9	6.9	134.8	7.2
$[\text{Cu}^{\text{II}}(\text{L})_2]^{2+}$	398.1	7.5	412.8	9.5
$[\text{Cu}^{\text{I}}(\text{L-H})_2]^{1-}$	230.2	6.9	228.1	7.1
$[\text{Cu}^{\text{II}}(\text{L-H})_2]$	686.0	7.3	687.5	7.5

Table 3.2: Binding Energies (in kcal/mol) of BG and PDI [Cu^{I/II}(L)₂] and [Cu^{I/II}(L-H)₂] complexes calculated using B3LYP, BP86, M06 and M06L with Def2-TZVPD basis set.

	L	B3LYP	BP86	M06	M06L
[Cu ^I (L) ₂] ⁺	BG	106.0	118.3	117.2	122.0
	PDI	124.8	139.7	134.4	140.4
[Cu ^{II} (L) ₂] ²⁺	BG	391.6	408.8	395.9	396.1
	PBI	406.0	426.8	408.6	409.9
[Cu ^I (L-H) ₂] ¹⁻	BG	220.5	233.3	230.3	236.7
	PBI	218.2	231.8	228.0	234.5
[Cu ^{II} (L-H) ₂]	BG	678.7	696.0	685.9	683.7
	PBI	680.1	697.9	686.3	685.5

3.4 Results

3.4.1 Comparison of X-ray Structures and Computed Complexes

There are several crystal structures known for bisbiguanide-copper complexes. Three describe the [Cu(BG)₂]²⁺ complex and contain different counterions.³⁶⁻³⁸ These complexes are planar and non-symmetric in terms of their bond lengths. Table 3.3, Table 3.5 and Table 3.6 present a comparison between critical structural parameters of calculated and crystal structures. Numbers in brackets for crystal structure bond lengths, where available, are estimated standard deviations or in the case where the bond length was averaged these represent the standard errors. The standard errors (SE) are calculated by propagating estimated standard deviations and dividing by the square root of number of averaged values. Further, uncertainty in calculated average values are presented. The uncertainties are calculated as $(max - min)/2$, which accounts for the best and worst case scenario for the averaged bond length. In Table 3.3 an average over all three structures is presented and compared to the DFT optimized structure. This table also contains a published structure for the neutral complex Cu(BG-H)₂ which has the deprotonated biguanide (BG-H).³⁹

The observed Cu-N1 bond length of 1.945 Å is in the normal range of Cu^{II}-N ligand bonds. The computed Cu-N bond distance of 1.980 Å is slightly longer, even though this is outside the range of crystal structure average bond length with uncertainty, as can be seen in the Table 3.4 the calculated Cu-N bond lengths vary significantly between functionals tested. Moreover, the individual Cu-N bond lengths in the

Table 3.3: Comparison of critical bonds^a (distance in angstroms) of [Cu^{II}(BG)₂]*X*_{1,2} {*X* = CO₃²⁻, Cl⁻, or [Cu^{II}(C₅H₇O₂)(Cl)]⁻} and Cu^{II}(BG-H)₂ crystal structures and computed [Cu^{II}(BG/BG-H)₂]^{2+/0} complexes.

BG	CSD code	X	Cu-N	N1-C1	C1-N2	C1-N3
X-ray	BGCUCB ³⁶	CO ₃ ²⁻	1.951(7)	1.296(10)	1.374(9)	1.351(10)
	COBMAH ³⁷	[Cu ^{II} (C ₅ H ₇ O ₂)(Cl)] ⁻	1.936(3)	1.286(3)	1.373(4)	1.337(4)
	ZZDZQ01 ³⁸	Cl ⁻	1.949(5)	1.291(7)	1.374(8)	1.342(8)
	∅ ^b {[Cu(BG) ₂] ²⁺ }		1.945	1.291	1.373	1.343
	SE ^c		0.005	0.007	0.007	0.008
	Uncertainty ^d		0.014	0.020	0.020	0.022
B3LYP	[Cu(BG) ₂] ²⁺		1.980	1.299	1.383	1.344
X-ray	SAPFUL ³⁹	-	1.941(4)	1.320(4)	1.355(4)	1.360(4)
B3LYP	Cu(BG-H) ₂		1.971	1.318	1.337	1.383

^aExperimental bond lengths are averaged for each crystal structure (BGCUCB *C*₁ symmetry, COBMAH *C*_i symmetry, and ZZDZQ01 *C*₁ symmetry).

^bAverage of all [Cu^{II}(BG)₂]*X*_{1,2} structures.

^cStandard error of averaged bond length

^dUncertainty in averaged bond length

different crystal structures can vary from 1.933 Å to 1.958 Å for complexes with the neutral BG ligand. The most symmetrical, coplanar X-ray structure COBMAH³⁷ is *C*_i symmetric with Cu-N distances of 1.933 and 1.939 Å. The same feature is observed in the DFT calculated structure with slightly longer Cu-N bonds of 1.978 and 1.982 Å. Interestingly, the computed minimum structure is slightly twisted and has *C*₂ symmetry with regards to the heavy atoms which is abolished by the non-planar H-atoms of the amine groups. The coplanar, *D*_{2h} symmetrical geometry is in fact computed to be a rotational transition state in the gas phase with a negligible barrier ΔE^\ddagger of 1.04 kcal/mol and a ΔG^\ddagger of 3.65 kcal/mol.

The observed N1-C1 bond length (X-ray_{av}: 1.291 Å; DFT: 1.299 Å) is slightly longer than a pure C-N double bond and whereas the C1-N2 (X-ray_{av}: 1.373 Å; DFT: 1.383 Å) and C1-N3 (X-ray_{av}: 1.343 Å; DFT: 1.344 Å) are much shorter than a C-N single bond, which indicates conjugation of the N2-lone pairs into the N1-C1 double bond. The computed N-C bonds are within the range of uncertainties of observed bond lengths and in much better agreement with the crystal structure compared to the metal-ligand bond because these bonds are less affected by crystal packing. Particularly, the changes upon deprotonation of the secondary amine N2H group in the N1-C1 and C1-N2 bonds that indicate a delocalization of the negative charge within the ligand bonds that form the metallacycle is very well reproduced in the computed structure. The observed differences between the different X-ray structures could be explained by the different counterions present. The axially positioned counterions could potentially affect equatorial bond lengths through a so

called Jahn-Teller effect. The Jahn-Teller effect describes a geometrical distortion of non-linear molecules with a degenerate electronic state that stabilizes the molecules by removing that degeneracy and leads to a system of lower symmetry and energy. This is typically observed in transition metal octahedral complexes with, for example, d^9 Cu^{2+} centres. The result of such a distortion is that the octahedral complex will either elongate with the axial bonds being longer than the equatorial bonds or compress with the equatorial bonds being longer than the axial bonds. The type and strength of distortion varies depending on the type of metal and ligands and are dictated by the amount of overlap between the metal and ligand orbitals. Interestingly, almost negligible shortening of -0.003 Å for the Cu-N bond length is observed for the $\text{Cu}(\text{BG-H})_2$ ³⁹ neutral complex compared to the average of the cationic complexes, whereas in the case of the DFT structure a stronger reduction of -0.009 Å is observed, indicating a slightly larger increase in the Cu-N bond strength than the experimental results are suggesting. As can be seen in the Table 3.4, although Cu-N bond lengths calculated using different functionals can vary up to ≈ 0.02 Å, the observed shortening of -0.009 Å between the neutral and cationic BG complexes is consistent across the functionals tested.

Table 3.4: Mean Cu-N bond lengths and bond length difference (in Å) for $\text{Cu}(\text{BG})_2$ neutral and cationic complexes calculated using B3LYP, BP86, M06 and M06L functionals with Def2TZVPD basis set.

Functional	Mean Cu-N bond length [Å]		Bond length difference
	$[\text{Cu}^{\text{II}}(\text{BG-H})_2]$	$[\text{Cu}^{\text{II}}(\text{BG})_2]^{2+}$	
B3LYP	1.971	1.980	-0.009
BP86	1.961	1.969	-0.009
M06	1.954	1.960	-0.006
M06L	1.966	1.974	-0.009

In the case of the Metf-Cu complexes, there are in total five crystal structures known, see Table 3.5, three include the neutral Metf^{14,40,41} and two the deprotonated metformin (Metf-H)^{40,41} with Cu^{II} . Some differences compared to the BG-Cu complexes in the bond distances can be observed which are due to the methyl groups that abolish the symmetry of the BG complex. The N1-C1 bond becomes slightly longer (X-ray_{av}: 1.305 Å; DFT: 1.307 Å) and the N1'-C1' slightly shorter (X-ray_{av}: 1.276 Å; DFT: 1.298 Å) compared to the N1-C1 bond (X-ray_{av}: 1.291 Å; DFT: 1.299 Å) in the BG complex. This alteration is also observed in the computed complex, although the decrease in the N1'-C1' bond is only marginal. The asymmetrical nature of the ligand is also noticeable in different Cu-N bond distances of Cu-N1 1.941 Å and Cu-N1' 1.932 Å, surprisingly the DFT computed Cu-N bond distances show an opposite trend with 1.973 Å and 1.980 Å, which might be due to crystal packing effects compared to the gas-phase computed, single-molecule structure. However, the other bond distances are either in excellent agreement or well within the estimated uncertainty of the average crystal bond lengths.

Table 3.5: Comparison of critical bonds^a (distance in angstroms) of [Cu^{II}(Metf)₂]X_{1,2} (X = ClO₄⁻, CO₃²⁻, or Cl⁻) and Cu^{II}(Metf-H)₂ crystal and computed Structures.

Metf	CSD code	X	Cu-N1	Cu-N1'	N1-C1	N1'-C1'	C1-N2	C1'-N2	C1-N3	C1'-N3'
X-ray	AJUHJ ¹⁴	ClO ₄ ⁻	1.944	1.944	1.303	1.268	1.374	1.384	1.354	1.344
	HIBPOX ⁴²	CO ₃ ²⁻	1.931(4)	1.920(4)	1.305(6)	1.282(6)	1.364(6)	1.392(6)	1.342(6)	1.323(6)
	HIHDUX ⁴³	Cl ⁻	1.948(7)	1.932(7)	1.308(11)	1.278(11)	1.376(11)	1.379(13)	1.342(12)	1.343(12)
	∅([Cu(Metf) ₂] ²⁺)		1.941	1.932	1.305	1.276	1.371	1.385	1.346	1.337
	SE ^b		0.006	0.006	0.009	0.009	0.009	0.010	0.009	0.009
	Uncertainty ^c		0.011	0.011	0.017	0.017	0.017	0.019	0.018	0.018
B3LYP	[Cu(Metf) ₂] ²⁺		1.973	1.980	1.307	1.298	1.389	1.379	1.346	1.348
X-ray	EFIXUM ⁴⁰	—	1.943(1)	1.921(1)	1.313(2)	1.306(2)	1.372(2)	1.350(2)	1.365(2)	1.386(2)
	ETOFOI ⁴¹ -A ^a	—	1.938(2)	1.928(2)	1.324(3)	1.320(3)	1.358(3)	1.350(3)	1.368(3)	1.371(3)
	ETOFOI ⁴¹ -B ^a	—	1.950(2)	1.923(2)	1.315(3)	1.310(3)	1.371(3)	1.342(3)	1.357(3)	1.391(3)
	∅(Cu(Metf-H) ₂)		1.944	1.924	1.317	1.312	1.367	1.347	1.363	1.383
	SE ^b		0.002	0.002	0.003	0.003	0.003	0.003	0.003	0.003
	Uncertainty ^c		0.005	0.005	0.008	0.008	0.008	0.008	0.008	0.008
B3LYP	Cu(Metf-H) ₂		1.970	1.967	1.323	1.320	1.343	1.332	1.383	1.388

^aThe unit cell of ETOFOI contains two Cu(Metf-H)₂ molecules.

^bStandard error of averaged bond length

^cUncertainty in averaged bond length

The two crystal structures Cu^{II}(Metf-H)₂·H₂O (ETOFOI)^[41] and Cu(Metf-H)₂·8H₂O (EFIXUM)⁴⁰ were synthesized under basic conditions. The ETOFOI structure complex contains two Cu^{II}(Metf-H)₂ molecules in the unit cell, with ETOFOI-A resembling the Cu^{II}(BG-H)₂ more closely than ETOFOI-B and EFIXUM. The best agreement with the DFT optimized Cu(Metf-H)₂ structure is also with ETOFOI-A. The lengthened N1-C1 and N1'-C1' double bond is particularly well reproduced by the B3LYP optimized structure.

Interestingly, in EFIXUM and ETOFOI-B, hardly any increase in the N1-C1 bond and decrease in the C1-N2 bond is observed, which most likely is due to strong H-bonding of crystal water in the proximity of N2. Two crystal waters are close to N2⁻ in EFIXUM at a distance of 2.86 Å and 2.91 Å (N2-O distance), whereas one water is found in ETOFOI-B to be 2.84 Å away from N2⁻.

Overall, the crystal structures of the neutral complex Cu^{II}(Metf-H)₂ indicate the possibility of the formation of stable Cu^{II} complex with deprotonated metformin at basic conditions.

Only one crystal structure for the homoleptic PDI complex is known.⁴⁴ The computed Cu-N bond is longer, similarly to the BG Cu-N bond length, than the observed crystal structure bond length. When comparing PDI and BG Cu-N bond lengths the Cu-N bond 1.956 Å in the [Cu^{II}(PDI)₂]²⁺ complex is slightly longer than in the BG complex 1.945 Å, which is also observed in the computed structure with 1.999 Å compared to 1.980 Å, for PDI and BG respectively. In contrast to the BG complexes the C1-C2 bond (1.504(2) Å) in the PDI complex is much longer compared to the C1-N2 bond (1.373 Å) in [Cu^{II}(BG)₂]²⁺ and closer to a pure single C-C bond

than a double bond.

In order to investigate this long C1-C2 bond the rotational barrier of the free, neutral ligand of 2.42 kcal/mol for PDI and 18.20 kcal/mol for BG were calculated. The much higher rotational barrier for BG gives an indication about the strength of the conjugation of the N2 lone pair into the adjacent N1-C1 double bond.

Table 3.6: Comparison of critical structural parameters (bond distances in angstroms and angles in degrees) of $[\text{Cu}^{\text{II}}(\text{PDI})_2][\text{ClO}_4]_2$ crystal structures and computed $[\text{Cu}^{\text{II}}(\text{PDI}/\text{PDI-H})_2]^{2+/0}$ complexes.

	Structure	Cu-N	N1-C1	C1-C2	C1-N3	\angle N1-N1'-C1'-C2
X-ray	MALDOU ⁴⁴	1.956(1)	1.289(2)	1.504(2)	1.333(2)	21.6
B3LYP	$[\text{Cu}(\text{PDI})_2]^{2+}$	1.999	1.297	1.514	1.336	22.1
	$[\text{Cu}(\text{PDI-H})_2]^0$	1.976	1.321	1.403	1.394	1.4

3.4.2 Binding Energies of $\text{Cu}^{\text{I/II}}$ Complexes

The binding energies related to the gas phase structures that are presented in Table 3.7 were computed in two different ways. The interaction energy ΔE_{int} corresponds to the binding energy of the Cu-centre or CuOH fragment with the ligand in its geometry found in the optimized complex structure. On the other hand, the binding free energy ΔG_{int} is determined using the lowest energy tautomer and conformer of the ligands. The negative ΔG_{int} is equal to the dissociation energy D_e . The difference between the energy of the ligand in its complex geometry and its lowest tautomer and conformer is called preparation energy ΔE_{prep} .

The binding energies were computed for Cu^{I} and Cu^{II} complexes of the mono-L complexes, the homoleptic, bis-L complexes, and the mixed $[\text{Cu}^{\text{I/II}}(\text{OH})(\text{L})]^{0/+}$ complexes. The latter is particular important in aqueous media as this is the major Cu^{II} -BG species at physiological pH in most biological compartments. In addition, the complexes with deprotonated ligands were also calculated as these might become important at higher physiological pH, occurring for example inside the mitochondria.

Firstly, the $[\text{Cu}^{\text{I/II}}(\text{L})]^{+/2+}$ complexes are discussed. Among all ligands Metf shows the strongest interaction energy with Cu^{I} , however, due to lower ΔE_{prep} PDI forms the strongest $[\text{Cu}^{\text{I}}(\text{L})]^+$ complex. Interestingly, for BG and PDI ΔE_{prep} is almost equal. En binds around 25-30 kcal/mol weaker to Cu^{I} compared to the other ligands, but D_e is only 6-16 kcal weaker, which as well is due to a small preparation energy. The weaker binding of en is possibly due to the lack of π -backbonding to the sp^3 -hybridized N centres of this ligand. Differences in ring strain (Figure 3.4) may also make a contribution.

Table 3.7: Binding Energies (in kcal/mol) of Cu Complexes calculated using B3LYP/Def2-TZVPD.

		BG	Metf	PDI	en	trien
[Cu ^I (L)] ⁺	ΔE_{int}	-119.77	-125.07	-120.74	-95.15	
	$\Delta G (-D_e)$	-84.71	-87.45	-94.18	-78.60	
[Cu ^{II} (L)] ²⁺	ΔE_{int}	-331.77	-347.81	-332.66	-270.92	
	$\Delta G (-D_e)$	-286.23	-299.91	-296.49	-250.70	
[Cu ^I (L) ₂] ⁺	ΔE_{int}	-183.80	-187.80	-186.28	-154.32	-151.04
	$\Delta G (-D_e)$	-105.97	-106.64	-124.85	-112.52	-117.58
[Cu ^{II} (L) ₂] ²⁺	ΔE_{int}	-489.52	-505.09	-488.51	-410.06	-409.90
	$\Delta G (-D_e)$	-391.59	-402.19	-405.96	-355.32	-364.10
[Cu ^I (OH)(L)]	ΔE_{int}	-50.88	-47.80	-51.05	-42.10	
	$\Delta G (-D_e)$	-16.26	-12.02	-34.12	-24.60	
[CuCu ^{II} (OH)(L)] ⁺	ΔE_{int}	-138.25	-144.61	-138.73	-112.33	
	$\Delta G (-D_e)$	-97.37	-101.23	-105.93	-88.99	
[Cu ^I (L-H)]	ΔE_{int}	-229.86	-231.38	-234.86		
	$\Delta G (-D_e)$	-200.71	-201.60	-203.80		
[Cu ^{II} (L-H)] ¹⁻	ΔE_{int}	-555.26	-561.38	-566.70		
	$\Delta G (-D_e)$	-511.20	-518.40	-530.24		
[Cu ^I (L-H) ₂] ¹⁻	ΔE_{int}	-353.80	-351.71	-359.31		
	$\Delta G (-D_e)$	-220.55	-220.70	-218.21		
[Cu ^{II} (L-H) ₂]	ΔE_{int}	-836.32	-837.06	-846.10		
	$\Delta G (-D_e)$	-678.65	-680.45	-680.12		

The Cu^{II} complexes for BG, Metf and PDI are more than 200 kcal/mol more stable than the Cu^{I} complex, which is due to stronger Coulomb and orbital interactions, whereas the en complex does not receive as strong a stabilisation compared to the other ligands. This could be due to the σ -bonding with the N lone pair being smaller in the sp^3 hybrid N compared to the slightly larger sp^2 hybrid lone pair with more s-character. Although, overall Metf binds strongest, the D_e of PDI is only 3.4 kcal/mol lower.

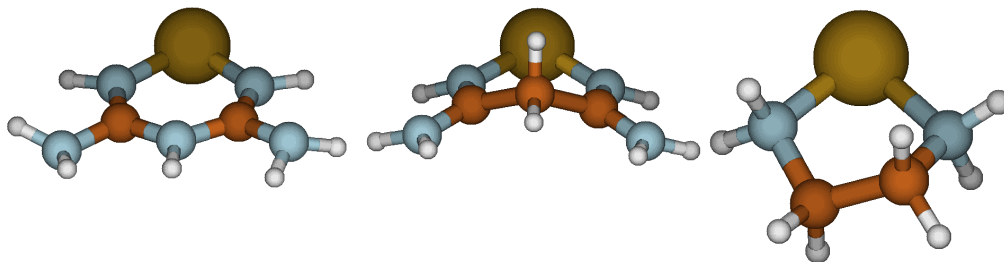


Figure 3.4: BG, PDI and en $[\text{Cu}^{\text{I}}(\text{L})]^+$ structures optimized with B3LYP/Def2-TZVPD.

Secondly, the homoleptic $[\text{Cu}^{\text{I/II}}(\text{L})_2]^{+/2+}$ complexes are discussed. For BG, Metf and PDI complexes similar trends are observed as in the mono-complexes, with an even stronger stabilisation for PDI compared to BG and Metf due to a much larger ΔE_{prep} for the latter ones. Trien is also included in this group of complexes. Since trien is tetradentate, its chelating properties are superior to those of BG, Metf and PDI at equal molarity. However, here it is included in the group for comparison of its binding properties to copper-ligand complexes with a saturated copper ligand sphere. Trien has almost the same ΔE_{int} than en, but a larger D_e due to entropic effects by 5 kcal/mol with Cu^{I} and by ≈ 10 kcal/mol with Cu^{II} which agrees with the experimentally observed stronger stabilisation of trien with Cu^{II} .

Next, the binding of BG, Metf, PDI and en in a mixed complex with $\text{Cu}(\text{OH})$, where OH is a stronger ligand than the neutral bidentate ligands, is investigated and discussed. The Cu^{I} cation forms a strong bond with the hydroxide anion, which results in weak binding of a second, non-anionic ligand. Here a surprising order is observed for the Cu^{I} complexes, with PDI ($D_e = 34.12$ kcal/mol) forming the strongest mixed complexes, en ($D_e = 24.60$ kcal/mol) following as the second strongest, then BG ($D_e = 16.26$ kcal/mol) and Metf ($D_e = 12.02$ kcal/mol) forming the weakest complex. The differences between the ligands is again mainly due to the larger ΔE_{prep} for BG and Metf compared to low ΔE_{prep} for PDI and en.

The mixed $\text{Cu}^{\text{II}}(\text{OH})(\text{L})$ complexes are slightly stronger than the $\text{Cu}^{\text{I}}(\text{L})$ complexes, with very similar trends and similar stabilities for BG, Metf and PDI.

In addition to the complexes with neutral ligands, the binding energies for the

deprotonated BG-H, Metf-H and PDI-H were also calculated. It is important to point out here that at higher pH BG and Metf can be deprotonated in aqueous medium, on the other hand PDI, even when in a metal complex which lowers its pK_a , will only be deprotonated above pH 14 in non-aqueous medium as the methylene group in PDI cannot be deprotonated by bases in aqueous media.

These anionic ligands bind much stronger than the neutral counterparts as they have much larger ionic bonding contributions than the neutral ligands. Also, the Cu^{II} complexes receive an even stronger stabilization than the Cu^{I} complexes. This could indicate an easier oxidation compared to the neutral ligands when a Cu^{I} ion is extracted from a protein by Metf-H. In addition, these deprotonated forms of the biguanides alone might be a strong enough as ligands to extract Cu^{I} from proteins with thiolate ligands. This modelling indicates that any copper-dependent effects of the drug may be restricted to or most prominent in the mitochondria and other compartments in the body where physiological pH is above the typical range, allowing deprotonation of the drug. Such pH-dependent activation or priming could potentially explain why metformin is almost invariably found in the biological literature to act on the mitochondria, with very few effects reported in other cellular compartments.

3.4.3 Electronic Properties

In order to gain a deeper understanding about the biguanide type ligands in comparison to the PDI the molecular orbitals (MO) of these ligands in their geometry in a complex are investigated, see Figure 3.5. For simplicity the main focus is on the π -orbitals and the MOs with the N1 lone pairs.

The lowest lying MOs with π -character in BG and PDI are the MO-19. PDI, which is not planar, still shows a π -like plane with one σ -C2-H bond above and the other σ -C2-H bond mixing with the N1-C1 double bond plus contribution from the N3 lone pairs. The MO-19 in BG, which is only 0.01 eV lower in energy than the PDI MO-19, is a mix of π and σ character. The lone pairs of N2 and N3 are mixing with the pz AO of the sp^2 hybridized C1, plus σ -character from the N1-H bond. For BG the MO-21 looks very similar to the MO-19 with σ - and π -character, except that it is the negative combination of the AOs and therefore higher in energy. The MO-21 in PDI is 1.04 eV higher than the BG MO-21 and only shows σ -character, which explains the much lower rotational barrier for PDI compared to BG. The MO-22 looks basically the same for both molecules, however the MO-22 in PDI lies 0.47 eV higher. MO-23 in BG, which lies 1.70 eV higher than MO-23 in PDI, is a pure combination of N2 and N3 lone pairs, whereas in PDI as there is no lone pair on C2

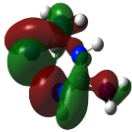
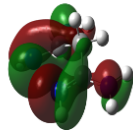
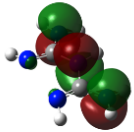
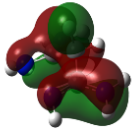
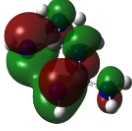
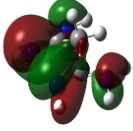
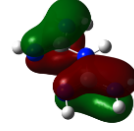
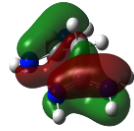
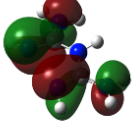
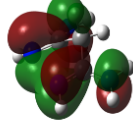
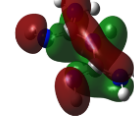
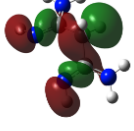
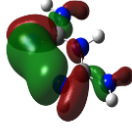
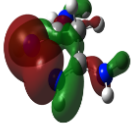
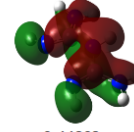
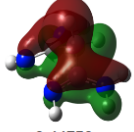
Orbital	BG	PDI	Orbital	BG	PDI
MO-27 HOMO	 -0.22031	 -0.21733	MO-23	 -0.28636	 -0.34896
MO-26	 -0.22492	 -0.22903	MO-22	 -0.38088	 -0.36353
MO-25	 -0.23019	 -0.23659	MO-21	 -0.43279	 -0.39439
MO-24	 -0.26919	 -0.26261	MO-19	 -0.44803	 -0.44750

Figure 3.5: Molecular orbitals for BG and PDI and the corresponding energies in hartrees.

this MO is a mix of π -MO with contributions from the N1-C1 double bonds and the N3 lone pairs plus out-of plane C2-H σ -bond character. The MO-24 is the positive combination of the N1 lone pairs which is responsible for bonding to the empty 4s AO of Cu. In the BG the MO-24 lies 0.18 eV lower in energy than the corresponding PDI orbital. The next two MOs 25 and 26 are very close in energy (0.17 eV and 0.11 eV, respectively) for BG and PDI and are pure π -MOs. The HOMO, MO-27, is the negative combination of the N1 lone pairs and donate electron density into the empty 4p AO of Cu. The HOMO orbitals of BG and PDI are energetically only 0.08 eV apart. These MOs show that the electron density on N1 is very similar in BG and PDI which explains the strong similarities in the observed binding energies for these ligands with Cu.

Table 3.8: NBO charges for $[\text{Cu}^{\text{II}}(\text{L})]^{2+}$, L=BG, PDI and en.

	BG	PDI	EN
Cu ^{II}	+1.38	+1.34	+1.30
N1	-0.87	-0.84	-0.80

To emphasise this point further the NBO charges are calculated and compared for the $[\text{Cu}(\text{L})]^{2+}$ complexes. As can be seen from Table 3.8, the charge on Cu decreases from +1.87, +1.84 to +1.80 for BG, PDI and en, respectively. This is consistent with a decreasing negative charge on the ligand N1 atoms of these ligands from -

0.87, -0.84 to -0.80 for BG, PDI and en, respectively. Further, Figure 3.3 illustrates possible orbital interactions for the sp^2 -type N in BG, Metf and PDI compared to the sp^3 -type N in en and trien. From this figure it can be seen that BG, Metf in comparison to en and trien are capable of stronger bonds due to σ -donation while at the same time receiving electron density from the metal centre via π -backdonation, these two types of bonding have a synergistic effect and reinforce each other. On the other hand, the pure σ -donor ligands en and trien cannot accept electron density in π -MOs, which results in weaker binding. The small difference between BG and PDI can be due to either slightly larger σ -donation or smaller π -backdonation in PDI or a combination of both.

3.4.4 ESP Maps

The electrostatic potential (ESP) maps for BG and PDI in their neutral forms are presented in Figure 3.6. Interestingly, the PDI-A shows a slightly more negative potential than BG-A around the N1 atoms which will form coordination bonds toward Cu. This means that PDI is a slightly stronger Lewis base than BG-A and is consistent with the findings that the PDI has a larger ΔE_{int} . It has to be pointed out here that the presented structure PDI-A is not a minimum energy structure, but a transition state structure, and therefore not stable in nature; however, this is the conformation that will bind to a metal center in a bidentate binding mode. BG-A, on the other hand, is a local minimum energy structure, which also is in one sense surprising as the two N1 lone pairs should strongly repel each other; however, it seems that the p-stabilisation as shown by the MOs exceeds the steric repulsion. Also, the methylene moiety causes a greater part of PDI-A to be hydrophobic (green) compared to BG-A, which could be important in terms of molecular recognition when binding to a Cu centre of a protein. Therefore, PDI not only causes greater steric hindrance due to its lack of planarity but also introduces repulsive or at least weaker interactions with H-bond acceptors.

The PDI-B represents the lowest energy conformer of the neutral PDI. An internal H-bond in PDI-B results in a very weak hydrophilicity, with strong, large areas that can be described as lipophilic. In contrast the BG-B, which is a minimum energy conformer, but not the lowest tautomer of BG, shows much more pronounced negative (red) and positive (blue) moieties which results in H-bond donor and acceptor properties that are stronger than those of PDI-B. This is suggestive evidence that PDI may be able to penetrate cell membranes, whereas BG and Metf need to be taken up via transmembrane transporters.

The lowest energy conformer and tautomer of BG-C shows qualitatively slightly

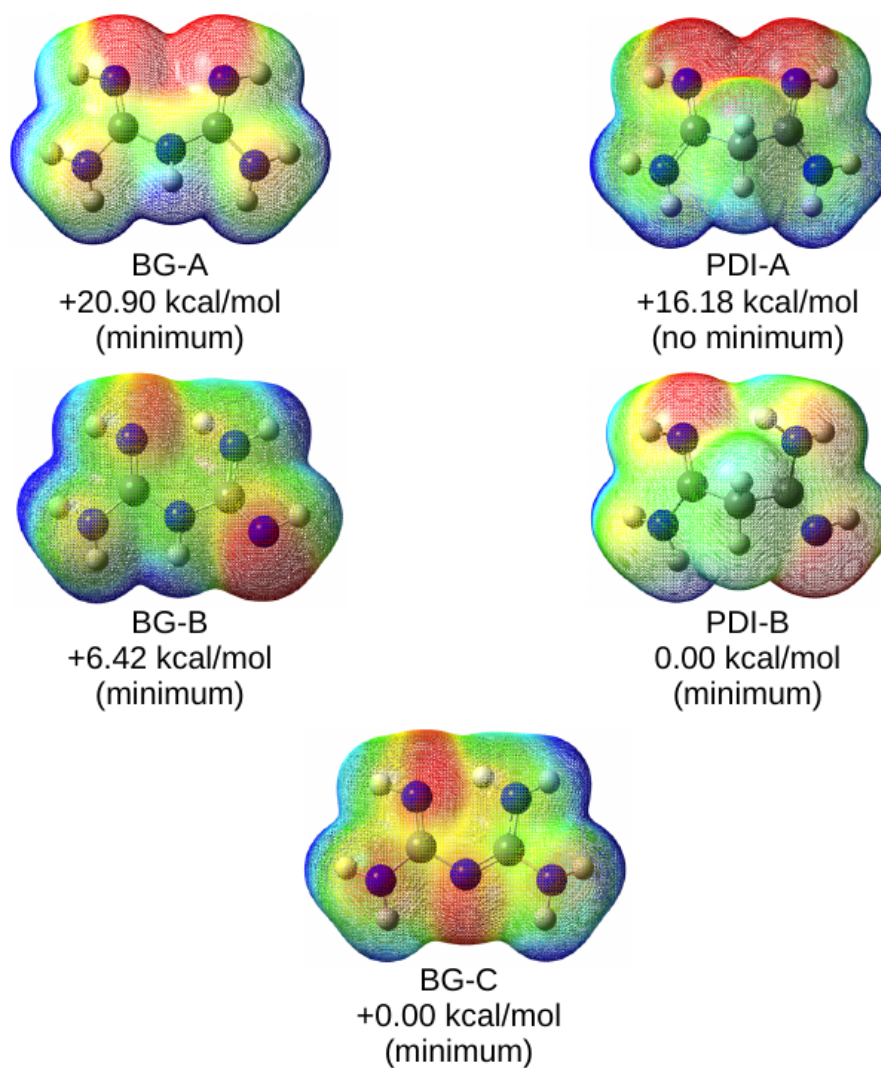


Figure 3.6: Electrostatic potential maps for BG and PDI. Red negative, green neutral and blue positive ESP values. BG-A and BG-B are local minimum energy conformers where BG-A is in the conformation that will bind to a metal center. BG-C is the lowest energy conformer and tautomer. PDI-A is a transition state structure in the conformation that will bind to a metal center and PDI-B is the lowest energy conformer. Color range: from -0.06 (Red) to +0.06 (Blue). Red: H-acceptor; Blue: H-donor; Green: neutral \approx hydrophobic.

smaller Lewis acid (blue) sites, but at the same time more intense Lewis basic (red) sites; however, there are also fewer hydrophobic areas above the plane of the molecules, which means that solvation and stabilisation due to H-bonding can be stronger not only on the edges of the molecules but also along the molecular plane.

3.4.5 Discussion and Conclusion

In this chapter copper binding properties of Metformin and structurally similar compounds were investigated. It was found that differences in the biologically observed

effects of neutral biguanide compounds (BG and Metf) and PDI cannot be solely explained by different Cu-binding energies. When examining the molecular orbitals it was shown that these ligands are electronically too similar and the substitution of the secondary amine to methylene has no negative effect on the complex formation via the N1 atoms for PDI. One of the possible mechanism explaining the difference in the biomolecular mode of action of biguanidines is that the secondary amine can be deprotonated in aqueous medium as the pK_a value is reduced when BG or Metf are coordinated to $Cu^{I/II}$. It is known that the mitochondrial matrix pH is higher than normal cellular or serum pH. Therefore, inside the mitochondria the equilibrium is potentially shifted towards the $Cu^{I/II}(\text{Metf-H})$ complex. Moreover, it is possible that biguanidines could potentially extract redox active Cu^I ions from proteins inside the mitochondria which after subsequent oxidation to Cu^{II} would further stabilise the complex. This suggests that metformin could act in cells at least in part as a copper-binding prodrug, becoming activated by elevated mitochondrial pH values. Further, this is consistent with the strong emphasis on the mitochondrial effects of metformin often found in the biological literature. In addition, this potentially explains the differences between mitochondrial responses to metformin and PDI, as the latter agent only becomes deprotonated at much higher pH values. There is a possibility that high binding affinities of Metf-H to copper could significantly affect the mitochondrial copper pool, which would probably have an impact on metal homeostasis of other metals and lead to mis-metallation of important metalloproteins.⁴⁵ The redox properties of such copper complexes may interfere with the sensitive redox chemistries occurring inside the cell, such as the mitochondrial electron transport chain.

Furthermore, ESP maps show that molecular recognition processes, which are copper-independent, could play a vital role in explaining the different drug properties of biguanides and PDI. Further work will establish if the much stronger hydrophilicity of BG facilitates its mitochondrial activity. On the other hand, in the case of PDI the higher lipophilicity might enable it to penetrate cell membranes without relying on membrane transport proteins.

In summary, the pH-dependent complex formation of BG with a pK_a within the physiological pH range^{23,24} together with the strongly hydrophilic character as shown by ESP maps demonstrate that BG potentially works as a pH-sensitive copper-binding agent. Together, these properties, which are at least qualitatively transferable to metformin, should be able to distinguish it from the other copper-binding agents studied, and these are also likely to account for many of the biological/therapeutic responses to the drug.

References

- [1] Repiščák, P.; Erhardt, S.; Rena, G.; Paterson, M. J. *Biochemistry* **2014**, *53*(4), 787–795.
- [2] Rena, G.; Pearson, E. R.; Sakamoto, K. *Diabetologia* **2013**, *56*(9), 1898–1906.
- [3] El-Mir, M. Y.; Nogueira, V.; Fontaine, E.; Averet, N.; Rigoulet, M.; Leverve, X. *J. Biol. Chem.* **2000**, *275*(1), 223–228.
- [4] Owen, M. R.; Doran, E.; Halestrap, A. P. *Biochem. J.* **2000**, *348*, 607–614.
- [5] Logie, L.; Harthill, J.; Patel, K.; Bacon, S.; Hamilton, D. L.; Macrae, K.; McDougall, G.; Wang, H. H.; Xue, L.; Jiang, H.; Sakamoto, K.; Prescott, A. R.; Rena, G. *Diabetes* **2012**, *61*(6), 1423–33.
- [6] Puig, S.; Thiele, D. J. *Curr. Opin. Chem. Biol.* **2002**, *6*(2), 171–180.
- [7] Bertini, I.; Rosato, A. *PNAS* **2003**, *100*(7), 3601–3604.
- [8] Nose, Y.; Rees, E. M.; Thiele, D. J. *Trends Biochem. Sci.* **2006**, *31*(11), 604–607.
- [9] Horn, D.; Barrientos, A. *IUBMB Life* **2008**, *60*(7), 421–429.
- [10] Boal, A. K.; Rosenzweig, A. C. *Chem. Rev.* **2009**, *109*(10), 4760–4779.
- [11] Wang, Y.; Hodgkinson, V.; Zhu, S.; Weisman, G. A.; Petris, M. J. *Adv. Nutr.* **2011**, *2*(2), 129–137.
- [12] Rubino, J. T.; Franz, K. J. *J. Inorg. Biochem.* **2012**, *107*(1), 129–143.
- [13] Olar, R.; Badea, M.; Marinescu, D.; Chifriuc, C. M.; Bleotu, C.; Grecu, M. N.; Iorgulescu, E. E.; Bucur, M.; Lazar, V.; Finaru, A. *Eur. J. Med. Chem.* **2010**, *45*(7), 2868–2875.
- [14] Olar, R.; Badea, M.; Marinescu, D.; Chifriuc, M.-C.; Bleotu, C.; Grecu, M. N.; Iorgulescu, E.-E.; Lazar, V. *Eur. J. Med. Chem.* **2010**, *45*(7), 3027–3034.
- [15] Solomon, E. I.; Szilagyi, R. K.; DeBeer George, S.; Basumallick, L. *Chem. Rev.* **2004**, *104*(2), 419–458.
- [16] Feldman, J.; McLain, S. J.; Parthasarathy, A.; Marshall, W. J.; Calabrese, J. C.; Arthur, S. D. *Organometallics* **1997**, *16*(8), 1514–1516.
- [17] Holland, P. L.; Tolman, W. B. *J. Am. Chem. Soc.* **1999**, *121*(31), 7270–7271.

- [18] Randall, D. W.; George, S. D.; Holland, P. L.; Hedman, B.; Hodgson, K. O.; Tolman, W. B.; Solomon, E. I. *J. Am. Chem. Soc.* **2000**, *122*(47), 11632–11648.
- [19] Bharatam, P. V.; Patel, D. S.; Iqbal, P. *J. Med. Chem.* **2005**, *48*(24), 7615–22.
- [20] Dias, H. V. R.; Singh, S. *Inorg. Chem.* **2004**, *43*(23), 7396–7402.
- [21] Flores, J. A.; Dias, H. V. R. *Inorg. Chem.* **2008**, *47*(11), 4448–4450.
- [22] Kopylovich, M. N.; Pombeiro, A. J. *Coord. Chem. Rev.* **2011**, *255*(1–2), 339–355.
- [23] Barman, T. R.; Mukherjee, G. N. *J. Chem. Sci. (Bangalore, India)* **2006**, *118*(5), 411–418.
- [24] Barman, T. R.; Mukherjee, G. N. *Indian J. Chem., Sect. A: Inorg., Bio-inorg., Phys., Theor. Anal. Chem.* **2009**, *48*(1), 38–44.
- [25] Becke, A. D. *J. Chem. Phys.* **1993**, *98*(7), 5648–5652.
- [26] Stephens, P. J.; Devlin, F. J.; Chabalowski, C. F.; Frisch, M. J. *J. Phys. Chem.* **1994**, *98*(45), 11623–11627.
- [27] Becke, A. D. *Phys. Rev. A* **1988**, *38*(6), 3098–3100.
- [28] Vosko, S. H.; Wilk, L.; Nusair, M. *Can. J. Phys.* **1980**, *58*(8), 1200–1211.
- [29] Lee, C.; Yang, W.; Parr, R. G. *Phys. Rev. B* **1988**, *37*(2), 785–789.
- [30] Rappoport, D.; Furche, F. *J. Chem. Phys.* **2010**, *133*(13), 134105–11.
- [31] Gaussian 09 Revision A.02. Frisch, M. J.; Trucks, G. W.; Schlegel, H. B.; Scuseria, G. E.; Robb, M. A.; Cheeseman, J. R.; Scalmani, G.; Barone, V.; Mennucci, B.; Petersson, G. A.; Nakatsuji, H.; Caricato, M.; Li, X.; Hratchian, H. P.; Izmaylov, A. F.; Bloino, J.; Zheng, G.; Sonnenberg, J. L.; Hada, M.; Ehara, M.; Toyota, K.; Fukuda, R.; Hasegawa, J.; Ishida, M.; Nakajima, T.; Honda, Y.; Kitao, O.; Nakai, H.; Vreven, T.; Montgomery, Jr., J. A.; Peralta, J. E.; Ogliaro, F.; Bearpark, M.; Heyd, J. J.; Brothers, E.; Kudin, K. N.; Staroverov, V. N.; Kobayashi, R.; Normand, J.; Raghavachari, K.; Rendell, A.; Burant, J. C.; Iyengar, S. S.; Tomasi, J.; Cossi, M.; Rega, N.; Millam, J. M.; Klene, M.; Knox, J. E.; Cross, J. B.; Bakken, V.; Adamo, C.; Jaramillo, J.; Gomperts, R.; Stratmann, R. E.; Yazyev, O.; Austin, A. J.; Cammi, R.; Pomelli, C.; Ochterski, J. W.; Martin, R. L.; Morokuma, K.; Zakrzewski, V. G.; Voth, G. A.; Salvador, P.; Dannenberg, J. J.; Dapprich, S.; Daniels, A. D.; Farkas, O.; Foresman, J. B.; Ortiz, J. V.; Cioslowski, J.; Fox, D. J.
- [32] Perdew, J. P. *Phys. Rev. B* **1986**, *33*(12), 8822–8824.

- [33] Zhao, Y.; Truhlar, D. *Theor. Chem. Acc.* **2008**, *120*(1-3), 215–241.
- [34] Zhao, Y.; Truhlar, D. G. *J. Chem. Phys.* **2006**, *125*(19), 194101–18.
- [35] Nbo version 3.1. Glendening, E. D.; Reed, A. E.; Carpenter, J. E.; Weinhold, F.
- [36] Coghi, L.; Lanfranchi, M.; Pelizzi, G.; Tarasconi, P. *Transition Met. Chem. (Dordrecht, Neth.)* **1978**, *3*(1), 69–76.
- [37] Hota, S. K.; Saha, C. R.; Pritzkow, H. *J. Coord. Chem.* **1984**, *13*(2), 131–142.
- [38] Kennard, C. H. L.; Smith, G.; O'Reilly, E. J. *Inorg. Chim. Acta* **1983**, *77*(0), L113–L115.
- [39] Su, Y. L.; Lu, L. P.; Li, X. M.; Zhu, M. L. *Acta Crystallogr. E61* **2005**, *61*, m910–m912.
- [40] Zhu, M.; Lu, L.; Yang, P.; Jin, X. *Acta Crystallogr. E58* **2002**, *58*, m217–m219.
- [41] Lu, L. P.; Yang, P.; Qin, S. D.; Zhu, M. L. *Acta Crystallogr. C60* **2004**, *60*, M219–M220.
- [42] Viossat, B.; Tomas, A.; Dung, N.-H. *Acta Cryst. C* **1995**, *51*(2), 213–215.
- [43] Lemoine, P.; Chiadmi, M.; Bissery, V.; Tomas, A.; Viossat, B. *Acta Crystallogr. C52* **1996**, *52*(6), 1430–1436.
- [44] Schwarzenbach, D.; Schmelzger, R. *Acta Crystallogr. B34* **1978**, *34*(Jun), 1827–1833.
- [45] Pierrel, F.; Cobine, P. A.; Winge, D. R. *Biometals* **2007**, *20*(3-4), 675–682.

Chapter 4

Protocols for Understanding the Redox Behaviour of Copper Containing systems

4.1 Introduction

Many fundamental chemical reactions include steps involving electron transfer from one reacting partner to another. Reduction and oxidation potentials are thermodynamic quantities that quantitatively describe the tendency of a chemical compounds to lose or acquire electrons. Experimentally, techniques such as cyclic voltammetry provide an experimental means for the measurement of redox potentials for the reversible electron-transfer processes. However, for measurement of experimentally more complicated non-reversible reactions use of rapid spectrophotometric techniques such as pulse radiolysis may be needed in order to obtain accurate redox potentials.¹ Moreover, a lot of information, such as structure-property relationship, is hidden due to the complex nature of experimental settings. On the other hand computational approaches provide deeper insight into the redox potential chemistry by, for example, separating various effects and breaking down the structural complexity into smaller building blocks.

Computational approach for redox potential calculations rely on the application of accurate quantum chemistry methods for electron affinity (ionization potential) calculations on the solute combined with a dielectric continuum models to account for the solvent effects. In general, a thermodynamic cycle that includes the free energies of products and reactants in the gas phase and their free energies of solvation is used in order to estimate the standard-state Gibbs free energy of the corresponding

half-reaction, which is then used to calculate the reduction potential. Solvation free energies are calculated using implicit solvent models, often referred to as continuum solvation models. Here, solute molecule is usually placed inside the suitably shaped cavity surrounded by the solvent in a form of an uniform structureless dielectric medium characterized by macroscopic (fixed or adaptive dielectric constant ϵ , density) and sometimes also by microscopic properties (molecule polarizability and an effective solvent radius). This approach, which mainly accounts for bulk electrostatic effects, is often sufficient and much computationally cheaper, which enables focusing computational resources on the higher theoretical level calculations of the solute. In the case when interaction with solvation sphere or encapsulating protein environment needs to be accounted for there is a possibility to include multiple layers treated at different levels of theory in a so called QM/QM or QM/MM approach. This would involve, for example, treating the active site (solute) at the high QM level (CC, MP2, DFT), first solvation sphere at the lower level (DFT, semi-empirical or molecular mechanical level) and if needed more extended environment beyond first solvation sphere at the MM level. However, this can eventually lead to computationally and technically more demanding calculations.

DFT in conjunction with continuum solvation models was successfully applied in studies involving the prediction of redox potentials of organic molecules, such as anilines² and polycyclic aromatic hydrocarbons³; transition metal complexes, such as ferricinium/ferrocene couple^{4,5} and copper complexes^{6,7}. A more detailed recent review by Marenich *et al.*⁸ discusses many more examples of successful application of DFT and other computational methods in calculations of reduction potentials.

In spite of encouraging results from DFT redox calculations, the redox potential studies often lack a more systematic approach in order to understand fundamental elements of the redox potential calculation in depth. Moreover, use of a huge variety of different functional and basis set combinations across the literature and insufficient benchmarking may lead to an unnecessarily difficult task for a new user to calculate redox potentials and assess their accuracy.

In general redox potential calculations of transition metal complexes present a challenge, because of usually large structural difference between oxidized and reduced form of the complex, excess charge of the complex and potential multireference character of the transition metal wave function. Some of these issues can be addressed by use of higher level methods or use of multiple conformers. Matsui *et al.*⁹ proposed a scheme to address the metal complexes with excess charge by putting an image counterion distribution around the charged complex in order to neutralize the system and improve often poor description of solvation energy.

Copper complexes play an essential role in living systems involving, for example, electron transfer, O₂ binding and various enzymatic reactions.^{10,11} Therefore, detailed understanding of the redox chemistry of copper-binding complexes can provide deeper insight into the mechanisms of copper metalloproteins and copper trafficking which is important in regulation of normal human physiology and homeostasis^{12,13}. Moreover, redox properties of copper-binding drugs, such as metformin (see chapter 3), may play a crucial role in the biomolecular function of these drugs as they can, for example, interfere with the sensitive redox chemistries occurring inside the cell, such as the mitochondrial electron transport chain.

The effect of coordination geometry, nature of the donor atoms of the ligands as well as number of substituents have been shown to affect the redox potential of the Cu(II)/Cu(I) couple.¹⁴⁻¹⁶ For example, there is a dependence of the Cu(II/I) redox potential on the relative number of N and S donor atoms, mainly guided by the Cu(II) preference for amine nitrogen relative to thioether sulfur.¹⁷ Moreover, the reduction of Cu(II) to Cu(I) is facilitated in the case of ligands containing both unsaturated nitrogen and thioether sulfur atoms.¹⁸

Comparison of the calculated geometries with the solid state structures obtained using X-ray diffraction and then trying to find correlation with electrochemical behaviour may give misleading results. The main reason is that the electrochemical behaviour may correspond to completely different geometries in solution. Here, theoretical calculations offer a possibility to study electrochemical mechanisms of the solution-phase structures.

4.2 Computational Electrochemistry

The thermodynamic (Born-Haber) cycle, as illustrated in the Figure 4.1, was used in the calculation of equilibrium redox potentials. The top part represents the condensed-phase free-energy changes associated with the reduction of metal complex and the bottom part relevant gas-phase processes. The thermodynamic cycle is completed with parts connecting gas phase and condensed phase, which represent differential solvation free energies of the oxidized and reduced species. After neglecting the free electron in the thermodynamic cycle, it is sufficient to compute a gas-phase free-energy change (at 0 K this would typically correspond to an electron affinity (EA) as an analog for reduction potential and an ionization potential (IP) for oxidation potential) and free energies of solvation.

Following the thermodynamic cycle absolute half-cell standard reduction potentials

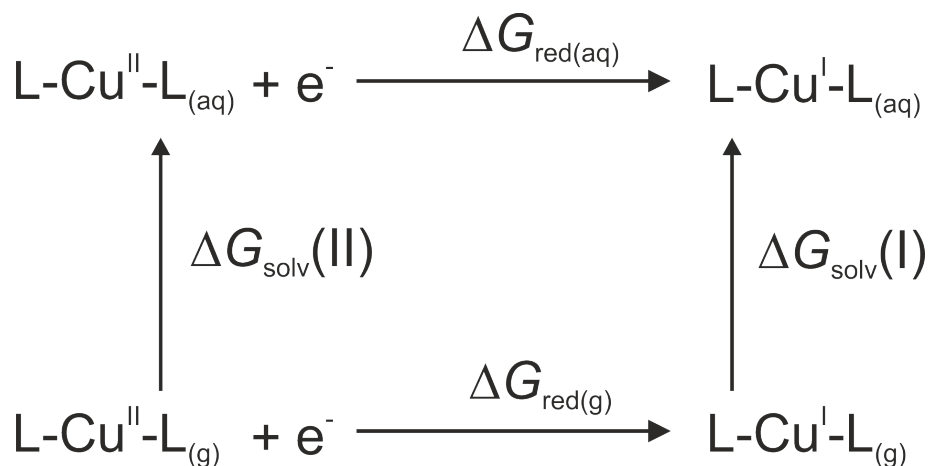


Figure 4.1: Born-Haber cycle for calculation of redox potential.

E_{Abs}^0 were calculated using the following equation:

$$E_{\text{Abs}}^0 = -\frac{\Delta G_{\text{red(aq)}}}{nF} - 0.03766 \text{ eV} \quad (4.1)$$

with the last term representing a free electron correction at 298 K,¹⁹ the Faraday constant $F = 23.06 \text{ kcal/mol.V}$, $n = 1$ the number of electrons involved in the redox couple and the Gibbs free energy change $\Delta G_{\text{red(aq)}}$ due to the reduction of copper complex in aqueous solution, computed as follows:

$$\Delta G_{\text{red(aq)}} = \Delta G_{\text{red(g)}} + \Delta G_{\text{solv}}(\text{I}) - \Delta G_{\text{solv}}(\text{II}) \quad (4.2)$$

In the eq. (4.2), the $\Delta G_{\text{red(g)}} = G_{(\text{g})}([\text{Cu}^{\text{II}}\text{L}_x]^y) - G_{(\text{g})}([\text{Cu}^{\text{I}}\text{L}_x]^y)$ in the gas phase and the solvation $\Delta G_{\text{solv}} = E_{(\text{elec,solv})} - E_{(\text{elec,g})}$ were calculated as a difference between electronic energies in the implicit solvent and in the gas phase. Further, a correction to the gas-phase Gibbs energy of reaction, $\approx 1.89 \text{ kcal/mol}$, placing it from the initial reference state of 1 atm to 1 mol/L, is included in the calculation. However, neglecting this correction would lead to a relatively small error of 80 mV to the calculated absolute potentials.

Absolute reduction potentials are reported as well as relative potentials referenced to a standard hydrogen electrode (SHE). In order to reference against SHE, a suggested absolute SHE potential value of +4.28 V,²⁰ which is in good agreement with experimentally determined value of +4.29 V,²¹ is subtracted from the calculated absolute potentials.

The following approach was used for reduction potential calculations. Minimum geometries of all the computed structures were obtained by gas phase optimization

at the DFT level of theory using various functionals and each structure was verified to be a true minimum by the absence of imaginary frequencies in the vibrational analysis. For each calculation stability of the wave function was tested. Basis sets used were Def2-TZVPD²² and cc-pVTZ^{23,24}. Calculations were performed using Gaussian09 (A.02 version)²⁵. Implicit solvent calculations were computed by using the standard self-consistent reaction field (SCRF) approach with PCM^{26–30}, the integral equation formalism variant (IEFPCM), and SMD³¹ solvation model, and water as a solvent.

Calculations were carried out using the following functionals SVWN^{32–35}, BP86^{36,37}, B3LYP^{35,38–40} (as implemented in Gaussian 09), B3PW91^{35,38,41–44}, CAM-B3LYP⁴⁵, B97D⁴⁶, ω B97xD⁴⁷, TPSSTPSS⁴⁸, PBE1PBE (PBE0)^{49–51} and Minnesota functionals with different % HF exchange included (in brackets): M06-L⁵² (0%), M06⁵³ (27%), M06-2X⁵³ (54%), M06-HF⁵⁴ (100%).

SVWN is a local spin density functional with the Slater exchange, $\rho^{4/3}$ with theoretical coefficient of 2/3 and Vosko, Wilk, and Nusair 1980 correlation functional (III) fitting the RPA solution to the uniform electron gas. BP86 represents functional from generalized gradient approximation (GGA), which incorporates Becke’s 1988 exchange functional B with Perdew’s 1986 correlation functional P86, family of functionals. B3LYP is the hybrid functional, which incorporates Becke’s three-parameter exchange functional B3 with the Lee, Yang, and Parr correlation functional LYP. The B3PW91 is similar to the B3LYP functional, but the non-local correlation is provided by Perdew/Wang 91. B97D is the GGA exchange-correlation functional including dispersion. TPSSTPSS represents the τ -dependent gradient-corrected functional and PBE1PBE (PBE0) is the hybrid functional that uses 25% exact exchange and 75% DFT exchange. Minnesota functionals contain M06-L functional, which is a fully local meta-GGA functional, accounts implicitly for dispersion effects, and should perform well for systems containing transition metals. In the same family of functionals M06, M06-2X and M06-HF represent the global hybrid functionals. In addition, inclusion of Grimme’s GD3 dispersion with Becke-Johnson damping⁵⁵ was tested with the B3LYP, B3PW91 and BP86 functionals. In the above functionals the long-range electron-electron exchange part typically dies off too rapidly and becomes very inaccurate at large distances, making these functionals unsuitable for modeling processes such as electron excitations and charge transfer states. Long range corrected functionals such as ω B97xD and CAM-B3LYP were designed to address these problems by separating the two-electron operator, $\frac{1}{r_{12}}$, into the short-range and long-range parts using the standard error function *erf*. The commonly used CAM-B3LYP functional uses 19% exact HF and 81% Becke’s 1988 exchange interaction at short-range, and 65% HF and 35% Becke’s 1988 at long-range. The intermediate region is smoothly described by the parameter $\mu =$

4.3 Results and Discussion

Computational protocol for calculation of reduction potentials of copper complexes is being developed and tested on the series of 14-membered quadridentate macrocyclic polyamino polyether ligands, see Figure 4.2. These molecules represent a valid copper-binding model systems, previously used as a model for blue copper binding sites. Moreover, in these series effect of thioether sulfur substitution for amine nitrogen on the electrochemical properties is examined. Although, in the original experimental paper by Rorabacher¹⁷ these macrocyclic complexes serve as model compounds for blue copper protein binding sites, their application as model systems can be potentially extended to other important copper binding complexes (e.g. metfomin copper complex).

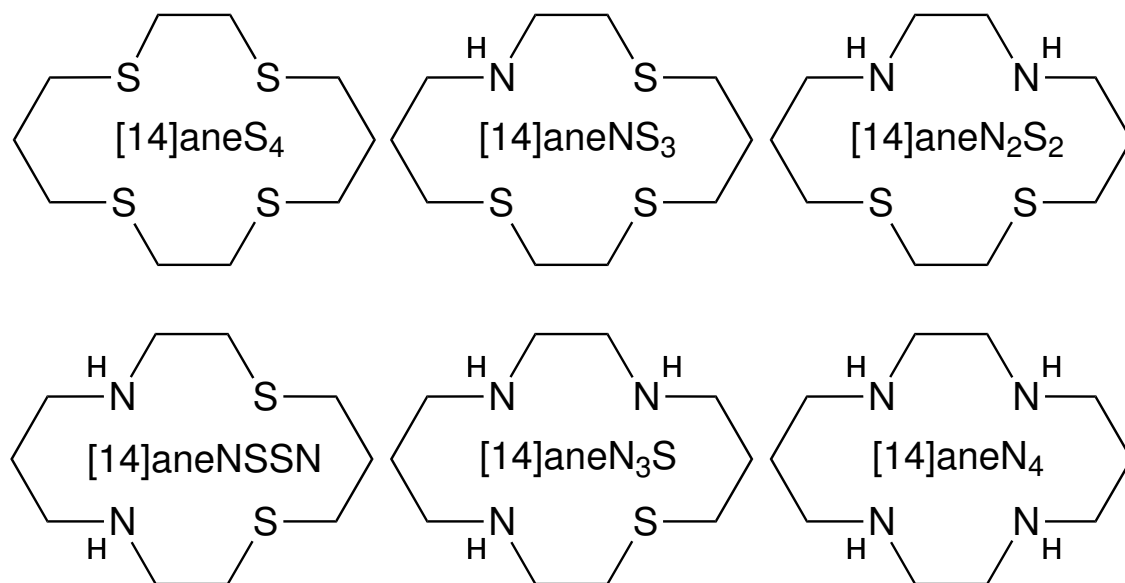


Figure 4.2: Macrocyclic ligands used in the reduction potentials study.

Experimental reduction potentials, listed in Table 4.1, are obtained from the article by Rorabacher¹⁷ and these were originally derived using the cyclic voltammetric measurements on aqueous $\text{Cu}^{\text{II}}\text{L}$ solutions at 25 °C. For the empirical estimation of potential values of the N_3S complex the following equation was used¹⁷:

$$E^f = E_{\text{aq}}^{\circ} - \frac{2.303RT}{nF} \log \frac{K_{\text{Cu}^{\text{II}}\text{L}}}{K_{\text{Cu}^{\text{I}}\text{L}}} \quad (4.3)$$

where the E_{aq}° is the standard electrode potential, in terms of molar concentrations, for the $\text{Cu}_{\text{aq}}^{2+}/\text{Cu}_{\text{aq}}^{+}$ couple of the aqueous $\text{Cu}(\text{II}/\text{I})$. In the original reference¹⁷ it was

measured as $E_{\text{aq}}^{\circ} \approx 0.13\text{V}$ at 25 °C.

Table 4.1: Experimental $E_{1/2}$ potentials for studied N_xS_{4-x} ($x = 0, 1, 2, 3, 4$) complexes.

N_xS_{4-x}	$E_{1/2}^a$ [mV]
N_4	-0.66 (est) ^b
N_3S	≤ -0.24 (est) ^c
N_2S_2	0.04 (pH > 5.0)
NSSN	-0.01 (pH > 5.0)
NS_3	0.38 (pH > 3.5)
S_4	0.58

^a Experimentally determined $E_{1/2}$ should be accurate to within ± 0.01 V¹⁷

^b Values estimated from the trend of methanolic potentials of copper complexes with related 14-membered macrocyclic N_4 ligands containing unsaturated nitrogen⁵⁶ assuming $E_{\text{H}_2\text{O}}^f = E_{\text{MeOH}}^f - 0.060$ V.^{57,58}

^c Value estimated using Equation 4.3 assuming $K_{\text{Cu}^{\text{II}}\text{L}} \geq 1 \times 10^{20}$ and $K_{\text{Cu}^{\text{I}}\text{L}} \approx 4 \times 10^{13}$ (see main text).

4.3.1 Assessing Appropriateness of DFT for Redox Potential Calculations.

In order to assess the correctness and reliability of the single reference DFT for the reduction potential calculations of the copper macrocycles following steps were considered. Multi-reference character of the wave function was assessed using T_1 ⁵⁹⁻⁶² diagnostics value calculated at the CCSD/cc-pVDZ level, spin contamination by looking at the expectation value of the total spin $\langle S^2 \rangle$ and the wave function stability⁶³⁻⁶⁵.

The T_1 diagnostics, which uses the Frobenius norm of the t_1 amplitudes of the CCSD wave function, provide an averaged indicator of the quality of a single-reference couple-cluster, but may fail to indicate a small problem region of a large molecule. A criteria of $T_1 > 0.05$ were proposed to identify 3d transition metal species with substantial nondynamical correlation, for which results obtained from a single-reference quantum method may suffer from large errors and unpredictable behaviour.⁶⁶ The T_1 diagnostic has not been used on many large copper complexes and so data is limited to only small copper complexes. In general, the T_1 values for small copper complexes tend to be lower than 0.05 and the only cases of large T_1 noted in the literature are small coordinately unsaturated species where multi-reference character would be expected.^{66,67} For the macrocyclic complexes presented in this chapter the T_1 diagnostic was calculated for completeness as it is readily available from the final CC wave function, however there is no a priori reason to expect large values.

The spin contamination is a result of unrestricted wave function being no longer an eigenfunction of the total spin $\langle S^2 \rangle$ and therefore the desired spin state may suffer from having other spin states mixed in (being spin contaminated), which may result in some errors, e.g. increase in the total energy.

Finally, the stability test ensures that resulting single-determinant wave function is a local minimum with respect to relaxing various constraints, e.g. allowing an RHF determinant to become UHF, allowing orbitals to become complex and reducing the symmetry of the orbitals.

Examining the T_1 values in the Table 4.2, all of the studied complexes and copper oxidation states exhibit T_1 values lower than the 0.05 criteria and thus should be accurately described by a single-reference method. Further, there is a slight increase in T_1 for the N_xS_{4-x} series where more thioether sulfur is substituted for amine nitrogen for the Cu^I complex as opposed to a slight decrease of T_1 values for the Cu^{II} complexes.

Table 4.2: Multireference character measured using T_1 diagnostics values. Calculated at CCSD/cc-pVDZ level using M06/cc-pVTZ geometry.

N_xS_{4-x}	Cu^I	Cu^{II}
S_4	0.016	0.026
N_1S_3	0.017	0.024
N_2S_2	0.016	0.022
NSSN	0.017	0.023
N_1S_3	0.018	0.021
N_4	0.019	0.019

Looking at the eigenfunctions of the total spin $\langle S^2 \rangle$ for all of the unrestricted calculations it can be concluded that a spin contamination, if present, was completely removed after a spin annihilation step and the calculated wave functions represent pure spin states, $\langle S^2 \rangle = 0.75$ (Cu^{II}). Lastly, the stability tests showed none of the calculations suffered with any stability problems.

4.3.2 Basis Set Dependence of Calculated Redox Potentials

In this subsection, convergence of the reduction potential results for M06 functional with the increase in the basis set quality is examined. Single point energy calculations are performed on the cc-pVTZ geometries using Dunning’s correlation-consistent basis sets, cc-pVnZ^{23,24,68-70} with $n=D,T,Q$ (D =double, T =Triple, Q =Quadruple) and 5 (5=Quintuple) zeta basis sets. The effect on EA , $\Delta G_{\text{solv}}(I)$ and $\Delta G_{\text{solv}}(II)$ components of the thermodynamic cycle and on the overall calculated reduction

potentials is examined. Reduction potentials for the cc-pVnZ series were calculated using the electronic energy calculated at the given basis set and the thermal correction to the Gibbs free energy ($G_{\text{corr}} = E_{\text{tot}} + k_{\text{B}}T - TS_{\text{tot}}$, see subsection 2.1.11) obtained with the cc-pVTZ basis set as a frequency calculation using larger basis sets would be prohibitively expensive. At the end of the subsection performance of Def2-TZVPD basis set, which is a triple-zeta-valence basis set with polarization and diffuse basis functions, as taken from the EMSL Basis Set Library^{71,72} is presented. The Def2-TZVPD is from a family of property-optimized (in this case optimized for dipole polarizabilities) diffuse augmented basis sets of the Karlsruhe def2-TZVP⁷³ basis sets, which are smaller and less diffuse than augmented Dunning basis sets and are well-known for their robustness and their excellent cost-to-performance ratio in large-scale DFT calculations.²² For these calculations the G_{corr} to the electronic energies for the reduction potentials were calculated with the Def2-TZVPD basis set.

As can be seen from figs. 4.3 to 4.8, solvation components ($\Delta G_{\text{solv}}(\text{I})$, $\Delta G_{\text{solv}}(\text{II})$) for both the SMD and PCM model very quickly converge to the cc-pV5Z basis set results with the largest deviation at the cc-pVTZ basis set not larger than 10 mV. In the case of calculated electron affinities (EA) there is much slower convergence towards more positive values with the basis set size, with the largest deviation of -36 mV at the cc-pVTZ for the S_4 complex.

For SMD solvation model, there is increase in the $\Delta G_{\text{solv}}(\text{I})$ solvation energies with the improvement of the basis set and exponential convergence to the cc-pV5Z result independent of the copper environment as opposed to the $\Delta G_{\text{solv}}(\text{II})$ component where the solvation energies decrease with improvement in the basis set for S_4 , N_1S_3 , N_2S_2 and NSSN complexes, but increase for the N_3S_1 and N_4 complexes. Similar environment dependence can be observed for both solvation components when calculated using the PCM solvation model. Improving basis set there is an oscillatory convergence of $\Delta G_{\text{solv}}(\text{II})$ for both SMD and PCM and in the case of $\Delta G_{\text{solv}}(\text{I})$ for PCM only. This behaviour is observed for most of the complexes with an exception of N_1S_3 ($\Delta G_{\text{solv}}(\text{II})$, SMD) and S_4 complexes.

Overall effect of improvement in the basis set quality on the calculated reduction potentials is that the absolute values of reduction potentials decrease with increase in the basis set size. This applies to both SMD and PCM solvation model and is mainly due to the largest change with increase in the basis set size affecting the EA component. At the cc-pVTZ basis set the results are already very close to the cc-pV5Z reduction potentials with the largest deviation no more than 32 mV (S_4 , SMD) and 33 mV (S_4 , PCM). As can be seen in Table 4.3 there is basically no effect of the basis set improvement on the mean absolute deviation (MAD) of

calculated reduction potentials for the SMD model, but a more significant effect on the MAD when PCM solvation is used. This again points to the fact that already at the cc-pVTZ basis set the calculated reduction potentials are well converged. The maximum absolute deviation is 173 mV, 139 mV, 105 mV and 113 mV for the N_1S_3 complex at the cc-pVDZ, cc-pVTZ, cc-pVQZ and cc-pV5Z, respectively.

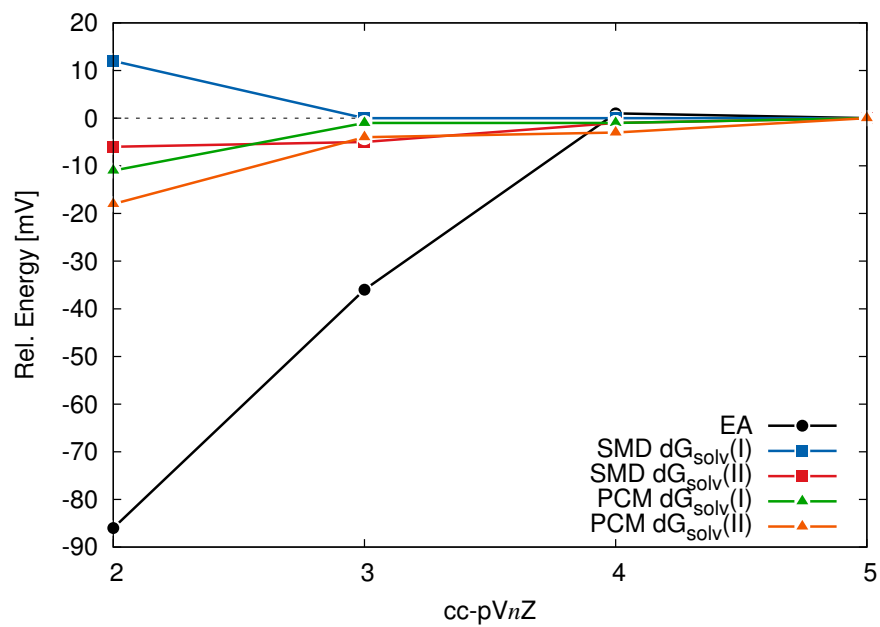
Table 4.3: Effect of basis set improvement on the MAD (mV) of calculated reduction potentials.

cc-pVnZ	MAD [mV]	
	SMD	PCM
2	75	568
3	75	527
4	75	492
5	76	499

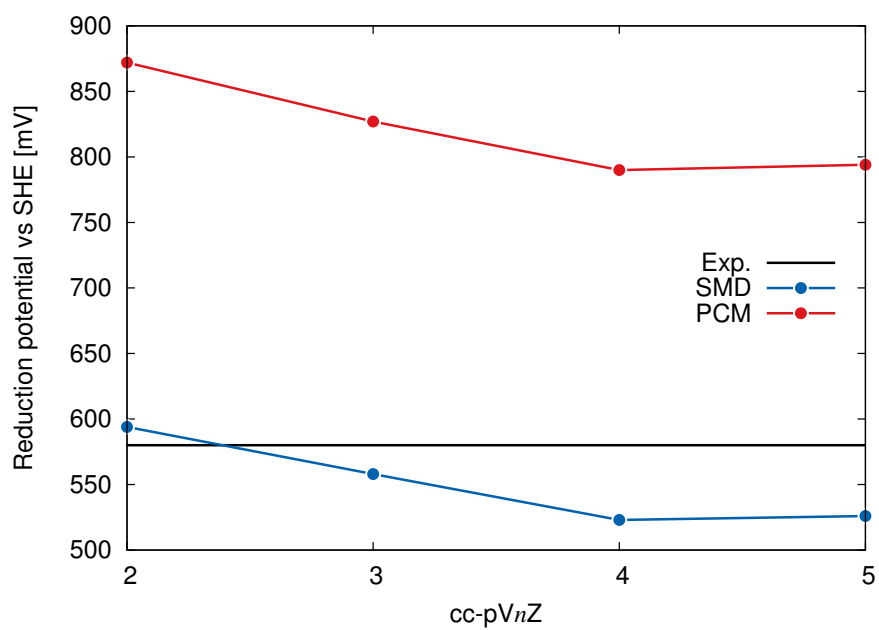
Table 4.4: Absolute deviations of calculated reduction potentials (mV) for cc-pVTZ and Def2-TZVPD basis sets with SMD solvation model.

N_xS_{4-x}	Absolute deviation [mV]	
	cc-pVTZ	Def2-TZVPD
S_4	22	10
N_1S_3	139	171
N_2S_2	50	3
NSSN	95	142
N_3S_1	75	131
N_4	70	7

Using the Def2-TZVPD basis set produces a MAD of 77 mV for reduction potentials calculated with the SMD model, which is comparable to MAD of 75 mV calculated using the cc-pVTZ basis set. Interestingly, for S_4 , N_2S_2 and N_4 complexes Def2-TZVPD yields absolute deviations from the experimental values that are significantly smaller than the corresponding cc-pVTZ values, see Table 4.4. It may be possible to lower the absolute deviations of the problematic complexes by optimizing them with the Def2-TZVPD rather than using the cc-pVTZ basis set geometries. However, this will be part of the follow up future study where structure-redox relationship will be examined in more details together with more detailed examination of the optimized geometries. The overall better performance of the Def2-TZVPD basis set may be attributed to the improved basis set convergence and thus smaller basis set error.

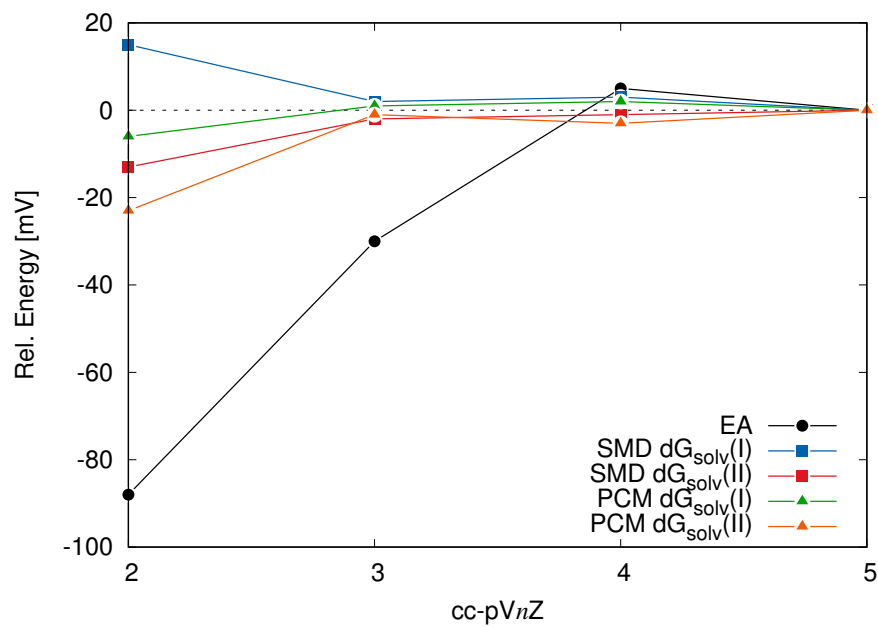


(a)

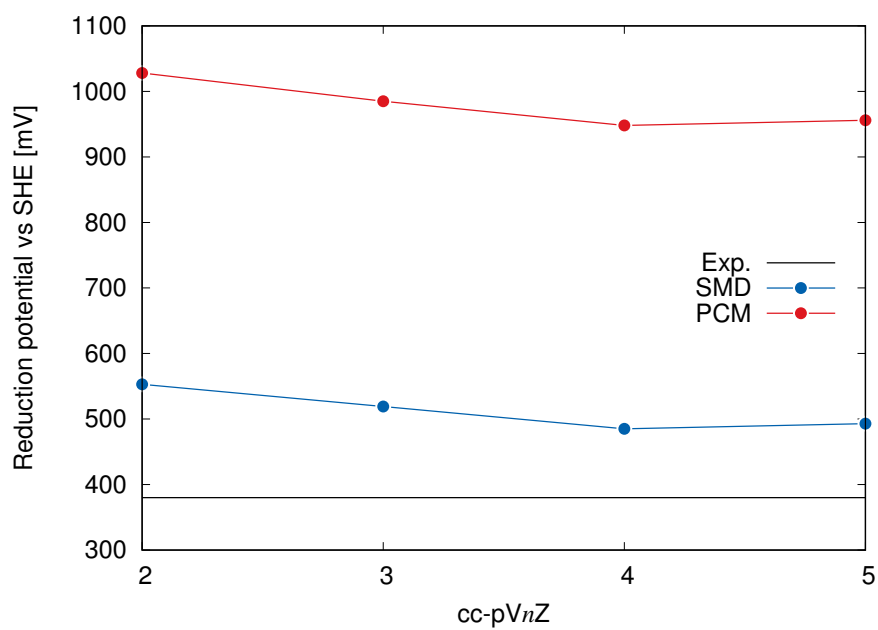


(b)

Figure 4.3: Convergence of (a) EA , $\Delta G_{\text{solv}}(\text{I})$ and $\Delta G_{\text{solv}}(\text{II})$; and (b) calculated reduction potentials with cc-pVnZ basis set for S_4 complex.

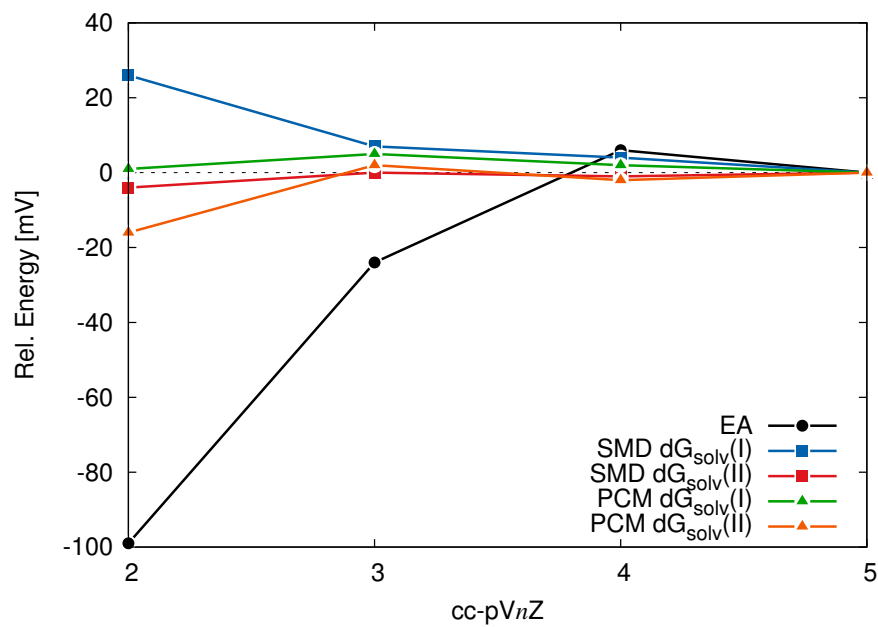


(a)

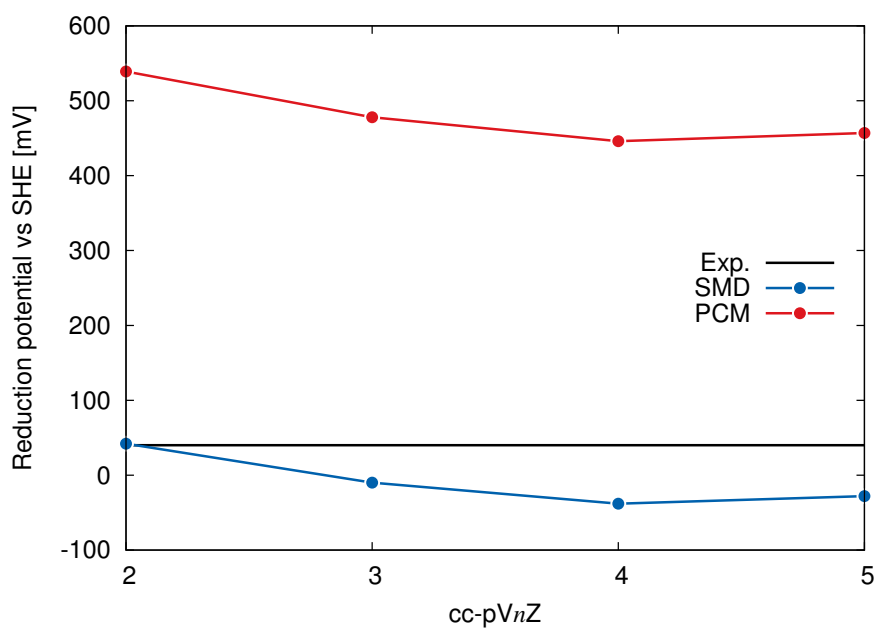


(b)

Figure 4.4: Convergence of (a) EA , $\Delta G_{\text{solv}}(\text{I})$ and $\Delta G_{\text{solv}}(\text{II})$; and (b) calculated reduction potentials with cc-pVnZ basis set for N_1S_3 complex.

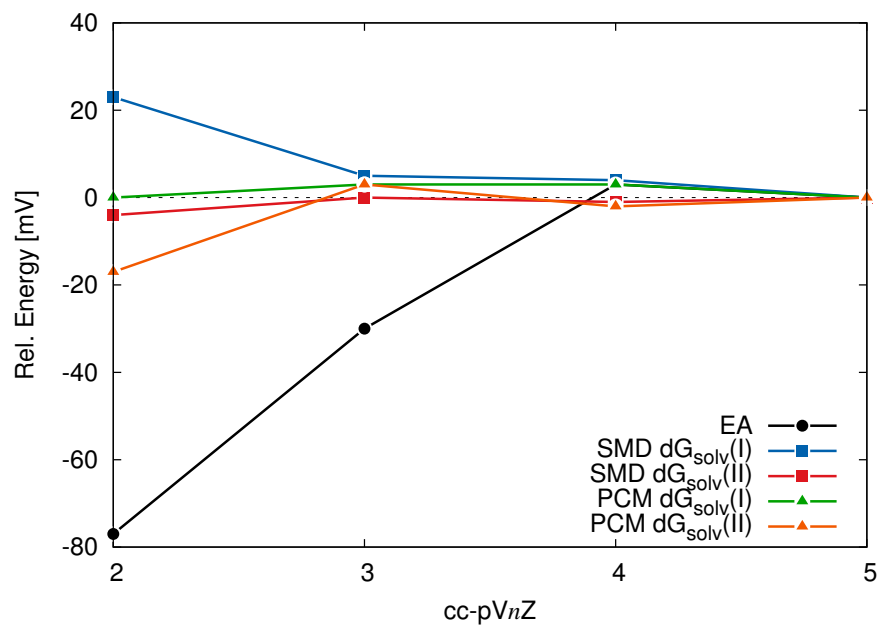


(a)

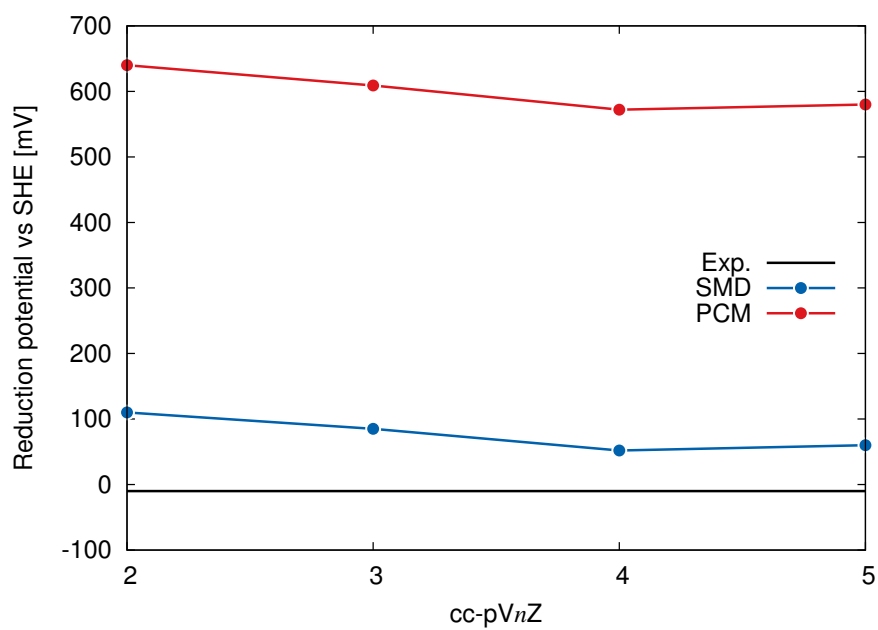


(b)

Figure 4.5: Convergence of (a) EA , $\Delta G_{\text{solv}}(\text{I})$ and $\Delta G_{\text{solv}}(\text{II})$; and (b) calculated reduction potentials with cc-pVnZ basis set for N_2S_2 complex.

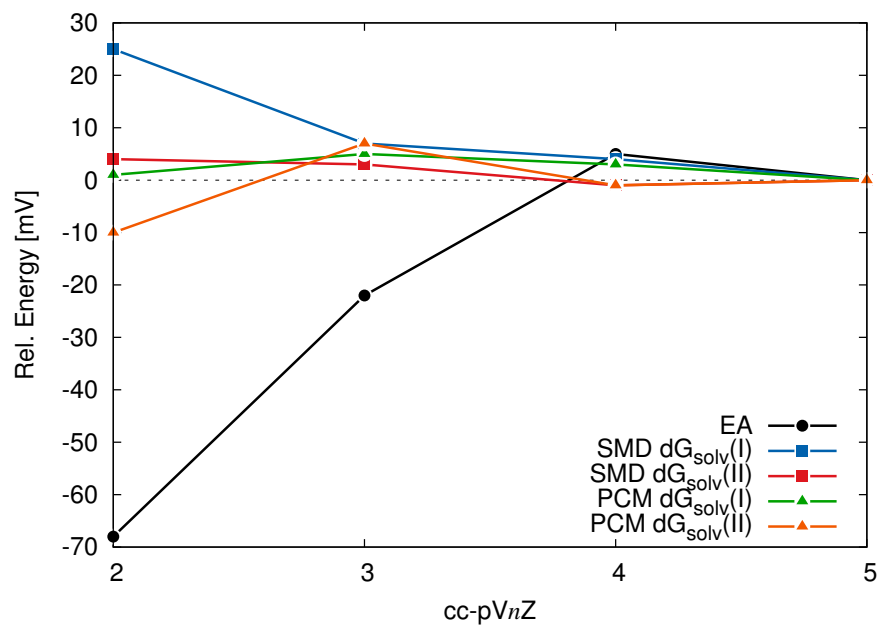


(a)

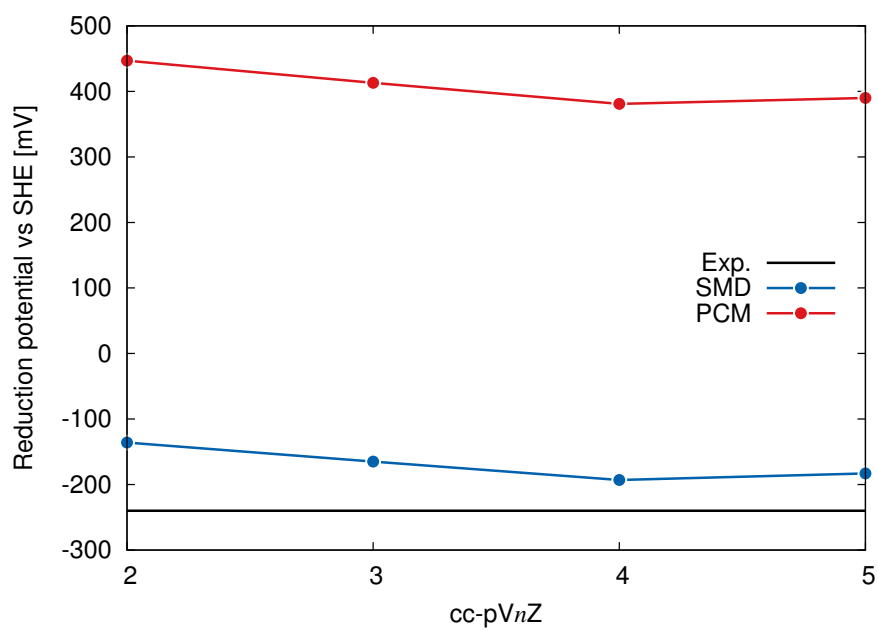


(b)

Figure 4.6: Convergence of (a) EA , $\Delta G_{\text{solv}}(\text{I})$ and $\Delta G_{\text{solv}}(\text{II})$; and (b) calculated reduction potentials with cc-pVnZ basis set for NSSN complex.

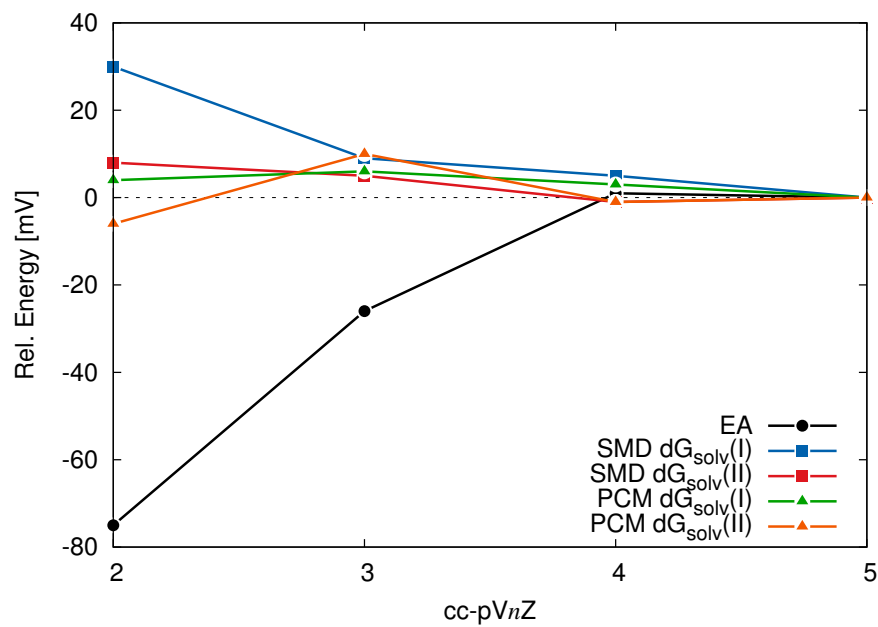


(a)

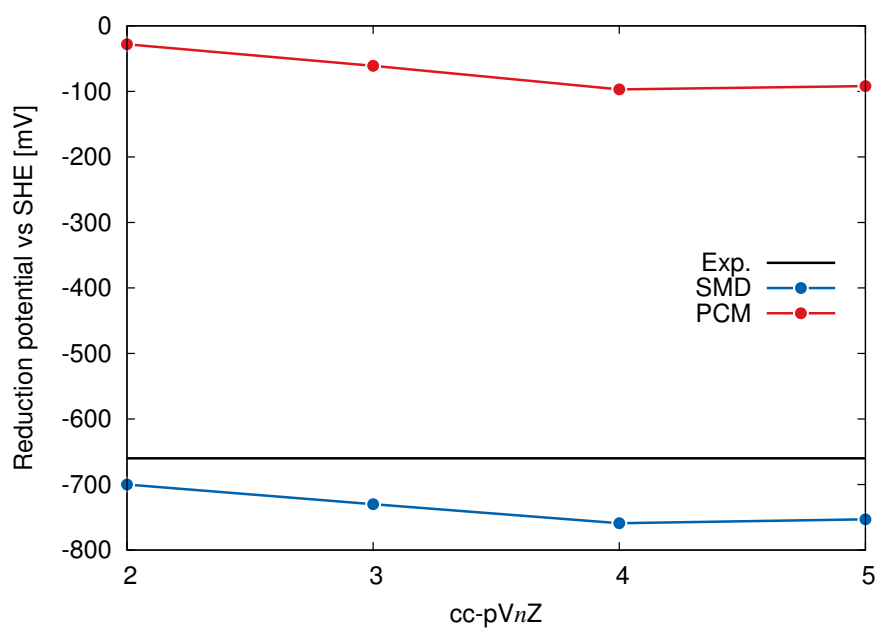


(b)

Figure 4.7: Convergence of (a) EA , $\Delta G_{\text{solv}}(\text{I})$ and $\Delta G_{\text{solv}}(\text{II})$; and (b) calculated reduction potentials with cc-pVnZ basis set for N_3S_1 complex.



(a)



(b)

Figure 4.8: Convergence of (a) EA , $\Delta G_{\text{solv}}(\text{I})$ and $\Delta G_{\text{solv}}(\text{II})$; and (b) calculated reduction potentials with cc-pVnZ basis set for N_4 complex.

4.3.3 Solvation Models

As can be seen in Figure 4.9, overall the best performing functional is the M06 (27% HF exchange) with MAD = 75 mV when used with SMD implicit solvation. On the other hand, this functional is one of the worst performing for PCM solvation where the best performing functionals are pure local M06L (27% HF) and meta-GGA TPSSSTPSS, both with MAD = 94 mV. Average MAD using SMD is 320 mV with the maximum MAD of 529 mV for M06HF functional. In the case of PCM solvation average MAD is 277 mV and the maximum MAD of 759 mV corresponds to the SVWN functional. However, when the local SVWN functional, which performs the worst in the PCM, is removed from the series the averaged MAD drops to 236 mV and the maximum MAD of 527 mV corresponds to the M06 functional. This SVWN removal could be justified as SVWN represents the simplest approximation to the density functional approximation. For the SMD solvation there is no obvious candidate that could be considered for removal from the series in order to lower the overall MAD. Therefore, when the SVWN is not considered, the PCM solvation model has better overall performance than the SMD solvation model with the lower average and maximum MAD from the experimental reduction potentials.

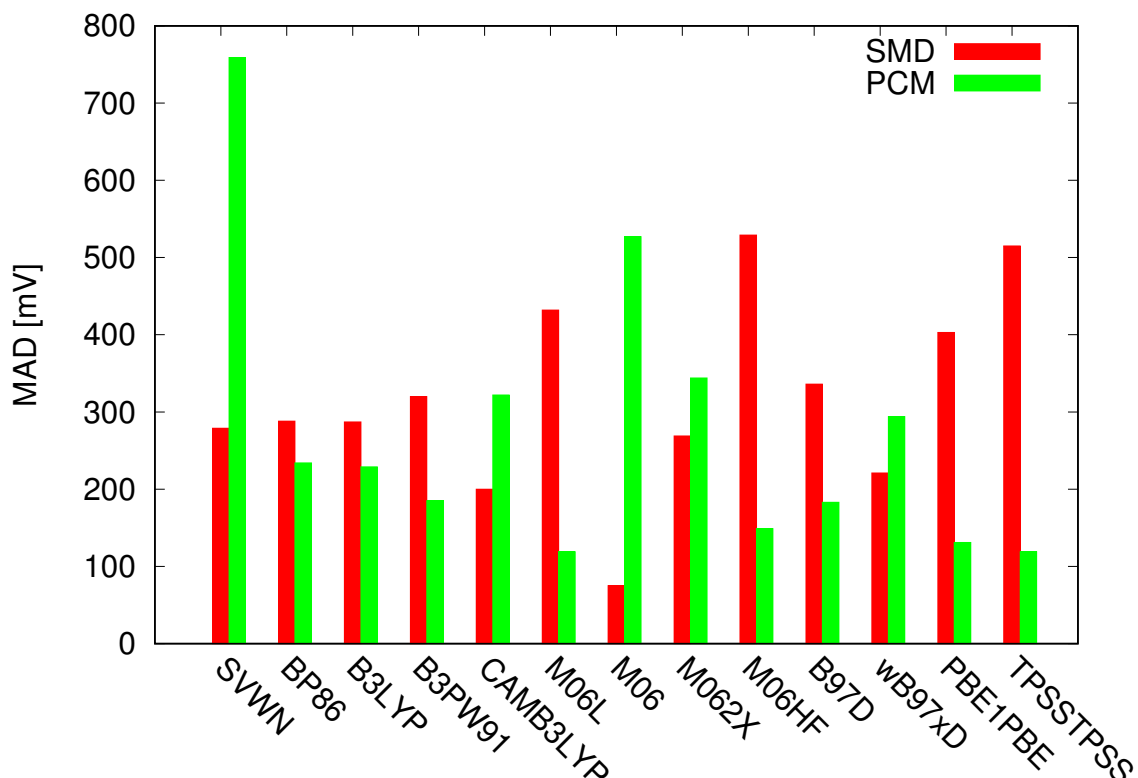


Figure 4.9: Overview of Mean Absolute Deviation (MAD) of theoretical values from experimental values for different functionals using cc-pVTZ basis set.

When we examine effect of functional improvement (climbing a so called "Jacob's ladder" of density functional approximations) on the calculated redox potentials

with SMD solvation, surprisingly, LDA (SVWN) performs slightly better than most of the GGA and hybrid functionals for the SMD model. In the case of PCM model there is a huge decrease in the MAD when further improvements to the functional approximations are included, e.g. gradient correction, moving from SVWN to BP86.

In the same Figure 4.9, it is shown that including long-range correction to B3LYP (CAM-B3LYP) decreases the MAD by ≈ 87 mV for the SMD, but increases the MAD by ≈ 93 mV for the PCM.

Including Grimme’s dispersion with Becke-Johnson damping (GD3BJ)⁵⁵ to the BP86, B3LYP and B3PW91 functionals, tables 4.5 and 4.6, has a minor effect on the MAD in both solvent models. Dispersion corrected functionals used with the SMD solvation, Table 4.5, increase the absolute deviation from the experimental values for S₄ and N₂S₂ complexes, have mixed effect in the case of N₁S₃, but decrease this deviation when more thioether sulfurs are substituted for amine nitrogens in the case of N₃S₁ and N₄. NSSN complex represents an exception as it has the same amount of sulfur for nitrogen substitutions as N₂S₂, but exhibit decrease in the absolute deviations. For PCM solvation model, Table 4.6, there seems to be exactly opposite trend when dispersion is considered, with exceptions of S₄ (BP86, B3PW91) and N₁S₃ (BP86, B3PW91).

Table 4.5: Effect of dispersion correction [in mV] on absolute deviation from experimental value of reduction potential for SMD water model. Using GD3BJ with BP86, B3LYP and B3PW91 and cc-pVTZ basis set.

	S ₄	N ₁ S ₃	N ₂ S ₂	NSSN	N ₃ S ₁	N ₄
BP86	26	-11	29	-37	-30	-26
B3LYP	43	11	46	-17	-8	-6
B3PW91	40	-5	42	-29	-20	-14

Table 4.6: Effect of dispersion correction [in mV] on absolute deviation from experimental value of reduction potential for PCM water model. Using GD3BJ with BP86, B3LYP and B3PW91 and cc-pVTZ basis set.

	S ₄	N ₁ S ₃	N ₂ S ₂	NSSN	N ₃ S ₁	N ₄
BP86	32	21	-20	35	32	31
B3LYP	-57	-1	-40	13	9	9
B3PW91	46	15	-32	26	21	16

Examining the performance of the M06 family of functionals, Figure 4.10, there is a strong dependence of calculated reduction potential on the percentage of exact HF exchange included in the functional with the opposite trend for SMD and PCM solvation models. The optimal value for the SMD model seems to be around 27% HF exchange corresponding to the M06 functional and increasing this value in either

direction increases the MAD. On the other hand, in the case of PCM model M06 is the worst performing functional and the M06L (0% HF) and M06HF (100% HF) produce the lowest MAD for reduction potentials. The difference between the MAD of the worst and best performing functionals of the M06 family is 454 mV (SMD) and 408 mV (PCM). This points towards a huge importance of %HF exchange used in a functional and solvation model used in the calculations. A possible explanation of the strong dependence of redox potentials on the % HF exchange stems from the fact that functionals with a high %HF exchange are not suitable especially for open-shell transition-metal systems due to potential multireference character. Although, this trend is observed for the SMD solvation it is not present in the case of PCM. This may be due to complex cancellation of errors present and thus further detailed investigation is required. Another possible explanation of the great performance of M06 functional with SMD solvation model is that electron affinities were used during its parametrization and that SMD solvation model was specifically designed and tested on the M06 family of functionals.

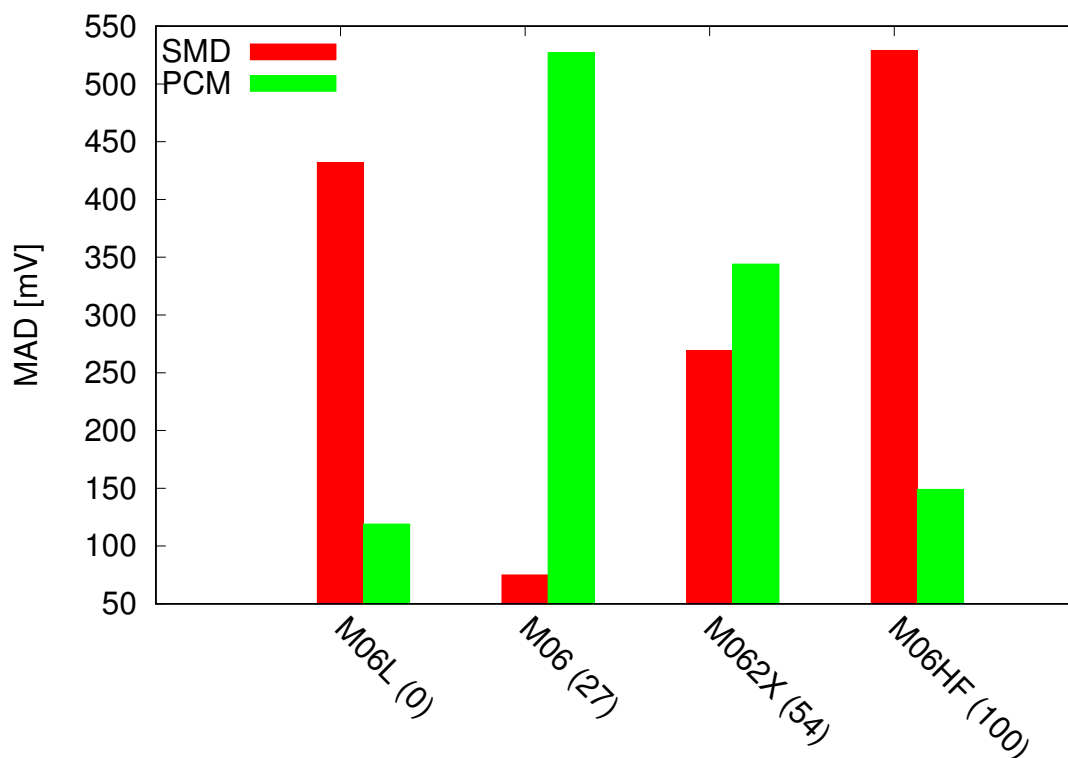


Figure 4.10: Performance of M06 family of functionals with varying %HF exchange (in brackets) is compared in SMD and PCM solvent model.

A table of variances of individual components of the thermodynamic cycle, Table 4.7, is presented in order to identify errors in these components and their sensitivity to the choice of functional. From this table it can be seen that electron affinities (EA or $\Delta G_{\text{red(g)}}$ in Figure 4.1) carry the biggest variation across the functionals, followed

by solvation energies of open-shell systems, $\Delta G_{\text{solv}}(\text{II})$. The solvation energies of closed-shell systems are the least sensitive to the choice of the functional. In the same table it is also shown that the functional sensitivity of the PCM solvation model is half of that of the SMD model for both $\Delta G_{\text{solv}}(\text{I})$ and $\Delta G_{\text{solv}}(\text{II})$.

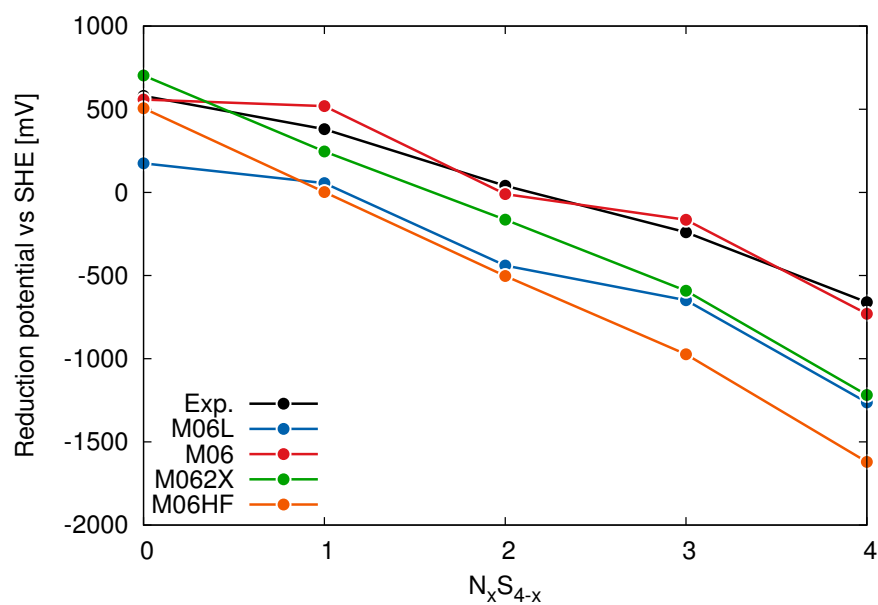
Table 4.7: Standard deviation (in mV) of EA ($\Delta G_{\text{red}(\text{g})}$ in fig. 4.1), $\Delta G_{\text{solv}}(\text{I})$ and $\Delta G_{\text{solv}}(\text{II})$ taken from the average over all functionals.

	Standard deviation [mV]				
	dGsolv(I)		dGsolv(II)		
	EA	SMD	PCM	SMD	PCM
S ₄	227	34	16	89	58
NS ₃	192	25	9	103	56
N ₂ S ₂	180	26	12	101	53
NSSN	195	26	9	108	58
N ₃ S	204	19	9	100	52
N ₄	211	15	8	98	48

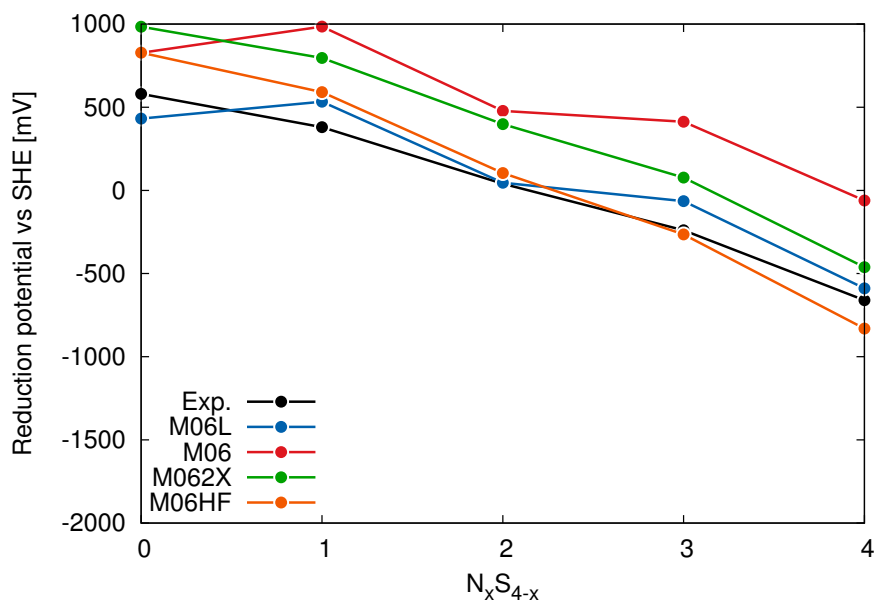
4.3.4 Effect of S for N substitution

In agreement with the experimental study by Rorabacher et al.¹⁷, for most of the functionals used the calculated reduction potentials show a fairly linear relationship with the value of x in the N _{x} S_{4- x} series. In the article by Rorabacher¹⁷ it was shown that each substitution of a nitrogen donor atom for a thioether sulfur donor atom resulted in an average decrease in the $E_{1/2}$ value ≈ 300 mV per nitrogen. As can be seen from Figure 4.11, the M06 with SMD closely follows the experimental profile and has the slope of -326 mV which is in the closest agreement to the experimentally observed slope. Further, the slope for M06L = -358 mV, M062X = -468 mV and M06HF = -523 mV deviates more significantly and this can also be related to their overall worse performance for SMD (as seen in Figure 4.10). In the case of PCM solvation none of the observed slopes (M06L = -264 mV, M06 = -235 mV, M062X = -361 mV, M06HF = -417 mV) is in as close agreement as M06/SMD decrease. However, it is interesting that the trend in slopes with the increasing %HF exchange is similar to the one observed for SMD.

Examining the calculated trends in the case of SMD the M06 functional closely follows the experimental curve, while the M06L curve also follows the shape of the experimental one it is shifted by a factor. In the case of M062X and M06HF functionals the calculated curves diverge from the experimental curve with the increase in the number of nitrogen substitutions. In the case of PCM solvation model the M06L curve is more closely following the experimental curve, however together with the M06 functional, these have a more distinct shape from the experimental one.

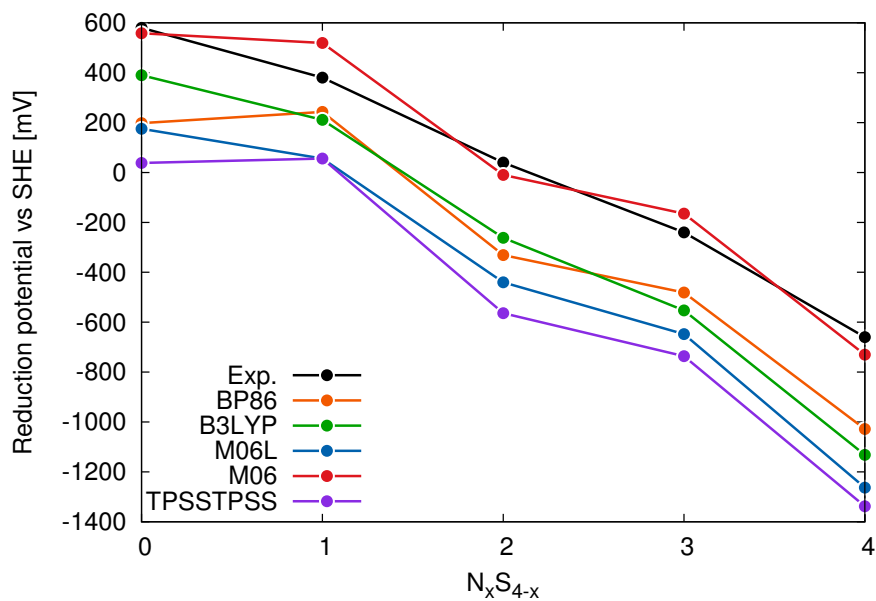


(a)

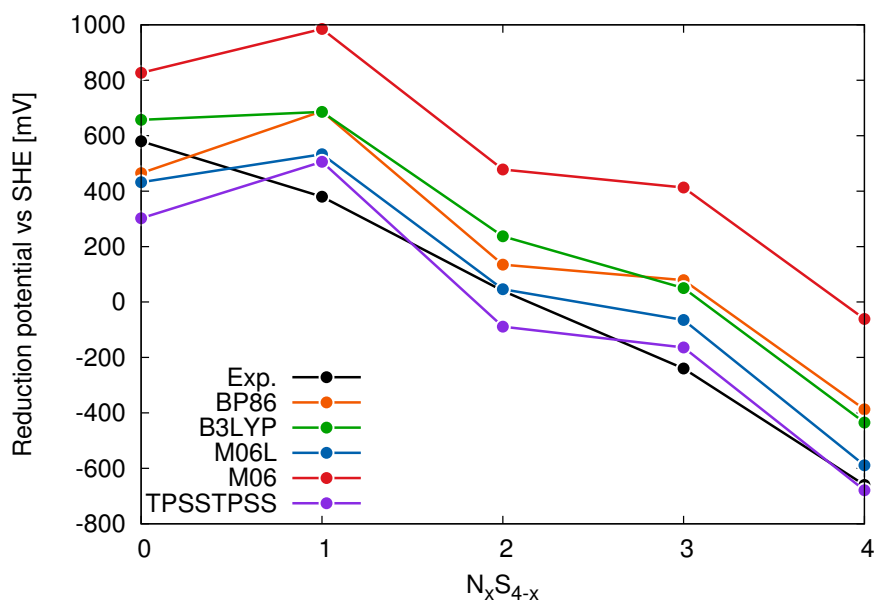


(b)

Figure 4.11: Comparison of calculated and experimental reduction potentials for the N_xS_{4-x} series. Performance of the M06 family of functionals with varying %HF exchange is compared using (a) SMD and (b) PCM solvent model. Note that NSSN was omitted for simplicity from this comparison as its redox potential is close to that of N_2S_2 .



(a)



(b)

Figure 4.12: Comparison of calculated and experimental reduction potentials for the N_xS_{4-x} series in the (a) SMD and (b) PCM solvent model. Performance of the BP86, B3LYP functionals and the best performing functionals in terms of the lowest MAD either in the SMD (M06) or the PCM (M06L, TPSSTPSS) solvation model. Note that NSSN was omitted for simplicity from this comparison as its redox potential is close to that of N_2S_2 .

The M062X and M06HF functional trends tend to slowly converge towards the experimental curve with the increase in the number of nitrogen substitutions with the M06HF intersecting the experimental profile at $x = 3$. Further, Figure 4.12 shows a comparison of reduction potential trends calculated using BP86, B3LYP and the best performing functionals in terms of the lowest MAD either in the SMD (M06) or the PCM (M06L, TPSSTPSS) solvation model. The SMD profiles calculated with BP86, B3LYP, M06L and TPSSTPSS have similar shape to the M06 curve which as mentioned above is closely following the experimental curve, but are shifted in respect to the experimental profile by a factor. Similarly, in the case of the PCM all of the functionals have similar profiles, however for PCM it is the M06L and TPSSTPSS that follow the experimental curve more closely.

The above findings raise a question whether trying lots of methods and choosing the one with the lowest MAD is any better than taking a different method with the best trend and adding an empirical correction. Indeed, it would be possible to add a correction to the calculated reduction potentials in the case of, for example, M06L/SMD in order to produce more accurate potentials. However, estimating an universal empirical correction may prove to be problematic and its applicability for other copper complexes would be questionable. On the other hand, a scheme such as M06/SMD is not just closely following the experimental profile and at the same time producing the lowest MAD, but seems to be potentially more robust to the small changes in the chemical environment and thus avoiding the need to derive any empirical correction.

4.4 Conclusion

This chapter described development and testing of computational protocol for calculation of reduction potentials of copper complexes. The series of 14-membered quadridentate macrocyclic polyamino polyether ligands were used as models systems in order to assess the limits of the computational protocol using DFT and implicit solvation.

It was found that the single-reference DFT is a suitable method for redox potential calculations of the studied copper macrocyclic complexes. This is further supported by no spin-contamination and wave function instabilities observed for the studied systems as well as no significant multireference character present. When examining the effect of improvement in the $cc\text{-p}VnZ$ basis set series on calculated redox potentials (with the $cc\text{-pVTZ}$ geometries), the results are already converged at the $cc\text{-pVTZ}$ level. The all-electron Def2-TZVPD basis set is a suitable choice of a basis

set for the redox potential calculation part (geometries optimized with the cc-pVTZ basis set) potentially leading to smaller absolute deviations from the experimental redox potential. This would be beneficial for a scheme where smaller basis sets are used for expensive parts of geometry optimization and frequency calculations and larger basis sets for more accurate redox calculations. However, a more thorough testing is needed. It was found the biggest error in the calculated redox potentials is coming from computed electron affinities. This points to the potential way of improving calculated results by using higher levels of theory for electron affinity calculations. When it comes to the choice of solvation model the PCM seems to be less sensitive to the choice of functional (excluding local functionals) in comparison to the SMD solvation model. Further, there is a strong dependence of accuracy of calculated redox potentials on the %HF exchange included in the functional and on the solvation model used. From the preliminary analysis of obtained geometries it seems that most of the functionals yield comparable geometries (see Appendix section 4.5) and thus critical steps in the redox calculations are the single-point energy calculations and the gibbs free energy correction calculations. Overall, the best performing functionals are M06 for the SMD and M06L and TPSSTPSS functionals for the PCM model. Summarizing the above findings a proposed scheme for redox potential calculations of copper macrocycles is using M06/cc-pVTZ with the SMD solvation or either M06L or TPSSTPSS functional/cc-pVTZ with the PCM solvation methods.

4.5 Appendix: Comparison of X-ray Structures and Computed Complexes

Examining the gas phase optimized geometries it seems that most of the functionals yield similar geometries. In the case of Cu^{II} complexes, tables 4.9, 4.11, 4.13, 4.15, 4.17 and 4.19, the standard deviation of copper nitrogen or copper sulfur distance and corresponding critical angles between functionals is less than 0.027 \AA and 1.3° , respectively. Further, in cases where X-ray structures are available and Cu^{II} complex has the square-planar geometry, tables 4.9 and 4.19, the DFT calculated values of critical bonds are within 0.05 \AA of the X-ray values and calculated angles have negligible deviation from the square-planarity. All of the calculated structures show angles between the opposing ligands of 180.00 when rounded up to two decimal places. This may seem a bit odd since no symmetry was imposed during optimization, but at the same time the angles for both the $\text{N}_4\text{-Cu}^{\text{II}}$ and $\text{S}_4\text{-Cu}^{\text{II}}$ X-ray structures are also very close to 180.00 degrees or are actually 180.00 degrees to within decimal places considered. In the case of mixed coordination, table 4.13, although, the DFT calculated values of critical bonds are still within 0.05 \AA of the X-ray values the corresponding angles deviates more significantly. In the case of Cu^{I} complexes, tables 4.8, 4.10, 4.12, 4.14, 4.16 and 4.18, more significant deviations are observed between the values of critical bonds and angles calculated using various functionals as well as available X-ray structure (table 4.10). This points towards more complex coordination chemistry for these complexes. However, a more detailed study in the future work is required in order to address this points.

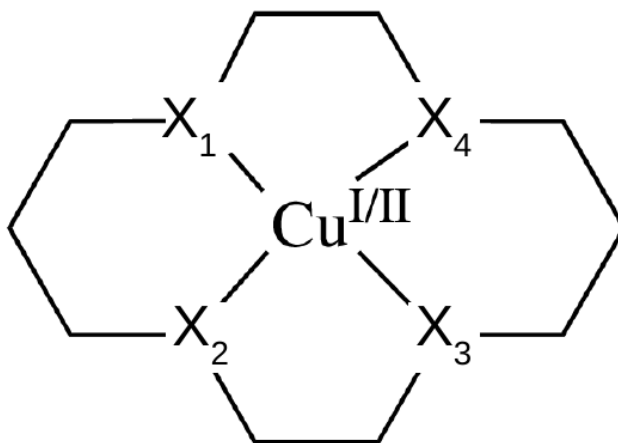


Figure 4.13: Illustrative drawing of labelling system for the critical bonds and angles of the X-ray and computed structures. The bond angles are defined between the $\text{X}_1\text{-Cu-X}_3$ and $\text{X}_2\text{-Cu-X}_4$.

Table 4.8: Comparison of critical bonds (distances in angstroms) and angles (in degrees) of X-ray structures and structures calculated using DFT for $S_4\text{-Cu}^I$ complexes. DFT structures were optimized with cc-pVTZ basis set. Average and standard deviation (STD) are only over all of the DFT functionals.

Structure	CSD code	X	$S_1\text{-Cu}$	$S_2\text{-Cu}$	$S_3\text{-Cu}$	$S_4\text{-Cu}$	$S_1\text{-Cu-S}_3$	$S_2\text{-Cu-S}_4$
HF			2.597	2.565	2.565	2.597	158.4	158.4
SVWN			2.959	2.157	2.289	2.211	173.2	158.7
BP86			3.114	2.223	2.358	2.274	172.3	157.7
B3LYP			2.937	2.288	2.455	2.333	170.6	162.2
CAMB3LYP			3.019	2.257	2.399	2.305	169.9	159.3
B3PW91			2.785	2.281	2.432	2.324	172.3	165.3
M06L			3.013	2.238	2.416	2.290	171.0	160.5
M06			2.923	2.261	2.441	2.304	170.2	162.4
M062X			2.572	2.466	2.512	2.507	165.0	165.6
M06HF			2.547	2.498	2.520	2.517	161.4	163.6
B97D			3.166	2.235	2.414	2.301	170.0	158.6
ω B97xD			3.020	2.254	2.407	2.302	169.5	159.9
PBE1PBE			2.652	2.308	2.446	2.352	172.0	167.7
TPSSTPSS			2.970	2.236	2.377	2.284	173.0	160.9
		AVERAGE	2.898	2.285	2.420	2.331	170.0	161.7
		STD	0.199	0.095	0.061	0.087	3.4	3.1

Table 4.9: Comparison of critical bonds (distances in angstroms) and angles (in degrees) of X-ray structures and structures calculated using DFT for $S_4\text{-Cu}^{II}$ complexes. DFT structures were optimized with cc-pVTZ basis set. Average and standard deviation (STD) are only over all of the DFT functionals.

Structure	CSD code	X	$S_1\text{-Cu}$	$S_2\text{-Cu}$	$S_1\text{-Cu-S}_3$
X-ray	VIMDOK ⁷⁴	$2x(\text{ClO}_4)^-$	2.292(1)	2.312(1)	179.97
	THCDCU ⁷⁵	$2x(\text{ClO}_4)^-$	2.297(1)	2.308(1)	179.97
	AVERAGE		2.288	2.309	179.97
	STD		0.009	0.001	0.00
HF			2.396		180.00
SVWN			2.266		180.00
BP86			2.333		180.00
B3LYP			2.347		180.00
CAMB3LYP			2.320		180.00
B3PW91			2.321		180.00
M06L			2.334		180.00
M06			2.332		180.00
M062X			2.364		180.00
M06HF			2.368		180.00
B97D			2.366		180.00
ω B97xD			2.319		180.00
PBE1PBE			2.314		180.00
TPSSTPSS			2.326		180.00
		AVERAGE	2.331		180.00
		STD	0.027		0.00

Table 4.10: Comparison of critical bonds (distances in angstroms) and angles (in degrees) of X-ray structures and structures calculated using DFT for $N_1S_3-Cu^I$ complexes. DFT structures were optimized with cc-pVTZ basis set. Average and standard deviation (STD) are only over all of the DFT functionals.

Structure	CSD code	X	N_1-Cu	S_2-Cu	S_3-Cu	S_4-Cu	N_1-Cu-S_3	S_2-Cu-S_4
X-ray	SOZZAI ¹⁷	$(ClO_4)^-$	2.061(5)	2.254(2)	2.277(2)	2.240(2)	114.2(2)	137.25(8)
HF			2.210	2.422	2.556	2.443	106.5	160.4
SVWN			2.033	2.209	2.233	2.218	115.1	134.8
BP86			2.115	2.279	2.315	2.287	118.4	136.6
B3LYP			2.142	2.314	2.374	2.325	117.0	141.4
CAMB3LYP			2.111	2.297	2.347	2.309	117.2	140.6
B3PW91			2.114	2.289	2.328	2.299	118.8	138.8
M06L			2.133	2.282	2.363	2.293	113.1	141.6
M06			2.122	2.294	2.368	2.306	113.7	140.9
M062X			2.159	2.389	2.468	2.406	114.2	146.8
M06HF			2.147	2.412	2.471	2.433	113.9	149.9
B97D			2.162	2.293	2.354	2.300	111.1	140.5
ω B97xD			2.122	2.289	2.354	2.300	113.2	142.5
PBE1PBE			2.108	2.285	2.326	2.295	117.8	139.5
TPSSTPSS			2.099	2.277	2.308	2.287	119.4	135.6
		AVERAGE	2.121	2.301	2.354	2.312	115.6	140.7
		STD	0.033	0.051	0.063	0.054	2.6	4.2

Table 4.11: Comparison of critical bonds (distances in angstroms) and angles (in degrees) of X-ray structures and structures calculated using DFT for $N_1S_3-Cu^{II}$ complexes. DFT structures were optimized with cc-pVTZ basis set. Average and standard deviation (STD) are only over all of the DFT functionals.

Structure	CSD code	X	N_1-Cu	S_2-Cu	S_3-Cu	S_4-Cu	N_1-Cu-S_3	S_2-Cu-S_4
HF			2.096	2.441	2.398	2.404	166.6	173.9
SVWN			2.023	2.292	2.246	2.280	169.7	169.9
BP86			2.091	2.358	2.310	2.341	170.7	169.9
B3LYP			2.089	2.375	2.330	2.355	170.2	170.8
CAMB3LYP			2.060	2.348	2.306	2.330	170.3	170.9
B3PW91			2.069	2.348	2.305	2.330	170.9	170.4
M06L			2.081	2.375	2.309	2.344	169.4	171.5
M06			2.056	2.357	2.313	2.341	170.0	170.5
M062X			2.068	2.396	2.360	2.376	169.0	172.1
M06HF			2.061	2.405	2.370	2.379	168.2	172.4
B97D			2.124	2.393	2.330	2.373	168.2	172.2
ω B97xD			2.064	2.350	2.303	2.329	169.8	171.2
PBE1PBE			2.060	2.342	2.300	2.324	170.7	170.7
TPSSTPSS			2.075	2.351	2.307	2.335	171.0	169.7
		AVERAGE	2.071	2.361	2.315	2.341	169.9	170.9
		STD	0.023	0.029	0.030	0.026	0.9	0.9

Table 4.12: Comparison of critical bonds (distances in angstroms) and angles (in degrees) of X-ray structures and structures calculated using DFT for $N_2S_2-Cu^I$ complexes. DFT structures were optimized with cc-pVTZ basis set. Average and standard deviation (STD) are only over all of the DFT functionals.

Structure	CSD code	X	N_1-Cu	N_4-Cu	S_2-Cu	S_3-Cu	N_1-Cu-S_3	N_4-Cu-S_2
HF			2.545	2.531	2.263	2.285	172.7	147.8
SVWN			2.155	2.068	2.296	2.215	167.6	156.1
BP86			2.256	2.156	2.379	2.300	171.3	156.9
B3LYP			2.205	2.252	2.395	2.406	174.3	154.5
CAMB3LYP			2.195	2.193	2.400	2.370	174.3	154.7
B3PW91			2.212	2.189	2.383	2.341	173.2	155.8
M06L			2.147	2.289	2.329	2.400	172.1	152.8
M06			2.199	2.180	2.399	2.364	172.6	156.1
M062X			2.211	2.221	2.495	2.462	176.8	153.1
M06HF			2.204	2.210	2.513	2.477	177.9	152.1
B97D			2.214	2.255	2.370	2.382	172.4	154.1
ω B97xD			2.190	2.242	2.373	2.377	174.1	153.5
PBE1PBE			2.204	2.183	2.380	2.338	173.5	155.4
TPSSTPSS			2.231	2.152	2.372	2.303	171.2	156.7
		AVERAGE	2.202	2.199	2.391	2.364	173.2	154.7
		STD	0.028	0.057	0.058	0.069	2.6	1.6

Table 4.13: Comparison of critical bonds^a (distances in angstroms) and angles (in degrees) of X-ray structures and structures calculated using DFT for $N_2S_2-Cu^{II}$ complexes. DFT structures were optimized with cc-pVTZ basis set.

Structure	CSD code	X	N_1-Cu	S_2-Cu	N_1-Cu-S_3	N_4-Cu-S_2
X-ray	ZUDSOG ⁷⁶	$2x(ClO_4)^-$	2.073(7)	2.344(3)	148.6(2)	178.6(2)
HF			2.071	2.411	173.3	162.7
SVWN			2.012	2.249	167.6	165.4
BP86			2.072	2.319	169.0	167.2
B3LYP			2.068	2.341	170.1	166.9
CAMB3LYP			2.041	2.315	169.7	166.5
B3PW91			2.050	2.315	169.4	167.3
M06L			2.066	2.321	170.1	165.6
M06			2.042	2.317	169.1	166.3
M062X			2.054	2.371	171.0	164.3
M06HF			2.047	2.381	170.9	163.2
B97D			2.101	2.336	170.3	164.6
ω B97xD			2.044	2.314	169.8	165.7
PBE1PBE			2.041	2.310	169.4	166.9
TPSSTPSS			2.059	2.316	169.1	167.6
		AVERAGE	2.053	2.323	169.6	166.0
		STD	0.021	0.032	0.9	1.3

^a Experimental/Calculated bond lengths are averaged for each crystal/calculated structure.

Table 4.14: Comparison of critical bonds (distances in angstroms) and angles (in degrees) of X-ray structures and structures calculated using DFT for NSSN-Cu^I complexes. DFT structures were optimized with cc-pVTZ basis set. Average and standard deviation (STD) are only over all of the DFT functionals.

Structure	CSD code	X	N ₁ -Cu	N ₂ -Cu	S ₃ -Cu	S ₄ -Cu	N ₁ -Cu-S ₃	N ₂ -Cu-S ₄
HF			2.140	2.095	2.306	2.376	144.9	119.9
SVWN			2.038	2.018	2.201	2.241	138.3	119.8
BP86			2.118	2.092	2.263	2.309	140.1	122.1
B3LYP			2.144	2.105	2.305	2.371	145.1	120.5
CAMB3LYP			2.114	2.082	2.292	2.351	144.4	120.3
B3PW91			2.116	2.092	2.280	2.323	142.3	122.0
M06L			2.146	2.083	2.259	2.376	147.6	114.8
M06			2.133	2.067	2.284	2.385	147.9	114.8
M062X			2.163	2.118	2.389	2.492	153.7	113.8
M06HF			2.149	2.138	2.430	2.489	155.6	114.2
B97D			2.168	2.112	2.268	2.373	146.7	114.9
ω B97xD			2.121	2.083	2.283	2.356	145.8	117.2
PBE1PBE			2.110	2.086	2.278	2.322	143.0	121.3
TPSSTPSS			2.104	2.083	2.262	2.304	139.3	122.5
		AVERAGE	2.125	2.089	2.292	2.361	145.4	118.3
		STD	0.033	0.029	0.058	0.070	5.1	3.4

Table 4.15: Comparison of critical bonds (distances in angstroms) and angles (in degrees) of X-ray structures and structures calculated using DFT for NSSN-Cu^{II} complexes. DFT structures were optimized with cc-pVTZ basis set. Average and standard deviation (STD) are only over all of the DFT functionals.

Structure	CSD code	X	N ₁ -Cu	S ₃ -Cu	N ₁ -Cu-S ₃
HF			2.054	2.385 (2.383)	148.4 (132.2)
SVWN			2.023	2.268	177.3
BP86			2.081	2.332	177.7
B3LYP			2.078	2.347	177.5
CAMB3LYP			2.053	2.321	177.4
B3PW91			2.061	2.322	177.5
M06L			2.073	2.332	177.5
M06			2.054	2.331	177.1
M062X			2.065	2.372	177.1
M06HF			2.059	2.381	176.9
B97D			2.110	2.351	178.3
ω B97xD			2.057	2.319	177.8
PBE1PBE			2.053	2.316	177.5
TPSSTPSS			2.069	2.327	177.4
		AVERAGE	2.064	2.332	177.5
		STD	0.020	0.028	0.3

Table 4.16: Comparison of critical bonds (distances in angstroms) and angles (in degrees) of X-ray structures and structures calculated using DFT for $N_3S_1-Cu^I$ complexes. DFT structures were optimized with cc-pVTZ basis set. Average and standard deviation (STD) are only over all of the DFT functionals.

Structure	CSD code	X	N_1-Cu	N_2-Cu	N_4-Cu	S_3-Cu	N_2-Cu-N_4	N_1-Cu-S_3
HF			2.149	2.146	2.080	2.248	123.7	149.2
SVWN			2.059	2.053	2.019	2.183	123.3	144.7
BP86			2.149	2.146	2.080	2.234	123.5	149.4
B3LYP			2.183	2.179	2.100	2.280	121.4	154.7
CAMB3LYP			2.149	2.143	2.084	2.274	122.3	152.7
B3PW91			2.147	2.144	2.086	2.256	123.5	151.3
M06L			2.178	2.170	2.082	2.234	117.6	155.0
M06			2.162	2.150	2.077	2.270	119.9	154.2
M062X			2.187	2.172	2.145	2.393	121.1	157.3
M06HF			2.174	2.163	2.160	2.434	121.8	158.1
B97D			2.181	2.187	2.108	2.246	116.4	156.3
ω B97xD			2.178	2.165	2.079	2.258	118.3	156.0
PBE1PBE			2.140	2.137	2.083	2.256	123.0	151.6
TPSSTPSS			2.132	2.127	2.076	2.235	124.6	147.6
		AVERAGE	2.155	2.149	2.091	2.273	121.3	153.0
		STD	0.034	0.034	0.034	0.067	2.6	4.0

Table 4.17: Comparison of critical bonds (distances in angstroms) and angles (in degrees) of X-ray structures and structures calculated using DFT for $N_3S_1-Cu^{II}$ complexes. DFT structures were optimized with cc-pVTZ basis set. Average and standard deviation (STD) are only over all of the DFT functionals.

Structure	CSD code	X	N_1-Cu	N_2-Cu	N_4-Cu	S_3-Cu	N_2-Cu-N_4	N_1-Cu-S_3
HF			2.047	2.055	2.050	2.299	145.9	149.0
SVWN			2.026	2.006	2.020	2.250	173.2	172.1
BP86			2.083	2.059	2.080	2.312	173.4	172.7
B3LYP			2.076	2.057	2.077	2.332	173.4	173.2
CAMB3LYP			2.050	2.034	2.053	2.308	173.5	173.3
B3PW91			2.060	2.041	2.061	2.308	173.7	173.1
M06L			2.072	2.057	2.071	2.315	173.5	173.2
M06			2.050	2.038	2.048	2.319	173.5	172.8
M062X			2.064	2.053	2.068	2.365	173.6	173.7
M06HF			2.063	2.048	2.069	2.374	173.4	173.9
B97D			2.104	2.080	2.101	2.326	172.6	173.3
ω B97xD			2.052	2.037	2.056	2.305	173.2	173.0
PBE1PBE			2.051	2.034	2.053	2.304	173.7	173.2
TPSSTPSS			2.070	2.051	2.068	2.310	173.6	172.7
		AVERAGE	2.063	2.046	2.063	2.318	173.4	173.1
		STD	0.018	0.017	0.019	0.030	0.3	0.5

Table 4.18: Comparison of critical bonds^a (distances in angstroms) and angles (in degrees) of X-ray structures and structures calculated using DFT for N₄-Cu^I complexes. DFT structures were optimized with cc-pVTZ basis set.

Structure	CSD code	X	N ₁ -Cu	N ₂ -Cu	N ₁ -Cu-N ₃	N ₂ -Cu-N ₄
HF			2.227	2.180	115.9	174.0
SVWN			2.070	1.993	123.8	152.7
BP86			2.171	2.047	122.3	159.3
B3LYP			2.198	2.070	120.8	163.1
CAMB3LYP			2.161	2.062	122.3	160.5
B3PW91			2.157	2.062	123.3	159.4
M06L			2.218	2.040	114.7	167.6
M06			2.194	2.038	116.9	165.6
M062X			2.194	2.129	119.7	165.4
M06HF			2.172	2.163	121.9	164.6
B97D			2.204	2.063	116.3	166.6
ω B97xD			2.186	2.057	118.7	164.2
PBE1PBE			2.148	2.060	122.8	159.5
TPSSTPSS			2.150	2.041	122.9	157.2
	AVERAGE		2.171	2.063	120.5	162.0
	STD		0.038	0.042	3.0	4.3

^a Experimental/Calculated bond lengths are averaged for each crystal/calculated structure.

Table 4.19: Comparison of critical bonds^a (distances in angstroms) and angles (in degrees) of X-ray structures and structures calculated using DFT for N₄-Cu^{II} complexes. DFT structures were optimized with cc-pVTZ basis set.

Structure	CSD code	X	N ₁ -Cu	N ₁ -Cu-N ₃
X-ray	HAFSUC ⁷⁷	2x(BH ₄) ⁻¹	2.021	179.97
	IPEYUX ⁷⁸	2x(C ₇ H ₅ O ₂) ⁻¹ , 2xH ₂ O	1.969	180.00
	IPEZAE ⁷⁸	2x(C ₁₁ H ₁₃ O ₂) ⁻¹ , 2xH ₂ O	2.011	180.00
	AVERAGE		2.000	179.99
	STD		0.028	0.01
HF			2.071	179.99
SVWN			2.009	180.00
BP86			2.062	180.00
B3LYP			2.060	180.00
CAMB3LYP			2.038	180.00
B3PW91			2.044	180.00
M06L			2.055	180.00
M06			2.036	180.00
M062X			2.057	180.00
M06HF			2.059	180.00
B97D			2.077	180.00
ω B97xD			2.040	180.00
PBE1PBE			2.037	180.00
TPSSTPSS			2.054	180.00
	AVERAGE		2.048	180.00
	STD		0.017	0.00

^a Experimental/Calculated bond lengths are averaged for each crystal/calculated structure.

References

- [1] Wardman, P. *J. Phys. Chem. Ref. Data* **1989**, *18*(4), 1637–1755.
- [2] Winget, P.; Weber, E. J.; Cramer, C. J.; Truhlar, D. G. *Phys. Chem. Chem. Phys.* **2000**, *2*(6), 1231–1239.
- [3] Méndez-Hernández, D. D.; Tarakeshwar, P.; Gust, D.; Moore, T. a.; Moore, A. L.; Mujica, V. *J. Mol. Model.* **2013**, *19*(7), 2845–2848.
- [4] Namazian, M.; Lin, C. Y.; Coote, M. L. *J. Chem. Theory Comput.* **2010**, *6*(9), 2721–2725.
- [5] Baik, M.-H.; Friesner, R. A. *J. Phys. Chem. A* **2002**, *106*(32), 7407–7412.
- [6] Cañon Mancisidor, W.; Spodine, E.; Venegas-Yazigi, D.; Rojas, D.; Manzur, J.; Alvarez, S. *Inorg. Chem.* **2008**, *47*(9), 3687–3692.
- [7] Arca, M.; Azimi, G.; Demartin, F.; Devillanova, F. a.; Escriche, L.; Garau, A.; Isaia, F.; Kivekas, R.; Lippolis, V.; Muns, V.; Perra, A.; Shamsipur, M.; Sportelli, L.; Yari, A. *Inorg. Chim. Acta.* **2005**, *358*(7), 2403–2412.
- [8] Marenich, A. V.; Ho, J.; Coote, M. L.; Cramer, C. J.; Truhlar, D. G. *Phys. Chem. Chem. Phys.* **2014**, *16*(29), 15068–106.
- [9] Matsui, T.; Kitagawa, Y.; Shigeta, Y.; Okumura, M. *J. Chem. Theory Comput.* **2013**, *9*(7), 2974–2980.
- [10] Festa, R. A.; Thiele, D. J. *Curr. Biol.* **2011**, *21*(21), R877–R883.
- [11] Solomon, E. I.; Heppner, D. E.; Johnston, E. M.; Ginsbach, J. W.; Cirera, J.; Qayyum, M.; Kieber-Emmons, M. T.; Kjaergaard, C. H.; Hadt, R. G.; Tian, L. *Chem. Rev.* **2014**, *114*(7), 3659–3853.
- [12] Lutsenko, S. *Curr. Opin. Chem. Biol.* **2010**, *14*(2), 211–217.
- [13] Leary, S. C.; Cobine, P. A.; Nishimura, T.; Verdijk, R. M.; de Krijger, R.; de Co, R.; Tarnopolsky, M. A.; Winge, D. R.; Shoubridge, E. A. *Mol. Biol. Cell* **2013**, *24*(6), 683–691.
- [14] Karlin, K. D.; Hayes, J. C.; Juen, S.; Hutchinson, J. P.; Zubieta, J. *Inorg. Chem.* **1982**, *21*(11), 4106–4108.
- [15] Navon, N.; Golub, G.; Cohen, H.; Paoletti, P.; Valtancoli, B.; Bencini, A.; Meyerstein, D. *Inorg. Chem.* **1999**, *38*(15), 3484–3488.

- [16] Taylor, M. K.; Reglinski, J.; Berlouis, L. E.; Kennedy, A. R. *Inorg. Chim. Acta* **2006**, *359*(8), 2455–2464.
- [17] Bernardo, M. M.; Heeg, M. J.; Schroeder, R. R.; Ochrymowycz, L.; Rorabacher, D. *Inorg. Chem.* **1992**, *31*(2), 191–198.
- [18] Kanters, R. P.; Ru, Y.; Addison, A. W. *Inorg. Chim. Acta* **1992**, *196*(1), 97–103.
- [19] Davis, A. P.; Fry, A. J. *J. Phys. Chem. A* **2010**, *114*(46), 12299–12304.
- [20] Isse, A. A.; Gennaro, A. *J. Phys. Chem. B* **2010**, *114*(23), 7894–7899.
- [21] Donald, W. A.; Leib, R. D.; O'Brien, J. T.; Williams, E. R. *Chem. Eur. J.* **2009**, *15*(24), 5926–5934.
- [22] Rappoport, D.; Furche, F. *J. Chem. Phys.* **2010**, *133*(13), 134105.
- [23] Kendall, R. A.; Dunning, T. H.; Harrison, R. J. *J. Chem. Phys.* **1992**, *96*(9), 6796–6806.
- [24] Davidson, E. R. *Chem. Phys. Lett.* **1996**, *260*(3), 514 – 518.
- [25] Gaussian 09 Revision A.02. Frisch, M. J.; Trucks, G. W.; Schlegel, H. B.; Scuseria, G. E.; Robb, M. A.; Cheeseman, J. R.; Scalmani, G.; Barone, V.; Mennucci, B.; Petersson, G. A.; Nakatsuji, H.; Caricato, M.; Li, X.; Hratchian, H. P.; Izmaylov, A. F.; Bloino, J.; Zheng, G.; Sonnenberg, J. L.; Hada, M.; Ehara, M.; Toyota, K.; Fukuda, R.; Hasegawa, J.; Ishida, M.; Nakajima, T.; Honda, Y.; Kitao, O.; Nakai, H.; Vreven, T.; Montgomery, Jr., J. A.; Peralta, J. E.; Ogliaro, F.; Bearpark, M.; Heyd, J. J.; Brothers, E.; Kudin, K. N.; Staroverov, V. N.; Kobayashi, R.; Normand, J.; Raghavachari, K.; Rendell, A.; Burant, J. C.; Iyengar, S. S.; Tomasi, J.; Cossi, M.; Rega, N.; Millam, J. M.; Klene, M.; Knox, J. E.; Cross, J. B.; Bakken, V.; Adamo, C.; Jaramillo, J.; Gomperts, R.; Stratmann, R. E.; Yazyev, O.; Austin, A. J.; Cammi, R.; Pomelli, C.; Ochterski, J. W.; Martin, R. L.; Morokuma, K.; Zakrzewski, V. G.; Voth, G. A.; Salvador, P.; Dannenberg, J. J.; Dapprich, S.; Daniels, A. D.; Farkas, O.; Foresman, J. B.; Ortiz, J. V.; Cioslowski, J.; Fox, D. J.
- [26] Miertuš, S.; Scrocco, E.; Tomasi, J. *Chem. Phys.* **1981**, *55*(1), 117–129.
- [27] Cancès, E.; Mennucci, B.; Tomasi, J. *J. Chem. Phys.* **1997**, *107*(8), 3032–3041.
- [28] Mennucci, B.; Tomasi, J. *J. Chem. Phys.* **1997**, *106*(12), 5151–5158.
- [29] Mennucci, B.; Cancès, E.; Tomasi, J. *J. Phys. Chem. B* **1997**, *101*(49), 10506–10517.

- [30] Tomasi, J.; Mennucci, B.; Cammi, R. *Chem. Rev.* **2005**, *105*(8), 2999–3094.
- [31] Marenich, A. V.; Cramer, C. J.; Truhlar, D. G. *J. Phys. Chem. B* **2009**, *113*(18), 6378–6396.
- [32] Hohenberg, P.; Kohn, W. *Phys. Rev.* **1964**, *136*, B864–B871.
- [33] Kohn, W.; Sham, L. J. *Phys. Rev.* **1965**, *140*, A1133–A1138.
- [34] The self-consistent field for molecular and solids, quantum theory of molecular and solids, vol. 4. Slater, J. **1974**.
- [35] Vosko, S.; Wilk, L.; Nusair, M. *Can. J. Phys.* **1980**, *58*(8), 1200–1211.
- [36] Becke, A. D. *Phys. Rev. A* **1988**, *38*(6), 3098.
- [37] Perdew, J. P. *Phys. Rev. B* **1986**, *33*(12), 8822.
- [38] Becke, A. D. *J. Chem. Phys.* **1993**, *98*(7), 5648–5652.
- [39] Lee, C.; Yang, W.; Parr, R. G. *Phys. Rev. B* **1988**, *37*, 785–789.
- [40] Stephens, P.; Devlin, F.; Chabalowski, C.; Frisch, M. J. *J. Phys. Chem.* **1994**, *98*(45), 11623–11627.
- [41] Perdew, J. P.; Chevary, J.; Vosko, S.; Jackson, K. A.; Pederson, M. R.; Singh, D.; Fiolhais, C. *Phys. Rev. B* **1992**, *46*(11), 6671.
- [42] Perdew, J. P.; Chevary, J.; Vosko, S.; Jackson, K. A.; Pederson, M. R.; Singh, D.; Fiolhais, C. *Phys. Rev. B* **1993**, *48*(7), 4978.
- [43] Perdew, J. P.; Burke, K.; Wang, Y. *Physical Review B* **1996**, *54*(23), 16533.
- [44] Electronic density function theory: Recent progress and new directions, eds. jf dobson, g. vignale, mp das. Burke, K.; Perdew, J.; Wang, Y. **1998**.
- [45] Yanai, T.; Tew, D. P.; Handy, N. C. *Chem. Phys. Lett.* **2004**, *393*(1–3), 51–57.
- [46] Grimme, S. *J. Comput. Chem.* **2006**, *27*(15), 1787–1799.
- [47] Chai, J.-D.; Head-Gordon, M. *Phys. Chem. Chem. Phys.* **2008**, *10*(44), 6615–6620.
- [48] Tao, J.; Perdew, J. P.; Staroverov, V. N.; Scuseria, G. E. *Phys. Rev. Lett.* **2003**, *91*(14), 146401.
- [49] Perdew, J. P.; Burke, K.; Ernzerhof, M. *Phys. Rev. Lett.* **1996**, *77*(18), 3865.
- [50] Perdew, J. P.; Burke, K.; Ernzerhof, M. *Phys. Rev. Lett.* **1997**, *78*, 1396–1396.

- [51] Adamo, C.; Barone, V. *J. Chem. Phys.* **1999**, *110*(13), 6158–6170.
- [52] Zhao, Y.; Truhlar, D. G. *J. Chem. Phys.* **2006**, *125*(19), 194101.
- [53] Zhao, Y.; Truhlar, D. G. *Theor. Chem. Acc.* **2008**, *120*(1-3), 215–241.
- [54] Zhao, Y.; Truhlar, D. G. *J. Phys. Chem. A* **2006**, *110*(49), 13126–13130.
- [55] Grimme, S.; Ehrlich, S.; Goerigk, L. *J. Comput. Chem.* **2011**, *32*(7), 1456–1465.
- [56] Fabbrizzi, L.; Lari, A.; Poggi, A.; Seghi, B. *Inorg. Chem.* **1982**, *21*(5), 2083–2085.
- [57] Addison, A. W. *Inorg. Chim. Acta* **1989**, *162*(2), 217–220.
- [58] Lever, A. B. P. *Inorg. Chem.* **1990**, *29*(6), 1271–1285.
- [59] Lee, T. J.; Rice, J.; Scuseria, G. E.; Schaefer, Henry F., I. *Theor. Chim. Acta* **1989**, *75*(2), 81–98.
- [60] Lee, T. J.; Taylor, P. R. *Int. J. of Quantum Chem.* **1989**, *36*(S23), 199–207.
- [61] Jayatilaka, D.; Lee, T. J. *J. Chem. Phys.* **1993**, *98*(12), 9734–9747.
- [62] Lee, T. J.; Scuseria, G. E. In *Quantum Mechanical Electronic Structure Calculations with Chemical Accuracy*; Langhoff, S. R., Ed., Vol. 13 of *Understanding Chemical Reactivity*; Springer Netherlands, 1995; pages 47–108.
- [63] Seeger, R.; Pople, J. A. *J. Chem. Phys.* **1977**, *66*(7), 3045–3050.
- [64] Schlegel, H.; McDouall, J. In *NATO ASI Series*; Ögretir, C., Csizmadia, I., Eds., Vol. 330; Springer Netherlands, 1991; pages 167–185.
- [65] Bauernschmitt, R.; Ahlrichs, R. *J. Chem. Phys.* **1996**, *104*(22), 9047–9052.
- [66] Jiang, W.; DeYonker, N. J.; Wilson, A. K. *J. Chem. Theory Comput.* **2012**, *8*(2), 460–468.
- [67] Niu, S.; Huang, D.-L.; Dau, P. D.; Liu, H.-T.; Wang, L.-S.; Ichiye, T. *JCTC* **2014**, *10*(3), 1283–1291.
- [68] Dunning, T. H. *J. Chem. Phys.* **1989**, *90*(2), 1007–1023.
- [69] Woon, D. E.; Dunning, T. H. *J. Chem. Phys.* **1993**, *98*(2), 1358–1371.
- [70] Peterson, K. A.; Woon, D. E.; Dunning, T. H. *J. Chem. Phys.* **1994**, *100*(10), 7410–7415.
- [71] Feller, D. *J. Comput. Chem.* **1996**, *17*(13), 1571–1586.

- [72] Schuchardt, K. L.; Didier, B. T.; Elsethagen, T.; Sun, L.; Gurumoorthi, V.; Chase, J.; Li, J.; Windus, T. L. *J. Chem. Inf. Model.* **2007**, *47*(3), 1045–1052.
- [73] Weigend, F.; Ahlrichs, R. *Phys. Chem. Chem. Phys.* **2005**, *7*(18), 3297–3305.
- [74] Desper, J. M.; Gellman, S. H. *J. Am. Chem. Soc.* **1991**, *113*(2), 704–706.
- [75] Glick, M. D.; Gavel, D. P.; Diaddario, L. L.; Rorabacher, D. B. *Inorg. Chem.* **1976**, *15*(5), 1190–1193.
- [76] Hörmann, E.; Riesen, P. C.; Neuburger, M.; Zehnder, M.; Kaden, T. A. *Helv. Chim. Acta.* **1996**, *79*(1), 235–243.
- [77] A.S.Antsyshkina.; M.A.Porai-Koshits.; V.D.Makhaev.; A.P.Borisov.; N.S.Kedrova.; N.N.Mal'tseva. *Koord.Khim.(Russ.)(Coord.Chem.)* **1992**, *18*, 474–480.
- [78] Lindoy, L. F.; Mahinay, M. S.; Skelton, B. W.; White, A. H. *J.Coord.Chem.* **2003**, *56*(14), 1203–1213.

Chapter 5

Development of general low-cost parameterisation scheme for MD simulations of conjugated materials

5.1 Introduction

The following chapter presents a step-by-step development of general scheme that can be applied to obtain classical molecular dynamics force-field parameters of conjugated polymers. Critical steps of such parametrization are identified and addressed together with the choice of appropriate computational methodology for calculations of, for example, accurate inter-monomer dihedral potentials and partial charges. Further, a two-step protocol of geometry optimisation and single-point energy calculations using DFT method was tested for production of accurate dihedral potentials comparable with high level theory calculations. In addition, the effects of varying the conjugated backbone length and alkyl side-chain lengths on the dihedral profiles and partial charges distributions were examined in order to determine the existence of converged lengths above which universality is observed in the force-field parameter sets. This could potentially allow extension of simulations to layers of conjugated polymers with relatively cheap parametrization step required. This study was done in collaboration with Jack Wildman and a group of Ian Galbraith and was recently published in the *Journal of Chemical Theory and Computation*.¹

Semiconducting conjugated polymer materials have a great potential in organic-based opto-electronics with several advantages over, for example, inorganic semiconductors including light-weight, flexibility, low toxicity and inexpensive fabrication for applications such as photovoltaic cells and light-emitting diodes.²⁻⁴ However,

there are some challenges for viable devices construction when using organic polymers such as ability to achieve sufficient power conversion efficiencies and durability. One of the key reasons behind this is the important role of material morphology and conformation within such materials.⁵

Detailed understanding of conjugated polymers morphology and conformation allows new modifications of existing materials as well as design of new materials with the desirable properties. For example, this can lead to more control over solubility, allowing solution processing and low bulk modulus accounting for flexibility². However, at the same time the polymeric nature of individual molecules and the statistical nature of their mixing may lead to the existence of phenomena such as deep-tail trap-states which can inhibit the conductivity.⁶ This is primarily due to the delicate physics of both intra-molecular conjugation - its sensitivity to local distortions along the backbone of a polymer⁷ and the effect this has on the resulting optical absorption and emission dynamics⁷⁻⁹ - and the inter-molecular excitation transfer dynamics - the interplay of alignment and separation of conjugated segments or 'chromophores' and their spectral overlaps with the Förster-type¹⁰ transfer of excitons and polarons.^{11,12}

Molecular Dynamics (MD) is a suitable method to address the questions of the interplay of the dynamics and statistical mechanics of conjugated polymer-based materials. It helps to understand and predict macroscopic properties of these systems based on the detailed knowledge on atomic scale. In MD simulations, the classical dynamics of molecules are generated using force-fields which describe the averaged effect of the molecular electrons on the covalent bonding and the Van der Waals type forces. Treating the system classically as well as using the predefined force-fields greatly reduces the computational expense of analysing questions of conformational properties and allows for the simulations of reasonably long chains.¹³⁻¹⁶

It is important that the force-fields used are able to reproduce experimental behaviour with sufficiently high accuracy. Historically, MD force-fields were mainly designed for applications in biochemical simulations of, for example, large proteins and DNA/RNA molecules. There exists a number of available force fields¹⁷⁻²⁵ which are parameterised in order to yield accurate results for the specific task. These force-fields usually contain many parameters transferable to the conjugated polymer systems, however, there are certain aspects that require a careful re-parameterisation due to the conjugated nature of the molecular physics involved. The key challenge is to utilise as many transferable parameters as is possible while identifying critical parameters that require further attention and re-parameterisation.

In the case of organic conjugated polymers one of the most important terms to be

considered is the energetic profile of the dihedral between monomers in a conjugated system. The excited-state landscape of conjugated molecules is governed by the dihedral angles²⁶; therefore accurate modelling of the dihedral profiles and energy barriers between conformers is of critical importance when studying the optical properties of polymer materials as these are crucially dependent on the torsional profiles.

Another key aspect to consider is how interatomic electrostatic interactions, which arise due to local deviations in electronic charge densities, are described. The most common implementation in MD force-fields is in a form of atom centred 'partial charges'. Derivation of these charges usually requires fitting atomic charges to the calculated electrostatic potentials of the molecule. While there exist a number of such fitting schemes²⁷⁻³⁰, the RESP scheme³¹ is generally considered to be one of the more robust and accurate procedures for this task.

There are already some methodological approaches^{15,32,33} available for generating MD parameters for simulations of conjugated polymers. However, there is often a lack of systematic parameter development and benchmarking of given methodology and many of these sources provide conflicting viewpoints on the appropriate levels of quantum chemical theory required. This leads to a large degree of ambiguity in the accuracy of a given method as well as whether or not a described computational scheme could be replaced by a significantly less computationally expensive one. Given the wide range of organic molecules which are of potential interest for applications in organic opto-electronics the computational cost and complexity of obtaining parameters is yet another aspect one needs to consider when aiming to simulate these systems using MD.

Additional point that has, to date, been neglected is how sensitive a given parameterisation scheme is to variation in length of molecules and lengths of their associated alkyl side chains. A typical solution-cast mixture of conjugated polymers requires the attachment of branched alkyl side chains to provide solubility. It has also been shown that these side chains and their interference with the intrinsic molecular motion of the conjugated backbone of the molecule has a key role in effects such as the inhibition of excitonic diffusion⁶ as well as the emergence of exotic bulk behaviour such as the well-studied β -phase of poly-fluorene³⁴.

For the above reasons, the work presented here establishes a systematic approach to the force-field parameterisation. Further, applicability of a given set of parameters for molecules of varying length and varying length of side chain is investigated and cases in which the universality of given parameters to these variations is broken are discussed. This results in a parameterisation protocol which conforms sufficiently

to both established benchmarks of accuracy; avoids unnecessarily computationally-intensive calculation methods; and in theory could be applied to any type of conjugated system with alkyl side chains.

5.2 Generating Molecular Dynamics Parameters

As described in the section 2.3 a set of force-field parameters typically contains parameters of five types: three describing the energetics due to covalent bonding between atoms and two describing non-covalent interactions. The covalent terms account for the bond-stretching, the angle bending and changes in the dihedral angles between four atoms. These are modelled by functions ranging from quadratic (particularly for two-atom vibrations) to Fourier-based functions for the angular types. Non-covalent interactions are of the form of Lennard-Jones and Coulomb potentials which account for London dispersion, Pauli repulsion and, in the case of the Coulomb potentials, electrostatic interactions between local variations in electronic density.

The OPLS^{18–24} force-field (as implemented in Gromacs 4.6.5^{35,36}) was chosen as a starting point for the parameterisation due to the availability of parameters for many atoms in a multitude of different molecular frameworks as well as its use in previous works parameterising conjugated polymers.^{15,33,37}

Thiophene and fluorene oligomers with and without alkyl side-chains were chosen as model systems (see Figure 5.1). One of the reasons behind this choice is that these molecules are experimentally^{34,38–40} well-characterised conjugated systems. The second reason is that there are already some parameters available for these molecules within the OPLS force-field, which greatly simplifies the task at hand.

In order to parameterise a given molecule, the first step is to build on the appropriate parameters found within OPLS for a monomer. In the case of thiophene and fluorene the OPLS parameters for monomers were already available. This leads to need to determine only the bonds, angles, and dihedrals associated with the linking bond between two connected units of thiophene/fluorene (hereafter referred to as a 2mer and, for molecules with x connected units, as an x mer) and partial charges. This is illustrated in Figure 5.2.

An initial expectation is that bond-stretching and angle-bending within the monomers are reliably parameterised by the existing OPLS force-field terms thus this leaves the inter-monomer dihedral profile as the primary unknown from the covalent terms. In the case of non-bonding interactions, existing Lennard-Jones terms are used without

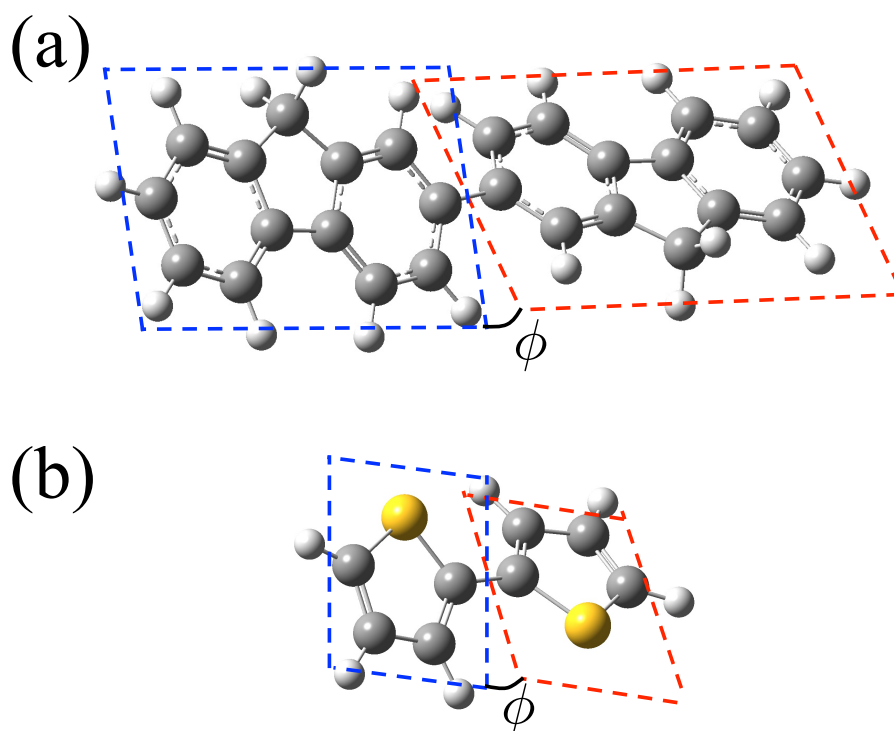


Figure 5.1: Schematic of (a) fluorene and (b) thiophene 2mers with the associated dihedral angle, ϕ , highlighted in each case.

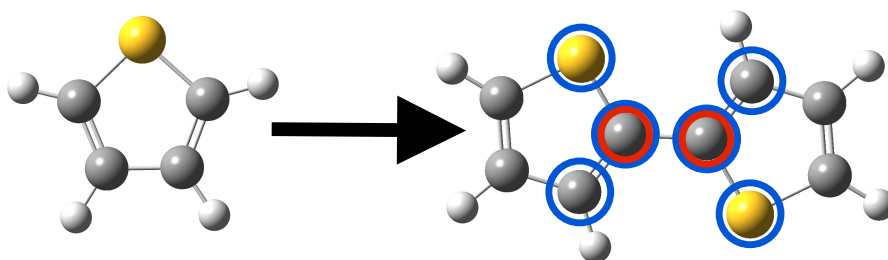


Figure 5.2: Schematic highlighting the required new parameters in going from a parameter set for thiophene to di-thiophene. The missing force-field parameters are the bond-stretching term between the two carbons circled in red; angle-bending term between each combination of three blue-circled atoms (two from one unit and one from the other); and the dihedral angle term for each combination of four blue-circled atoms (two from one unit and two from the other).

any modifications, and the main focus is on partial charge generation and validation.

In order to generate sufficiently accurate dihedral potentials at low computational expense, a two-step Scan - Single Point (SP) approach^{33,41} was adopted. The main idea behind this approach is to use a computationally inexpensive lower level of theory such as DFT to perform geometry optimisations over the span of a dihedral rotation (Scan) and subsequently refine these results with a higher level of theory, for example, local methods (MP2, CCSD, CCSD(T)) or DFT with a larger basis set to obtain more accurate SP energies.

In the first step, the Scan, involves determining, by relaxed scan geometry optimisation, a series of molecular geometries for different values of dihedral angle between the units of 2mer. Geometry optimisation can become computationally very expensive task, especially when large molecules are considered. However, it is possible to obtain reliable geometries in the case of many conjugated molecules using moderate level of theory, such as DFT, as previously shown by DuBay *el al.*³³ and Bhatta *el al.*³⁷

While it is possible to obtain accurate geometries in the Scan step, as will be shown, the energies obtained from this step are often quite inaccurate. This is why the second step, the SP step, using higher levels of theory in order to obtain accurate energetic profiles is necessary.

Partial charges are generated using the RESP³¹ scheme with input electronic densities calculated at the above SP step. Further, effects of varying backbone length on the net charges of the internal monomer units were studied in order to investigate a possibility to determine a length at which the net charges go to zero and thus to obtain converged charge distributions which are generalisable to any length of molecule. Furthermore, similar possibility to generalise charges with respect to variations of side-chains was examined.

Once the appropriate partial charges have been determined, these are directly implemented into the force-field. The dihedral profile, on the other hand, must be implemented by means of a 'subtraction' method so as to ensure that energetic terms already described by the force-field and partial charges are not double-counted. This involves performing a dihedral scan using the force-field parameters (without the required dihedral) in order to obtain the contribution already accounted for by the force-field and subtracting this from the calculated DFT profile. The resulting 'subtracted' profile is then implemented into the force-field.

Throughout this work the 'polymer convention' for dihedral angle labelling is used. This convention casts the *trans* conformation at 0° and the *cis* conformation at 180°. Dihedral potentials taken from other works have been transformed so as to fit with this convention.

5.3 Determination of the Appropriate Methodology.

The most important terms identified in the organic conjugated systems parametrization are the torsional (dihedral) profiles between monomers and the partial charges. In order to obtain accurate torsional potentials it is necessary to fit the torsional profiles to potentials obtained from a high level *ab initio* calculation.

Some of the methodology for computational studies of conjugated systems in the literature involved using the second-order Møller-Plesset perturbation theory (MP2)^{15,41-44}, local MP2 (LMP2)³³, coupled cluster theory (CCSD(T))^{41,42} and DFT^{41,42,44-47}. The following section examines performance of some of these methods as well as the possibility to obtain highly accurate torsional profiles using moderate levels of theory.

In the first part, performance of wave function based methods, such as MP2, CCSD(T) and their local variations such as LMP2 and LCCSD(T), were examined for the SP step of dihedral calculations. This is followed by testing various DFT functionals such as SVWN, BP86, B3LYP, CAM-B3LYP, ω B97X, ω B97X-D and the family of M06 functionals (M06L, M06, M062X, M06HF). These calculations were mainly performed for thiophene dihedral profiles and the results were also compared to the CCSD(T)/CBS result of Bloom *et al.*⁴¹.

Once, the appropriate functional was determined the effects of basis set choice on the Scan step of the dihedral profile calculation were examined. Further, the effects of including dispersion correction GD3BJ^{48,49} were also investigated for thiophene and fluorene 2mers with no-, methyl- and ethyl-side-chains.

5.3.1 Technical Details

Following procedures were employed when performing calculations presented in this section, geometries for both thiophene and fluorene dimer were generated using relaxed scan geometry optimization at the B3LYP/6-31+G(d,p) level for structures with dihedral angle ranging from 0° (*trans*) to 180° (*cis*) with 10° step. Generated geometries were used for a Single-Point energy (SP) calculations using cc-pVTZ as basis set. All DFT calculations presented were performed in Gaussian 09 (Revision D.01)⁵⁰ and all other calculations, such as canonical MP2, CCSD(T) and their local variants, were performed in Molpro 2012^{51,52}. The CCSD(T)/CBS result of Bloom *et al.*⁴¹, which was used as a benchmark profile for thiophene dihedral, uses

geometries obtained at the MP2/*aug-cc-pVTZ* level. Further, the possibility of using density fitting to approximate the integrals, was tested as a potential option to decrease the computational cost of some of the calculations.

Two settings were modified in local methods (e.g. LCCSD(T) and LMP2) in order to control the size of local domains, mainly the threshold for selecting atoms contributing to orbital domains utilising the Boughton - Pulay algorithm (THRBP)^{53,54} and MERGEDOM directive (MDom).

Domains are geometry dependent as a result of the restriction of the virtual space in local calculations and this may result in discontinuities on the potential energy surface. For this reason, the MERGEDOM directive was employed to generate augmented (merged) domains, that are appropriate for a whole range of geometries in the scan. Further, the THRBP criterion is somewhat basis set dependent with the default selection criterion value of 0.98, which should work usually well for small basis sets like cc-pVDZ. For larger basis sets like cc-pVTZ and cc-pVQZ a slightly larger values of 0.985 and 0.990, respectively, are recommended to ensure that enough atoms are included in each domain. For illustration, in the case of THRBP=1.0 this includes all atoms into each orbital domain, i.e. leads to full domains, and if no pairs are neglected, this should theoretically yield the canonical MP2 energy.

The following calculations were performed in this section in order to address different questions:

- MP2 and density-fitted MP2 (DF-MP2) to see the effect of density fitting on dihedral profiles.
- Density-fitted local MP2 (DF-LMP2) calculations were performed in order to assess the performance of DF-LMP2, specifically different choices of domain size. These results were then compared to canonical DF-MP2. Various mergedom (MDom) and THRBP values were tested; such as MDom=0, 1, 2, 3 and THRBP=0.980, 0.985, 0.990, 0.995.
- Results of DF-LCCSD(T) calculations with the optimal choice of THRBP and MDom were compared with the canonical CCSD(T) calculations.
- Various DFT functionals such as: SVWN, BP86, B3LYP, CAM-B3LYP, ω B97X, ω B97X-D and the family of M06 functionals (M06L, M06, M062X, M06HF) were tested and compared against CCSD(T)/CBS.
- Performance of CAM-B3LYP with various combinations of Scan step basis sets and with further SP calculation with cc-pVTZ were examined for fluorene

and thiophene.

- The effects of GD3BJ dispersion correction with the Scan CAM-B3LYP/6-31G* and SP CAM-B3LYP/cc-pVTZ were investigated for thiophene and fluorene 2mers with no-, methyl- and ethyl-side-chains.

Most of the functionals used in this section were already described in the previous chapters. From the new ones the ω B97X⁵⁵ and ω B97X-D⁵⁶ are both long-range (LC) corrected hybrid functional that also include a small fraction of exact short-range exchange (16%) and in the case of ω B97X-D also empirical dispersion is included.

5.3.2 Results of Methodology Testing

Examining the results for thiophene, as shown in the Figure 5.3, introduction of the density fitting (DF-MP2) into MP2 calculation to approximate the integrals has no noticeable effect on the dihedral profile, other than speeding up the calculations (on average 20% speedup in the case of bithiophene dihedral scan). The profile obtained using the Density-Fitted Local-MP2 (DF-LMP2) was calculated using THRBP=0.985 and MDom=1, more on this choice will be discussed below. From the same figure it can be seen that MP2 dihedral profiles (MP2, DF-MP2 and DF-LMP2) are closely copying CCSD(T)/CBS calculated profile with slightly shifted *trans* minimum and the largest deviation of ≈ 0.6 kJ/mol ($\approx 0.2 RT$) (DF-LMP2) for the *trans* minimum to *trans* planar structure barrier which is deemed to be modest deviation. In general, deviations in the calculated torsional profiles from the CCSD(T)/CBS profile affect the population distribution of conformers at a given simulation temperature. The ratio of probabilities of two populations which differ by ΔE is defined as $\frac{N_2}{N_1} = \exp(-\Delta E/RT)$. When the energy difference is affected by an error d , where d is the error in energy difference in units of RT , the population ratio would be affected by a factor of $\exp(-d)$. In the situation of $d = 1 RT$ ($RT = 2.479$ kJ/mol at $T = 298K$), this leads to a factor of change in the population ratio larger than 0.6.

Testing various THRBP (THRBP=0.980, 0.985, 0.990 and 0.995) and mergedom (MDom=0-3) options, figs. 5.4 to 5.7, in the cases where augmented domains are not used (MDom=0) this gives poorly converged results across all THRBP choices and leads to discontinuities in the calculated dihedral potentials. On the other hand, augmented domains with MDom=1 and 2 give results close to the canonical MP2, with almost identical profile to that of MP2 in the case of THRBP=0.995. It was found, generally, that MDom=3 gives slightly poorer results than MDom=1 or 2

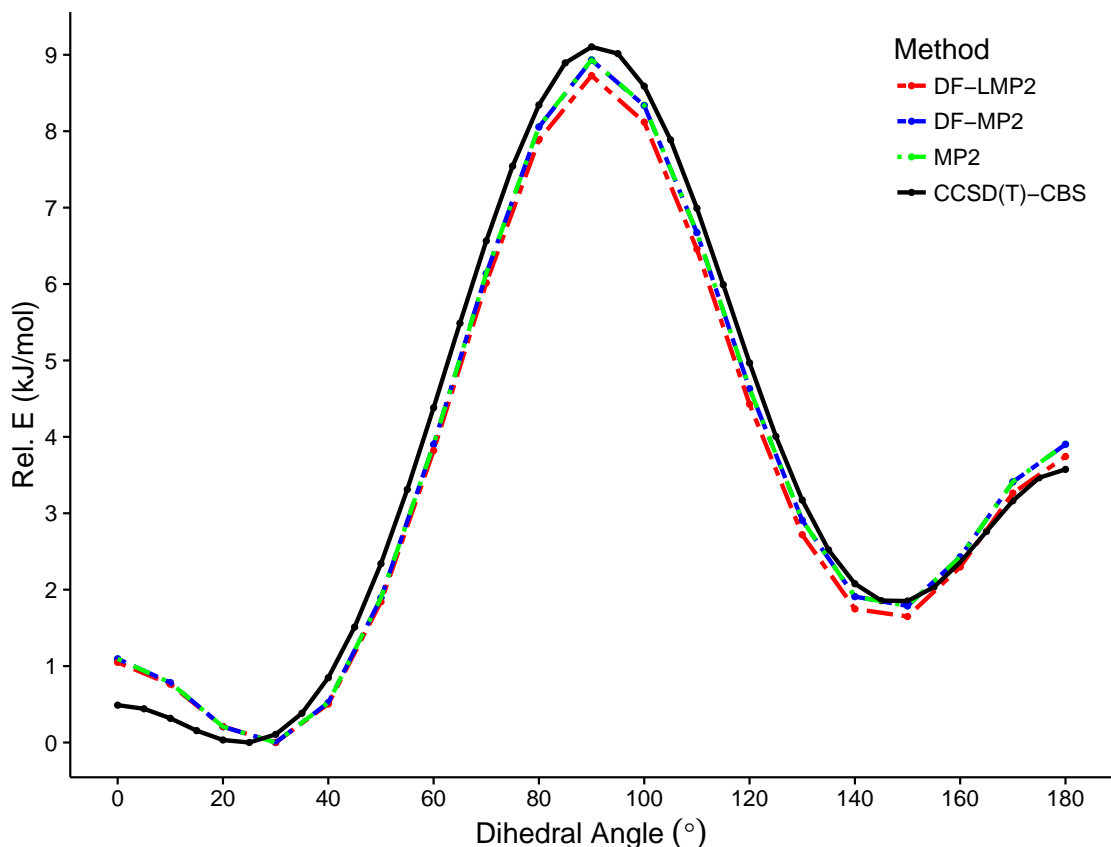


Figure 5.3: Dihedral profiles of thiophene dimers calculated using DF-LMP2 (using THRBP=0.985 and MDom=1), DF-MP2 and MP2 with cc-pVTZ basis set. CCSD(T)/CBS results of Bloom *et al*⁴¹ is used for comparison.

for all THRBP values except THRBP=0.995. For THRBP=0.995, the choice of MDom=3 results in unphysical domain formation which is reflected in the resulting profile. Given that THRBP=0.985 and MDom=1 provides the least computationally intensive and suitably accurate choice, the subsequent DF-LCCSD(T) calculations were performed using these parameters.

Finally, as can be seen in Figure 5.8, using the THRBP=0.985 and MDom=1 leads to the dihedral profile for DF-LCCSD(T) almost exactly copying canonical CCSD(T) profile. Compared to CCSD(T)/CBS, the CCSD(T)/cc-pVTZ result over-estimates the *cis* minimum slightly by ≈ 0.8 kJ/mol ($\approx 0.3 RT$) while at the same time underestimating the 90° barrier by ≈ 1.3 kJ/mol ($\approx 0.5 RT$), which leads to an overall reduction of ≈ 2.1 kJ/mol ($\approx 0.9 RT$) in the *cis* to 90° conformation barrier. Given the scale of this overall deviation, it would be expected that this would considerably affect the resulting dynamics. Further, Table 5.1 shows some illustrative timing results between canonical methods and their local versions. Note, however, that timing benchmark in the table is very limited as there may be more optimal settings such as number of procesors, memory and using integral-direct calculations (recomputing two-electron integrals in the AO basis whenever needed and avoiding the

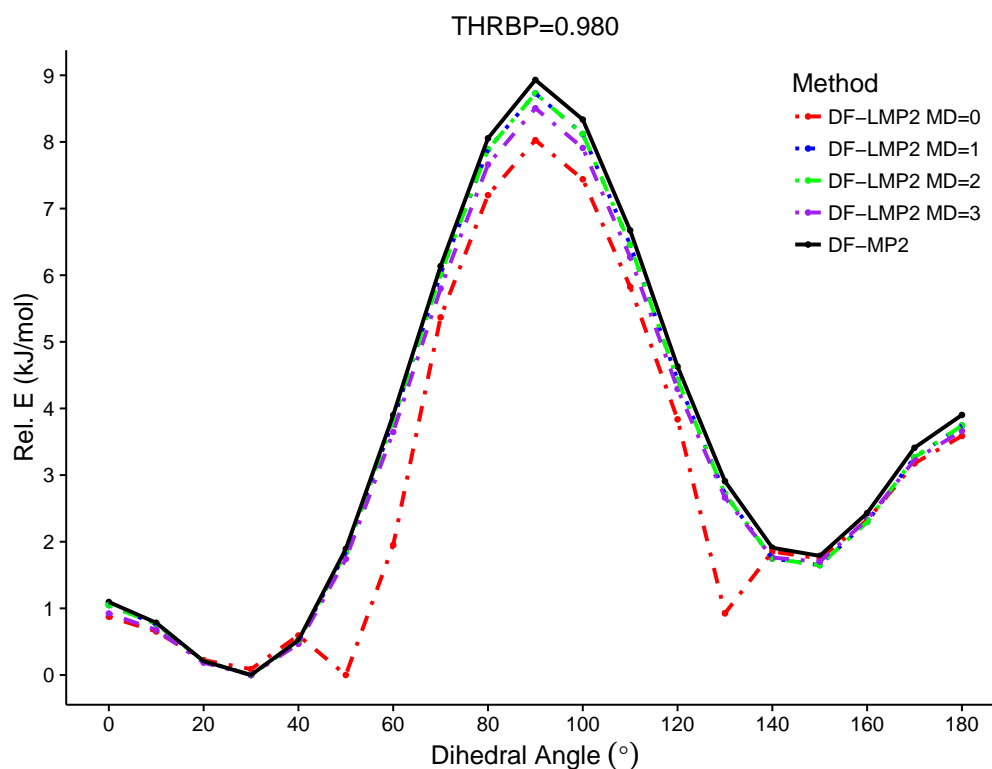


Figure 5.4: Dihedral profiles of thiophene dimers calculated using DF-MP2 and DF-LMP2 with THRBP=0.980 and varying mergedom (MDom) value; MDom = 0,1,2,3.

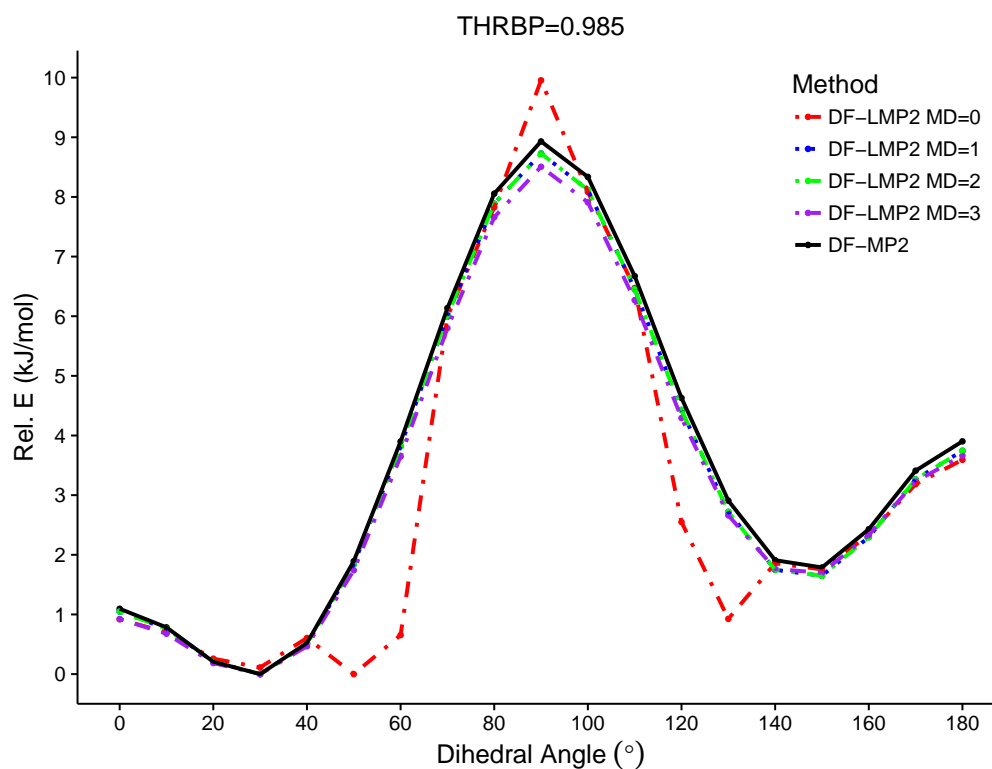


Figure 5.5: Dihedral profiles of thiophene dimers calculated using DF-MP2 and DF-LMP2 with THRBP=0.985 and varying mergedom (MDom) value; MDom = 0,1,2,3.

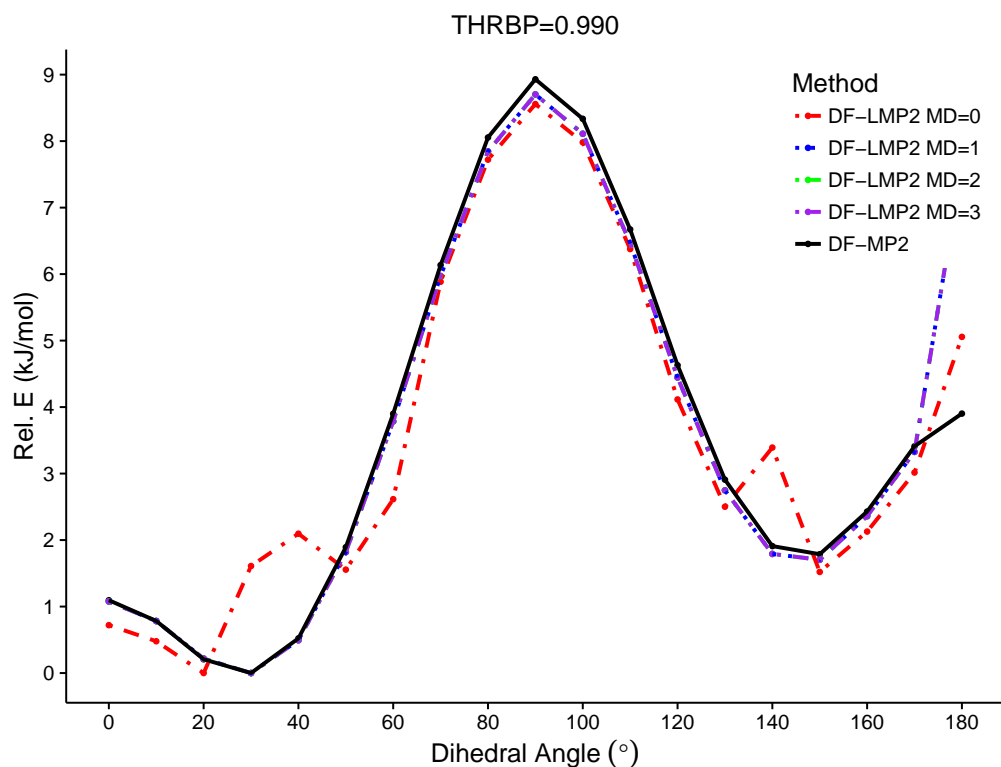


Figure 5.6: Dihedral profiles of thiophene dimers calculated using DF-MP2 and DF-LMP2 with THRBP=0.990 and varying mergedom (MDom) value; MDom = 0,1,2,3.

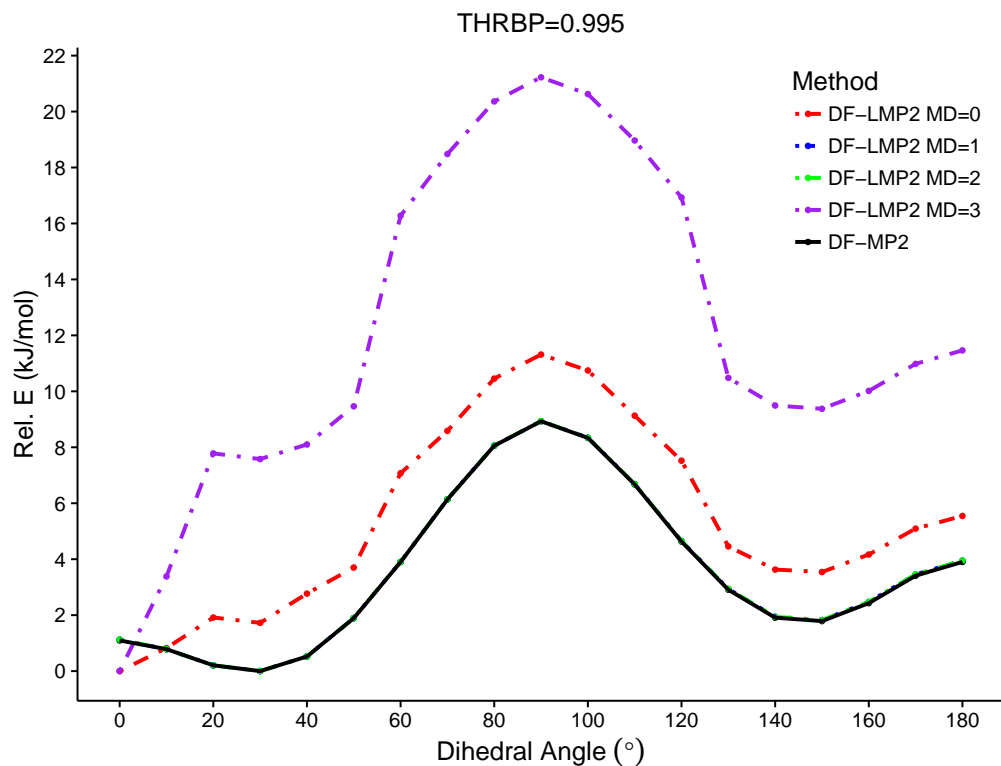


Figure 5.7: Dihedral profiles of thiophene dimers calculated using DF-MP2 and DF-LMP2 with THRBP=0.995 and varying mergedom (MDom) value; MDom = 0,1,2,3.

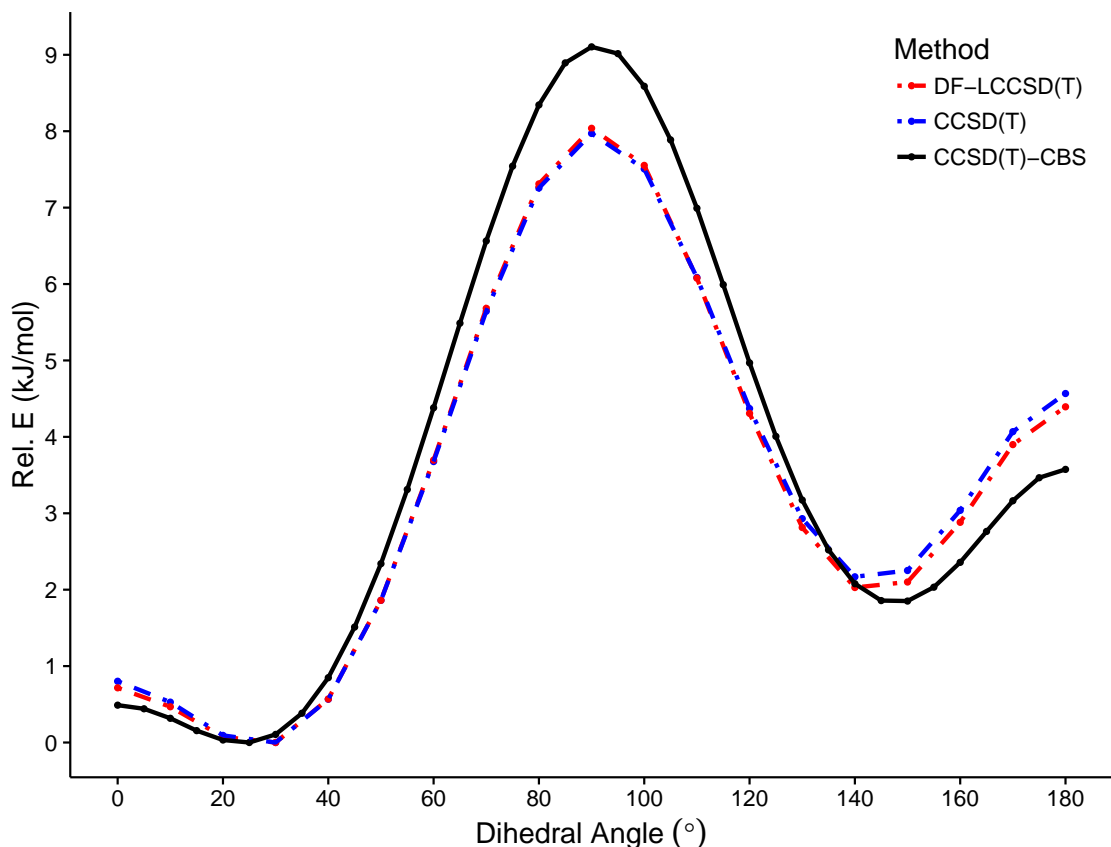


Figure 5.8: Dihedral profiles of thiophene dimers calculated using CCSD(T) and DF-LCCSD(T) (THRBP=0.985 and MDom=1) with *cc*-pVTZ basis set. These are compared against CCSD(T)/CBS results of Bloom *et al.*⁴¹.

bottleneck of storing these quantities on disk). Nevertheless, from this table it can be seen that DF-LCCSD(T) runtime is $\approx 70\%$ of the canonical CCSD(T) runtime.

Table 5.1: Average runtime (Real) time in minutes, averaged over runtimes for all the points along the dihedral potential, for different methods with *cc*-pVTZ basis set. All of the calculations were run at 6 processors with ≈ 7.5 GB memory per processor (5 processors, since one is helper processor). Local methods were run with THRBP=0.985 and MDom=1.

Method	Runtime [minutes]
CCSD(T)	378
DF-LCCSD(T)	264
MP2	10
DF-MP2	8
DF-LMP2	9

Both the Figure 5.8 and Table 5.1 point to very promising results for local methods since for thiophene dimer they are able to achieve accuracy comparable to that of canonical methods at the reduced computational cost. However, as can be seen in Table 5.2, trying to apply local methods to larger conjugated systems such as fluorene monomer the deviation from MP2 energies are in order of tenths of kJ/mol

and only at much larger THRBP=0.995 and MDom=2 it is possible to achieve accuracy of the canonical MP2. In the case of fluorene dimer, Table 5.3, it was not possible to achieve the accuracy of canonical MP2 not even at THRBP=0.995 and MDom=0. Further, for values beyond THRBP=0.995 and MDom=0 the domain size becomes prohibitively too expensive and localization procedure convergence problems were encountered. Further, Figure 5.8 shows that even if local methods are able to achieve accuracy of their canonical counterparts both the CCSD(T) and DF-LCCSD(T) with cc-pVTZ result in a considerably different profile from that of the CCSD(T)/CBS. This appears to be the result of basis set incompleteness and, in comparison to results using DFT, the generally slower convergence to CBS limit of Coupled-Cluster methods.

Table 5.2: Relative energies of single fluorene unit against canonical MP2 and running time in seconds. In the brackets are the values when DF-HF is used.

cc-pVTZ	Method	Relat. to MP2 [kJ/mol]	Real time [sec]
	HF DF-MP2	0.0 (1.3)	555 (70)
Full dom ^a	HF DF-LMP2	0.0	805
Full dom ^b	HF DF-LMP2	0.0	730
THRBP=0.980			
MDom=0	HF DF-LMP2	84.5	716
MDom=1	HF DF-LMP2	73.4	762
MDom=2	HF DF-LMP2	73.4	760
MDom=3	HF DF-LMP2	73.4	761
THRBP=0.985			
MDom=0	HF DF-LMP2	80.1	1063
MDom=1	HF DF-LMP2	70.3	704
MDom=2	HF DF-LMP2	70.3	698
MDom=3	HF DF-LMP2	70.3	667
THRBP=0.990			
MDom=0	HF DF-LMP2	72.0	751
MDom=1	HF DF-LMP2	51.7	1226
MDom=2	HF DF-LMP2	51.7	1220
MDom=3	HF DF-LMP2	59.3	854
THRBP=0.995			
MDom=0	HF DF-LMP2	40.7	867
MDom=1	HF DF-LMP2	0.0 (1.3)	3160(2753)
MDom=2	HF DF-LMP2	0.0	3745
MDom=3	HF DF-LMP2	11.5	2434

^arepresents full domain (THRBP=1) with and ^b without very distant pairs being neglected.

From Figure 5.9, it can be seen that for DFT results improving the functional approximation by moving from local SVWN to gradient corrected BP86 and to hybrid functionals leads to a significant improvement of not only the important energy

Table 5.3: Relative energies against canonical MP2 and running time in seconds for a minimum structure of fluorene dimer (39.3°). In the brackets are the values when DF-HF is used.

cc-pVTZ	Method	Relat. to MP2 [kJ/mol]	Real time [sec]
	HF DF-MP2	0.0 (2.6)	2876 (672)
	THR _B =0.980		
MDom=0	HF DF-LMP2	182.8	3152
MDom=1	HF DF-LMP2	159.4	3984
MDom=2	HF DF-LMP2	159.4	4016
MDom=3	HF DF-LMP2	159.4	3779
	THR _B =0.985		
MDom=0	HF DF-LMP2	171.7	3199
MDom=1	HF DF-LMP2	152.9	3501
MDom=2	HF DF-LMP2	152.9	3500
MDom=3	HF DF-LMP2	152.9	3528
	THR _B =0.990		
MDom=0	HF DF-LMP2	146.9	3549
MDom=1	HF DF-LMP2	102.3	13141
MDom=2	HF DF-LMP2	102.3	11268
MDom=3	HF DF-LMP2	123.8	4272
	THR _B =0.995		
MDom=0	HF DF-LMP2	81.9	4659
MDom=1	HF DF-LMP2	*	*
MDom=2	HF DF-LMP2	*	*
MDom=3	HF DF-LMP2	*	*

barriers of calculated profiles of thiophene dimers, but also of the overall shape of the profiles. Further, including long-range correction in the case of CAM-B3LYP provides dihedral profile with accuracy close to the benchmark CCSD(T)/CBS result. The only notable deviation between CAM-B3LYP and CCSD(T)/CBS profile is that CAM-B3LYP modestly over-estimates the energy of the cis minimum by ≈ 0.8 kJ/mol ($\approx 0.3 RT$), which is similar to the CCSD(T)/cc-pVTZ over-estimation of this minimum. Testing the choice of different long-range corrected ω B97X functional, Figure 5.10, also results in a highly accurate profile, however in comparison to CAM-B3LYP slightly more underestimating the perpendicular barrier height. Further, inclusion of empirical dispersion in the case of ω B97XD does not provide any significant improvement over the ω B97X, but actually makes it a little worse for the perpendicular barrier height and *trans* minimum to *trans* planar barriers. Examining the effects of different %HF exchange included, Figure 5.11, it can be seen that the M06-2X gives the closest agreement to the CCSD(T)/CBS result. On the other hand, the M06-L is not able to identify any of the minima and the overall dihedral profile deviates the most from the CCSD(T)/CBS profile. Further, this figure points to a strong dependence of the dihedral profile shape and energetics on the %HF exchange included in the functional.

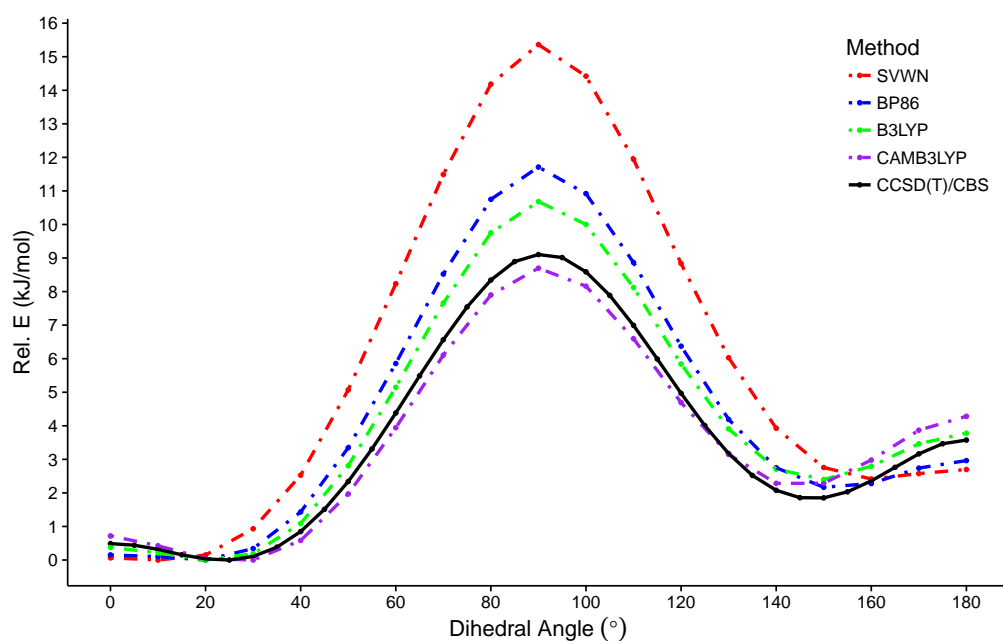


Figure 5.9: Comparison of thiophene dimer dihedral profiles calculated using various DFT functionals with cc-pVTZ basis set and CCSD(T)/CBS profile.

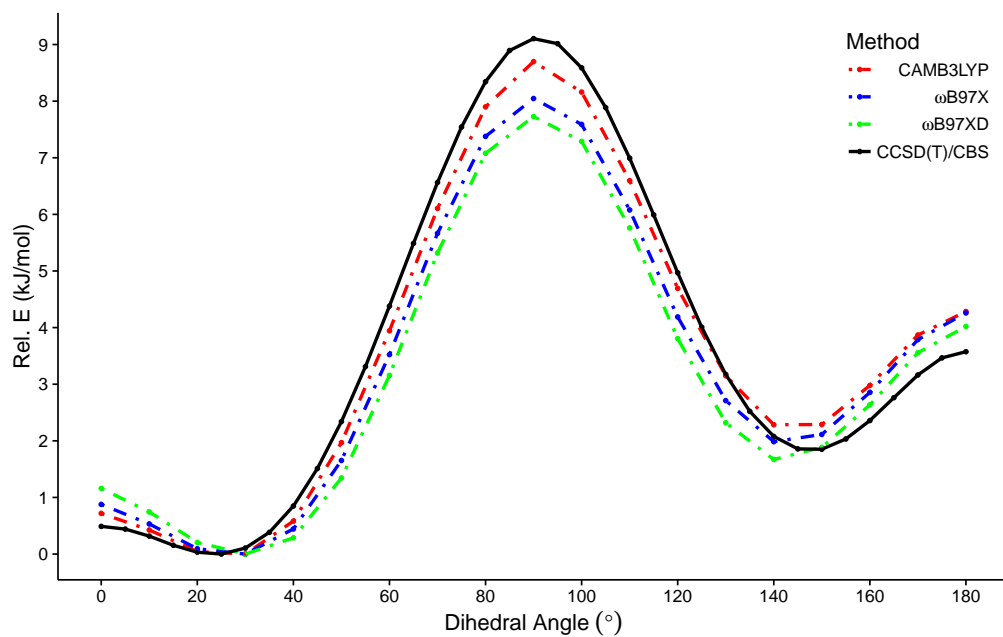


Figure 5.10: Comparison of thiophene dimer dihedral profiles calculated using the long-range corrected functionals with cc-pVTZ basis set and CCSD(T)/CBS profile.

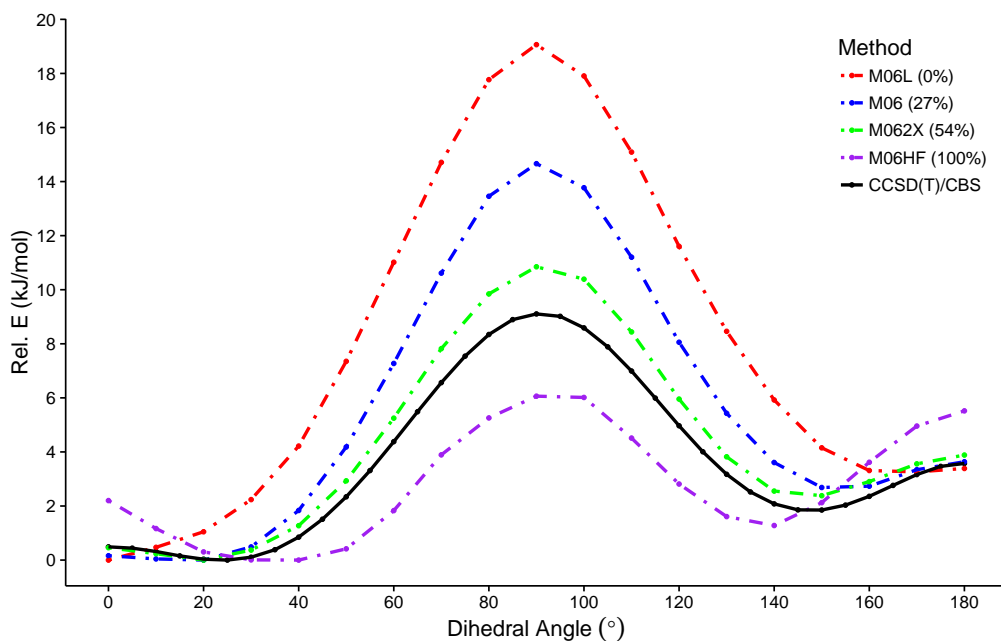


Figure 5.11: Comparison of thiophene dimer dihedral profiles calculated using the M06 family of functionals with increasing value of %HF exchange (in brackets) and CCSD(T)/CBS profile. All calculations are performed with cc-pVTZ basis set.

Summary of some of the key results for thiophene is given in the Figure 5.12 and Table 5.4. In addition, these results show that CCSD(T) and MP2 with cc-pVTZ basis set provide comparable bitiophene dihedral profiles, with MP2 predicting a slightly larger *trans* to *cis* barrier and lower lying *cis* minimum and *cis* planar structure. Moreover, MP2/cc-pVTZ is overall in better agreement with CCSD(T)/CBS dihedral profile taken from the article by Bloom *et al.*⁴¹, which was obtained at the MP2/aug-cc-pVTZ geometries.

Table 5.4: Relative energies (E , in $\text{kJ}\cdot\text{mol}^{-1}$) and dihedral angles (ϕ , in deg) for stationary points along dihedral potential of bitiophene calculated using different methods with cc-pVTZ basis set.

Method	<i>trans</i>		TS		<i>cis</i>		barrier to planarity	
	E	ϕ	E	ϕ	E	ϕ	<i>trans</i>	<i>cis</i>
CCSD(T)/CBS ^a	0.0	≈ 25.0	9.10	≈ 90.0	1.85	≈ 150.0	0.49	1.72
CCSD(T)	0.0	<30.0	7.97	≈ 90.0	2.17	>140.0	0.80	2.40
MP2	0.0	<30.0	8.94	≈ 90.0	1.79	<150.0	1.09	2.11
CAM-B3LYP	0.0	<30.0	8.70	≈ 90.0	2.28	>140.0	0.72	2.00

^aCCSD(T)/CBS values, calculated at the MP2/aug-cc-pVTZ geometries, were taken from the article by Bloom *et al.*⁴¹.

5.3.3 Results of Basis Set Testing

In order to examine effects of basis set choice on the 2mer dihedral profile calculations using Scan-SP approach various basis sets from the 6-31G⁵⁷⁻⁶⁶ family with added

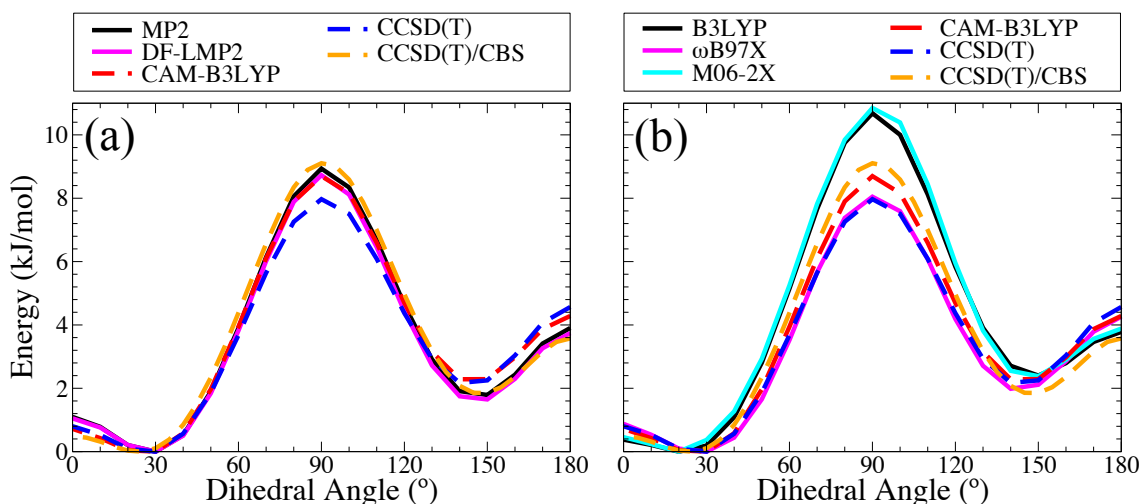


Figure 5.12: Dihedral profiles of thiophene dimers for various choices of SP calculation methods. In (a), results for MP2 and DF-LMP2 are presented with (b) containing results for B3LYP, ω B97X, and M06-2X. In each graph, results for CAM-B3LYP and CCSD(T) are also provided for comparison as well as the CCSD(T)/CBS results of Bloom *et al*⁴¹. All geometries are obtained at the B3LYP/6-31G(d,p) level except for the CCSD(T)/CBS which were obtained at the MP2/*aug-cc-pVTZ* level.

polarization and diffuse functions for scans and the cc-pVTZ⁶⁷ basis set for SP calculations were tested. For both fluorene and thiophene, comparisons are made against a scan performed using cc-pVTZ for both Scan and SP (herein referred to as the cc-pVTZ result), and further comparison is made against the benchmark CBS-limit CCSD(T) calculations of Bloom *et al*⁴¹ for thiophene. The CBS-limit CCSD(T) calculations, which are further referred to as the CCSD(T)/CBS result, were performed with MP2/*aug-cc-pVTZ* for the Scan and CCSD(T) in the Complete Basis Set (CBS) limit for the SP.

Figure 5.13 gives an overview of performance of the basis sets tested. It can be seen from Figure 5.13(b) that the cc-pVTZ result of thiophene is in good agreement with the CCSD(T)/CBS result. As performing such a high-level calculation as that of Bloom *et al* for as large a molecule as fluorene is computationally prohibitive, the cc-pVTZ result is used as a benchmark in the case of fluorene.

From the results for fluorene, Figure 5.13(a), it is observed that the energetics of the geometry optimisation alone are quite inaccurate when compared to the cc-pVTZ result. In the case of basis sets without diffuse functions a considerable over-estimation (≈ 2 kJ/mol or $0.8 RT$) of both the planar conformations barrier and the barrier at 90° is present. On the other hand, the basis sets with diffuse functions over-estimate the planar barrier but considerably underestimate the 90° barrier to a similar degree.

For thiophene, Figure 5.13(b), inclusion of diffuse functions in the basis set pro-

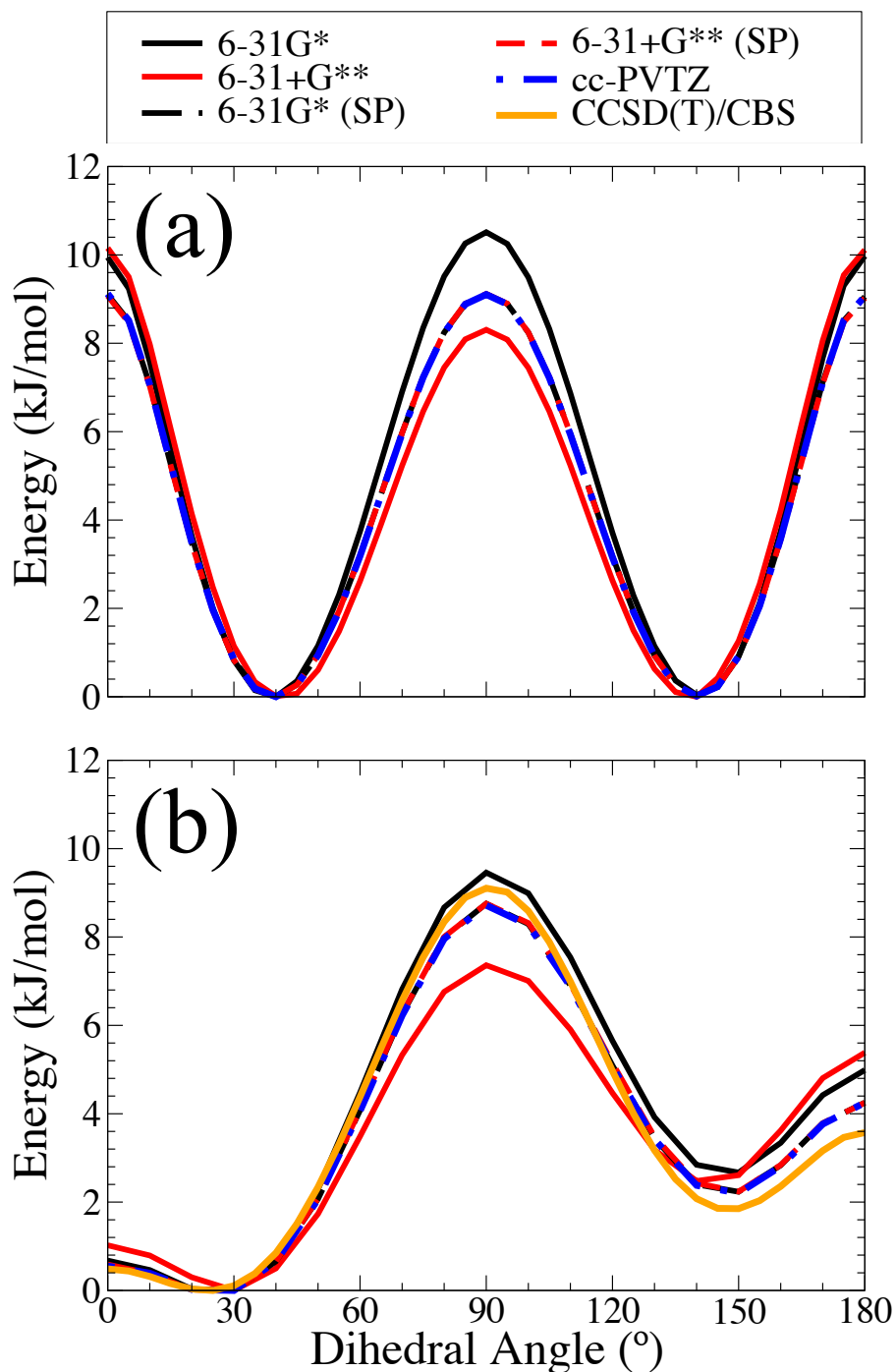


Figure 5.13: Dihedral profiles from geometry scans for CAM-B3LYP with various basis sets in (a) fluorene and (b) thiophene 2mers. Those with additional cc-pVTZ single-point calculations are labelled (SP). Full geometry optimisations using cc-pVTZ are also included and in (b) comparison is made to the CCSD(T)/CBS thiophene result of Bloom *et al*⁴¹.

vide considerably less accurate results when compared to results without diffuse functions. In details, using the diffuse functions, the energetics of conjugation barrier ($\approx 90^\circ$) appear to be underestimated when compared to the cc-pVTZ and CCSD(T)/CBS results. This difference is ≈ 3 kJ/mol ($\simeq 1.2 RT$) which at ≈ 20 - 30% of the barrier itself, is a significant discrepancy. However, it is also observed that none of the 6-31G-type basis sets exhibit suitable accuracy as both overestimate the height of the 180° energy barrier in thiophene by ≈ 2 kJ/mol ($\simeq 0.8 RT$).

Note that while there exists significant deviation in the energetic barrier heights due to the inclusion of diffuse functions, upon performing SP calculations with cc-pVTZ this difference becomes negligible. This implies that all the above discussed choices of basis-set provide very similar geometries and that the final accuracy of the dihedral profile is more dependent on the choice of basis set for the following SP calculation. It follows from this that 6-31G* basis set for the geometry optimisation is an appropriate choice providing accurate enough geometries at much cheaper computational cost.

Further, it was found that utilising a subsequent SP calculation offers a significant improvement to the resulting potentials. In thiophene, it is observed that the error in the SP curves is $\approx 50\%$ of that of the initial 6-31G* calculation when compared to the CCSD(T) curve. For the largest deviation, at the 180° barrier, this translates to a reduction of the absolute error to < 1 kJ/mol ($\simeq 0.4 RT$) from ≈ 2 kJ/mol ($\simeq 0.8 RT$). When compared to the 6-31+G** curve, this error reduction is considerably greater.

Finally, when comparison is made to the results of a full optimisation using cc-pVTZ (i.e. performing the Scan step with cc-pVTZ without any further SP calculation) it is shown that the results of the Scan-SP approach are almost identical to that of using cc-pVTZ for geometry optimisation. This is yet another proof that reliable geometries are obtained from basis set choices as low as 6-31G*. With the above in mind, the choice of CAM-B3LYP/6-31G* Scans and CAM-B3LYP/cc-pVTZ SP's is well justified.

5.3.4 Results of Dispersion Corrected DFT

The results of dihedral profiles with and without the dispersion correction GD3BJ^{48,49} for 2mers with no-, methyl- and ethyl-side-chains are summarized in Figure 5.14. In the case of fluorene 2mers, Figure 5.14(a), the use of dispersion correction has essentially no effect for all side-chains considered. On the other hand, in the case of thiophene, Figure 5.14(b), it is found that there is little effect only for no and

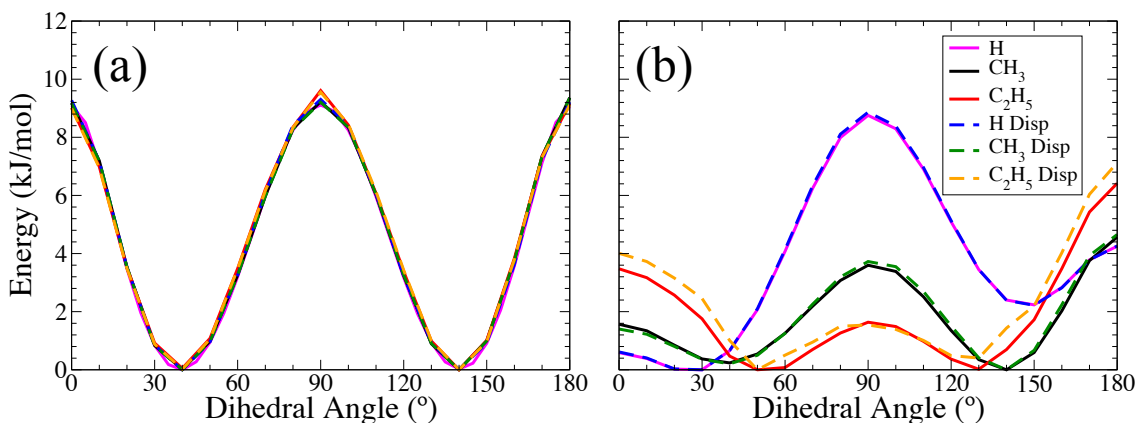


Figure 5.14: Dihedral energetics from DFT with and without dispersion correction for 2mers of (a) fluorene, and (b) thiophene. For each molecule, the profile with no side-chains, with methyls, and with ethyls is given.

methyl-side-chains. However, ethyl-thiophene is affected in two ways. Firstly, there is a slight variation of certain energies of ≈ 0.5 kJ/mol ($\approx 0.2 RT$) - particularly those at the planar points. Secondly, the overall profile is far less smooth than those given without dispersion.

One of the reasons is that the inclusion of dispersion interactions in DFT calculations of this type often lead to convergence problems as the relatively high flexibility of the side chains allows for many possible local minimal conformations. Due to this, the calculations both become increasingly computationally expensive and generate results which are strongly-dependent on initial conditions; resulting in ambiguity in their translation into force-field parameters. The second reason is that by effectively removing the side chain - side chain interactions, what is observed is the effect of the presence of the side chains on the electronic properties of the backbone. For the purposes of generating good force-fields for MD calculations, this is the crucial point as this determines whether or not, in principle, the bare dihedrals along the molecular backbone require modification due to the presence of the side chain. Therefore, the dispersion correction is not used in the force-field scheme presented here.

5.3.5 Discussion and Conclusion

The main result is that two step approach with CAM-B3LYP/6-31G* Scans and CAM-B3LYP/cc-pVTZ SP performs with accuracy close to that of the benchmark CCSD(T)/CBS result of Bloom *et al.* While it was found that MP2 and DF-LMP2 (with the above MDom and THRBP choices) give slightly better agreement than CAM-B3LYP, given that the method used will be applied to longer molecules and molecules of larger constituent unit size (for example, fluorene in this work), a

strongly performing DFT functional will provide highly accurate results with much better scaling with the system size. Further, although local methods gives us the possibility for a systematic improvement of calculated results and minimization of basis set superposition error at lower computational costs, as opposed to their canonical counterparts these methods are not black-box methods. They depend on the choice of the domain for the local calculations. Furthermore, domains are geometry dependent and restriction of the virtual space in local calculations may result in discontinuities on the potential energy surface. For this reason domains have to be defined that are appropriate for a whole range of geometries in order to obtain smooth potential energy profile along the scan coordinate.

In the case of strongly conjugated systems local methods may suffer due to the intrinsic delocalisation of the conjugated molecular orbitals, which results in the necessity of impractically large domains. Another problem one may encounter for strongly conjugated systems is a poor localization of molecular orbitals or that the localization procedure does not converge at all. Therefore, for the above reasons, better scaling of DFT when applied to longer polymer chains and side-chains and for the consistency with the subsequent optical studies CAM-B3LYP was used for the dihedral modelling in this study. Further, it was shown that basis set choices as low as 6-31G* are sufficient in order to provide reliable geometries. Furthermore, it was demonstrated that two step approach using CAM-B3LYP/6-31G* Scans and CAM-B3LYP/cc-pVTZ SP is needed in order to obtain accurate dihedral profiles.

5.4 Determining Dihedral Profiles

Now, with the above established methodology it is possible to examine the effects of neighbouring dihedral angles, position of the dihedral along the conjugated backbone and the length of conjugated backbone on the dihedral energetics. Examining the effect of neighbouring dihedral angles, as can be seen from individual graphs in Figure 5.15 and Figure 5.16, in the case of fluorene there is no difference between dihedral profiles for all neighbouring values while in the case of thiophene there exists a slight deviation of ≈ 0.5 kJ/mol ($\simeq 0.2 RT$) in the barrier height. In the same figures when comparison is made between dihedral profiles on the left (a) and right (b), a set of curves corresponding to a different position along the conjugated chain, the differences observed are in both cases small. The above findings point to the invariance of the dihedral energetic profiles to the value of the neighbouring dihedral angle and its position along a chain longer than a 2mer. With this in mind it is possible to examine the sensitivity of dihedral profile to the length of the conjugated backbone by performing a scan over one dihedral for any chosen values of the others

in various lengths of molecule.

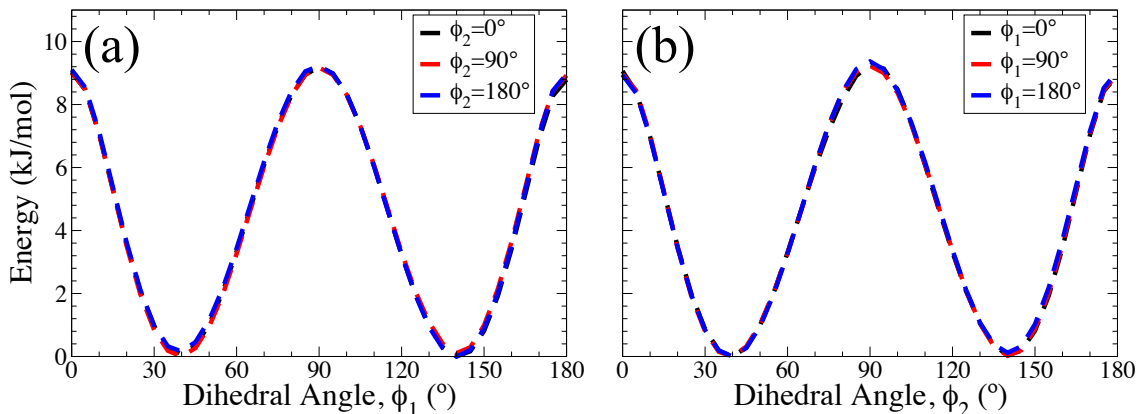


Figure 5.15: Dihedral profiles obtained from scans of 4mers of fluorene. The profiles obtained for (a) the end-most dihedral, ϕ_1 , and (b) the second dihedral, ϕ_2 , were calculated for various values of the other dihedral (ϕ_2 and ϕ_1 , respectively). The third dihedral, ϕ_3 , is optimised to its minimal value in all cases.

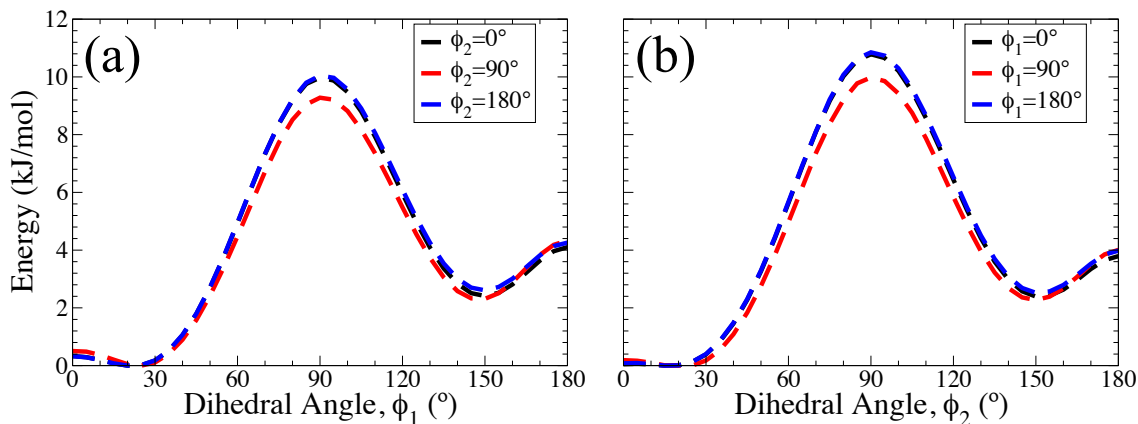


Figure 5.16: Dihedral profiles obtained from scans of tetramers of thiophene. The profiles obtained for (a) the end-most dihedral, ϕ_1 , and (b) the second dihedral, ϕ_2 , were calculated for various values of the other dihedral (ϕ_2 and ϕ_1 respectively). The third dihedral, ϕ_3 , is optimised to its minimal value in all cases.

Figure 5.17 demonstrates the invariance of the calculated dihedral profile of the end-most inter-monomer junction for both molecules over a backbone length range of 2-10 units. In fluorene, there is almost no dependence on the chain length while in thiophene there is a very slight deviation of $\lesssim 1$ kJ/mol ($\simeq 0.4 RT$) in the energetic barrier heights. The above results suggest it is possible to utilise the same dihedral energy profile for all inter-monomer dihedrals within any length of molecule. This greatly reduces the amount of parameterisation required for MD simulations.

In order to examine the influence of alkyl side chains on the dihedral energy profiles scans have been performed for side chains of lengths varying from 1-10 units. In the case of fluorene, initial geometries with side chains on opposing sides of the molecule were used.

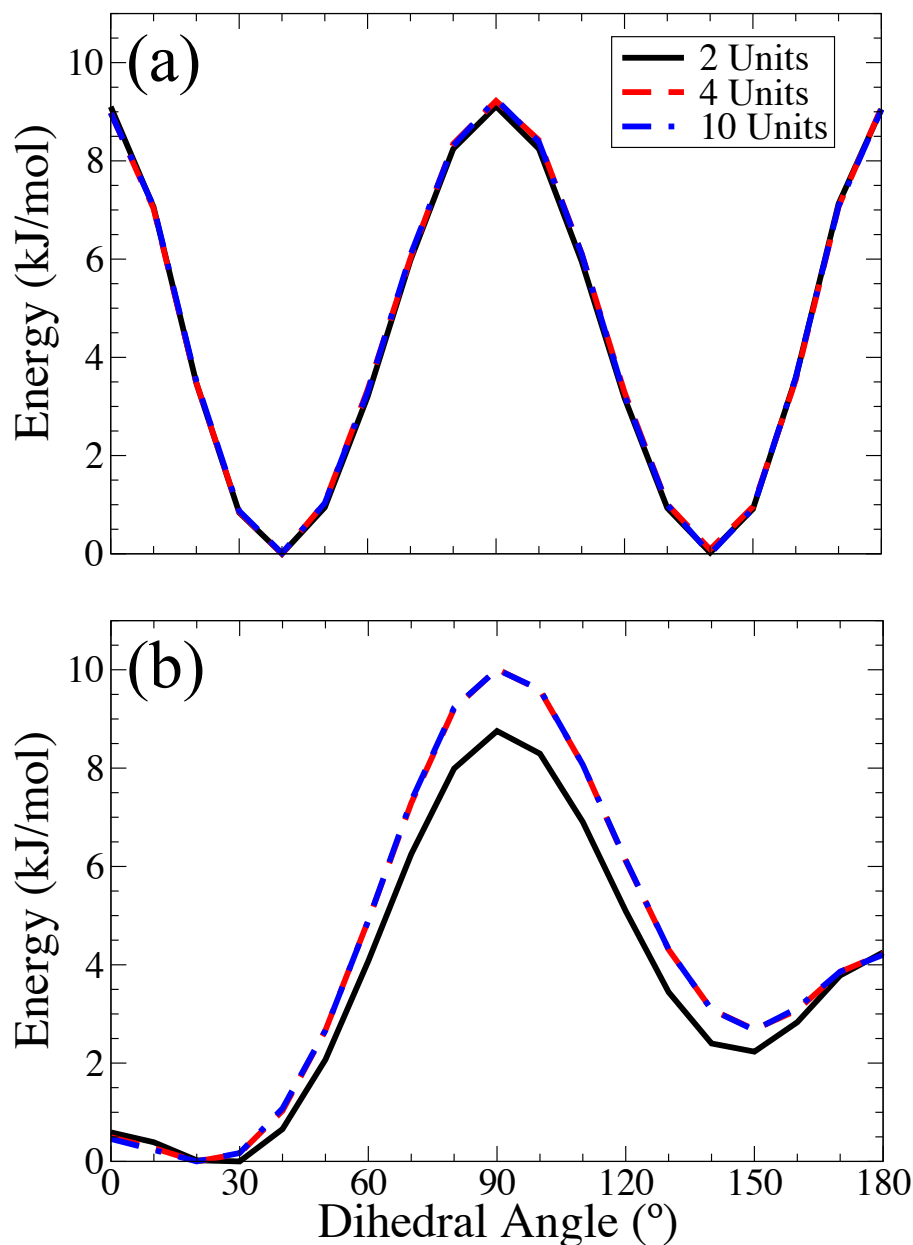


Figure 5.17: Dihedral profiles for various backbone lengths of (a) fluorene and (b) thiophene. (Legend applies to both graphs.)

With the above considered, Figure 5.18(a) gives the resulting dihedral profiles calculated for fluorene with various lengths of side-chains. It is observed that increasing side-chain length has very little effect on the energetics of the dihedral. However, in the case of thiophene (Figure 5.18(b)), the problem becomes considerably more complex due to the dihedral energetics being strongly influenced by steric repulsion of the side-chain in close proximity to the dihedral. This is illustrated in Figure 5.19. In the case of fluorene side-chains are much further from the centre of dihedral rotation than in the case of thiophene. Therefore, the notion of separating long-range interactions from those due to the electronic conjugation is considerably more complicated for thiophene while it does not pose any issues in fluorene.

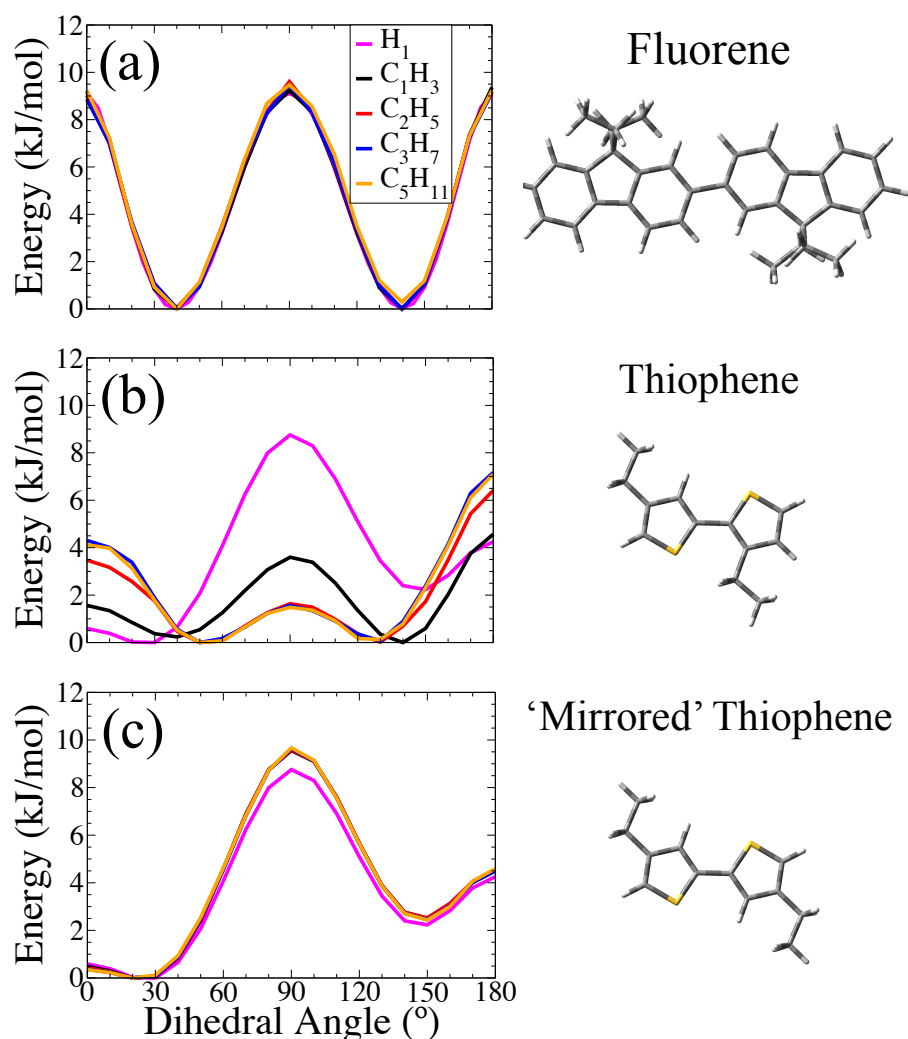


Figure 5.18: Dihedral profiles for 2mers of: (a) fluorene, (b) thiophene, and (c) 'mirrored' thiophene for varying lengths of side-chain(s). The side-chain(s) are labelled by chemical formula e.g. H_1 and C_5H_{11} refer to no side-chain(s) and pentyl side-chain(s) respectively. Each graph has a schematic of the associated molecule to the right. (Legend in (a) applies to all graphs.)

The issue of this unavoidable steric repulsion creates a problem in interpreting the dihedral profiles. The parameterisation is built on the ability to transfer parameters for long-range dispersive forces, the steric contribution to the dihedral profile due to the side-chains is captured by the existing terms in the force-field. Therefore, a 'mirrored' thiophene 2mer (Figure 5.18(c)) approximation is introduced in order to investigate the effect of the side-chain on the covalently-bound component of the dihedral rotation, i.e. the effect it has on orbital conjugation, as it is this component which comprises the required parameters in the force-field.

In the mirrored 2mer, in order to remove the steric conflict the side-chain of one unit is moved from the 3 carbon position to the 2 carbon position. The nature of the approximation is that the effect of the side-chain on the conjugation-dependent component of the dihedral energetics are the same in both cases. The idea behind

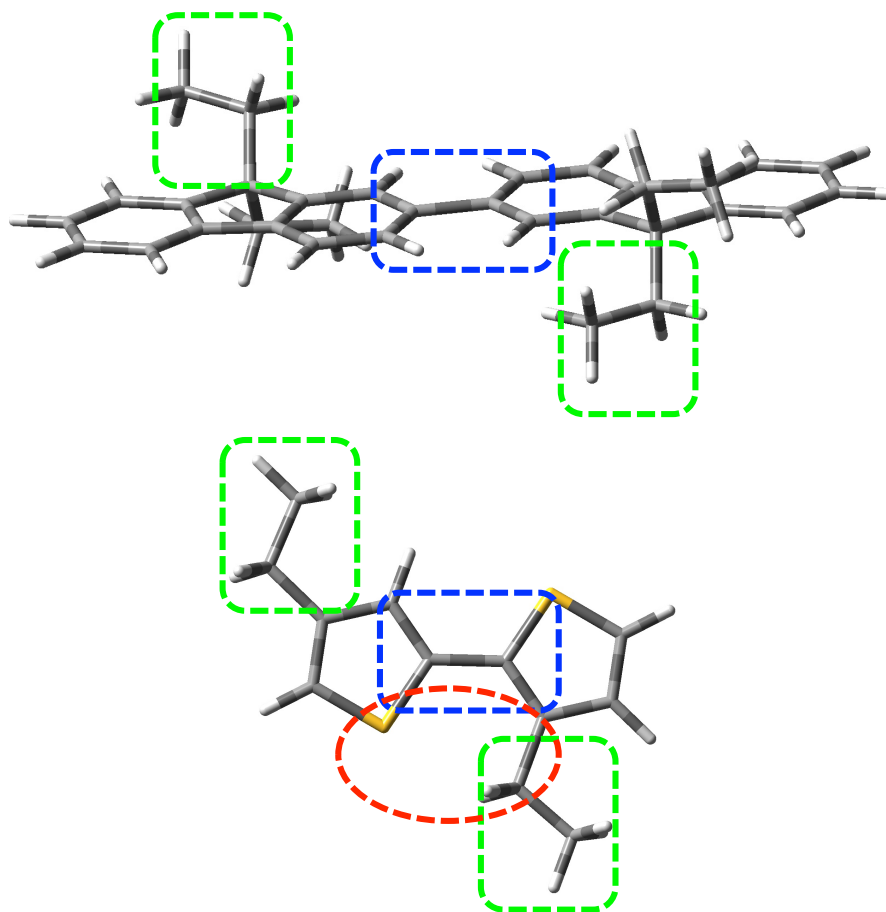


Figure 5.19: Schematic highlighting the difference in the location of the alkyl side-chains in 2mers of fluorene and thiophene. The blue area represents the location of the inter-monomer dihedral; the green the alkyl side-chain; and, in thiophene, the red area highlights the steric conflict involved.

this approximation is justified by agreement of the fundamental transition energies (Table 5.5) and transition densities (Figure 5.20) between thiophene dimers with no side-chains and with ethyl side-chains in the normal and mirrored case.

Both the transition densities and energies suggest that there is very little effect on the excitations in all cases. This implies that the side-chains have little effect on the properties of the orbital conjugation along the backbone. Between the cases with side-chains and without, the transition energies deviate by $\sim 0.05\%$ of the excitation energy and between the two side-chain cases, the deviation is $\sim 0.1\%$.

0-1 Transition Energies: Thiophene Dimers	
None	4.5632 eV
Normal	4.5873 eV
Mirrored	4.5434 eV

Table 5.5: Transition energies of the fundamental bright transition of thiophene dimers in the three cases shown in Figure 5.20.

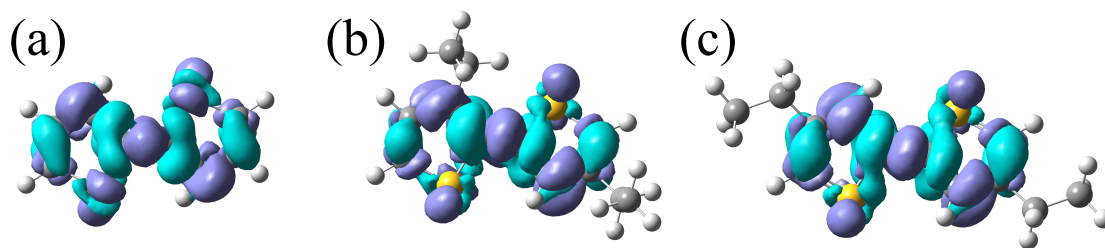


Figure 5.20: 0-1 transition densities of thiophene dimers with (a) no side-chains, (b) 3-position side-chains (the normal case), and (c) ‘mirrored’ side-chains.

With the above in mind, it can be seen from Figure 5.18(c) that the presence of side-chains introduces only a small deviation (≈ 1 kJ/mol) to the dihedral energetic profile of the mirrored thiophene. This deviation is attributed, in a similar manner to those seen in Figure 5.17, to small remaining dispersive forces between the mirrored side-chain and the neighbouring unit. These results strongly suggest that any variance in the dihedral energetics on account of the inclusion of side-chains is mediated entirely by known long-range, non-covalent interactions. This suggests that the dihedral profile is invariant to the addition of side-chains and this is further analysed in section 5.6.

5.5 Partial Charge Calculations

Partial charges are obtained using the RESP scheme³¹ within the Antechamber program, which is a part of the AmberTools 14 suite⁶⁸. The choice of this scheme is based both on consistency with the recommended methodology for OPLS parameterisation as well as the robustness of the method to slight perturbations in geometry as opposed to, for example, ESP charges. Not only does this result in more accurate partial charges for utilisation within MD force-field, the robustness of the method also allows to accurately determine variations due to the changes in molecular environment. Input electronic densities for the RESP calculations are obtained from SP calculations with CAM-B3LYP/cc-pVTZ using geometries taken from CAM-B3LYP/6-31G* optimisation.

When generating parameters for MD simulations of repeating structures of many units, such as polymers or oligomers, partial charges are often implemented using a ‘three residue’ model in which three sets of charges are built: one for each end unit and one for the central unit. In order to build such a model that is fully scalable to a variety of lengths, a first pre-requisite is the requirement that the net charge for each individual central residue and the sum of the end residues have a net zero charge. This ensures the overall charge neutrality of the molecule and that this

neutrality will remain when generating longer molecules by inserting extra central units. As it is possible for the end residues to have a non-zero net charge, if one wishes for a model with which scaling to many lengths is possible, it is necessary to determine the length of molecule at which the above criteria are met. Only for molecule lengths greater than this length will the application of the three-residue model be valid.

As an example, Figure 5.21 presents the total charge of each monomer unit for 9mer of fluorene, 9,9-dioctyl-fluorene, thiophene, and 3-hexyl-thiophene. For the first three of these, the total charge for each monomer is close to zero across the entire molecule, whereas for hexyl-thiophene, there is a small but notable residual charge on the two end units. The key feature that distinguishes hexyl-thiophene from the other molecules is the breaking of reflection symmetry between each end of the molecule. At one end of the hexyl-thiophene molecule, the hexyl side-chain is on the side of the thiophene nearest the neighbouring unit while, at the other end, the side-chain is on the side further from the neighbouring unit. This asymmetry of molecular structure forms an intrinsic asymmetry in the charge distribution of each end of the molecule which leads to a small net charge difference ($\approx 0.1 e$), i.e. resulting in a dipole. Therefore, in order to build a three-residue model for hexyl-thiophene with accurate partial charges, the end residues must encompass two units of the molecule. In doing so, these two end residues will each have a non-zero net charge which cancel each other.

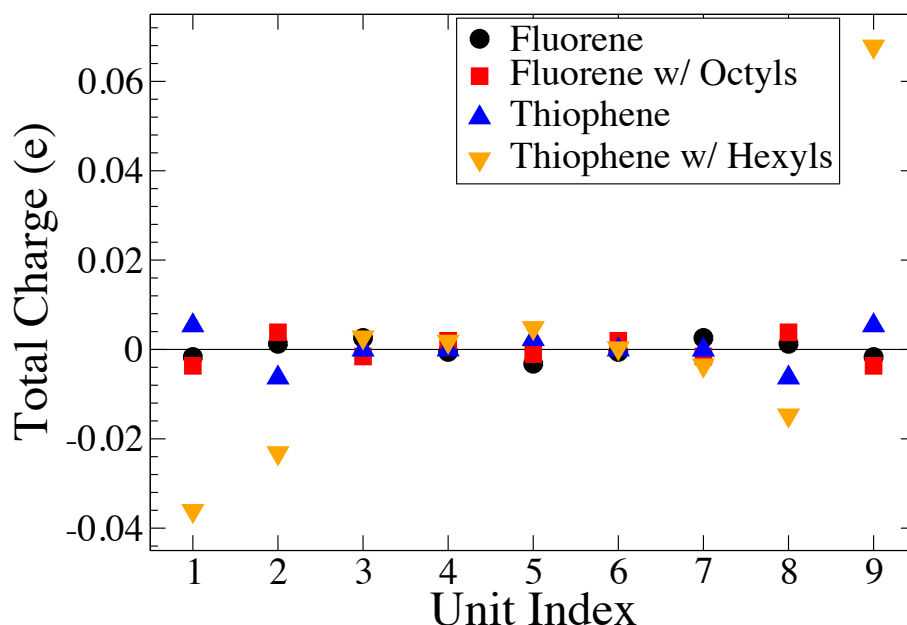


Figure 5.21: Total charge on each monomer unit of 9mers of fluorene, dioctyl-fluorene, thiophene, and hexyl-thiophene. The end monomers of hexyl-thiophene retain a considerably larger net charge than those of the other molecules.

In order to build a partial charges model generalisable to all lengths of side-chain there must exist a length of side-chain beyond which the charge distribution of

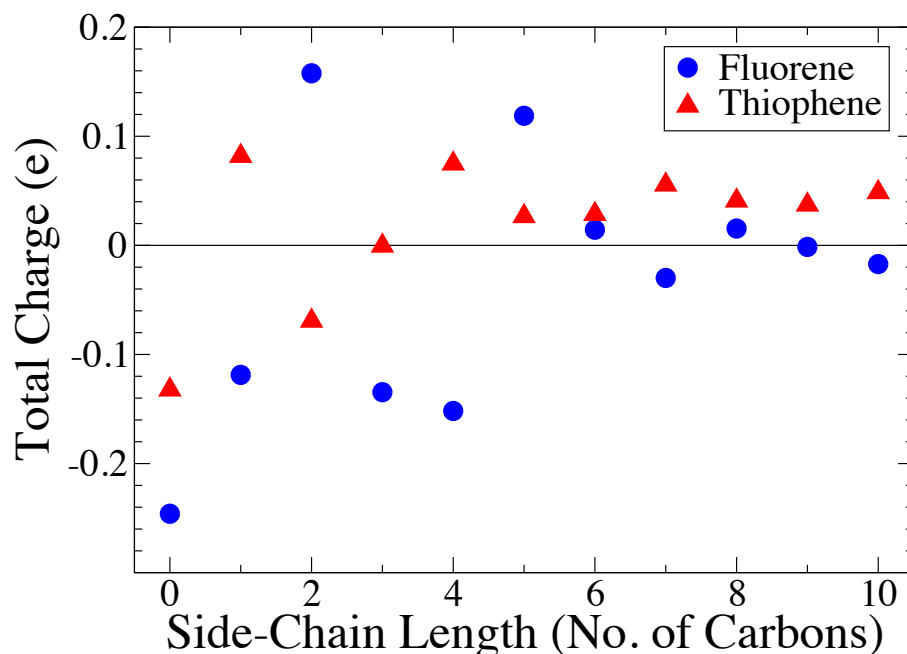


Figure 5.22: Relationship of the total charge, excluding side-chains, of monomers of dialkyl-fluorene and 3-alkyl thiophene of various lengths of alkyl chain. Each display a convergence to near zero at around 6 carbons side-chain length.

the conjugated backbone is invariant. Further, it must be possible to generate a standardised methylene (CH_2) and methyl (CH_3) groups which allows addition of these groups in order to create longer structures. The first requirement is investigated by analysing the charge distributions of a monomer with varying lengths of side chain, Figure 5.22. From this figure it can be seen that for both fluorene and thiophene the total charge on the main conjugated component excluding the side chain converge near zero at around six carbons side-chain length. This implies that the charges on this part of the molecule are invariant to the side-chain length beyond this point. Examining the charge distributions of the side-chains in the case of monomer of alkyl-thiophene, Figure 5.23, suggests that at the lengths of side chain considered (up to 10 carbons) it is not possible to satisfy the second requirement to generate standardised charge groups for methylene. The reason is that while there are convergences in the end-most and inner-most groups on a given side-chain, the charge on the methylene group in the middle of a long chain still fluctuates considerably as side-chain length is varied. This can be attributed to the strong asymmetry between each end of the side-chain - one is connected to a large molecule while the other is terminated only by a hydrogen. However, as can be seen in Figure 5.24, the overall effect of the residual partial charges would not be as dramatic as these are balanced by the neighbouring carbons. It may be possible to generate a sufficiently accurate standardised methylene group charges using much longer side-chains. However, since lengths of side chains greater than 12 are not often used in practical settings, it remains that if one wishes to include partial charges for use with side-chains, it is necessary to compute these charges for each

length of side-chain required.

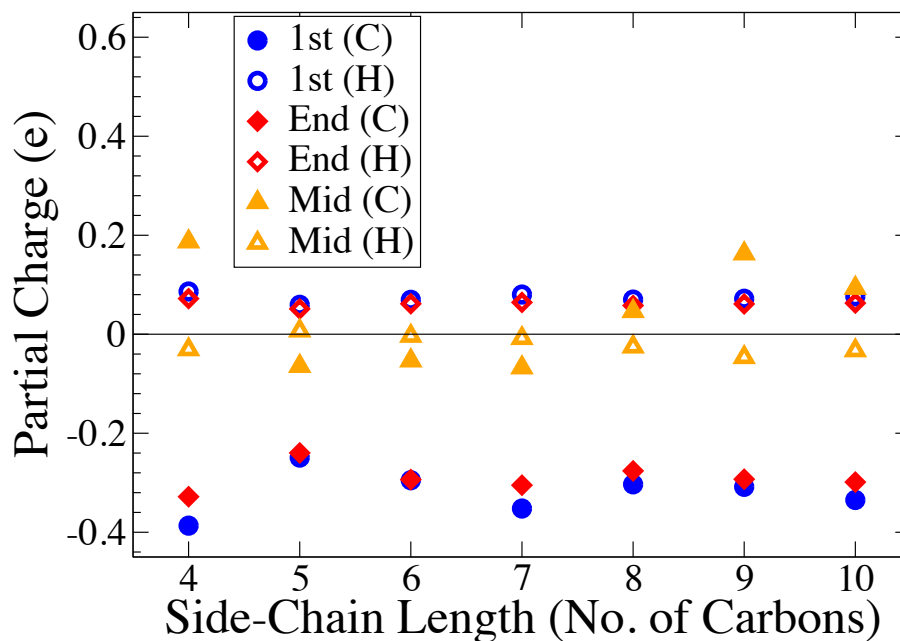


Figure 5.23: Sample of beginning, middle, and end side-chain charges for various lengths of side-chain in a monomer of alkyl-thiophene. It is observed that, in contrast to the end groups, the charge of the carbon on the inner methylene group (yellow triangles) does not converge with increased side-chain length.

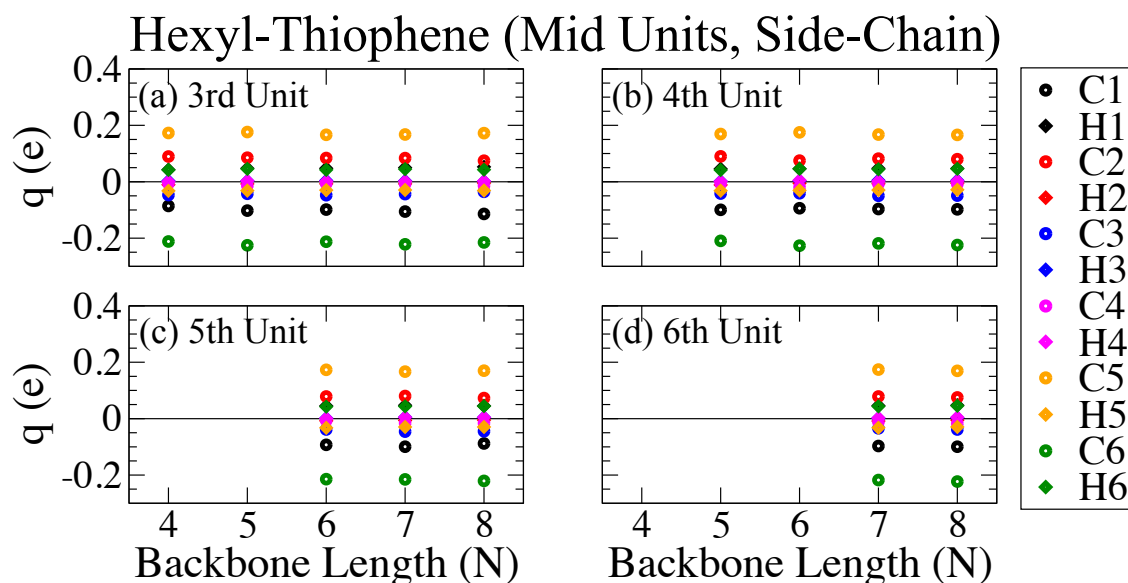


Figure 5.24: Individual atomic charges of the side-chain atoms of the third through sixth units ((a) through (d) respectively) of hexyl-thiophenes of various backbone lengths.

5.6 Force-Field Implementation

Force-field parameters for molecular building blocks of fluorene and thiophene are generated using pre-existing bond-stretching and angle-bending terms for monomer

Table 5.6: Comparison of the un-modified and modified OPLS force-fields (MD₀ and MD₁ respectively) with DFT calculations for 2mers of fluorene (F0), methyl-fluorene (F1), thiophene (T0), and ethyl-thiophene (T2). The properties compared are: the difference in energy between the *cis* and *trans* minima (ΔE); the dihedral angle of each minimum (ϕ); and the end-end length associated with each minimum (l_{EE}).

	ΔE (kJ/mol)			ϕ_{trans} (°)			ϕ_{cis} (°)			$l_{EE,trans}$ (Å)			$l_{EE,cis}$ (Å)		
	DFT	MD ₀	MD ₁	DFT	MD ₀	MD ₁	DFT	MD ₀	MD ₁	DFT	MD ₀	MD ₁	DFT	MD ₀	MD ₁
F0	0.04	0.00	0.08	39	39	40	141	135	140	15.3	15.2	15.4	15.1	15.0	15.2
F1	-0.05	0.03	0.05	39	41	38	141	139	142	15.3	15.2	15.4	15.1	15.0	15.2
T0	2.23	2.23	2.09	26	31	28	147	145	145	6.4	6.4	6.4	6.3	6.3	6.3
T2	0.84	1.43	0.86	45	20	50	129	129	135	6.4	6.5	6.4	6.3	6.5	6.3

units from the OPLS force-field. In the case of fluorene also parameters for the bonds and angles around the inter-monomer junction are available. However, since inter-monomer parameters are lacking for oligo-thiophenes, the fluorene inter-monomer parameters are used.

Partial charges which were generated following the procedure described in section 5.5 are directly implemented in the force-field parameter set. However, in the case of dihedral potentials these require the extra 'subtraction' step, as already described in section 5.2, before implementation in the force-field (FF). This is to avoid a double-counting of interactions, such as dispersive and electrostatic interaction, that are already described by the existing FF terms.

It was found that in order to achieve better agreement between the DFT and MD results the equilibrium bond lengths and angles of the parameters taken from the OPLS force-field need to be modified while keeping the original force-constants. Equilibrium values were taken from the global minimal geometries obtained from the CAM-B3LYP/6-31G* optimisation. Table 5.6 contains a breakdown of these changes on: the resulting minimal energy difference, ΔE ; the values of each dihedral minimum, $\phi_{trans/cis}$; and the end-to-end length of each minimal geometry, $l_{EE,trans/cis}$. In all cases, it was found that there is either improvement in particular values or changes which are negligible (~ 0.1 kJ/mol, 1° , 0.1 \AA in each value).

In the case of fluorene with and without methyl-side chains (F0 and F1, respectively), it was found that the only slight improvement is in the location of ϕ_{cis} of F0. While there are other values which seem to agree less well after modification, these deviations are generally negligible as mentioned above. Overall, there is good correspondence between F0 and F1 values.

In the case of thiophene with and without ethyl-side chains (T0, T2), there are some substantial improvements introduced by this modification as the changes are

made to the inter-monomer junction parameters. While there are significant improvements in ΔE and ϕ_{trans} for T2, the deviation of ϕ_{cis} slightly increased by $\approx 6^\circ$. For the T0 there is a small improvement in the ϕ_{trans} , but on the other hand the ΔE value is worsened. This may play a role when considering properties of more microscopic interest (e.g. if utilising geometries for optical calculations). Overall, the improvements made in T2 are substantial and the energetic improvement strongly impacts the resulting dynamics.

The force-field contribution to the dihedral potential is isolated by performing a dihedral scan using the FF parameters (without the required dihedral) over intervals of 10° from 0° to 180° in a manner analogous to that of the scans performed using DFT. In order to isolate all interactions relevant in the dihedral rotation which are not the covalent interaction and also to restrain the dihedral at each value in the scan, the four covalent energetic functions at each inter-monomer juncture are used to impose restraints.

The effective restraints at a given angle, ϕ_0 , are generated by placing each of the four dihedral terms under the influence of a periodic potential, V_R , given by:

$$V_R(\phi) = k_c[1 - \cos(\phi - \phi_0)]. \quad (5.1)$$

When it comes to the choice value k_c care must be taken so as to find a balance between forming an effective restraint without inducing any unwanted distortion to the molecule. For example, for molecules with methyl or no side-chains, the choice of $k_c = 5 \times 10^4$ kJ/mol is suitable. However, in the case of ethyl-thiophene, a large reduction is necessary $k_c = 10^3$ kJ/mol which may be attributed to the prevalence of large forces in the side-chain - dihedral area. For each point along the scan the geometry is then optimised in vacuum using the conjugate-gradients minimisation algorithm within Gromacs 4.6.5^{35,36} and the total energy of each point is used to generate the corresponding profile.

With the FF contribution isolated, the required dihedral profile is obtained by subtracting the FF contribution from the DFT scan. The resulting 'subtracted' profile is then fit to a 5th order Ryckaert-Bellmans function:

$$V_{RB}(\phi) = 4 \sum_{n=0}^5 c_n [\pm \cos(\phi)]^n \quad (5.2)$$

The fit function described in Equation 5.2 yields two sets of parameters. This results

from the difference of 180° between one pair of dihedral angles and another of the four used. For example, for a dihedral angle of 0° in the polymer convention, the dihedral angle of the two pairs of four atoms in the *trans* position is ϕ° while the two pairs in the *cis* position have a $(\phi + 180)^\circ$ dihedral angle. As such, the function cosine terms in Equation 5.2 must be modified to $\cos(\phi + 180) = -\cos(\phi)$ in order to yield the appropriate energy.

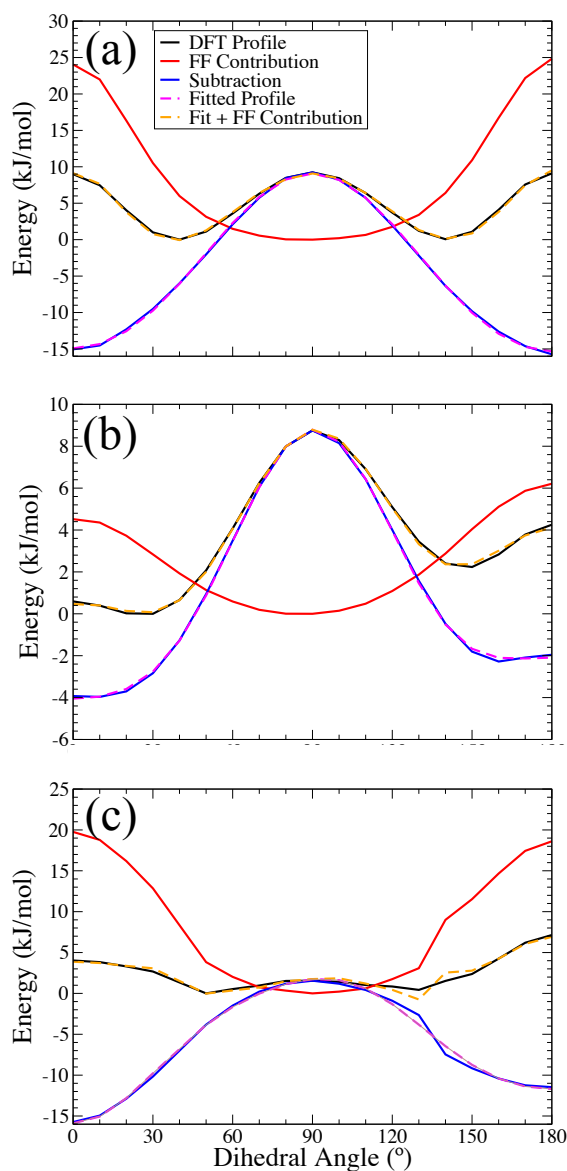


Figure 5.25: Subtraction profiles for (a) fluorene, (b) thiophene and (c) ethyl-thiophene. Each figure displays the calculated DFT profile; the profile obtained from the MD 'scan'; the resulting subtracted profile; the fit of the subtracted profile to a 5th order Ryckaert-Bellmans function; and the resulting 'effective' profile given by the addition of the MD scan profile and the fitted profile. (Legend applies to all graphs.)

Figure 5.25 provides examples of the curves obtained in the subtraction process for 2mers of fluorene, thiophene, and ethyl-thiophene. In the cases with no side-chains, Figure 5.25(a) and (b), it can be seen that this procedure and the fitting with the

Table 5.7: Height of the energetic barriers at 0° (E_0) and 180° (E_{180}) for 2mers ethyl-thiophene, methyl-thiophene, and thiophene using fitted profiles obtained from scans using different side-chain lengths. Each barrier is calculated relative to the closest local minimum (i.e. the *trans* minimum for ΔE_0 and the *cis* minimum for ΔE_{180}). The labels Tx (Ty) denote the energies of a 2mer with an x -yl side-chain with energetic profile taken from a y -yl side-chain scan. The DFT values shown are those from the dihedral scan of the Tx molecule.

	ΔE_0 (kJ/mol)		ΔE_{180} (kJ/mol)	
	DFT	MD	DFT	MD
T0 (T0)	0.59	0.33	2.02	1.75
T1 (T0)	1.20	5.35		7.21
T1 (T1)	1.20	1.33	4.65	5.00
T2 (T0)	4.02	11.07	6.71	12.00
T2 (T1)	4.02	6.67	6.71	9.18
T2 (T2)	4.02	3.90	6.71	7.66

Ryckaert-Bellemans function result in a force-field which quantitatively mimics the DFT dihedral potential to a very high degree of accuracy.

It is noted that this procedure results in a far less smooth fit for ethyl-thiophene, Figure 5.25(c). As discussed with respect to the DFT scans, the introduction of side-chains is a potential source of inconsistency in the calculations due to the relative freedom of side-chains. To minimise this inconsistency, the starting geometries are taken from the DFT calculations so as to reproduce the side-chain conformations as well as possible. However, this does not, in all cases, lead to a perfect agreement in the side-chain conformations between the DFT and FF scans.

As seen from the DFT results for alkyl-fluorenes, Figure 5.18(a), addition of methyl side-chains to fluorene has no effect on the dihedral profile which means no further modification are needed. In the case of alkyl-thiophenes, section 5.4, it was argued that the steric interactions responsible for large changes in dihedral potential should be already accounted for by the force-field. However, as is shown in Table 5.7, utilising the dihedral potential fitted from a thiophene with a shorter side-chain leads to drastically overestimated barriers at the planar positions. As such, reparameterisation of the dihedral term must be performed to accommodate for this. Therefore, given the tendency for inconsistency observed in ethyl-thiophene due to the side-chain degrees of freedom and that the difference in DFT dihedral potential between ethyl and propyl-thiophene is small (≈ 0.5 kJ/mol at the planar barriers, Figure 5.18(b)), the ethyl-thiophene potential is used for thiophene molecules with longer side-chains.

5.7 Molecular Dynamics Results

All MD simulations were carried out using Gromacs 4.6.5^{35,36} with an integrator step-size of 2 fs and system coordinates sampled every 10 ps. Each simulation was performed at ambient temperature and pressure (298.15 K, 1.01325 bar). In all cases, the following measures have been taken prior to the MD run: steepest-descent minimisation; followed by 0.5 ns of both *NVT* and *NPT* ensemble equilibration with position restraints on the heavy atoms of the molecule followed by 5 ns of unrestrained *NPT* equilibration.

Calculations were performed in a fully-solvated manner i.e. in a periodic cubic box large enough to avoid any possible interactions of periodic images. This condition leads, in the case of the largest molecules simulated (32 units in length), to the majority of computational effort being spent on calculating the solvent dynamics. Simulations were performed with chloroform as a solvent. The solvent parameters were obtained from the molecule database at virtualchemistry.org^{69,70}.

Long-range electrostatics in all of the simulations have been treated using the Reaction-Field (RF) scheme⁷¹ with a dielectric constant ϵ_{RF} of 4.81 for chloroform. The RF method for treating the coulomb interaction assumes a constant dielectric environment beyond the cut-off r_c with a dielectric constant of ϵ_{rf} . This leads to the modified Coulomb potential of the following form:

$$V_{RF}(r_{ij}) = f \frac{q_i q_j}{\epsilon_r r_{ij}} \left[1 + \frac{\epsilon_{rf} - \epsilon_r}{2\epsilon_{rf} + \epsilon_r} \frac{r_{ij}^3}{r_c^3} \right] - f \frac{q_i q_j}{\epsilon_r r_c} \frac{3\epsilon_{rf}}{2\epsilon_{rf} + \epsilon_r} \quad (5.3)$$

where the constant expression on the right ensures that the potential V_{RF} is zero at the cut-off r_c . The relative dielectric constant ϵ_r describes the dielectric behaviour within a volume defined by the cut-off radius and is usually set to $\epsilon_r = 1$ which represents a vacuum dielectric environment with local dielectrics emerging from the explicit short-range electrostatics. The ϵ_{rf} defines the dielectric effects within the cut-off volume due to the electrostatics of the solvent used in the simulation.

Table 5.8 summarizes some of the simulation details of 16mers and 32mers of thiophene with hexyl side-chains and fluorene with octyl side-chains. In this table it can be seen that both the temperature and pressure are stable during the simulation and are well within the target values.

As an initial test of derived parameters simulations in chloroform of 32mers of fluorene with octyl side-chains (PF8) and thiophene with hexyl side-chains (P3HT) were

Table 5.8: Simulation details of 16mers and 32mers of thiophene with hexyl side-chains (T6) and fluorene with octyl side-chains (F8). All statistics are over first 50 ns of the simulation time.

Molecule – length	Chloroform molecules	Box dimensions (x=y=z) [nm]	Density [kg/m ³]	Temperature [K]	Pressure [bar]
T6 – 16mer	3289	7.684 ± 0.000	1446.9 ± 0.1	298.14 ± 0.00	0.98 ± 0.06
T6 – 32mer	18621	13.743 ± 0.000	1425.6 ± 0.1	298.12 ± 0.00	0.99 ± 0.03
F8 – 16mer	20750	14.240 ± 0.000	1428.0 ± 0.1	298.11 ± 0.00	1.03 ± 0.02
F8 – 32mer	151644	27.689 ± 0.001	1417.0 ± 0.1	298.09 ± 0.00	1.01 ± 0.01

performed over the course of 50 ns and 100 ns, respectively. Simulations were analysed and persistence lengths, n_p (in number of monomer units) and l_p (in nm) were calculated in order to assess the accuracy of derived parameters. The quantity of persistence length provides a length along the chain over which the tangent vectors of the chain become de-correlated, i.e. it defines how long a straight segment ‘persists’ for and provides an intuitive measure of the overall rigidity of a polymer. For a very large polymer ($L \gg l_p$), a persistent chain effectively behaves like a freely-jointed chain and the persistence length is one half of a so-called Kuhn statistical length (l_K^2), which is the length of hypothetical Kuhn segment in an ideal chain of freely joined segments. Moreover, the persistence length can be inferred from the experimental dynamic light scattering measurements of the radius of gyration (R_g) of polymers in solution. The R_g is defined as a mean-squared quantity that measures the average squared distance of each mass in the molecule from the centre of mass point and for a freely-jointed chain is given as $R_g^2 = \langle R^2 \rangle / 6$ with $\langle R^2 \rangle = N_K l_K^2$ representing the mean square end-to-end distance and N_K , l_K representing the Kuhn segment and Kuhn length, respectively. The persistence length calculations were performed by generating vectors, \mathbf{v}_i , across the first and last carbon of unit i and generating a correlation function, $A(\theta_n)$, of the angles between each pair of vectors, θ_n :

$$A(\theta_n) = \frac{\langle \mathbf{v}_i \cdot \mathbf{v}_{i+n} \rangle}{\langle \mathbf{v}_i \cdot \mathbf{v}_i \rangle} = \langle \cos(\theta_n) \rangle. \quad (5.4)$$

The persistence length^{72,73} is defined by the e^{-1} -point of $A(\theta_n)$ i.e.,

$$A(\theta_n) = \langle \cos(\theta_n) \rangle \approx \exp(-n/n_p). \quad (5.5)$$

The correlation curves for fluorene and thiophene with their respective side-chains

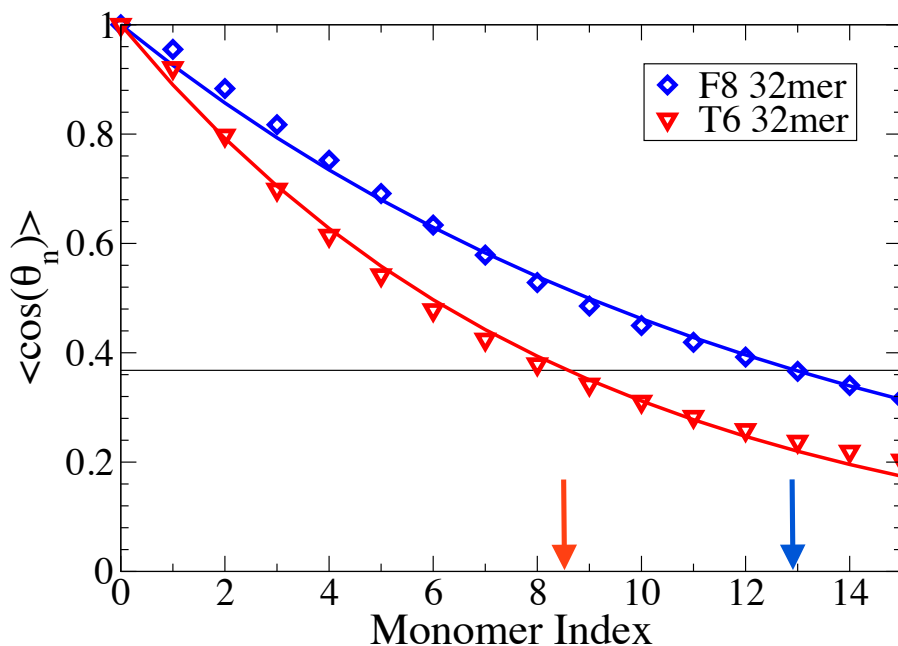


Figure 5.26: Angle correlation functions, $A(\theta_n)$, of 32mers of dioctyl-fluorene (F8) and hexyl-thiophene (T6) simulated in chloroform. Each calculated correlation function is given along with their respective fitted curves (solid lines, given by eq. 5.5). From the fitted curves, n_p , indicated by arrows corresponding to the crossing of the fitted curve and the e^{-1} line, is found to be 12.9 and 8.5 respectively.

are shown in Figure 5.26. By fitting these to the exponential decay function given in Equation 5.5, the persistence lengths are $n_p = 12.9$ and $n_p = 8.5$ units, respectively. In order to recast these into nm, the average unit length, l , are calculated from the MD simulation to be $l = 0.832$ nm for PF8 and $l = 0.397$ nm for P3HT which gives $l_p = 10.8$ nm and $l_p = 3.4$ nm respectively. As a means of comparison, persistence lengths for the polymer in each case have been reported as $l_p = 8 \pm 1$ nm for PF8^{38,39} and $l_p = 2.4 \pm 0.3$ nm for P3HT⁴⁰; both measured by a combination of gel permeation chromatography and light scattering in THF solution.

Although the calculated persistence lengths were obtained from MD simulations in chloroform they show a remarkable agreement with experimental persistence lengths obtained in THF solution. The main reason behind the choice of chloroform in simulations was that simulations with THF are ≈ 5 times more expensive computationally. This stems from the fact when calculations are performed in a fully-solvated manner i.e. in a periodic cubic box large enough to avoid any possible interactions of periodic images, $\approx 2 \times 10^5$ and 2×10^4 solvent molecules per simulation are needed for fluorene and thiophene, respectively. Furthermore, in order to obtain a converged result it was found that it is necessary to use molecules considerably larger than the persistence length. For example, simulating only a 16mer of fluorene resulted in ≈ 2 times larger value of $l_p = 19.5$ units which corresponds to 16.24 nm in comparison to the value obtained for the 32mer. Similar behaviour, but to a considerably lesser extent, was observed for thiophenes with simulation lengths near

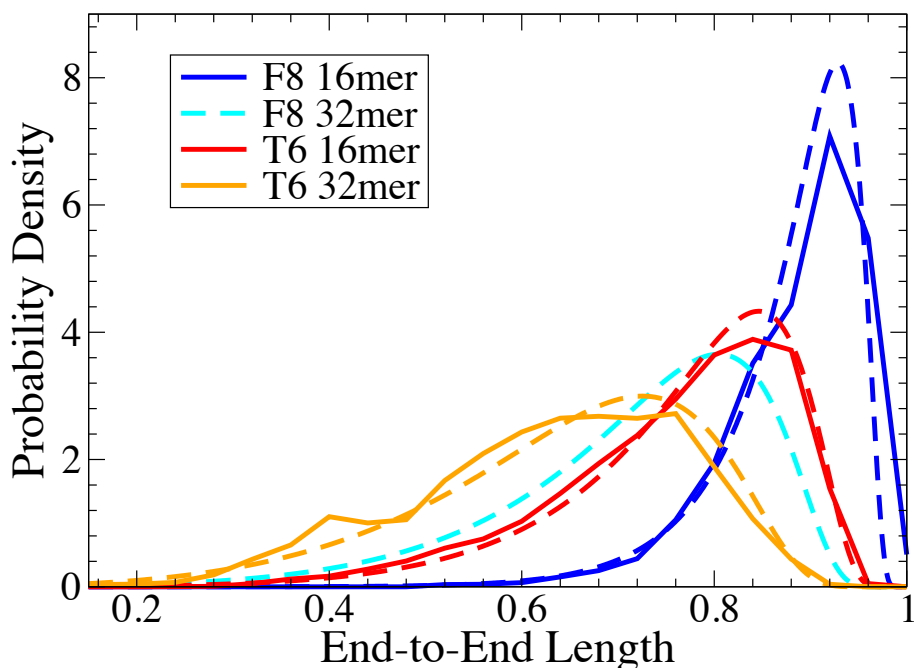


Figure 5.27: End-to-end length distributions (solid lines) for a 16mer of dioctyl-fluorene (F8) and a 16mer and 32mer hexyl-thiophene (T6) in chloroform. The end-to-end length is scaled to give each length as a fraction of the fully extended length of each molecule. Comparison is given for each distribution to the distribution $r^2 P_{ee}(r)$ obtained using Equation 5.6 (dashed lines)^{74,75} with a curve for an F8 32mer given based on the calculated persistence length.

the persistence-length (e.g. $l_p = 9.5$ units for a 5mer).

Figure 5.27 shows distributions of end-to-end length computed from simulations for 16mers of dioctyl-fluorene and 16mers and 32mers of hexyl-thiophene in chloroform. The distributions for 32mers of dioctyl-fluorene have not been shown as, while the tangent correlation curves were converged, after 50ns the end-to-end length distributions were far from converged. In each example, the end-to-end length is given as a fraction, r , of the straight length of the molecule, Nl , where N is the number of units and l is the mean unit length given above.

When a comparison is made between each length of thiophene, it can be seen that the 32mer has a much wider distribution which peaks at a lower length fraction (0.7) than that of the 16mer which is narrower and peaked at ≈ 0.85 . Given the shorter persistence length calculated, the distribution for the 16mer of fluorene is less spread and peaked at a higher length fraction ≈ 0.9 than the 16mer and 32mer of thiophene. The distribution obtained for the 16mer of fluorene are consistent with measurements performed by Muls *et al.* Using end-marked hexyl-fluorenes of a similar length scale (≈ 42 monomer units with a polydispersity of 1.8) in an inert Zeonex matrix, they measured end-end length distributions which are centred at a length fraction (based on the fully-extended 42mer) of ≈ 0.89 ⁷⁶.

Both the progression of the distributions and the difference in overall spread between fluorene and largely spread thiophene can be understood qualitatively by considering the increase in conformational entropy with increasing length and is consistent with the persistence lengths calculated previously. For a quantitative insight, we have also calculated the end-to-end length distributions, $P_{ee}(r)$, using the expression derived by a path-integral approach for semi-flexible polymers by Wilhelm and Frey^{74,75}:

$$P_{ee}(r) = \mathcal{N} \sum_{k=1}^{\infty} (-1)^{k+1} k^2 \pi^2 e^{-k^2 \pi^2 \xi (1-r)} \quad (5.6)$$

Where r is the end-to-end length fraction, $\xi = n_p/N$ is the persistence length fraction, and \mathcal{N} is the normalisation constant such that $\int_0^1 dr r^2 P_{ee}(r) = 1$. The values of ξ used are $\xi = 1.219, 0.403, 0.531, 0.266$ for the 16mer and 32mer of fluorene, and the 16mer and 32mer of thiophene respectively. For each fluorene, the corresponding persistence length was used due to the large difference for both lengths (as described above). The value calculated for the 32mer was used for both thiophenes. For all the distributions calculated, each MD distribution agrees well with the corresponding calculated result and we expect that this behaviour would be replicated by a fully converged fluorene 32mer distribution.

5.8 Discussion and Conclusion

It was shown, for the two systems considered, that it is possible to reproduce dihedral profiles obtained at high level of theory using a much more economical two-step approach with CAM-B3LYP/6-31G* and CAM-B3LYP/cc-pVTZ for geometry optimisation scans and single-point energy calculations, respectively. Further, it has been found that dihedral potentials are invariant to the length of the molecular conjugated backbone and that any effect due to the inclusion of side-chains seems to stem from long-range interactions alone.

When it comes to the partial charge distributions it was shown that these converge quickly with varying length of molecule. However, one must take into account potential deviations in end monomer distributions for molecules which do not possess end-to-end reflection symmetry. In terms of varying side-chains, it seems that there is no simple way of generalising the inclusion of partial charges to this variation.

Utilising the above findings a parameterisation scheme has been developed which is potentially applicable to a wide range of conjugated molecules. This scheme assumes

pre-existing parameters for monomeric units (e.g. bond-stretching, angle-bending parameters and L-J terms) where some of the missing parameters can be derived from similar chemical groups. For example, substituting internal dihedrals, which are not specified, with the dihedral potential for four aromatic carbons. In the next step dihedral profiles are generated using two-step CAM-B3LYP/6-31G**//CAM-B3LYP/cc-pVTZ approach for 2mer without side-chains for molecules with side-chains far from the inter-monomer junction. In the case of molecules with side-chains close to the inter-monomer junction, such as in 3-alkyl-thiophenes, a more detailed re-parameterisation may be needed due to potential high steric contributions of these side-chains to the dihedral energetics. The following step involves partial charges calculation with electron density calculated at the CAM-B3LYP/cc-pVTZ SP step. This step involves calculating partial charges using the three residue model with the RESP scheme, finding a convergence length for total charges of the backbone units and derive partial charges for side-chains. The final step involves implementing the above derived parameters either directly as in the case of partial charges or using the subtraction procedure as in the case of dihedral profile.

Preliminary results of persistence lengths and end-to-end lengths calculations using the MD simulations with newly derived parameters indicate that these are consistent with experimentally derived values with long thiophene oligomers displaying far greater flexibility than their fluorene counterparts.

References

- [1] Wildman, J.; Repiscak, P.; Paterson, M. J.; Galbraith, I. *J. Chem. Theory Comput.* **2016**, *12*(8), 3813–3824.
- [2] Guo, X.; Baumgarten, M.; Müllen, K. *Prog. Polym. Sci.* **2013**, *38*(12), 1832–1908.
- [3] Sekine, C.; Tsubata, Y.; Yamada, T.; Kitano, M.; Doi, S. *Sci. Technol. Adv. Mater.* **2014**, *15*(3), 034203–034217.
- [4] Khan, N.; Kausar, A.; Rahman, A. U. *Polym.-Plast. Technol. Eng.* **2014**, *54*(2), 140–154.
- [5] Hedley, G. J.; Ward, A. J.; Alekseev, A.; Howells, C. T.; Martins, E. R.; Serrano, L. A.; Cooke, G.; Ruseckas, A.; Samuel, I. D. W. *Nat. Commun.* **2013**, *4*, 2867–2876.
- [6] Kilina, S.; Dandu, N.; Batista, E. R.; Saxena, A.; Martin, R. L.; Smith, D. L.; Tetriak, S. *J. Phys. Chem. Lett.* **2013**, *4*, 1453 – 1459.

- [7] Schumacher, S.; Ruseckas, A.; Montgomery, N. A.; Skabara, P. J.; Kanibolotsky, A. L.; Paterson, M. J.; Galbraith, I.; Turnbull, G. A.; Samuel, I. D. W. *J. Chem. Phys.* **2009**, *131*(15), 154906–154913.
- [8] Schumacher, S.; Galbraith, I.; Ruseckas, A.; Turnbull, G. A.; Samuel, I. D. W. *Phys. Rev. B* **2010**, *81*, 245407–245417.
- [9] Montgomery, N. A.; Hedley, G. J.; Ruseckas, A.; Denis, J.-C.; Schumacher, S.; Kanibolotsky, A. L.; Skabara, P. J.; Galbraith, I.; Turnbull, G. A.; Samuel, I. D. W. *Phys. Chem. Chem. Phys.* **2012**, *14*, 9176–9184.
- [10] Förster, T. *Ann. Phys.* **1948**, *437*, 55–75.
- [11] Denis, J.-C.; Schumacher, S.; Galbraith, I. *J. Chem. Phys.* **2012**, *137*, 224102.
- [12] Denis, J.-C.; Schumacher, S.; Hedley, G. J.; Ruseckas, A.; Morawska, P. O.; Wang, Y.; Allard, S.; Scherf, U.; Turnbull, G. A.; Samuel, I. D. W.; Galbraith, I. *J. Phys. Chem. C* **2015**, *119*(18), 9734–9744.
- [13] Guilbert, A. A. Y.; Frost, J. M.; Agostinelli, T.; Pires, E.; Lilliu, S.; Macdonald, J. E.; Nelson, J. *Chem. Mater.* **2014**, *26*(2), 1226–1233.
- [14] Cheung, D. L.; McMahon, D. P.; Troisi, A. *J. Phys. Chem. B* **2009**, *113*(28), 9393–9401.
- [15] Bhatta, R. S.; Yimer, Y. Y.; Perry, D. S.; Tsige, M. *J. Phys. Chem. B* **2013**, *117*, 10035–10045.
- [16] Guo, Z.; Lee, D.; Liu, Y.; Sun, F.; Sliwinski, A.; Gao, H.; Burns, P. C.; Huang, L.; Luo, T. *Phys. Chem. Chem. Phys.* **2014**, *16*, 7764–7771.
- [17] Ricci, C. G.; de Andrade, A. S. C.; Mottin, M.; Netz, P. A. *The J. Phys. Chem. B* **2010**, *114*(30), 9882–9893.
- [18] Jorgensen, W. L.; Maxwell, D. S.; Tirado-Rives, J. *J. Am. Chem. Soc.* **1996**, *118*(45), 11225–11236.
- [19] Jorgensen, W. L.; McDonald, N. A. *J. Mol. Struct.: THEOCHEM* **1998**, *424*(1, Äi2), 145–155.
- [20] McDonald, N. A.; Jorgensen, W. L. *J. Phys. Chem. B* **1998**, *102*(41), 8049–8059.
- [21] Rizzo, R. C.; Jorgensen, W. L. *J. Am. Chem. Soc.* **1999**, *121*(20), 4827–4836.
- [22] Price, M. L. P.; Ostrovsky, D.; Jorgensen, W. L. *J. Comput. Chem.* **2001**, *22*(13), 1340–1352.

- [23] Watkins, E. K.; Jorgensen, W. L. *J. Phys. Chem. A* **2001**, *105*(16), 4118–4125.
- [24] Kaminski, G. A.; Friesner, R. A.; Tirado-Rives, J.; Jorgensen, W. L. *J. Phys. Chem. B* **2001**, *105*(28), 6474–6487.
- [25] Oostenbrink, C.; Villa, A.; Mark, A. E.; Van Gunsteren, W. F. *J. Comput. Chem.* **2004**, *25*(13), 1656–1676.
- [26] Ho Choi, C.; Kertesz, M.; Karpfen, A. *J. Chem. Phys.* **1997**, *107*(17), 6712–6721.
- [27] Singh, U. C.; Kollman, P. A. *J. Comput. Chem.* **1984**, *5*(2), 129–145.
- [28] Chirlian, L. E.; Francl, M. M. *J. Comput. Chem.* **1987**, *8*(6), 894–905.
- [29] Besler, B. H.; Merz, K. M.; Kollman, P. A. *J. Comput. Chem.* **1990**, *11*(4), 431–439.
- [30] Breneman, C. M.; Wiberg, K. B. *J. Comput. Chem.* **1990**, *11*(3), 361–373.
- [31] Bayly, C. I.; Cieplak, P.; Cornell, W.; Kollman, P. A. *The J. Phys. Chem.* **1993**, *97*(40), 10269–10280.
- [32] Marcon, V.; van der Vegt, N.; Wegner, G.; Raos, G. *J. Phys. Chem. B* **2006**, *110*, 5253–5261.
- [33] DuBay, K. H.; Hall, M. L.; Hughes, T. F.; Wu, C.; Reichman, D. R.; Friesner, R. A. *J. Chem. Theory Comput.* **2012**, *8*, 4556–4569.
- [34] Bright, D. W.; Dias, F. B.; Galbrecht, F.; Scherf, U.; Monkman, A. P. *Adv. Funct. Mater.* **2009**, *19*(1), 67–73.
- [35] Van Der Spoel, D.; Lindahl, E.; Hess, B.; Groenhof, G.; Mark, A. E.; Berendsen, H. J. C. *J. Comput. Chem.* **2005**, *26*(16), 1701–1718.
- [36] Hess, B.; Kutzner, C.; van der Spoel, D.; Lindahl, E. *J. Chem. Theory Comput.* **2008**, *4*(3), 435–447.
- [37] Bhatta, R. S.; Yimer, Y. Y.; Tsige, M.; Perry, D. S. *Comput. Theor. Chem.* **2012**, *995*, 36–42.
- [38] Grell, M.; Bradley, D.; Long, X.; Chamberlain, T.; Inbasekaran, M.; Woo, E.; Soliman, M. *Acta Polym.* **1998**, *49*(8), 439–444.
- [39] Fytas, G.; Nothofer, H. G.; Scherf, U.; Vlassopoulos, D.; Meier, G. *Macromolecules* **2002**, *35*(2), 481–488.
- [40] Heffner, G. W.; Pearson, D. S. *Macromolecules* **1991**, *24*(23), 6295–6299.

- [41] Bloom, J. W. G.; Wheeler, S. E. *J. Chem. Theory Comput.* **2014**, *10*(9), 3647–3655.
- [42] Raos, G.; Famulari, A.; Marcon, V. *Chem. Phys. Lett.* **2003**, *379*(3–4), 364–372.
- [43] Marcon, V.; Raos, G. *J. Phys. Chem. B* **2004**, *108*(46), 18053–18064.
- [44] Sánchez-Sanz, G.; Alkorta, I.; Elguero, J. *Comp. Theor. Chem.* **2011**, *974*(1–3), 37–42.
- [45] Fabiano, E.; Della Sala, F. *Chem. Phys. Lett.* **2006**, *418*(4–6), 496–501.
- [46] Salzner, U.; Aydin, A. *J. Chem. Theory Comput.* **2011**, *7*(8), 2568–2583.
- [47] Sutton, C.; Körzdörfer, T.; Gray, M. T.; Brunsfeld, M.; Parrish, R. M.; Sherrill, C. D.; Sears, J. S.; Brédas, J.-L. *J. Chem. Phys.* **2014**, *140*(5), –.
- [48] Grimme, S. *J. Comput. Chem.* **2006**, *27*(15), 1787–1799.
- [49] Grimme, S.; Ehrlich, S.; Goerigk, L. *J. Comput. Chem.* **2011**, *32*(7), 1456–1465.
- [50] Gaussian09 Revision D.01. Frisch, M. J.; Trucks, G. W.; Schlegel, H. B.; Scuse-ria, G. E.; Robb, M. A.; Cheeseman, J. R.; Scalmani, G.; Barone, V.; Mennucci, B.; Petersson, G. A.; Nakatsuji, H.; Caricato, M.; Li, X.; Hratchian, H. P.; Izmaylov, A. F.; Bloino, J.; Zheng, G.; Sonnenberg, J. L.; Hada, M.; Ehara, M.; Toyota, K.; Fukuda, R.; Hasegawa, J.; Ishida, M.; Nakajima, T.; Honda, Y.; Kitao, O.; Nakai, H.; Vreven, T.; Montgomery, Jr., J. A.; Peralta, J. E.; Ogliaro, F.; Bearpark, M.; Heyd, J. J.; Brothers, E.; Kudin, K. N.; Staroverov, V. N.; Kobayashi, R.; Normand, J.; Raghavachari, K.; Rendell, A.; Burant, J. C.; Iyengar, S. S.; Tomasi, J.; Cossi, M.; Rega, N.; Millam, J. M.; Klene, M.; Knox, J. E.; Cross, J. B.; Bakken, V.; Adamo, C.; Jaramillo, J.; Gomperts, R.; Stratmann, R. E.; Yazyev, O.; Austin, A. J.; Cammi, R.; Pomelli, C.; Ochterski, J. W.; Martin, R. L.; Morokuma, K.; Zakrzewski, V. G.; Voth, G. A.; Salvador, P.; Dannenberg, J. J.; Dapprich, S.; Daniels, A. D.; Farkas, O.; Foresman, J. B.; Ortiz, J. V.; Cioslowski, J.; Fox, D. J.
- [51] Werner, H.-J.; Knowles, P. J.; Knizia, G.; Manby, F. R.; Schütz, M. *WIREs Comput Mol Sci* **2012**, *2*, 242–253.
- [52] Molpro, version 2012.1, a package of ab initio programs. Werner, H.-J.; Knowles, P. J.; Knizia, G.; Manby, F. R.; Schütz, M.; Celani, P.; Korona, T.; Lindh, R.; Mitrushenkov, A.; Rauhut, G.; Shamasundar, K. R.; Adler, T. B.; Amos, R. D.; Bernhardsson, A.; Berning, A.; Cooper, D. L.; Deegan, M. J. O.; Dobbyn, A. J.; Eckert, F.; Goll, E.; Hampel, C.; Hesselmann, A.; Hetzer, G.; Hrenar, T.; Jansen, G.; Köppl, C.; Liu, Y.; Lloyd, A. W.; Mata, R. A.; May, A. J.; Mc-Nicholas, S. J.; Meyer, W.; Mura, M. E.; Nicklass, A.; O’Neill, D. P.; Palmieri,

- P.; Peng, D.; Pflüger, K.; Pitzer, R.; Reiher, M.; Shiozaki, T.; Stoll, H.; Stone, A. J.; Tarroni, R.; Thorsteinsson, T.; Wang, M. **2012**.
- [53] Boughton, J. W.; Pulay, P. *J. Comput. Chem.* **1993**, *14*(6), 736–740.
- [54] Hampel, C.; Werner, H.-J. *J. Chem. Phys.* **1996**, *104*(16), 6286–6297.
- [55] Chai, J.-D.; Head-Gordon, M. *J. Chem. Phys.* **2008**, *128*(8).
- [56] Chai, J.-D.; Head-Gordon, M. *Phys. Chem. Chem. Phys.* **2008**, *10*, 6615–6620.
- [57] Ditchfield, R.; Hehre, W. J.; Pople, J. A. *J. Chem. Phys.* **1971**, *54*(2), 724–728.
- [58] Hehre, W. J.; Ditchfield, R.; Pople, J. A. *J. Chem. Phys.* **1972**, *56*(5), 2257–2261.
- [59] Hariharan, P.; Pople, J. *Theor. Chem. Acc.* **1973**, *28*(3), 213–222.
- [60] Hariharan, P.; Pople, J. *Mol. Phys.* **1974**, *27*(1), 209–214.
- [61] Gordon, M. S. *Chem. Phys. Lett.* **1980**, *76*(1), 163–168.
- [62] Francl, M. M.; Pietro, W. J.; Hehre, W. J.; Binkley, J. S.; Gordon, M. S.; DeFrees, D. J.; Pople, J. A. *J. Chem. Phys.* **1982**, *77*(7), 3654–3665.
- [63] Binning, R. C.; Curtiss, L. A. *J. Comput. Chem.* **1990**, *11*(10), 1206–1216.
- [64] Blaudeau, J.-P.; McGrath, M. P.; Curtiss, L. A.; Radom, L. *J. Chem. Phys.* **1997**, *107*(13), 5016–5021.
- [65] Rassolov, V. A.; Pople, J. A.; Ratner, M. A.; Windus, T. L. *J. Chem. Phys.* **1998**, *109*(4), 1223–1229.
- [66] Rassolov, V. A.; Ratner, M. A.; Pople, J. A.; Redfern, P. C.; Curtiss, L. A. *J. Comput. Chem.* **2001**, *22*(9), 976–984.
- [67] Dunning, T. H. *J. Chem. Phys.* **1989**, *90*(2), 1007–1023.
- [68] Amber 14. Case, D. A.; Darden, T. A.; Cheatham, T. E.; Simmerling, C. L.; Wang, J.; Duke, R. E.; Luo, R.; Walker, R. C.; Zhang, W.; Merz, K. M.; Roberts, B.; Hayik, S.; Roitberg, A.; Seabra, G.; Swails, J.; Goetz, A. W.; Kolossváry, I.; Wong, K. F.; Paesani, F.; Vanicek, J.; Wolf, R. M.; Liu, J.; Wu, X.; Brozell, S. R.; Steinbrecher, T.; Gohlke, H.; Cai, Q.; Ye, X.; Wang, J.; Hsieh, M. J.; Cui, G.; Roe, D. R.; Mathews, D. H.; Seetin, M. G.; Salomon-Ferrer, R.; Sagui, C.; Babin, V.; Luchko, T.; Gusarov, S.; Kovalenko, A.; Kollman, P. A. **2014**.
- [69] Caleman, C.; van Maaren, P. J.; Hong, M.; Hub, J. S.; Costa, L. T.; van der Spoel, D. *J. Chem. Theory Comput.* **2012**, *8*(1), 61–74.

- [70] van der Spoel, D.; van Maaren, P. J.; Caleman, C. *Bioinformatics* **2012**, *28*(5), 752–753.
- [71] Barker, J.; Watts, R. *Mol. Phys.* **1973**, *26*(3), 789–792.
- [72] Flory, P. J. *Statistical Mechanics of Chain Molecules*; Wiley (Interscience), New York, 1969.
- [73] Doi, M.; Edwards, S. F. *The Theory of Polymer Dynamics*; Clarendon, Oxford University Press, New York, 1986.
- [74] Wilhelm, J.; Frey, E. *Phys. Rev. Lett.* **1996**, *77*, 2581–2584.
- [75] Kleinert, H. *FRONT MATTER*; World Scientific: Singapore, 5th ed., 2012.
- [76] Muls, B.; Uji-i, H.; Melnikov, S.; Moussa, A.; Verheijen, W.; Soumillion, J.-P.; Josemon, J.; Müllen, K.; Hofkens, J. *ChemPhysChem* **2005**, *6*(11), 2286–2294.

Chapter 6

Summary and Future Work

This thesis covers two different areas of computational chemistry. First two chapters use the electronic structure theory methods in order to study transition metal organic molecule interactions which play important role in biological effects of type 2 diabetes drug and redox potential calculations of copper systems. The complexity of dealing with open-shell transition metal systems is examined and addressed. The last chapter uses the *ab initio* methods in order to establish accurate and reliable methodology for development of molecular dynamics parameterisation scheme applicable to organic conjugated materials with the aim of allowing molecular dynamics simulations to start to understand how conformation affects morphology.

Chapter 3 examined metal-binding properties of important type 2 diabetes drug metformin and structurally similar compounds. It was concluded that the copper-binding properties of neutral biguanide compounds (BG and Metf) and PDI cannot solely explain the differences in the biomolecular mode of action of these compounds. One of the proposed mechanism explaining the difference in biological effect is a possible deprotonation of biguanide compounds, in contrast to PDI, under higher mitochondrial pH which would lead to formation of more stable copper complexes and potentially affecting the mitochondrial copper homeostasis. Further, redox properties of copper-biguanide complexes could interfere with the sensitive redox machinery, such as the electron transport chain, present in the mitochondria. Furthermore, ESP maps of ligands showed that stronger hydrophilicity of BG could play a role in molecular recognition processes and its mitochondrial activity. Further work will mainly investigate redox properties of these compounds in more details. In addition, potential interaction of these compounds with metalloproteins will be studied.

Chapter 4 described a systematic development and testing of computational protocol for calculation of reduction potentials of copper complexes. It was proposed that

suitable method for redox protocol of copper complexes is to use M06/cc-pVTZ with the SMD solvation or either M06L or TPSS/PSS functional with cc-pVTZ basis set and the PCM solvation model. Future work would involve in-depth investigation of functional and basis sets choice on various properties, for example, implicit solvent cavity shape/size and HOMO/LUMO gap. Moreover, use of other methods in order to obtain more accurate electron affinities (ionization potentials) and free-energies of solvation will be considered. For example, this would involve use of an electron propagator theory for calculations of correlated electron affinities and ionization potentials. Also, a potential way of systematically improving calculated electron affinities and ionization potentials is by using local wave function methods, such as local MP2 or CC, which by using orbital localization allows to obtain results close to results from canonical methods for much larger systems of interest. Including one or more explicit solvent molecules in conjunction with implicit solvent in an extended QM/MM scheme would potentially lead to improvement of free-energies of solvation. An ideal protocol for computation of redox potentials would involve *ab-initio* QM/MM molecular dynamics simulations. The QM part would involve high level of theory (e.g. CASSCF) ideally able to treat multireference character of transition metal complexes. The MM part would include enough explicit solvent molecules or protein environment in order to account for short-range interaction with the solute and the whole system would be immersed in an implicit solvent to account for bulk electrostatic effects. The molecular dynamics would provide time-evolution of the system accounting for conformational sampling and thus potentially generate ensemble similar to the experimental one. Also within this scheme since the studied complexes had a rather rigid framework it would be interesting to investigate the effect of more flexible binding sites and environmental effects. This way it would be possible to address some of the issues arising from the use of the implicit solvation.

In Chapter 5 a scheme is developed that can be used to obtain force-field parameters for simulations of large organic conjugated polymers applicable in opto-electronic materials. This chapter first systematically tested the required methodology in order to obtain accurate critical force-field parameters. Some preliminary results of persistence lengths and end-to-end lengths obtained from simulations using the derived parameters show promising agreement with the experimental values. Future work will involve further validation and testing of obtained parameters as well as application of molecular dynamics of these systems to, for example, conformational sampling and subsequent optical studies.